On the Calculation of Dynamic Derivatives Using Computational Fluid Dynamics

Thesis submitted in accordance with the requirements of
the University of Liverpool for the degree of Doctor in Philosophy
by

Andrea Da Ronch
M.Sc. [Aeronautics], Politecnico di Milano (Italy) and
Royal Institute of Technology (Sweden), 2008
B.E. [Aerospace], Politecnico di Milano (Italy), 2006

March 2012

Abstract

In this thesis, the exploitation of computational fluid dynamics (CFD) methods for the flight dynamics of manoeuvring aircraft is investigated. It is demonstrated that CFD can now be used in a reasonably routine fashion to generate stability and control databases. Different strategies to create CFD-derived simulation models across the flight envelope are explored, ranging from combined low-fidelity/high-fidelity methods to reduced-order modelling.

For the representation of the unsteady aerodynamic loads, a model based on aerodynamic derivatives is considered. Static contributions are obtained from steady-state CFD calculations in a routine manner. To more fully account for the aircraft motion, dynamic derivatives are used to update the steady-state predictions with additional contributions. These terms are extracted from small-amplitude oscillatory tests. The numerical simulation of the flow around a moving airframe for the prediction of dynamic derivatives is a computationally expensive task. Results presented are in good agreement with available experimental data for complex geometries. A generic fighter configuration and a transonic cruiser wind tunnel model are the test cases. In the presence of aerodynamic non-linearities, dynamic derivatives exhibit significant dependency on flow and motion parameters, which cannot be reconciled with the model formulation. An approach to evaluate the sensitivity of the non-linear flight simulation model to variations in dynamic derivatives is described.

The use of reduced models, based on the manipulation of the full-order model to reduce the cost of calculations, is discussed for the fast prediction of dynamic derivatives. A linearized solution of the unsteady problem, with an attendant loss of generality, is inadequate for studies of flight dynamics because the aircraft may experience large excursions from the reference point. The harmonic balance technique, which approximates the flow solution in a Fourier series sense, retains a more general validity. The model truncation, resolving only a small subset of frequencies typically restricted to include one Fourier mode at the frequency at which dynamic derivatives are desired, provides accurate predictions over a range of two- and three-dimensional test cases. While retaining the high fidelity of the full-order model, the cost of calculations is a fraction of the cost for solving the original unsteady problem.

An important consideration is the limitation of the conventional model based on

aerodynamic derivatives when applied to conditions of practical interest (transonic speeds and high angles of attack). There is a definite need for models with more realism to be used in flight dynamics. To address this demand, various reduced models based on system-identification methods are investigated for a model case. A non-linear model based on aerodynamic derivatives, a multi-input discrete-time Volterra model, a surrogate-based recurrence-framework model, linear indicial functions and radial basis functions trained with neural networks are evaluated. For the flow conditions considered, predictions based on the conventional model are the least accurate. While requiring similar computational resources, improved predictions are achieved using the alternative models investigated.

Furthermore, an approach for the automatic generation of aerodynamic tables using CFD is described. To efficiently reduce the number of high-fidelity (physics-based) analyses required, a kriging-based surrogate model is used. The framework is applied to a variety of test cases, and it is illustrated that the approach proposed can handle changes in aircraft geometry. The aerodynamic tables can also be used in real-time to fly the aircraft through the database. This is representative of the role played by CFD simulations and the potential impact that high-fidelity analyses might have to reduce overall costs and design cycle time.

Acknowledgements

I would like to acknowledge my supervisors Profs. K. J. Badcock and G. N. Barakos. I would also like to extend my thanks to Dr. M. Ghoreyshi, now at USAF Academy, and all the colleagues, both past and present, in the Computational Fluid Dynamics Laboratory at the University of Liverpool for fruitful discussions and for creating a stimulating working environment over the past three years.

I particularly wish to thank Prof. K. J. Badcock who has been a great mentor and an example of continuous inspiration. His encouragement and ideas were of utmost help to this work and are very much appreciated. Last, but not least, my family shall not be forgotten for their support and patience.

The financial support of the "SimSAC" project of the Sixth framework program of the European Union under grant FP6-030838 is appreciated.

Declaration

I confirm that the thesis is my own work, that I have not presented anyone else's work as my own and that full and appropriate acknowledgement has been given where reference has been made to the work of others.

Andrea Da Ronch
March 2012

List of Publications

Refereed Journals

Da Ronch, A., Vallespin, D., Ghoreyshi, M., and Badcock, K. J., "Evaluation of Dynamic Derivatives Using Computational Fluid Dynamics," AIAA Journal, 2012; 50(2): 470–484. doi: 10.2514/1.J051304.

Da Ronch, A., Ghoreyshi, M., and Badcock, K. J., "On the Generation of Flight Dynamics Aerodynamic Tables by Computational Fluid Dynamics," Progress in Aerospace Sciences, 2011; 47(8): 597–620. doi: 10.1016/j.paerosci.2011.09.001.

Da Ronch, A., McCracken, A., Badcock, K. J., Widhalm, M., and Campobasso, M. S., "Linear Frequency Domain and Harmonic Balance Predictions of Dynamic Derivatives," submitted to Journal of Aircraft, 2011.

Vallespin, D., Da Ronch, A., Badcock, K. J., and Boelens, O., "Validation of Vortical Flow Predictions for a UCAV Wind Tunnel Model," Journal of Aircraft, 2011; 48(6): 1948–1959. doi: 10.2514/1.C031385.

Ghoreyshi, M., Badcock, K. J., Da Ronch, A., Vallespin, D., and Rizzi, A., "Automated CFD Analysis for the Investigation of Flight Handling Qualities," Mathematical Modelling of Natural Phenomena, 2011; 6(3): 166–188. doi: 10.1051/mmnp/20116307.

Ghoreyshi, M., Badcock, K. J., Da Ronch, A., Marques, S., Swift, A., and Ames, N., "Framework for Establishing the Limits of Tabular Aerodynamic Models for Flight Dynamics Analysis," Journal of Aircraft, 2011; 48(1): 42–55. doi: 10.2514/1.C001003.

Vallespin, D., Badcock, K. J., Da Ronch, A., White, M., Perfect, P., and Ghoreyshi, M., "Computational Fluid Dynamics Framework for Aerodynamic Model Assessment," to appear in Progress in Aerospace Sciences, 2012.

Mialon, B., Khrabrov, A., Khelil, S. B., Huebner, A., Da Ronch, A., Badcock, K. J., Cavagna, L., Eliasson, P., Zhang, M., Ricci, S., Jouhaud, J.-C., Rogé, G., Hitzel, S., and Lahuta, M., "Validation of Numerical Prediction of Dynamic Derivatives: The DLR-F12 and the Transcruiser Test Cases," Progress in Aerospace Sciences, 2011;

47(8): 674–694. doi: 10.1016/j.paerosci.2011.05.002.

Richardson, T., McFarlane, C., Isikveren, A., Badcock, K. J., and Da Ronch, A., "Analysis of Conventional and Asymmetric Aircraft Configurations Using CEASIOM," Progress in Aerospace Sciences, 2011; 47(8): 647–659. doi: 10.1016/j.paerosci.2011.08.008

Richardson, T., Beaverstock, C., Isikveren, Meheri, A., Badcock, K. J., and Da Ronch, A., "Analysis of the Boeing 747–100 Using CEASIOM," to appear in Progress in Aerospace Sciences, 2011; 47(8): 695–705. doi: 10.1016/j.paerosci.2011.08.009

Badcock, K. J., Timme, S., Marques, S., Khodaparast, H., Prandina, M., Mottershead, J. E., Swift, A., Da Ronch, A., and Woodgate, M., "Transonic Aeroelastic Simulation for Envelope Searches and Uncertainty Analysis," Progress in Aerospace Sciences, 2011; 47(5): 392–423. doi: 10.1016/j.paerosci.2011.05.002.

Papers in Conference Proceedings

Da Ronch, A., McCracken, A., Badcock, K. J., Ghoreyshi, M., and Cummings, R. M., "Modeling of Unsteady Aerodynamic Loads," AIAA–2011–2376, AIAA Atmospheric Flight Mechanics Conference, Portland, Oregon, 8–11 Aug 2011.

Da Ronch, A., Ghoreyshi, M., Vallespin, D., Badcock, K. J., Mengmeng, Z., Oppelstrup, J., and Rizzi, A., "A Framework for Constrained Control Allocation Using CFD-based Tabular Data," AIAA–2011–925, 49th AIAA Aerospace Sciences Meeting and Exhibit, Orlando, Florida, 4–7 Jan 2011.

Da Ronch, A., McFarlane, C., Beaverstock, C., Oppelstrup, J., Mengmeng, Z., and Rizzi, A., "Benchmarking CEASIOM Software to Predict Flight Control and Flying Qualities of the B–747," ICAS 2010–282, Proceedings of the 27th Congress of the International Council of the Aeronautical Sciences, Nice, France, 19–24 Sep, 2010.

Mialon, B., Khrabrov, A., Da Ronch, A., Cavagna, L., Mengmeng, Z., and Ricci, S., "Benchmarking the Prediction of Dynamic Derivatives: Wind Tunnel Tests, Validation, Acceleration Methods," AIAA–2010–8244, AIAA Guidance, Navigation and Control Conference, Toronto, Canada, 2–5 Aug, 2010.

McFarlane, C., Richardson, T. S., Da Ronch, A., and Badcock, K. J., "Comparison of Conventional and Asymmetric Aircraft Configurations Using CEASIOM," AIAA–2010–8243, AIAA Guidance, Navigation and Control Conference, Toronto, Canada, 2–5 Aug, 2010.

Ghoreyshi, M., Vallespin, D., Badcock, K. J., Da Ronch, A., Vos, J. B., and Hitzel, S., "Flight Manoeuvre Validation of Data Tables Generated Using an Aerodynamic Model Hierarchy," AIAA–2010–8239, AIAA Guidance, Navigation and Control Conference, Toronto, Canada, 2–5 Aug, 2010.

Eliasson, P., Vos, J. B., Da Ronch, A., Mengmeng, Z., and Rizzi, A., "Virtual Aircraft Design of TransCRuiser – Computing Break Points in Pitch Moment Curve," AIAA–2010–4366, 28th AIAA Applied Aerodynamics Conference, Chicago, IL, 28 Jun–1 Jul, 2010.

Vallespin, D., Da Ronch, A., Boelens, O., and Badcock, K. J., "Validation of Vortical Flow Predictions for a UCAV Wind Tunnel Model," AIAA–2010–4560, 28th AIAA Applied Aerodynamics Conference, Chicago, IL, 28 Jun–1 Jul, 2010.

Da Ronch, A., Badcock, K. J., Ghoreyshi, M., Görtz, S., Widhalm, M., Dwight, R., and Campobasso, S., "Linear Frequency Domain and Harmonic Balance Predictions of Dynamic Derivatives," AIAA–2010–4699, 28th AIAA Applied Aerodynamics Conference, Chicago, IL, 28 Jun–1 Jul, 2010.

Da Ronch, A., Vallespin, D., Ghoreyshi, M., and Badcock, K. J., "Computation and Evaluation of Dynamic Derivatives using CFD," AIAA–2010–4817, 28th AIAA Applied Aerodynamics Conference, Chicago, IL, 28 Jun–1 Jul, 2010.

Ghoreyshi, M., Badcock, K. J., Da Ronch, A., Swift, A., Marques, S., and Ames, N., "Framework for Establishing the Limits of Tabular Aerodynamic Models for Flight Dynamics," AIAA–2009–6273, AIAA Atmospheric Flight Mechanics Conference, Chicago, IL, 10–13 Aug 2009.

Ghoreyshi, M., Da Ronch, A., Badcock, K. J., Dees, J., Berard, E., and Rizzi, A., "Aerodynamic Modelling for Flight Dynamics Analysis of Conceptual Aircraft Designs," AIAA–2009–4121, 27th AIAA Applied Aerodynamics, San Antonio, Texas, 22–25 Jun 2009.

Rizzi, A., Grabowski, T., Vos, J., Mieszalski, D., Da Ronch, A., Tomac, M., and Ghoreyshi, M., "Creating Aero-Databases by Adaptive-Fidelity CFD Coupled with S&C Analysis to Predict Flying Qualities," Paper in Special Technology Session, CEAS Paper, Manchester, UK, 26–29 Oct 2009.

Presentations without Proceedings

Da Ronch, A., "Computation of Dynamic Derivatives Using CFD and Acceleration Techniques," Seminar at Duke University (E. H. Dowell's research group), Durham, NC, Jul 2010.

Technical Reports

Da Ronch, A., "CFD Star Documentation," SimSAC Report, Deliverable Number D 3.2-6, 2009.

Table of Contents

Abstract **5**

Acknowledgements **7**

Declaration **9**

List of Publications **11**

List of Figures **19**

List of Tables **25**

List of Symbols **27**

1 Introduction **31**
1.1 Example Applications of CFD 33
1.2 Predictive Aerodynamic Models 34
1.2.1 Linear and Non-linear Indicial Functions 34
1.2.2 Regression Models 35
1.2.3 Radial Basis Functions Interpolation 36
1.2.4 Volterra Theory 36
1.2.5 Proper Orthogonal Decomposition 37
1.2.6 Surrogate-Based Models 38
1.3 Review of Dynamic Derivatives 38
1.4 Thesis Outline 40

2 Formulation **43**
2.1 Introduction 43
2.2 Nonlinear Quasi-Steady Aerodynamic Model 44
2.3 Kriging-Based Framework 46
2.3.1 Initial Sampling 47
2.3.2 Kriging Interpolation 47
2.3.3 Iterative Sampling 49
2.3.4 Data Fusion 50

2.4 Hierarchy of Aerodynamic Models . . . 51
2.4.1 Semi-Empirical Method . . . 51
2.4.2 Linear Potential Solver . . . 52
2.5 CFD Flow Solver . . . 52
2.5.1 PMB (University of Liverpool) . . . 52
2.5.2 TAU (German Aerospace Center) . . . 54
2.5.3 COSA (University of Glasgow) . . . 55
2.5.4 Cobalt . . . 55
2.6 Calculation of Dynamic Derivatives . . . 56

3 Dynamic Derivatives from Unsteady Time-Domain CFD Simulations 61
3.1 Introduction . . . 61
3.2 Test Cases . . . 62
3.2.1 Standard Dynamic Model Aircraft . . . 62
3.2.2 Transonic CRuiser Wind Tunnel Model . . . 64
3.3 Numerical Results . . . 65
3.3.1 Standard Dynamic Model Aircraft . . . 66
3.3.1.1 Mach Number . . . 67
3.3.1.2 Mean Angle of Incidence . . . 70
3.3.1.3 Reduced Frequency . . . 75
3.3.1.4 Oscillatory Amplitude . . . 79
3.3.1.5 Large Amplitude Motions . . . 80
3.3.2 Transonic CRuiser Wind Tunnel Model . . . 82
3.3.2.1 Static Cases . . . 84
3.3.2.2 Small Amplitude Motions . . . 85
3.3.2.3 Large Amplitude Motions . . . 88
3.4 Conclusions . . . 93

4 Dynamic Derivatives from Frequency-Domain Methods 95
4.1 Introduction . . . 95
4.1.1 Harmonic Balance Method . . . 96
4.1.2 Small Disturbance Method . . . 97
4.2 Frequency-Domain Methods . . . 99
4.2.1 Harmonic Balance Method . . . 99
4.2.2 Linear Frequency Domain Method . . . 101
4.2.3 Method of Data Analysis . . . 102
4.3 Two-Dimensional Case . . . 103
4.3.1 Numerical Setup . . . 103
4.3.2 Validation . . . 104
4.3.3 Frequency-Domain Results . . . 109
4.3.4 Computational Efficiency . . . 114

4.4 Three-Dimensional Case . . . 118
4.4.1 Numerical Setup . . . 118
4.4.2 Results . . . 119
4.5 Conclusions . . . 122

5 Reduced Models for Flight Dynamics 125
5.1 Introduction . . . 125
5.2 Two-Dimensional Case . . . 126
5.2.1 Numerical Setup . . . 126
5.2.2 Validation . . . 127
5.2.3 Large Amplitude Manoeuvre . . . 128
5.3 Model Formulation . . . 129
5.3.1 Volterra Series . . . 130
5.3.2 Surrogate-Based Recurrence-Framework . . . 132
5.3.3 Indicial Function . . . 133
5.3.4 Radial Basis Function . . . 134
5.4 Numerical Results . . . 134
5.4.1 Model based on Aerodynamic Derivatives . . . 134
5.4.2 Volterra Series . . . 137
5.4.3 Surrogate-Based Recurrence-Framework . . . 139
5.4.4 Indicial Function and Radial Basis Function . . . 142
5.5 Model Evaluation . . . 143
5.6 Conclusions . . . 145

6 Conclusions and Outlook 147

Bibliography 153

A Applications to Flight Dynamics 171
A.1 Transonic CRuiser Model . . . 171
A.2 Asymmetric Aircraft Model . . . 177
A.3 DLR-F12 Model . . . 180
A.4 Large Transport Civil Aircraft Model . . . 186
A.5 Standard Dynamic Model . . . 193
A.6 Ranger 2000 Aircraft . . . 196
A.7 Conclusions . . . 201

B Applications of Indicial Aerodynamics 203
B.1 Formulation . . . 204
B.2 Validation . . . 205
B.3 Prediction . . . 210
B.4 Conclusions . . . 212

List of Figures

3.1 SDM layout [125] 62
3.2 Surface grid for the SDM model geometry [131] 63
3.3 Viscous grid of TCR wind tunnel model [131] 64
3.4 Chordwise grid section on the wing 65
3.5 Pitching moment coefficient loops for the SDM model geometry at two values of Mach number; the term "tsc" indicates the number of physical time steps per cycle of unsteadiness 68
3.6 Influence of Mach number on the pitch damping derivative for the SDM model geometry; experimental data were obtained in TsAGI [134] 68
3.7 Amplitude ratio, $R(\bar{\omega})$, and phase angle, $\phi(\bar{\omega})$, between the fundamental harmonic of the angle of attack and the fundamental harmonic of pitching moment coefficient; $\bar{\omega}$ indicates the oscillatory frequency of the applied forced motion 70
3.8 Flow field visualization for the SDM model geometry at Mach number of 0.3 71
3.9 Fixed-geometry unsteady calculations for the SDM model geometry at a Mach number of 0.3 and angle of attack of twenty degrees; the term "ts" indicates the number of real time steps; horizontal thick lines mark the variation obtained in forced motion of five degrees amplitude for the half-fine grid 72
3.10 Influence of mean angle of attack on the damping derivatives for the SDM model geometry at Mach number 0.3; experimental data were obtained in IHU [128] and AWT [129] 74
3.11 Isosurface of pressure at mean angle of attack of fifteen degrees for direction increasing and decreasing angle; the axis of rotation is illustrated 75
3.12 Pitching moment coefficient for the SDM model geometry for the coarse grid at mean angle of attack of 0 and 15 degrees; in (a), the term "1 Harmonic" indicates a reconstructed signal with the fundamental frequency only; in (b), the magnitude is plotted as function of the Strouhal number, St 76

3.13 Time history of pitching moment coefficient and phase lag in aerodynamic loads as a function of the reduced frequency; in (a), $\alpha_0 = 15.0°$ and $\alpha_A = 5.0°$; in (b), the mean angle of attack is ten degrees 77

3.14 Influence of reduced frequency on the damping derivatives for the SDM geometry model at Mach number 0.3 ($\alpha_A = 5.0°$); experimental data were obtained in IHU [128] and AWT [129] 78

3.15 Pitching moment coefficient loop for the SDM geometry model for the coarse grid at Mach number 0.3 and several values of the amplitude of motion, α_A 79

3.16 Influence of amplitude on the damping derivatives for the SDM geometry model at Mach number 0.3; experimental data were obtained in IHU [128] and AWT [129] 81

3.17 Non-linear mathematical model and unsteady CFD for a large amplitude manoeuvre ($\alpha_0 = 10.0°$, $\alpha_A = 10.0°$ and $k = 0.0493$); (a) and (b) show the small amplitude effects on the stability derivatives; (c) and (d) show the frequency effects 83

3.18 Differences between time-accurate and time-averaged solutions of local contributions to the normal force coefficient; the axis of rotation is illustrated 84

3.19 Static longitudinal aerodynamic characteristics for the TCR wind tunnel model ($M = 0.117$ and $Re = 0.778 \times 10^6$) 86

3.20 Surface streamlines and flow field visualization of the TCR wind tunnel model at several angles of attack 87

3.21 Damping derivatives for the TCR wind tunnel model ($\alpha_A = 3.0°$); (a) and (b) show the dependence on mean angle of attack (left triangles, $f = 0.5\,Hz$; circles, $f = 1.0\,Hz$; right triangles, $f = 1.5\,Hz$) 89

3.22 Influence of frequency on the damping derivatives for the TCR wind tunnel model at mean angle of attack of ten degrees 90

3.23 Dynamic dependencies for the TCR wind tunnel model for a large amplitude manoeuvre ($\alpha_0 = 8.0°$, $\alpha_A = 10.0°$ and $f = 1.0\,Hz$) 91

3.24 Mathematical model based on aerodynamic stability derivatives from wind tunnel (top) and CFD (bottom) simulations for the prediction of a large amplitude manoeuvre ($\alpha_0 = 8.0°$, $\alpha_A = 10.0°$ and $f = 1.0\,Hz$) 93

4.1 Grid used for the NACA 0012 aerofoil, medium grid (212×51) 105

4.2 NACA 0012: predictions of unsteady time-accurate Euler solutions ($M = 0.755$, $\alpha_0 = 0.016°$, $\alpha_A = 2.51°$, and $k = 0.0814$); experimental data from Landon [173] 106

4.3 Instantaneous pressure coefficient distribution compared to experimental data of Landon [173]; the terms up and down in parenthesis indicate the direction increasing and decreasing angle, respectively (continued) . . . 107

4.4 Instantaneous pressure coefficient distribution compared to experimental data of Landon [173]; the terms up and down in parenthesis indicate the direction increasing and decreasing angle, respectively (concluded) . . . 108

4.5 NACA 0012: influence of amplitude of oscillatory motion, α_A, on the pitching moment coefficient dynamic derivatives ($M = 0.755$, $\alpha_0 = 0.016°$, and $k = 0.0814$) . . . 110

4.6 NACA 0012: normal force and pitching moment coefficients dynamic dependence ($M = 0.755$, $\alpha_0 = 0.016°$, $\alpha_A = 2.51°$, and $k = 0.0814$) . 111

4.7 NACA 0012: zeroth and first harmonic unsteady surface pressure coefficient distribution ($M = 0.755$, $\alpha_0 = 0.016°$, $\alpha_A = 2.51°$, and $k = 0.0814$) . . . 113

4.8 NACA 0012: magnitude and phase of pitching moment coefficient ($M = 0.755$, $\alpha_0 = 0.016°$, $\alpha_A = 2.51°$, and $k = 0.0814$) . . . 115

4.9 NACA 0012: CPU time speed up of the frequency-domain methods with respect to the underlying time-domain method; "Nr Har" indicates the number of harmonics . . . 116

4.10 NACA 0012: error norm in the prediction of the damping-in-pitch obtained using the PMB solver pair; in (b), the term tsc indicates the number of time steps per cycle . . . 117

4.11 Structured and unstructured grids for the DLR-F12 model [182] . . . 119

4.12 DLR-F12 model: normal force and pitching moment coefficients dynamic dependence ($M = 0.73$, $\alpha_0 = 0.70°$, $\alpha_A = 0.50°$, $k = 0.034$, and $h = 6000\,m$) . . . 120

4.13 DLR-F12 model: zeroth and first harmonic unsteady surface pressure coefficient distribution at $Y/s = 0.148$ ($M = 0.73$, $\alpha_0 = 0.70°$, $\alpha_A = 0.50°$, $k = 0.034$, and $h = 6000\,m$) . . . 123

5.1 Viscous grids used for the NACA 0012 aerofoil . . . 127

5.2 NACA 0012: predictions of unsteady time-accurate viscous solutions ($M = 0.6$, $\alpha_0 = 3.16°$, $\alpha_A = 4.59°$, $k = 0.0811$, and $Re = 4.8 \times 10^6$); experimental data from Landon [173] . . . 128

5.3 NACA 0012: unsteady time-accurate viscous solutions for the manoeuvre to be predicted ($M = 0.764$, $\alpha_0 = 0.0°$, $\alpha_A = 8.5°$, $k = 0.0811$, and $Re = 3.0 \times 10^6$); in (c) and (d), pressure contour . . . 129

5.4 Dynamic derivatives for the NACA 0012 aerofoil ($M = 0.764$ and $\alpha_0 = 0.0°$); in (a)-(b), $k = 0.10$ and several values of amplitude; in (c)-(d), $\alpha_A = 0.1°$ and several values of reduced frequency; in (e)-(d), $\alpha_A = 5.0°$ and several values of reduced frequency 136

5.5 Non-linear mathematical model and unsteady CFD for a large amplitude manoeuvre ($M = 0.764$, $\alpha_0 = 0.0°$, $\alpha_A = 8.5°$, and $k = 0.10$); in (a)-(b), dependence on the oscillatory amplitude at reduced frequency $k = 0.10$; in (c)-(d), dependence on the reduced frequency at oscillatory amplitude $\alpha_A = 0.1°$; in (e)-(f), dependence on the reduced frequency at oscillatory amplitude $\alpha_A = 5.0°$ 138

5.6 NACA 0012: predictions of pitching moment dynamic dependence ($M = 0.764$, $\alpha_0 = 0.0°$, $\alpha_A = 8.5°$, and $k = 0.10$); "Model" refers to the discrete-time multi-input Volterra model 139

5.7 Response surfaces of the time evolution of aerodynamic coefficients throughout the parameter space of oscillatory amplitude, α_A ($M = 0.764$, $\alpha_0 = 0.0°$, and $k = 0.10$); the solid curve indicates the solution at an amplitude of 5 deg 140

5.8 Aerodynamic coefficients dynamic dependence for several value of oscillatory amplitude ($M = 0.764$, $\alpha_0 = 0.0°$, and $k = 0.10$); curves are plotted every one-degree increment in amplitude 141

5.9 Model predictions and unsteady CFD for a large amplitude manoeuvre ($M = 0.764$, $\alpha_0 = 0.0°$, $\alpha_A = 8.5°$, and $k = 0.10$); "Model" refers to the surrogate-based recurrence-framework 142

5.10 NACA 0012: indicial responses of pitching moment coefficient to step change in angle of attack and in pitch rate ($M = 0.764$ and $Re = 3.0\times10^6$) 143

5.11 NACA 0012: predictions of pitching moment dynamic dependence ($M = 0.764$, $\alpha_0 = 0.0°$, $\alpha_A = 8.5°$, $k = 0.10$, and $Re = 3.0 \times 10^6$); in (a), "Model" refers to the linear indicial functions, and in (b) to radial basis functions 144

A.1 Mission profile for the TCR configuration 172

A.2 Wind-tunnel testing of the TCR model in TsAGI [148] 172

A.3 TCR wind tunnel model; in (a), flow development computed using the PMB solver at 18° angle of attack at low speed; in (b), canard deflections of ±10° on a grid for use with the EDGE solver 173

A.4 Pitching moment coefficient at low speed for the TCR model; the reference point is located at the centre of gravity given in Table A.1 174

A.5 Distribution of low- and high-fidelity calculations in the two-dimensional parameter space of angle of attack and Mach number; the shaded area illustrates many solutions obtained using the linear potential method, TORNADO; CFD solutions were obtained at an ensemble of isolated points 176
A.6 Baseline configuration representative of the EA500 Very Light Jet . . . 178
A.7 Asymmetric three-lifting surface configuration 179
A.8 Wind-tunnel testings of the DLR-F12 model in DNW-NWB [200] 181
A.9 Different fidelity geometry representations of the DLR-F12 model; XML and WT indicate, respectively, the low- and high-fidelity configurations; the elevator is highlighted in the XML geometry and the WT geometry has been mirrored to facilitate the geometry comparison 182
A.10 Geometry increments to simulate a design study, featuring variation of wing quarter-chord sweep angle, Λ_w, and wing area, S; the arrow points at the wing tip trailing-edge of the baseline XML configuration, which represents the original XML design 183
A.11 Trim conditions for the DLR-F12 full aircraft model at an altitude of $6000\,m$ comparing DATCOM and Euler solutions on the XML configuration and RANS solution on WT configuration 185
A.12 Short-period and phugoid characteristics for the DLR-F12 full aircraft model at an altitude of $6000\,m$ compared to ICAO recommendations [201] 187
A.13 Impact of geometry increments in the short-period characteristics for the DLR-F12 full aircraft model at an altitude of $6000\,m$ 187
A.14 Overlay of a three-view of a B747 aircraft model and lifting surfaces for low-fidelity aerodynamics 188
A.15 Medium-fidelity surface geometry for the B747-like model with control surfaces 188
A.16 Variation of aerodynamic coefficients with angle of attach and rudder deflection at a Mach number of 0.9; the black cubes indicate sample points 190
A.17 Illustration of the aerodynamic table for ailerons deflection; black cubes indicate sample points 190
A.18 Variable-fidelity aerodynamic predictions compared to experimental data at Mach number of 0.8 for the B747-like model; experimental data are from [204] 191
A.19 Trim conditions at transonic speed range for the B747-like model at an altitude of $11000\,m$ using different fidelity aerodynamic models 192
A.20 Deflected control surfaces for the SDM model 193
A.21 Response of aerodynamic coefficients to angle of attach and elevator deflection at a Mach number of 0.4 195

A.22 Wing-over and a 90-degree turn manoeuvres were simulated for the SDM model in [23] 196
A.23 A three-view of the Ranger 2000 aircraft 196
A.24 Grid for the Ranger 2000 aircraft; the surface solution is obtained at $\alpha = 6.0°$ and $M = 0.8$ 197
A.25 Response of aerodynamic coefficients to angle of attach and Mach number at zero sideslip angle; the black cubes indicate sample points 198
A.26 Illustration of the aerodynamic tables for deflection of control surfaces at a Mach number of 0.25; black squares indicate sample points 199
A.27 Simulation of manoeuvres for the Ranger 2000 aircraft compared to flight test data 200

B.1 Indicial response of lift coefficient for a step change in angle of attack ($\Delta\alpha = 4.58°$) 206
B.2 Indicial response of lift coefficient for a step change in angle of attack for small times ($\Delta\alpha = 4.58°$); reference data are from Lomax [213] 207
B.3 Indicial response of lift coefficient for a sharp-edged gust at Mach number 0.20 normalized by its asymptotic value ($w_g/U = 0.08$) 208
B.4 Indicial response of lift coefficient for a sharp-edged gust for small times ($w_g/U = 0.08$); reference data are from Lomax [213] 209
B.5 Indicial response of lift coefficient for a moving sharp-edged gust at Mach number 0.20 normalized by its asymptotic value ($w_g/U = 0.08$); the solution for $\lambda = 1$ is not plotted, see Fig. B.3 209
B.6 Lift dynamic dependence from unsteady CFD calculations and two convolution models in response to gust of different shapes; in (a), $\tau_g = 10$ and $w_g/U = 0.08$; in (b), $\tau_g = 25$ and $w_g/U = 0.08$; and in (c), $\tau_g = 25$ and $w_g/U = 0.14$ 211

List of Tables

2.1 Aerodynamic database format [81]; "x" indicates a column vector of non-zero elements 45

3.1 Reference values of the SDM model geometry 64
3.2 Reference values of the TCR wind tunnel model 66
3.3 Description of the SDM test cases; terms in parentheses indicate secondary dependencies of the investigations 67
3.4 Experimental conditions for testing of the TCR wind tunnel model at TsAGI T–103 facility [148] 84

4.1 Description of the AGARD CT5 conditions for the NACA 0012 aerofoil [173] 103
4.2 NACA 0012: grid influence on static and dynamic derivatives obtained from the time-domain PMB solution for the AGARD CT5 conditions . . 104
4.3 NACA 0012: amplitude ratio and phase angle of the fundamental harmonic between the input, α, and the outputs, C_N and C_m 112
4.4 NACA 0012: normal force and pitching moment coefficient dynamic derivatives ($M = 0.755$, $\alpha_0 = 0.016°$, $\alpha_A = 2.51°$, and $k = 0.0814$) . . 114
4.5 NACA 0012: time reduction of the PMB-HB solution compared to unsteady PMB solution using the damping-in-pitch as the figure of merit; the terms tsc and n_c indicate, respectively, the number of time-steps per cycle and the number of oscillatory cycles 118
4.6 Description of the conditions for the DLR-F12 aircraft model 120
4.7 DLR-F12 model: normal force and pitching moment coefficient dynamic derivatives ($M = 0.73$, $\alpha_0 = 0.70°$, $\alpha_A = 0.50°$, $k = 0.034$, and $h = 6000\,m$) 121

5.1 Description of the AGARD CT2 conditions for the NACA 0012 aerofoil [173] 128
5.2 Error norm in the model predictions of pitching moment coefficient and related cost for model generation 144

A.1 Reference values and mass and inertia properties of the TCR aircraft model 176
A.2 Reference values and mass and inertia properties of the DLR-F12 full aircraft model 184
A.3 Reference values and mass and inertia properties of the B747-like model 192
A.4 Mass and inertia properties of the SDM model 194
A.5 Reference values and mass and inertia properties of the Ranger 2000 aircraft 197

B.1 Asymptotic values of the indicial response of lift coefficient for a step change in angle of attack, $C_L(\infty)/\Delta\alpha$ 206

List of Symbols

$\mathbf{A}$	= matrix in frequency domain equation
$\mathcal{A}$	= response to a step change function
a	= speed of sound, $[m/s]$
b	= reference wing span, $[m]$
b_0, b_1, b_2, b_3	= coefficients in approximation to Küssner function for compressible flows
c	= mean aerodynamic chord, $[m]$
d	= fuselage total length, $[m]$
C_m	= pitching moment coefficient
$C_{m\,0}$	= non-linear static pitching moment coefficient
$C_{m_q} + C_{m_{\dot{\alpha}}}$	= pitching moment coefficient damping, $[1/rad]$
C_N	= normal force coefficient
$C_{N\,0}$	= non-linear static normal force coefficient
$C_{N_q} + C_{N_{\dot{\alpha}}}$	= normal force coefficient damping, $[1/rad]$
$\mathbf{D}$	= matrix in harmonic balance equation
$\mathscr{F}[\psi(t)]$	= Fourier transform of quantity $\psi(t)$, equivalent to $\tilde{\psi}(j\,\omega)$
f	= dimensional frequency, $[Hz]$
$\mathscr{F}[\psi(t)]$	= Fourier transform of quantity $\psi(t)$, equivalent to $\tilde{\psi}(i\,\omega)$
$G(i\omega)$	= transfer function of input/output pair
$\mathbb{H}_i$	= i-th order Volterra operator
H_i	= i-th order Volterra kernel
$\mathcal{H}$	= response to a unit impulse function
h	= altitude, $[m]$
i	= imaginary unit, $\sqrt{-1}$
k	= reduced oscillation frequency, $\omega\,c/(2\,U_\infty)$
M_∞	= freestream Mach number
n_c	= number of oscillatory cycles
n_H	= number of harmonics
$\mathbf{R}$	= residual vector
$R(\omega)$	= amplitude ratio of transfer function
Re	= Reynolds number, $U_\infty c/\nu$
S	= reference wing area, $[m^2]$

s = non-dimensional time used in analytical formulation, $2\,t\,U_\infty/c$
t = physical time, $[s]$
t^* = non-dimensional time used in CFD, $t\,U_\infty/c$
u_g, w_g = horizontal and vertical velocity components of gust, $[m/s]$
W_g = gust vertical velocity function of time, $[m/s]$
U_∞ = freestream speed, $[m/s]$
$\mathbf{W}$ = vector of conserved variables
$\angle\tilde{\psi}(i\,\omega)$ = phase angle of the Fourier transform of quantity $\psi(t)$

Greek Symbols

α = angle of attack, $[deg]$
α_0 = mean angle of attack, $[deg]$
α_A = amplitude of oscillatory motion, $[deg]$
β = angle of sideslip, $[deg]$
$\beta_1, \beta_2, \beta_3$ = coefficients in approximation to Küssner function for compressible flows
ν = kinematic viscosity of air, $[m^2/s]$
$\phi\,(\omega)$ = phase angle between output and input
λ = advance ratio for gust
Φ = Wagner function
Ψ = Küssner function
$\Phi_1, \Phi_2, \varepsilon_1, \varepsilon_2$ = coefficients in Wagner function
$\Psi_1, \Psi_2, \varepsilon_3, \varepsilon_4$ = coefficients in Küssner function
τ_g = gust gradient
ω = oscillation frequency, $2\,\pi\,f$, $[rad/s]$

Acronyms

CFD = computational fluid dynamics
CFL = Courant–Friedrichs–Lewy number
Cobalt = commercially available CFD solver
COSA = CFD solver from University of Glasgow
DLR = German Aerospace Center
EDGE = CFD solver from FOI
EIF = expected improvement function
FOI = Swedish defence agency
F12 = large transport aircraft
HB = harmonic balance
LFD = linear frequency domain
LUR = linearized unsteady Reynolds-averaged Navier-Stokes equations
MSE = mean squared error

MUSCL	= monotonic upstream–centered scheme for conservation laws
NSMB	= Navier–Stokes multiblock
PMB	= parallel multiblock
RANS	= Reynolds–averaged Navier–Stokes
RBF	= radial basis function
ROM	= reduced order model
SBRF	= surrogate-based recurrence-framework
SDM	= standard dynamic model
TAU	= CFD solver from DLR
TCR	= transonic cruiser
TsAGI	= Russian central aerohydrodynamic institute

Chapter 1

Introduction

Determining the stability and control characteristics of aircraft at the edge of the envelope is one of the most difficult and expensive aspects of the aircraft development process. Non-linearities and unsteadiness in the flow are associated with shock waves, separation, vortices and their mutual interaction, which can lead to uncommanded motion and uncontrollable departure. If these issues are discovered at flight test, the aircraft development can suffer significant delays, a rise in production costs and detrimental effects on performance. There have been numerous examples of aircraft experiencing uncommanded activity, as reported, for instance, in [1]. Following an extensive resolution process, immediate improvements are typically achieved by minor configuration changes and modifications to the flight control system and control augmentation laws. To provide a better fundamental understanding of the flow physics causing degraded characteristics, computational approaches have been used [2]. The development of a reliable computational tool for prediction of these important issues would allow the designer to screen different configurations prior to building the first prototype, reducing overall costs and limiting risks [3].

For flight dynamics analysis, force and moment dependency on flight and control states is often expressed in tabular form. There are several possible sources of data for this aerodynamic database. Flight testing the aircraft is the most accurate but also the most expensive of these methods [4]. Wind-tunnel testing of scaled models is cheaper than flight testing. However, blockage, scaling and Reynolds number effects together with support interference issues limit the proper modelling of the full scale aircraft behaviour [5]. The third approach combines data sheets, linear aerodynamic theory and empirical relations [6]. Due to simplicity, this method is in widespread use and is a common choice to obtain aerodynamic characteristics in the conceptual design stage [7, 8]. In the absence of a background database, empiricism is strongly limited when confronted with novel configurations and flight conditions dominated by non-linear aerodynamic effects.

A possible useful addition to the high-fidelity/high-cost of testing and low-fidelity/low-cost of semi-empirical approaches is Computational Fluid Dynamics (CFD), which represents the state of the art in predicting non-linear flow physics. Success has been reported in predicting the non-linear aerodynamic behaviour of aircraft at full scale Reynolds numbers [9]. However, the generality realized in a CFD simulation comes at the expense of computational cost. Due to the "curse of dimensionality" (a term coined by Bellman [10]), routine use of high-fidelity CFD simulations is costly to cover a large parameter space of conditions, such as in multidisciplinary optimization [11], aeroelasticity [12] and studies of flight dynamics [13]. The term fidelity here indicates the level of physical modelling realized in the numerical techniques used. High-fidelity analyses refer to mathematical models for the description of the relevant physics in the problem to be simulated.

To generate the aerodynamic database of forces and moments for the expected flight envelope, a large number of flow conditions for different aircraft control settings are required. Considering that the total number of table entries can be in the order of hundreds of thousands or even millions, the task to simulate aerodynamic loads for each single entry is extremely expensive, and is intractable using CFD as a source of the data. An alternative method to the "brute-force" approach was presented in [14], and is based on the kriging interpolation [15,16], which is well suited to approximate non-linear functions [17,18] and does not require a priori knowledge of the function to be approximated. While approximating the non-linear CFD results throughout the parameter space from a limited number of full-order simulations, the key to the methodology is the location of sample points. In addition to creating a high-fidelity aerodynamic database for improved predictions of the aircraft stability and control behaviour, CFD can be used to establish the limits of tabular models. The mathematical model typically used for flight dynamic investigations is based on the concept of stability or aerodynamic derivatives. Forces and moments are assumed to be a function of the instantaneous values of the disturbance velocities, control angles and their rates [19]. Whilst consistent with a quasi-steady representation of the aerodynamics, the time-invariant assumption is questionable in many studies of unsteady aerodynamics [20]. Therefore, several attempts were made to improve the modelling of unsteady aerodynamic loads [21, 22]. The ability of CFD to perform unsteady simulations creates a framework for assessing the limits of the tabular model due to the neglect of time-history effects on the flow development. Various maneouvers were created in [23] solving an optimal-control problem, and aerodynamic predictions obtained from the look-up tables were compared to the unsteady aerodynamic loads simulated from a time-accurate CFD analysis.

The work presented in this thesis investigates the use of CFD to a variety of application studies, ranging from aircraft stability and control predictions to applications of flight dynamics. The main contribution is toward a comprehensive understanding of the limitations of the current aerodynamic model used in flight dynamics when aerody-

namic non-linearities are present. Alternative model formulations are evaluated, and advances in the prediction of non-linear unsteady aerodynamic loads are likely based on the results presented.

1.1 Example Applications of CFD

Progress made in reducing the time required to generate an aerodynamic database of forces and moments for a Harrier aircraft in ground effect was reported in [24]. With access to large-scale parallel computers, 35 time-dependent Reynolds-Averaged Navier-Stokes (RANS) simulations were completed in one week. A monotone cubic-spline interpolation procedure [25] was used to extend the 35 solution database to over 2500 cases for a range in angle of attack between 4° and 10° and in height above the ground between 10 and 30 ft. A step towards the generation of a stability and control database to simulate take-off and landing scenarios for a YAV-8B Harrier was described in [26]. The aerodynamic model for the force and moment coefficients was expressed in terms of the static and dynamic stability derivatives. It was envisioned that a few hundred solutions could be obtained, and the remainder of the parameter space filled out with the use of an interpolation procedure or neural networks. A system to automate the process of running a large number of expensive CFD simulations on grid resources based on Globus [27] was developed, allowing the generation of one hundred RANS and one thousand Euler simulations in one week for a second generation Langley glide-back booster design [28]. The database of forces and moments was computed varying the angle of attack, Mach number and angle of sideslip, and was compared against experimental data.

A modular framework built around existing stand-alone applications with control scripts to link the different components was described for the generation of aerodynamic databases with and without control surfaces [29]. A Cartesian CFD method, providing an efficient and robust mesh generation capability for any arbitrary complex geometry, was a key part in the setup. Several configurations were tested. A parametric study on a second generation glide-back booster was conducted examining static effects due to variations in angle of attack, sideslip and Mach number. The database consisted of approximately 2900 flow conditions and was compared to experimental and numerical data to establish confidence in the predictions. Two examples of parametric databases with control surface deflections were also described. The configurations were flown through the database by integrating the six degrees-of-freedom equations of motion of a rigid body using Feldberg's modified Runge-Kutta scheme [30]. Forces and moments were then computed from the database with a multi-linear interpolation. The applications included the validation of a generic neural network control system and trajectory simulation with the development of a closed-loop feedback pitch controller. The approach considered only static and control aerodynamic derivatives and neglected the

influence of any dynamic derivatives. The databases were created from a set of discrete points at the minimum, median and maximum values for each independent parameter. While this approach drastically reduces the number of computations, it also presumes that these points capture all the relevant non-linearities in aerodynamic loads. Further tests were not reported to investigate the validity of this assumption.

1.2 Predictive Aerodynamic Models

The references cited above exemplify the need for improvements in computational efficiency. While access to high-end computing facilities is essential for numerous examples of intensive CFD simulations [31,32], to make progress in routinely using CFD, research has been concentrated on the development of computationally efficient predictive aerodynamic models to use in combination with CFD generated data.

1.2.1 Linear and Non-linear Indicial Functions

Linearized aerodynamic models based on a functional representation for the indicial aerodynamic force and moment responses (see Appendix B) in terms of blade motion and gust functions were used in subsonic flow [33]. A method was developed to calculate the indicial and gust responses of an airfoil in compressible flow directly using CFD [34]. The step change was incorporated into an existing CFD solver using a grid-velocity approach, and accurate solutions compared to exact analytical results were obtained at low speed. The agreement degraded with non-linear compressibility effects. The fidelity of linearized indicial methods for aerodynamic load predictions was assessed, and it was found that these methods are sufficiently accurate to be used as a practical design tool [35]. However, simplifying assumptions from the flow physics limits the generality of the linear indicial approach. When non-linear effects are significant, such as when there is the appearance/disappearance of a shock wave or topological changes of the flow, the indicial approach becomes inaccurate [36]. In addition, flowfields with hysteresis exhibit memory-effects, which violate the assumption of time-invariance underlying the linear indicial approach.

Interest has also concentrated on the use of non-linear indicial functions [37, 38], which are a generalization of the linear convolution model. This formulation was shown to be equivalent to a non-linear functional expansion of which the classical Volterra series is a subset. A non-linear indicial model to predict time-dependent unsteady aerodynamic loads associated with flight maneuvers at high angles of attack and high pitch rate was developed. An analytical model approximating the flight test aerodynamic responses of a full scale fighter aircraft performing Cobra-type maneuvers was used to generate the required indicial functions and to compare the indicial predictions for novel maneuvers [39]. The model was based on the state-space formulation, which was

demonstrated to accurately describe unsteady aerodynamic effects observed in experimental investigations [22]. The model extends the usual flight dynamics equations by introducing a first order delay differential equation for an additional internal state variable which accounts for unsteady effects associated with separated and vortical flow. It was claimed that an efficient parametrization of the indicial function space can be obtained based only on local information, such as instantaneous angle of attack and pitch rate. The non-linear indicial prediction model was also tested for a rectangular wing undergoing dynamic stall [40]. An artificial neural network trained on wind tunnel data was used to reproduce the detailed aerodynamic characteristics of the pitching wing, and deemed accurate enough to provide a reference solution for the prediction model at negligible cost. In view of the mathematical formulation adopted in this work, it is significant that a comparison between the non-linear indicial method and the aerodynamic stability derivatives method was reported. First, a model with constant coefficient aerodynamic derivatives, retaining a quadratic term in angle of attack and expressing the damping derivative as a function of the angle of attack, was considered. Constant coefficient derivatives were determined from the neural network using an identification technique. A second model using a look-up table for static aerodynamics, augmented with alpha-dependent damping derivatives, was built. Both models were used to predict aerodynamic loads for a constant pitch rate maneuver at a reduced frequency of 0.02, from zero up to sixty degrees angle of attack. It was demonstrated that the indicial method was significantly more accurate than the conventional model based on aerodynamic stability derivatives for the unsteady maneuver tested, particularly when critical states were crossed. It was concluded that efficient parametrization of the indicial and critical state function space appears to be achievable using only local information, such as the instantaneous angle of attack and pitch rate. The accuracy of the non-linear indicial method was also reported for the prediction of the airloads for a 65° delta wing performing forced roll oscillations at high angle of attack [41].

1.2.2 Regression Models

Research has focused on simulations of complete aircraft configurations, as reported in [42–45]. While this was motivated by the need of assessing the accuracy of CFD simulations to predict the unsteady non-linear aerodynamic behaviour, the development of alternative mathematical models was hindered by the slow turn-around time of the simulations. A generic fighter with abrupt asymmetric vortex breakdown leading to uncommanded lateral instability [46] was chosen as a test case [44]. The availability of experimental and computational investigations made the configuration a good testing ground to assess the validity of low-order aerodynamic models. The procedure adopted to create the reduced-order model follows the description given in [43]. First, adequate computational training maneuvers designed to excite the flow physics of interest are

calculated with CFD. A reduced-order mathematical model is then built from the simulated aerodynamic loads using system identification methods [47], and the prediction model is compared with the training maneuvers used to generate it. Finally, the prediction model is applied to novel maneuvers, and for the prediction of aerodynamic loads at all flight test points at negligible cost. SIDPAC [48] has been a common choice to build reduced-order models [49]. It is a least squares regression based method that generates an explicit relationship between the computed aerodynamic loads and the independent variables of the aircraft motion. Unsteady time-accurate Delayed Detached-Eddy Simulations (DDES) were calculated at a Mach number of 0.4, constant angle of attack of 30° and sinusoidally varying angle of sideslip. Five maneuvers were performed at constant frequency, and a chirp frequency maneuver was additionally performed for a frequency sweep between zero and 17 Hz. To assess validity, the prediction model built from the chirp frequency motion was used to reproduce the aerodynamic loads for a maneuver at constant frequency included within the bounds of the training signal used to generate the model. It was demonstrated [44] that a regression model is incapable of generating an accurate low-order model of the airloads based on the analysis of one single training maneuver.

1.2.3 Radial Basis Functions Interpolation

The determination of an appropriate training maneuver is a challenging task, which is vital for the successful generation of a reduced-order model. Past research has focused on the development of training maneuvers, and used the frequency content and power spectral density of the motion variables as figures of merit [50, 51]. This approach is not always valid as the functional dependences relating the aerodynamic loads to the aircraft motion are far more complex. A different approach, based on the ability to cover the relevant regressor space and to capture a range of flow phenomena, was adopted for the investigation of training maneuvers for a two-dimensional airfoil [52]. Several training maneuvers, such as chirp, spiral and Schroeder maneuvers, were considered, and used to build reduced-order models. To assess the accuracy of the prediction models, aerodynamic loads were compared against time-accurate CFD solutions. The reduced order models were based on radial basis functions [53], and an improvement in the ability to predict linear and non-linear aerodynamic characteristics using one single training signal was observed. It was concluded that the chirp maneuver resulted in the most robust and reliable reduced order model, and the spiral maneuver was found adequate for low-frequency and static aerodynamic predictions.

1.2.4 Volterra Theory

Alternative mathematical formulations have been investigated. Since formally introduced into CFD [54], the Volterra functions have been successfully applied for aeroe-

lastic studies of limit cycle oscillations [55, 56]. The extension into the area of stability and control was considered in [57]. Two test cases were evaluated, a NACA 0012 airfoil and a X-31 aircraft model. The Volterra kernels were identified from a set of Gaussian shaped impulses, and the accuracy of the prediction model for different pitching motions was assessed. The applications were limited to linear cases, and a good agreement of the Volterra reduced-order modeling was observed when compared to time-accurate CFD simulations in the linear aerodynamic range. With weakly non-linear characteristics, the performance of the prediction model quickly degraded. As stated in the review [56], an important issue is the excitation of multiple degrees of freedom to properly identify non-linear cross-coupling of the degrees of freedom, and because of the non-linear nature of the aerodynamic system the principle of superposition is invalid. A method for the inclusion of Volterra cross-kernels applied to a transonic two-dimensional airfoil undergoing forced pitch and plunge harmonic oscillations was investigated [58]. The prediction model was compared to time-accurate CFD solutions, and the improvement in accuracy over approaches that ignore the cross-kernels was demonstrated. Addressing the convergence issue of the Volterra series and the need for the inclusion of higher-order kernels, an alternative formulation was presented [59]. The pruned Volterra series, with a simplified parametric structure of the kernels, was tested for a two-dimensional transonic airfoil undergoing forced sinusoidal pitch oscillations for two AGARD test cases. The identification of kernels up to fourth order demonstrated a feasible undertaking and a good agreement compared to the time-accurate CFD solution was achieved. The formulation of the pruned Volterra series was then used to approximate the flutter boundary and limit-cycle oscillation amplitudes of the NACA 0012 benchmark model [60]. Showing favourable results, a computational saving of several orders of magnitude compared to full-order CFD simulations was achieved.

1.2.5 Proper Orthogonal Decomposition

With just a handful of basis vectors, the Proper Orthogonal Decomposition (POD) technique, also known as the Karhunen-Loève expansions [61], has been used to reduce the complexity and dimension of aerodynamic models. An overview of the POD method along with details of how the method has been applied to study a wide variety of fluid problems can be found in [62]. Reduced-order models constructed using basis vectors from the POD of an ensemble of small-disturbance frequency-domain solutions were presented [63]. The technique was applied to two model flow problems, that is, unsteady transonic flow about an isolated airfoil and subsonic flow through a cascade of flat-plate airfoils. A reduced-order aeroelastic model was also developed to compute the flutter boundary of a typical airfoil. In all cases presented, it was demonstrated that the technique produced low-order high-accurate models of the unsteady flow over a wide range of reduced frequencies. The computation of the unsteady small-disturbance

solutions, e.g. snapshots, was identified as the most expensive task. Once the POD basis vectors were found, the construction and solution of the reduced-order model was done at negligible cost, making it suitable for parametric studies. Recent studies have been conducted to bring the POD theory in combination with standard identification methodologies in the analysis of maneuvering aircraft [64, 65]. A prescribed maneuver designed to densely populate a given flight parameter envelope was simulated with an unsteady CFD solver. The ensemble of snapshots used in the POD method consists of surface solutions taken at regular time increments. Time-dependent surface data were decomposed into a set of orthogonal modes in the spatial coordinate, and a set of time-dependent coefficients for each mode. The key for the described method is that the time-dependent coefficients are fitted to a polynomial function of the time histories of the relevant flight parameters. Once constructed, the model can be used to predict the surface data for an arbitrary maneuver, again at negligible cost compared to the full-order simulation.

1.2.6 Surrogate-Based Models

Despite the progress made in the development of reduced-order models, the selection of appropriate training data remains a key issue. The routine generation of reduced-order models has not been reported in any previous work. An alternative approach is based on surrogate modeling [66–68]. First described in [14], the framework builds on kriging interpolation [15, 16]. Note that the development of a similar framework applied to a two-dimensional airfoil restricted to one- and two-parameter variables was reported [69].

In addition to creating a high-fidelity aerodynamic database for improved predictions of the aircraft stability and control behaviour, CFD can be used to establish the limits of the tabular models. The mathematical model typically used for investigations of flight dynamics is based on the concept of stability or aerodynamic derivatives. Forces and moments are assumed to be a function of the instantaneous values of the disturbance velocities, control angles and their rates [19]. Whilst consistent with a quasi-steady representation of the aerodynamics, these models cannot predict the non-linearities associated with post-stall aerodynamics, including bifurcations and hysteresis. The ability of CFD to perform unsteady simulations allows the assessment of the limits of a tabular model arising from the neglect of time-history effects.

1.3 Review of Dynamic Derivatives

The concept of stability or aerodynamic derivatives was introduced by Bryan [19] in 1911 and remains essentially unchanged as the conventional model for the representation of the aerodynamic loads in the equations of motion. It is assumed that the

aerodynamic forces and moments are a function of the instantaneous values of the disturbance velocities, control angles and their rates. The dependence of the forces and moments on these variables is obtained by a Taylor series expansion, discarding higher order terms [70]. For slow motions at low angle of attack, the static derivatives are generally sufficient to model the aerodynamic loads [6]. At higher angles of attack and rates, the inclusion of dynamic derivatives in the aerodynamic model can have a significant effect on the calculated stability characteristics of an airframe [71]. The addition of non-linear terms to take into account changes of stability derivatives with the angle of attack extended the range of flight conditions to high angles of attack and/or high amplitude manoeuvres. In the linear and non-linear methods, it is assumed that the aerodynamic parameters are time invariant [47]. This assumption was often questioned based on many studies of unsteady aerodynamics [20]. In the 1920s, Wagner [72] conducted a series of studies for the unsteady lift generated on an airfoil due to abrupt changes in angle of attack. Theodorsen extended these studies investigating the forces and moments on an oscillating airfoil. The lift response of an airfoil penetrating sharp-edge and harmonically-varying gusts was studied by Küssner [73] and Sears [74], respectively. The first attempts to investigate unsteady aerodynamic effects on aircraft motion were made by Jones and Fehlner [75], studying the effect of the wing wake on the lift of the horizontal tail. A more general formulation of linear unsteady aerodynamics in the aircraft longitudinal equations of motion was introduced by Tobak [76]. Tobak and Schiff [21] replaced the indicial functions within the integrals with functionals [77], themselves dependent of the past motion. A different approach was proposed by Goman et al. [78] introducing additional state variables, named internal state variables, in the functional relationships for the aerodynamic forces and moments. The coordinates of a separation point or vortex breakdown location can be taken as internal state variables, and modelled by differential equations. Goman and Khrabrov [22] formulated state space models with internal state variables describing the flow state. A good agreement was achieved with experimental data for a separated flow on an airfoil and flow with vortex breakdown about a slender delta wing.

Traditionally, wind tunnel testing has been used to produce derivatives for production aircraft [79]. The physical realism of wind tunnel data is well known, but can be limited by blockage, scaling, and Reynolds-number effects together with support interference issues that prevent the proper modelling of the full-scale vehicle behaviour. Computational Fluid Dynamics (CFD) solvers have reached a level of robustness and maturity to allow routine use on relatively inexpensive computer clusters. The prediction of dynamic derivatives requires the ability to compute the aerodynamic response to time-dependent prescribed motions which are used to excite the aerodynamics of interest. This can be done with present off-the-shelf CFD tools. CFD has potential for complementing experimental testing techniques for obtaining these values. The physical limitations and kinematic restrictions of wind tunnel testing including model

motion as well as the interference effects of the model support are not factors in the computational analysis. Physical effects can be separated in the CFD solutions in a way which can be difficult from wind tunnel or flight test data. CFD can also be used for investigating the modelling of data from flight tests. There is of course a significant question about the ability of CFD to predict the relevant aerodynamics, and this must be demonstrated through validation studies. It is therefore possible to use CFD as a complement to costly experimental campaigns. However, CFD is not meant to replace testing techniques.

1.4 Thesis Outline

The work in this thesis was partly developed within the SimSAC (Simulating Aircraft Stability and Control Characteristics for Use in Conceptual Design) project [1] funded by the European Commission 6th Framework Programme. The project consisted of a partnership of European academics and industrial contributors. The main driver of the project was the inadequacy of standard semi-empirical approaches currently used in conceptual design when confronted with more advanced aircraft configurations [80]. This may cause errors in the design process, which may prove expensive to rectify via additional design work, wind tunnel and flight testing, in addition to a delay in certification and performance degradation. To overcome these potential issues, it is worthwhile to introduce high-fidelity (physics-based) approaches early in the design process.

In this thesis, the exploitation of CFD is investigated for the generation of the aerodynamic database. A framework for the automated generation of tabular aerodynamic models for studies of flight dynamics is discussed, allowing stability and control considerations to be developed early in the design process. For the representation of the aerodynamic loads, a model based on stability or aerodynamic derivatives is assumed because traditionally used by flight dynamicists. In the model formulation, dynamic derivatives are used to update the static predictions to account for the aircraft motion. Emphasis is on the evaluation of dynamic derivatives with various CFD methods. As the limitations of the aerodynamic model are exposed for several test cases, there is a need for models of more realism and fidelity to be used in flight dynamics. Advances in this direction are discussed.

Chapter 2 introduces the framework for the generation of aerodynamic tables using CFD as the source of the data. The framework has been developed at Liverpool by the author and a colleague. A method to efficiently reduce the number of high-fidelity analyses is accomplished by use of a kriging-based surrogate model. Low-fidelity estimates are augmented with higher fidelity data, and data fusion combines the two datasets

[1] More details at `http://www.simsacdesign.eu` and `http://www.ceasiom.com/` [retrieved March 19, 2012]

into one single database. Once constructed, the look-up tables can be used in real-time to fly the aircraft through the database. Two methods for the evaluation of dynamic derivatives are also discussed.

Chapter 3 discusses the evaluation of dynamic derivatives computed using unsteady time-domain CFD simulations. Two configurations are considered: a generic fighter model and a transonic cruiser concept design. Numerical results are compared to experimental measurements, and a good agreement is noted in all cases. A systematic study to evaluate the dependencies of dynamic derivatives on aircraft motion and flow parameters, beyond the range of motions performed in dynamic testing facilities, is presented. It is recognized that in the presence of aerodynamic non-linearities, mainly due to three dimensional separated flow and concentrated vortices, dynamic derivatives exhibit a dependence on motion and flow parameters. These dependencies are not reconcilable with the model formulation, which is based on a Taylor series expansion. An approach to evaluate the sensitivity of the non-linear unsteady aerodynamic loads to variations in dynamic derivatives is introduced.

Chapter 4 introduces the use of reduced models, based on the manipulation of the full-order model, for the fast computation of dynamic derivatives. The underlying idea is to exploit the periodicity of the resulting aerodynamic system for oscillatory motions to decrease the cost of calculations. A linearized solution in the frequency domain and a harmonic balance technique are illustrated for two- and three-dimensional configurations. To stress the potential of the frequency-domain methods in conditions of practical interest for aircraft applications, flow conditions were in the transonic regime. For the formation of moving shock waves, the energy of aerodynamic modes redistribute at higher frequencies than the predescribed frequency of motion. While a time-domain calculation supports a continuum of frequencies up to the frequency limits given by the temporal and spatial resolution, the reduced models considered resolve only a small subset of frequencies typically restricted to include one Fourier mode at the frequency at which dynamic derivatives are desired. While providing good estimates of dynamic derivatives, the cost of the reduced models is a fraction of the cost for solving the original unsteady problem.

Chapter 5 addresses the demand for alternative model formulations of more realism to be used in the representation of non-linear unsteady aerodynamic loads. The conventional model based on aerodynamic derivatives is recognized to be adequate in benign flow conditions. There is, however, the consideration that any model in principle is applicable to linear cases, and the generality realized in a CFD solver is therefore not needed. The point of the discussion here is that conditions of practical interest feature aerodynamic non-linearities. Various reduced models, based on system-identification methods, are evaluated in presence of aerodynamic non-linearities. While retaining complex flow features due to shock-induced phenomena, a two-dimensional test case is considered. For the flow conditions considered, the predictions obtained using the

conventional model are misleading and not representative of the unsteady time-domain solution. While providing good approximations for the non-linear unsteady aerodynamic loads, reduced models investigated were generated with no more computational resources than that required for the conventional model.

Chapter 6 concludes the thesis and offers an outlook and suggestions for future work.

The framework for creating CFD-derived stability and control databases described in Chapter 2 was exercised for several aircraft configurations. The application to six test cases is presented in Appendix A. The point of the work is to show the range of applications that this framework has opened up, illustrating the aerodynamic model generation for each case in the form of a review. Through the range of examples which have actually been computed, the review shows the progress achieved because of the adoption of the framework. The work presented in the appendix is the result of a collaborative effort, and the author contributed directly to the creation of the aerodynamic database in each case. In addition, the author has led the review article in [81].

Appendix B illustrates the use of the indicial theory applied to unsteady aerodynamic problems. The indicial theory can also be used to predict the unsteady aerodynamic loads in response to a gust perturbation, which is of interest for aircraft loads calculation and certification. The CFD-based simulation of the interaction between a gust and a rigid or flexible airframe poses few practical questions. The author has implemented a new functionality in the CFD solver of the University of Liverpool based on the field velocity approach. Validation studies demonstrate the readiness of the approach for cases featuring linear and weakly non-linear aerodynamics.

Finally, Appendix C formulates a multi-linear interpolation, which is implemented in the computational framework described in Chapter 2 as an alternative approach to kriging interpolation.

Chapter 2

Formulation

2.1 Introduction

Modeling the aircraft aerodynamics raises the fundamental question of what the mathematical structure of the model should be. The functional dependencies of the force and moment coefficients are in general complex, as they depend in a non-linear fashion on present and past values of several quantities, such as airspeed, angles of incidence, etc. Reasonable simplifications are that fluid properties change slowly and the airplane mass and inertia are significantly larger than the surrounding fluid mass and inertia. The flow is often considered quasi-steady, which presumes that the flow reaches a steady state instantaneously and the dependence on the history of the motion variables can be neglected. One exception to this assumption is the retention of the reduced frequency effects. With these underlying hypotheses [47], the characterization of the functional dependencies is broken down as

$$C_i = f_1(\alpha, \beta, M, \delta) + f_2(Re) + f_3\left(\frac{\Omega\, c}{2\, U_\infty}\right) + f_4\left(\frac{\omega\, c}{2\, U_\infty}\right) \qquad (2.1)$$
$$\text{for } i = L, D, m, Y, l \text{ and } n$$

which is the common practice from wind tunnel testing. The first term on the right hand side is obtained in static wind-tunnel tests, the second term represents Reynolds number corrections and the last two terms are measured performing, respectively, rotary balance and forced oscillation tests. The above decomposition is valid when the effects are separable and the superposition principle can be used, that is, under the hypothesis of linear and uncoupled functional dependencies. The effects of rotary and forced oscillation are typically modeled as a function of the body axis angular rates, angles of incidence and their first time derivatives [82]. These derivatives were introduced to obtain a closer correlation between predicted and observed aircraft longitudinal motion [83], and for a conventional aircraft they represent the finite time that aerodynamic loads at the tail lag the changes in downwash convected downstream from the wing.

The aircraft symmetry with respect to the vertical plane motivates the neglection of the dependence of symmetric (longitudinal) forces and moments on asymmetric (lateral) variables, and vice versa. While the dependence on $\dot{\beta}$ is typically neglected for a quasi-state flow, the inclusion of the $\dot{\alpha}$ term leads to an identifiability problem when estimating the $\dot{\alpha}$ and q derivatives [84]. To avoid this problem, the two terms are lumped together and an equivalent derivative is defined as $\bar{C}_{i_q} = C_{i_{\dot{\alpha}}} + C_{i_q}$ for $i = L$, D and m.

2.2 Nonlinear Quasi-Steady Aerodynamic Model

Here a non-linear model for quasi-steady flow based on the above assumptions is considered. The dependence of longitudinal and lateral coefficients on state and control variables is formulated as

$$C_i = C_{i\,0}\,(\alpha, M, \beta) + \bar{C}_{i_q}\,(\alpha, M, q) \cdot \frac{c\,q}{2\,U_\infty} + C_{i_\delta}\,(\alpha, M, \delta) \cdot \delta \tag{2.2}$$

$$\text{for } i = L, D, \text{ and } m$$

$$C_i = C_{i\,0}\,(\alpha, M, \beta) + C_{i_p}\,(\alpha, M, p) \cdot \frac{b\,p}{2\,U_\infty} + C_{i_r}\,(\alpha, M, r) \cdot \frac{c\,r}{2\,U_\infty} + C_{i_\delta}\,(\alpha, M, \delta) \cdot \delta \tag{2.3}$$

$$\text{for } i = Y, l, \text{ and } n$$

As the applications presented range from the low-subsonic to transonic regimes, the aerodynamic coefficients are formulated as non-linear functions of the Mach number. The static terms, $C_{i\,0}$, depend non-linearly on the angles of incidence. The dynamic and control derivatives, while non-linear functions in the arguments, are linear with respect to the body axis angular rates and control deflections, respectively. Additional simplifications in the functional dependencies of dynamic derivatives might be inconsistent when compared with experimental and computational findings, see e.g. [85].

The aerodynamic coefficients in Eqs. (2.2) and (2.3) are commonly obtained from tunnel testing. The aerodynamic model is implemented in tables, with measured or computed values. Forces and moments are tabulated as functions of the aircraft states and control settings representing the expected flight envelope. Aerodynamic coefficients are in wind axes, and the aircraft states feature the angles of incidence and sideslip, α and β, the Mach number, M, and the body axis angular rates, p, q and r. All required control deflections are also included. The format of the aerodynamic tables is illustrated in Table 2.1. Several assumptions have led to the formulation used, limiting its validity when confronted with uncommanded departures involving aerodynamic and aircraft motion cross-coupling. In the general case, the six aerodynamic coefficients would be function of all input variables in a coupled fashion, resulting in a very large table. To illustrate, if five values are used to provide a coarse resolution for each parameter in the table, the total number of table entries would be 5^9, which is of

magnitude 2 million. This is not normally necessary, and a less coupled formulation of the aerodynamic coefficients is used instead. Each term in the above equations is formulated as dependent on three input variables. The main aerodynamic variables are taken to be the angle of attack, α, and Mach number, M. Forces and moments are assumed to depend on these variables in combination with each of the remaining variables separately. The complete aerodynamic database is then divided into three-parameter sub-tables. Let n_x denote the number of values for the parameter x in the table, and let N_c denote the number of aircraft control effectors. The dimension of the complete database, n_{db}, is given by

$$n_{db} = n_\alpha \cdot n_M \cdot \left(n_\beta + \sum_{i=1}^{N_c} n_{\delta_i} + \sum_{i=1}^{3} n_{\omega_i} \right) \tag{2.4}$$

where ω_i indicates the body axis angular rates. For the same example illustrated above, the total number of table entries would be less than two-hundred. However, a reasonable aerodynamic database to cover the expected flight envelope can easily require one hundred-thousand entries. When using the "brute force" approach in combination to high-fidelity aerodynamic models to fill the tables, an unrealistic time of 158 years was estimated [13]. An alternative to the "brute force" approach was proposed based on sampling, reconstruction and data fusion of aerodynamic data [14].

α	M	β	δ_{ele}	δ_{rud}	δ_{ail}	...	p	q	r	C_L	C_D	C_m	C_Y	C_l	C_n
x	x	x	-	-	-	-	-	-	-	x	x	x	x	x	x
x	x	-	x	-	-	-	-	-	-	x	x	x	x	x	x
x	x	-	-	x	-	-	-	-	-	x	x	x	x	x	x
x	x	-	-	-	x	-	-	-	-	x	x	x	x	x	x
x	x	-	-	-	-	x	-	-	-	x	x	x	x	x	x
x	x	-	-	-	-	-	x	-	-	x	x	x	x	x	x
x	x	-	-	-	-	-	-	x	-	x	x	x	x	x	x
x	x	-	-	-	-	-	-	-	x	x	x	x	x	x	x

Table 2.1: Aerodynamic database format [81]; "x" indicates a column vector of non-zero elements

Two scenarios were considered, based on a requirement for generating tables for a completely new design and for updating the database of the existing configurations which are being altered. In the first scenario, there is a requirement for a high fidelity aerodynamic model which can be generated offline without the user waiting for the database to be generated during an interactive session. The emphasis of the sampling algorithm is on an efficient search for the non-linearities in the force and moment coefficients. Two approaches to this sampling, based on the Mean Squared Error criterion of kriging and the Expected Improvement Function [86, 87], were assessed, and are described in the next section. In the second scenario, a designer is involved in an inter-

active session. It is assumed that the aircraft geometry is incremented from an initial design, and that a high-fidelity model is available for the initial design from the first scenario. Data fusion based on co-kriging is then used to update the initial high-fidelity aerodynamic model with a small number of additional calculations. In this scenario it is assumed that the flow topology resulting from the initial geometry does not change during the geometry increments. If this is not the case, e.g. the wing sweep angle increases so that vortical flow starts to dominate at moderate angles, then either a new initial geometry needs to be selected, or the interactive session needs to be suspended so that a new high-fidelity model can be generated under the first scenario.

The static dependencies of the aerodynamic coefficients are stored in the (α, M, β) sub-table, which is referred to hereafter as the baseline table. This table provides a fundamental overview of the aerodynamic loads throughout the flight envelope of interest, and has the potential to represent non-linear phenomena such as static stall, compressibility effects and onset and breakdown of vortical flows. The baseline table is generally the most expensive to generate and, if not otherwise stated, it is obtained using sampling techniques. Starting with a high-fidelity aerodynamic model based on the Euler or RANS equations, the dependencies of the control surface deflections are treated as geometry increments with respect to the initial design, and sub-tables are populated using co-kriging.

2.3 Kriging-Based Framework

The framework for the generation of a computationally efficient approximation of aerodynamic loads determined from expensive high-fidelity calculations consists of the following steps:

1. The independent variables and their range are specified, and initial sampling is used to begin the procedure and to provide a quick overview of aerodynamic data throughout the parameter space. Aerodynamic data are calculated at preset initial sample points using aerodynamic models appropriate for the given task.

2. A surrogate model based on kriging interpolation fitting data in the form of input/output combinations is generated.

3. The parameter space is iteratively refined by adding sample points at untried locations to improve the accuracy and verify the robustness of the surrogate model.

4. If aerodynamic data have been obtained using different fidelity models, data fusion is then used to combine the low- and high-fidelity predictions in one single dataset of forces and moments.

2.3.1 Initial Sampling

The task of the initial sampling is to provide an informative picture of the function at minimum cost [88]. When confronted with a deterministic computer simulation as opposed to wind-tunnel or flight tests, a given set of input parameters always produces the same aerodynamic data. Without information on the function, a design optimal distribution method can only apply space-filling sampling, in the sense that all areas of the parameter space are sampled. Several space-filling methods requiring only information on the domain are available in the literature, such as Monte Carlo [89], latin hypercube sampling [90] and Sobol [91]. A major disadvantage of space-filling methods is that samples are randomly selected, can cluster together and each high-fidelity simulation may not provide significant additional information. To overcome the potential lack of uniformity, optimal latin hypercube sampling [92] ensures a more uniform design of experiment obtained by optimizing a spreading criteria, e.g. minimum distance or correlation, of the sample points. However, sampling methods which include information on the full-order function in sample distribution are preferable. These methods are named a posteriori sequential sampling methods, as opposed to a priori sampling used for the space-filling methods. The set of sample points is iteratively refined and an additional high-fidelity simulation is run for a combination of input parameters in which the model exhibits maximum error. The drawback is that the high-fidelity simulations are launched one at a time, whereas they would be launched in parallel with an a priori method.

The a priori approach is first considered to initialize the procedure. Each three-parameter sub-table defines a three-dimensional domain. An initial set of ten sample points is generated as follows. Eight samples are placed at the vertices of the parameter space, and two sample points are located within the parameter space, typically at the highest value of the angle of attack and for a given Mach number. This choice is sound because it avoids the need for extrapolation, and high-fidelity simulations are located in regions where aerodynamic loads are likely to exhibit non-linearities due to vortical flow developments, compressible effects and their mutual interaction. The simulations at the ten sample points provide an initial view of the behaviour of the aerodynamic data. A sequential sampling approach is then considered to iteratively refine the parameter space and to verify the accuracy of the approximation model when including additional data.

2.3.2 Kriging Interpolation

Kriging interpolation is used to approximate non-linear multi-dimensional deterministic functions by interpolating available sampled data, typically, from a full-order simulation. It is a parametric approach which presumes that the global functional form of the relationship between the response and the design variables is known.Once constructed,

kriging is a computationally cheap model to be used in place of the expensive full-order simulation for prediction of the function at untried points. Kriging has been successfully applied in different areas and, in particular, to problems involving fixed- and rotary-wing aerodynamics [17, 18].

Here, the mathematical formulation of the aerodynamic coefficients in Eqs. (2.2) and (2.3) represents the function to be approximated with kriging interpolation. With suitable assumptions, the $4 + N_c$ aerodynamic terms have been expressed as a function of three input parameters. To illustrate, consider the baseline table with $n_\alpha \cdot\, n_M \cdot\, n_\beta$ entries and the requirement for a high-fidelity representation of the static aerodynamic force and moment coefficients, $C_{i\,0}$ for $i = L, D, m, Y, l$ and n. From a small ensemble of sample points, kriging interpolation is used to predict the aerodynamic data at the $n_\alpha \cdot\, n_M \cdot\, n_\beta$ flight conditions. For convenience, let y be a single scalar function representative of each aerodynamic coefficient in turn, $y = C_i$. Assume a given set of n_{sp} numerical samples, $[\mathbf{x}_1, \ldots, \mathbf{x}_{n_{sp}}]^T$, where $\mathbf{x}_i = [\alpha_i,\, M_i,\, \beta_i]^T$ is a vector of input parameters, and the corresponding full-order aerodynamic coefficients, $\mathbf{y}_x = [y(\mathbf{x}_1), \ldots, y(\mathbf{x}_{n_{sp}})]^T$. Initial samples are selected according to the above guidelines. In kriging, the unknown function of interest y is assumed to be a realization of a stochastic process

$$\widehat{y}\,(\mathbf{x}) \;=\; f\,(\mathbf{x}) \;+\; Z\,(\mathbf{x}) \tag{2.5}$$

The first term is a low-order regression function (constant, linear or quadratic) and the second term is a stochastic process, assumed to be Gaussian and with variance σ^2. The regression model, $f\,(\mathbf{x})$, realizes a globally valid trend function, and the $Z\,(\mathbf{x})$ adjusts the prediction for local deviations from $f\,(\mathbf{x})$, and guarantees that the kriging predictor $\widehat{y}$ gives the exact value of y at a sample location. The assumption that the system response in Eq. (2.5) is a random process is made because the deviations from the regression model can resemble the realization of a stochastic process [15]. The covariance matrix of $Z\,(\mathbf{x})$ is a measure of how strongly correlated two points are, and is equal to the variance σ^2 multiplied by the correlation matrix, $\mathbf{R}$. The correlation matrix of the samples has dimensions $n_{sp} \times n_{sp}$, and each element is given by

$$R_{ij}(\mathbf{p},\, \mathbf{x}_i,\, \mathbf{x}_j) \;=\; \prod_k \; scf\left(p_k,\, x_i^{(k)} \;-\; x_j^{(k)}\right) \tag{2.6}$$

where scf is a user defined spatial correlation function, and $x_i^{(k)}$ denotes the k-th component of the i-th sample point. This matrix is dense symmetric positive definite with diagonal elements equal to one, and becomes ill-conditioned when samples are too close together. The order of the kriging correlation matrix depends only on the number of samples considered, n_{sp}, and not on the dimension of the input vector, in this case $n_\alpha \cdot\, n_M \cdot\, n_\beta$. Several correlation functions are available, such as exponential, linear and spline functions, and the choice should be motivated by the underlying

phenomenon being approximated [86]. For a continuously differentiable problem, the spline function should be considered because it has a parabolic behaviour near the origin. To model physical phenomena, which usually have a linear behaviour near the origin, the use of exponential or linear functions was suggested [93]. The exponential is the most common correlation function, which is adapted to a wide range of physical applications. Depending on the correlation function selected and for a large dimension of the input vector, $\mathbf{x}$, the corresponding correlation matrices can be ill-conditioned, which is an issue when using kriging for high-dimensional interpolation. In this study, the correlation function used is the exponential. The regression model is formulated as a low-order function, $f(\mathbf{x}) = \mathbf{f}(\mathbf{x})^T \boldsymbol{\beta}$, with the two vectors having dimension equal to the number of basis functions of the selected polynomial, N_{basis}. Here, the regression model was taken as a linear function and, for the example illustrated, $\mathbf{f}(\mathbf{x}) = \left[1,\, \alpha,\, M,\, \beta\right]^T$. A matrix $\mathbf{F}(\mathbf{x})$, of dimension $n_{sp} \times N_{basis}$, is constructed from the vectors $\mathbf{f}(\mathbf{x})$, where the i-th row corresponds to the evaluation of the basis functions at the i-th sample input. With the generalized least-squares estimates of $\boldsymbol{\beta}$ and σ, denoted by $\widehat{\boldsymbol{\beta}}$ and $\widehat{\sigma}$, the unknown correlation parameters p_k are found by maximizing a likelihood function [16], which represents the probability that the stochastic process $Z(\mathbf{x})$ produced the value of the aerodynamic coefficients at the sampled data points. The estimated p_k represent the fitting parameters that are most consistent with the sampled data. The kriging interpolation of the function $y(\mathbf{x})$ is given as

$$\widehat{y}(\mathbf{x}) \;=\; \mathbf{f}(\mathbf{x})^T\,\widehat{\boldsymbol{\beta}} \;+\; \mathbf{r}(\mathbf{x})^T\left(\mathbf{R}^{-1}(\mathbf{y}_x \;-\; \mathbf{F}\,\widehat{\boldsymbol{\beta}})\right) \tag{2.7}$$

where the correlation vector, written as

$$\mathbf{r}(\mathbf{x}) = \left[R_{11}(\mathbf{p}, \mathbf{x}_1, \mathbf{x}), \ldots, R_{n_{sp}1}(\mathbf{p}, \mathbf{x}_{n_{sp}}, \mathbf{x})\right]^T \tag{2.8}$$

represents the correlation between the provided set of sampled points $[\mathbf{x}_1, \ldots, \mathbf{x}_{n_{sp}}]^T$ and an arbitrary unsampled location $\mathbf{x}$ in the parameter space. The parameters of the kriging model are determined from a small ensemble of expensive numerical simulations, likely obtained from a CFD solver, and the system response is approximated at an arbitrary unsampled location not included in the initial set at the expense of two scalar products on $\mathbf{f}(\mathbf{x})$ and $\mathbf{r}(\mathbf{x})$, as shown in Eq. (2.7). A Matlab toolbox implements the kriging interpolation [86], and is freely available [1].

2.3.3 Iterative Sampling

The quality of the kriging interpolation depends on the number of sample points and their location, which is case-dependent. For a systematic methodology to be efficient and reduce the uncertainty in the prediction of the full-order function, there is a need

[1] `http://www2.imm.dtu.dk/~hbn/dace/` [retrieved March 19, 2012]

to minimize a suitable figure of merit. Two methodologies are currently adopted, based on the root Mean Squared Error (MSE) and Expected Improvement Function (EIF). The goal of both methodologies is to improve the accuracy of the kriging model at untried sample points, adding additional samples until a criterion for termination is fulfilled.

The root Mean Squared Error, φ, is referred to as the standard error of the kriging model and is a measure of uncertainty in the prediction. It is evaluated as

$$\varphi^2(\mathbf{x}) = \sigma^2 \left(1 - \mathbf{r}(\mathbf{x})^T \mathbf{R}^{-1} \mathbf{r}(\mathbf{x}) + \mathbf{u}^T \left(\mathbf{F}^T \mathbf{R}^{-1} \mathbf{F}\right)^{-1} \mathbf{u}\right) \tag{2.9}$$

with the vector $\mathbf{u}(\mathbf{x}) = \mathbf{F}^T \mathbf{R}^{-1} \mathbf{r}(\mathbf{x}) - \mathbf{f}(\mathbf{x})$ and the process variance

$$\sigma^2 = \frac{1}{n_{sp}} \left(\mathbf{y}_x - \mathbf{F}\,\widehat{\boldsymbol{\beta}}\right)^T \mathbf{R}^{-1} \left(\mathbf{y}_x - \mathbf{F}\,\widehat{\boldsymbol{\beta}}\right) \tag{2.10}$$

By construction, the MSE is zero at a sample point and increases as the distance between samples increases, with its maximum value being σ. To further improve the kriging interpolation, an additional high-fidelity simulation is run at the untried sample point $\mathbf{x}$ where the MSE is maximum. This criterion seeks for a global approximation of the exact function because it is driven by the weighted distance correlation for the error terms.

The Expected Improvement Function can be used to concentrate new sample points around the global minimum or maximum. This is very useful when, for instance, the maximum lift coefficient is of interest. The kriging predictor in Eq. (2.5) can be interpreted as a random variable with mean given by the predictor and variance given by the mean standard error. A probability can then be computed so that the system response at any point will fall below (or above) the current minimum (or maximum). The kriging model is iteratively refined placing an additional high-fidelity simulation at the untried sample point where the EIF has a maximum. This method is suited for searches of the global maxima or minima but is unable to find local maxima or minima. A good practice is the use of a combined global and local search [94].

As a high-fidelity evaluation of the system response is obtained in a new suitable sample point, the procedure is repeated until the maximum error in the prediction is below a threshold. The number of high-fidelity simulations is likely to be limited by constraints on computational time and resources, and typically this requirement is regarded as an additional criterion to stop the sampling procedure.

2.3.4 Data Fusion

The aerodynamic coefficients can be obtained using different aerodynamic sources. Data fusion combines aerodynamic predictions from different sources. Consider that data are available from two sources, which are, respectively, cheap (low-fidelity) and

expensive (high-fidelity) to evaluate. The cheap samples are considered to provide information at least about the trend of the target function, whereas the expensive samples give quantitative information. The cheap estimates are usually available in more locations than the expensive ones. A Kriging function $\widehat{\eta}$ is calculated from the samples of the cheap aerodynamic evaluations. This Kriging function is then evaluated at the locations at which expensive predictions are available, $\widehat{\eta}(\mathbf{x}_i)$. The vector of the input parameters at the expensive samples, $\mathbf{x}_i$, is augmented by the evaluation of the kriging function for the cheap samples. In the case of the baseline table, the augmented vector would have dimension four and be $\mathbf{x}_i^{aug} = [\alpha_i, M_i, \beta_i, \widehat{\eta}(\mathbf{x}_i)]^T$, with corresponding aerodynamic coefficients $y_i = y(\mathbf{x}_i)$ for each of the n_{sp} sample points. A Kriging function is calculated for these augmented samples, $\widehat{\eta}(\mathbf{x}_i^{aug})$, with the extra component bringing information to the correlation calculation from the cheap samples.

2.4 Hierarchy of Aerodynamic Models

A prerequisite for realistic predictions of the stability and control characteristics of an aircraft is the availability of a complete and accurate aerodynamic database. Here aerodynamic models are used as the source of the force and moment information. The choice of which aerodynamic model to use is based on available information and demand for cheap estimates or for detailed analyses. The higher the fidelity of the aerodynamic model to be used, the higher the execution time is normally. In the early phases of aircraft development, the geometry is defined with limited fidelity which might render expensive methods of limited use. More comprehensively, the review paper of Da Ronch et al. [81] examines the wide range of applications accessed by the use of different fidelity aerodynamic models, see also Appendix A. A number of models are used in this thesis and these are now summarized.

2.4.1 Semi-Empirical Method

The Data Compendium (DATCOM) is a document of more than 1500 pages covering detailed methodologies for determining stability and control characteristics of a variety of aircraft configurations. In 1979, it was programmed in Fortran and renamed the USAF stability and control digital DATCOM [6]. Digital DATCOM is a semi-empirical method which can rapidly produce the aerodynamic derivatives based on geometry details and flight conditions. This code was primarily developed to estimate aerodynamic derivatives of conventional configurations [95], and to provide all the individual component contributions and the aircraft forces and moments. A design uncertainty factor is often needed to account for validity of aerodynamic characteristics estimated using this method.

2.4.2 Linear Potential Solver

Based on a Vortex-Lattice Method (VLM), TORNADO [2] is an open source Matlab implementation of a modified horse-shoe vortex singularity method for computing steady and low reduced frequency time-harmonic unsteady flows over wings. It can predict aircraft stability and control aerodynamic derivatives. The lifting surfaces are created as unions of thin, not necessarily flat, quadrilateral surface segments. The effect of aerofoil camber is modeled by surface normal rotation, which is also used to model leading- and trailing-edge control surfaces deflection. The steady wake can be fixed in the body coordinate system or can follow the free stream. The influence of compressibility is included from Prandtl-Glauert similarity [96], and zero-lift drag estimates are obtained by Eckert's flat plate analogy. A fuselage can be modelled using a combination of flat plates or the slender body theory developed by Munk [97].

2.5 CFD Flow Solver

Due to the collaborative nature of the work presented in this thesis, several CFD solvers were used. A more detailed description is given for the CFD solver of the University of Liverpool, which has been modified by the author for the simulation of the gust loads, see Appendix B for more details. A general overview is provided for the remaining CFD solvers used throughout the work, with emphasis on differences in the numerical implementation. Deviations in the numerical predictions obtained using different solvers are therefore expected around complex geometries with challenging flow conditions.

2.5.1 PMB (University of Liverpool)

The Euler and Reynolds-averaged Navier-Stokes (RANS) equations are discretised on curvilinear multi-block body conforming grids using a cell-centred finite volume method which converts the partial differential equations into a set of ordinary differential equations. The equations are solved on block structured grids using an implicit solver. A wide variety of unsteady flow problems, including aeroelasticity, cavity flows, aerospike flows, delta wing aerodynamics, rotorcraft problems and transonic buffet have been studied using this code. A validation against flight data for the F-16XL aircraft has also been performed [9]. The main features of the CFD solver are detailed in Badcock et al. [98].

The three-dimensional Navier-Stokes equations may be written in non-dimensional conservative form as

$$\frac{\partial \mathbf{W}}{\partial t} + \frac{\partial \left(\mathbf{F}^i - \mathbf{F}^v\right)}{\partial x} + \frac{\partial \left(\mathbf{G}^i - \mathbf{G}^v\right)}{\partial y} + \frac{\partial \left(\mathbf{H}^i - \mathbf{H}^v\right)}{\partial z} = 0 \tag{2.11}$$

[2] `http://www.redhammer.se/tornado/` [retrieved March 19, 2012]

where $\mathbf{W} = (\rho,\, \rho\,u,\, \rho\,v,\, \rho\,w,\, \rho\,E)^T$ is the vector of conserved variables, ρ is the density and u, v, and w are the components of velocity given by the Cartesian velocity vector $\mathbf{U} = (u,\, v,\, w)^T$. The total energy per unit mass is E. The superscripts $(^i)$ and $(^v)$ denote the inviscid and viscous components of the flux vectors, $\mathbf{F}$ (x-direction), $\mathbf{G}$ (y-direction) and $\mathbf{H}$ (z-direction). The inviscid flux vectors, $\mathbf{F}^i$, $\mathbf{G}^i$ and $\mathbf{H}^i$, are given by

$$\begin{aligned}
\mathbf{F}^i &= \left(\rho\,u,\, \rho\,u^2 + p,\, \rho\,u\,v,\, \rho\,u\,w,\, u\,(\rho\,E + p)\right)^T \\
\mathbf{G}^i &= \left(\rho\,v,\, \rho\,v\,u,\, \rho\,v^2 + p,\, \rho\,v\,w,\, v\,(\rho\,E + p)\right)^T \\
\mathbf{H}^i &= \left(\rho\,w,\, \rho\,w\,u,\, \rho\,w\,v,\, \rho\,w^2 + p,\, w\,(\rho\,E + p)\right)^T
\end{aligned} \tag{2.12}$$

while the viscous flux vectors, $\mathbf{F}^v$, $\mathbf{G}^v$ and $\mathbf{H}^v$, contain terms of the heat flux and viscous forces exerted on the body, and can be represented by

$$\begin{aligned}
\mathbf{F}^v &= \frac{1}{Re}\,(0,\, \tau_{xx},\, \tau_{xy},\, \tau_{xz},\, u\,\tau_{xx} + v\,\tau_{xy} + w\,\tau_{xz} + q_x)^T \\
\mathbf{G}^v &= \frac{1}{Re}\,(0,\, \tau_{xy},\, \tau_{yy},\, \tau_{yz},\, u\,\tau_{xy} + v\,\tau_{yy} + w\,\tau_{yz} + q_y)^T \\
\mathbf{H}^v &= \frac{1}{Re}\,(0,\, \tau_{xz},\, \tau_{yz},\, \tau_{zz},\, u\,\tau_{xz} + v\,\tau_{yz} + w\,\tau_{zz} + q_z)^T
\end{aligned} \tag{2.13}$$

The stress tensor components, τ_{ij}, and the heat flux vector components, q_i, can be found in numerous text books, e.g. Anderson [99]. The Navier-Stokes equations are discretised using a cell-centred finite volume approach. The computational domain is divided into a finite number of non-overlapping control volumes and the governing equations are applied to each cell in turn. A fully implicit steady solution of the RANS equations is obtained by advancing the solution forward in time by solving the discrete non-linear system of equations

$$\frac{\mathbf{W}_{ijk}^{n+1} - \mathbf{W}_{ijk}^{n}}{\Delta\,t^*} = -\frac{1}{V_{ijk}}\mathbf{R}_{ijk}\left(\mathbf{W}_{ijk}^{n+1}\right) \tag{2.14}$$

where V_{ijk} denotes the cell volume, $\mathbf{W}_{ijk}$ represents the fluid variables and $\mathbf{R}_{ijk}(\mathbf{W}_{ijk}^{n+1})$ the flux residuals. The pseudo time step is indicated by $\Delta\,t^*$. Equation (2.14) represents a system of non-linear algebraic equations and to simplify the solution procedure, the flux residual is linearised in time. The flux residual is the discretisation of the convective terms, given here by Osher's approximate Riemann solver [100], MUSCL interpolation [101], and Van Albada's limiter. An iterative Generalised Conjugate Gradient method is used to solve the linear system. A Block Incomplete Lower-Upper factorisation is used as preconditioner for the system of equations.

The implicit dual-time method proposed by Jameson [102] is used for time-accurate calculations. The solution iterates in pseudo time for each real time step to achieve

convergence. In the current application, a key functionality of the CFD solver is the ability to move the mesh conforming to the motion of the body. Rigid body motions can be treated by moving the mesh rigidly in response to the applied sinusoidal motion. The mesh is deformed once per real time step during the unsteady calculation. A curvilinear time dependent formulation is used to formulate the mapping between the computational space and the physical space.

The steady state solver for the turbulence model is formulated and solved in a similar manner to the mean flow as described, with the vector **W** replaced by the equivalent turbulent vector and an equivalent substitution for the flux residual. The eddy viscosity is calculated from the turbulent quantities as specified by the model and is used to advance the mean flow solution. This new mean flow solution is then used to update the turbulence solution, freezing the mean flow values. Several turbulence models are implemented in the PMB solver, including algebraic, one-equation and two-equation models. In this study, the model used is $k-\omega$ with P_ω enhancer proposed by Brandsma et al. [103] for the TCR case.

Control surfaces are blended into the geometry following the approach given in [104]. Mesh block faces are placed on the control surfaces and the mesh points on these faces are deflected to define the control surface mode shapes. After the surface grid point deflections are specified, transfinite interpolation is used to distribute these deflections to the volume grid. Mode shapes are defined for the control surface deflections [105]. Each mode shape specifies the displacement of the grid points on the aircraft surface for a particular control surface.

2.5.2 TAU (German Aerospace Center)

The DLR TAU code [106, 107] is a modern massively parallel software system for the simulation of flows around complex geometries from low subsonic to hypersonic flow regimes. The different modules of TAU can be used stand-alone or in a more efficient way within a Python scripting framework which allows for inter-module communication without file I/O by using common memory allocations. The unsteady compressible RANS flow solver is based on hybrid unstructured grids with a finite volume discretization. The flow solver uses an edge-based dual-cell approach, either cell-vertex or cell-centred, employing either a second-order central scheme or a variety of upwind schemes with linear reconstruction for second order accuracy.

As for the PMB solver, unsteady simulations use Jameson's dual-time-stepping method [102] to integrate the equations in the time-domain. Additionally, the solver respects the geometric conservation law, and bodies which are deforming and in arbitrary motion can be simulated. For the pseudo time stepping various explicit Runge-Kutta and a semi-implicit Lower-Upper Symmetric Gauss-Seidel (LU-SGS) scheme are avail-

able for enhancing convergence acceleration with a geometrical multi-grid algorithm and local time-stepping.

TAU includes an adjoint-solver for gradient based numerical shape optimization. The discrete adjoint method [108] consists of the explicit construction of the exact flux Jacobians of the spatial discretization with respect to the unknown flow variables allowing the adjoint equations to be formulated and solved, and is an important part of the linear frequency domain solver and error estimation methods.

2.5.3 COSA (University of Glasgow)

The structured multi-block Navier-Stokes solver COSA is an explicit multigrid finite volume cell-centered code. It solves the integral conservation laws in generalized curvilinear coordinates making use of a second order discretisation method. The discretisation of the convective fluxes is based on Van Leer's MUSCL extrapolations and the approximate Riemann solver of Roe's flux difference splitting. The discretisation of the viscous fluxes uses centered finite differences. The set of nonlinear algebraic equations resulting from the spatial discretisation of the conservation laws is solved with an explicit approach based on the use of a four-stage Runge-Kutta smoother. The convergence rate is greatly enhanced by means of local time-stepping, variable-coefficient central implicit residual smoothing and a full approximation storage multigrid algorithm. When solving problems at very low flow speed, computational accuracy and high rates of convergence are maintained by using a carefully designed low-speed preconditioner [109].

In the case of unsteady problems, Jameson's dual-time-stepping method [102] is used to integrate the equations in the time-domain. The interested reader is referred to references [109–111] for further details on the COSA solver and a thorough validation of its inviscid and viscous capabilities for steady and unsteady problems.

2.5.4 Cobalt

The Cobalt code solves the unsteady, three-dimensional and compressible Navier-Stokes equations. The Navier-Stokes equations are discretised on arbitrary grid topologies using a cell-centered finite volume method. Second order accuracy in space is achieved using the exact Reimann solver of Gottlieb and Groth [112] and least squares gradient calculations using QR factorization. To accelerate the discretized system, a point-implicit method using analytic first-order inviscid and viscous Jacobian is used. A Newtonian sub-iteration method is used to improve time accuracy of the point-implicit method. The method is second order accurate in time. Tomaro et al. [113] converted the code from explicit to implicit, enabling CFL numbers as high as 10^6. Cobalt uses an arbitrary Lagrangian-Eulerian formulation and hence allows all translational and rotational degrees of freedom. For the control surface simulations, an overset grid

capability is available. The code can simulate both free and specified six degrees of freedom motions.

2.6 Calculation of Dynamic Derivatives

The estimation of dynamic derivatives is obtained by imposing a forced sinusoidal motion around the aircraft centre of gravity. For the computation of the longitudinal dynamic derivative values from the time-histories of the forces and moments, it is assumed that the aerodynamic coefficients are linear functions of the angle of attack, α, pitching angular velocity, q, and rates, $\dot{\alpha}$ and $\dot{q}$. To illustrate, the increment in the longitudinal aerodynamic coefficients (lift, drag and pitching moment) with respect to the mean value during the applied pitching sinusoidal motion is formulated as

$$\Delta C_j = C_{j_\alpha} \Delta \alpha + C_{j_{\dot{\alpha}}} \frac{c}{2 U_\infty} \dot{\alpha} + C_{j_q} \frac{c}{2 U_\infty} q + C_{j_{\dot{q}}} \left(\frac{c}{2 U_\infty} \right)^2 \dot{q} \qquad (2.15)$$
$$\text{for } j = L, D, \text{ and } m$$

The harmonic motion in pitch defines the kinematic relations for the angle of attack, pitching angular velocity and rate as

$$\begin{aligned} \Delta \alpha &= \alpha_A \, sin(\omega t) \\ \dot{\alpha} = q &= \omega \, \alpha_A \, cos(\omega t) \\ \ddot{\alpha} = \dot{q} &= -\omega^2 \alpha_A \, sin(\omega t) \end{aligned} \qquad (2.16)$$

Eq. (2.15) can then be rewritten as

$$\Delta C_j = \alpha_A \bar{C}_{j_\alpha} \sin(\omega t) + \alpha_A \, k \, \bar{C}_{j_q} \cos(\omega t) \qquad (2.17)$$

where $k = \omega \, c/(2 U_\infty)$ indicates the non-dimensional reduced frequency of the applied motion. The in-phase and out-of-phase components of ΔC_j, respectively indicated as $\bar{C}_{j_\alpha}$ and $\bar{C}_{j_q}$ [114], are defined as

$$\bar{C}_{j_\alpha} = \left(C_{j_\alpha} - k^2 \, C_{j_{\dot{q}}} \right) \qquad (2.18)$$

$$\bar{C}_{j_q} = \left(C_{j_{\dot{\alpha}}} + C_{j_q} \right) \qquad (2.19)$$

The dynamic derivative values can be calculated taking the first Fourier coefficients of the time history of ΔC_j over n_c cycles

$$\bar{C}_{j_\alpha} = \frac{2}{\alpha_A \, n_c \, T} \int_0^{n_c T} \Delta C_j(t) \; sin(\omega t) \; dt \tag{2.20}$$

$$\bar{C}_{j_q} = \frac{2}{k \, \alpha_A \, n_c \, T} \int_0^{n_c T} \Delta C_j(t) \; cos(\omega t) \; dt \tag{2.21}$$

where $T = 2\pi / \omega$ is the period of one cycle of unsteadiness. The model formulation given in Eq. (2.15) is adequate for aircraft operating at low angles of attack or in linear and steady aerodynamic flight regimes, with the out-of-phase approximating well the aerodynamic damping. However, many applications of common interest are in the transonic speed range and high angle of attack [114, 115]. Under these conditions, the non-linear unsteady aerodynamic behaviour may not be well predicted using the above linear model, and more advanced mathematical models are then required [38, 39, 56]. The first harmonic is an important term even under conditions where higher order terms might be required. Due to the orthogonal nature of the model series, the first harmonic remains unchanged when higher order terms are required to model the non-linear aerodynamic behavior. The in-phase component, $\bar{C}_{j_\alpha}$, is comprised of a static derivative and a rotational derivative, whereas the out-of-phase component, $\bar{C}_{j_q}$, includes a rotary derivative and a translation acceleration derivative. The frequency influence is accounted for explicitly in the equations for the in-phase component, while the equations for the out-of-phase component used to determine the damping derivatives do not include the frequency effect. Models for an aircraft performing a one degree of freedom oscillatory motion in either roll or yaw can be developed in a similar fashion to that for the pitching oscillations [116, 117].

Two techniques to post-process time-domain sampled data obtained from numerical investigations have been used. First, the transformation to the frequency domain is considered to gain insights into the frequency spectra of aerodynamic loads. Then, a regression-based approach is addressed. In the present study and in all test cases, no significant difference in dynamic derivative values was obtained from the use of the two implemented post-processing techniques.

Frequency domain analysis has many advantages and is currently used in different research areas. The computation of the in-phase and out-of-phase components of the aerodynamic coefficients is performed by a numerical technique [118] applied to the last cycle of the steady harmonic outputs. The transformation of the sampled time-domain data into the frequency domain is achieved by an approximation of the finite Fourier integral. The finite Fourier integral of a continuous scalar time function, $x(t)$, on a

finite time interval, $t \in [0, T]$, is defined as

$$\mathscr{F}[x(t)] \equiv \tilde{x}(i\omega) = \int_0^T x(t)\, e^{-i\,2\pi f\, t}\, dt \tag{2.22}$$

where i is the imaginary unit and f the dimensional frequency. The accuracy of the transformation to the frequency domain can be improved using quadrature methods. The finite Fourier integral is evaluated at discrete values of frequency, f_k, evenly spaced between zero frequency and the Nyquist frequency, f_N, with a frequency resolution equal to the reciprocal of the length of the time record [119]. Arbitrary frequency resolution in a selected frequency band of interest can be obtained using the Chirp-z transform [120], decoupling the frequency resolution from the length of the time record. A cubic Lagrange polynomial interpolation scheme was implemented in the current framework. A Chirp-z cubic approximation to the finite Fourier integral is also available.

The system response, quantified by the amplitude ratio and phase lag with respect to the input, can be determined by the transfer function between the input and the output. For the pitching moment coefficient, this is

$$G(i\omega) = \frac{\mathscr{F}[C_m(t)]}{\mathscr{F}[\alpha(t)]} = R(\omega)\, e^{i\,\phi(\omega)} \tag{2.23}$$

where $R(\omega)$ and $\phi(\omega)$ are the amplitude ratio and phase lag, respectively, and are defined as

$$R(\omega) = \frac{\|\tilde{C}_m(i\omega)\|}{\|\tilde{\alpha}(i\omega)\|} \tag{2.24}$$

$$\phi(\omega) = \angle\tilde{C}_m(i\omega) - \angle\tilde{\alpha}(i\omega) \tag{2.25}$$

An alternative approach to the calculation of dynamic derivatives is to use the solution of a least squares problem [121]. Within a general framework, Eq. (2.15) can be formulated as

$$y = a_0 + a_1 x_1 + a_2 x_2 + \ldots + a_p x_p + e \tag{2.26}$$

for a dependent variable, y, and the p independent arguments, $x_1, x_2, \ldots, x_p$. Here $a_0, a_1, \ldots, a_p$ are unknown parameters of the mathematical model and, e, the approximation error. The dependent variable represents the dependency upon time of the integrated aerodynamic coefficients. For small amplitude pitch oscillations, the independent arguments are the instantaneous angle of attack and its rate of change. The parameters of the mathematical model are estimated using the n values of the instantaneous numerical values of the $p+1$ variables, $y, x_1, x_2, \ldots, x_p$. The vector of the dependent variable sampled in time and the vector of unknown regression parameters are denoted, respectively, by $\mathbf{y} = (y_1, y_2, \ldots y_n)^T$ and $\mathbf{x} = (x_1, x_2, \ldots, x_p)^T$. The

vector of approximation errors is $\mathbf{e} = (e_1, e_2, \ldots, e_p)^T$ and the matrix relating the unknowns with the independent variables, of dimension $n \times (p+1)$, is given by

$$\mathbf{A} = \begin{bmatrix} 1 & a_{1\,1} & \ldots & a_{p\,1} \\ 1 & a_{1\,2} & \ldots & a_{p\,2} \\ \vdots & \vdots & \ddots & \vdots \\ 1 & a_{1\,n} & \ldots & a_{p\,n} \end{bmatrix} \tag{2.27}$$

The corresponding linear regression model is given by

$$\mathbf{y} = \mathbf{A}\,\mathbf{x} + \mathbf{e} \tag{2.28}$$

The unknown vector of the approximate solution which minimizes the error is found by minimizing the functional $J = \|\mathbf{e}\|^2 / 2$

$$\frac{\partial J}{\partial x_i} = 0, \qquad \text{for } i = 1, 2, \ldots, p \tag{2.29}$$

which results in $\left(\mathbf{A}^T \mathbf{A}\right) \mathbf{x} = \mathbf{A}^T \mathbf{y}$. The use of the linear regression technique provides the estimation of the aerodynamic derivatives stored in the vector $\mathbf{x}$. In general, the matrix $\mathbf{A}$ is non-square, with more rows than columns. Several numerical methods are available to solve least squares problems [122], e.g., direct inversion of $\mathbf{A}^T \mathbf{A}$, Gaussian elimination, Moore-Penrose generalized inverse approach and the QR factorization. However, the Moore-Penrose approach and the QR factorization are more accurate than the Gaussian elimination and the direct inversion solutions. The cost of the QR factorization is $\mathcal{O}\left(n^2\right)$, and the Moore-Penrose inversion involves $\mathcal{O}\left(n^3\right)$ operations.

Chapter 3

Dynamic Derivatives from Unsteady Time-Domain CFD Simulations

3.1 Introduction

The manoeuvre capabilities of combat aircraft have highlighted the limitations and shortcomings of the conventional stability or aerodynamic derivative model for the representation of the aerodynamic loads in the aircraft equations of motion [123]. An important consideration is the presence of significant motion frequency effects on the dynamic derivatives measured in small-amplitude oscillatory wind tunnel tests at higher mean angles of attack. This frequency dependence cannot be reconciled with the stability derivatives model. Although these effects were first recognised in the 1950s, they mostly played an insignificant role for conventional aircraft operating at benign conditions. The changing interest in the determination of dynamic stability derivatives due to the requirements of increasing angle of attack and Mach number during the 1970s is described in Orlik-Rückemann [124]. Modern combat aircraft are capable of performing agile manoeuvres involving high pitch rates at extreme angles of attack. Vehicles manoeuvring in this regime are subject to non-linear aerodynamic loads. The non-linearities are mainly due to three dimensional separated flow and concentrated vortices. The appearance of these features alters the dynamic behaviour, in ways that are not predictable on the basis of linearised formulations of the aerodynamic forces and moments. Accurate prediction of the non-linear airloads is of importance in the analysis of aircraft flight motion and in the design of suitable flight control systems.

This work investigates the use of CFD in the prediction of dynamic derivatives for aircraft configurations. The influence of motion parameters and flight conditions on the damping values is considered. The traditional mathematical model of unsteady aerodynamics based on the concept of dynamic derivatives is used to predict large amplitude

oscillations. Results are presented for the Standard Dynamic Model (SDM) [125] and the Transonic CRuiser (TCR) [80] geometries.

3.2 Test Cases

3.2.1 Standard Dynamic Model Aircraft

The Standard Dynamic Model (SDM) is a generic fighter configuration based loosely on the F-16 planform. The model includes a slender strake-delta wing with leading-edge extensions, horizontal and vertical stabilizers, ventral fins and a blocked-off inlet (Fig. 3.1). Further details on the geometry can be found in Huang [125]. The SDM configuration has been tested extensively at various wind tunnel facilities to compare different measurement techniques [126–129].

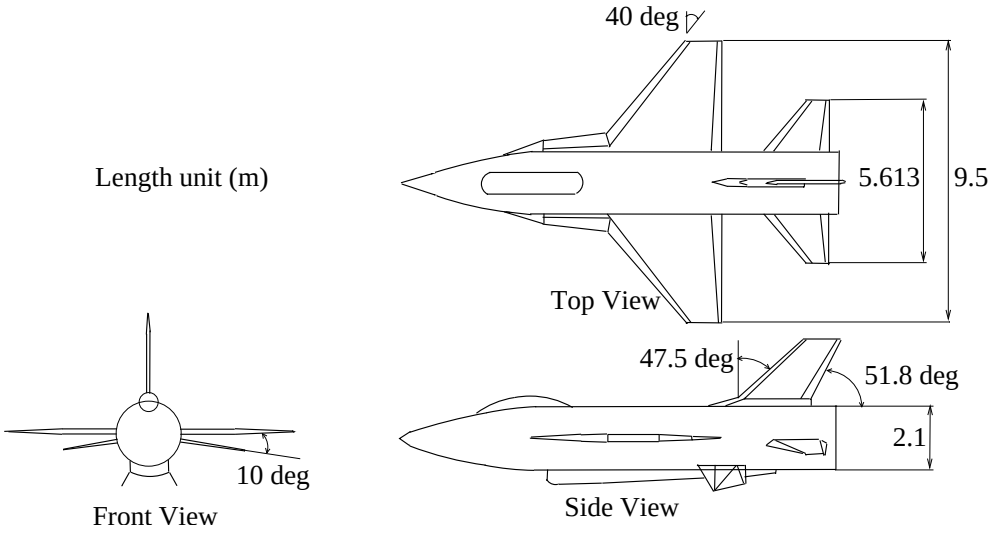

Figure 3.1: SDM layout [125]

A block structured mesh was generated for a previous study [23] and is shown in Fig. 3.2. The geometry was slightly simplified by removing the blocked-off intake and the ventral fins. These were considered reasonable simplifications because the main interest here is on the impact of the vortical flow developments on the upper lifting surfaces. A fine Euler mesh was generated with 2.4 million points representing one half of the SDM configuration. A coarse mesh for the full configuration was obtained with 701 thousand points by omitting every second point in each direction. The lifting surfaces all have sharp leading-edges. This allows the Euler equations to approximate the development of vortical flow since the separation points are fixed at the leading-edge. In this way, the Euler equations can correctly describe the transport of vorticity and entropy from the leading-edge, along the vortex sheet, to the roll up into the leading-edge vortices. However, it is well known that varying the grid refinement in the leading-edge region alters significantly the solution [130]. Two grids were used to

evaluate the impact of mesh refinement on the flow development and on the prediction of dynamic derivatives.

The SDM model geometry has dimensions given in Table 3.1. The moment reference point is taken at the centre of gravity of the wind tunnel model. Calculations are first described for the coarse and half-fine mesh to investigate the mesh dependency. In the following figures, findings for the coarse and half-fine configurations are presented and indicated, respectively, by *C* and *HF*. The temporal resolution of the unsteady CFD calculations is also addressed to demonstrate that results are well-converged with respect to time step.

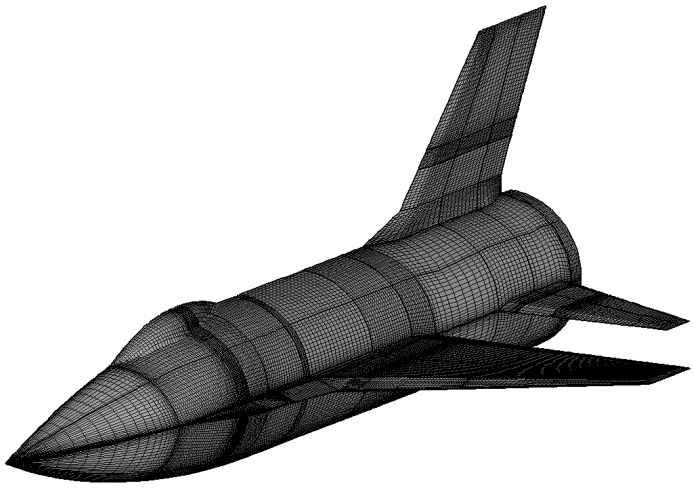

(a) Half-fine, 2.4 million points

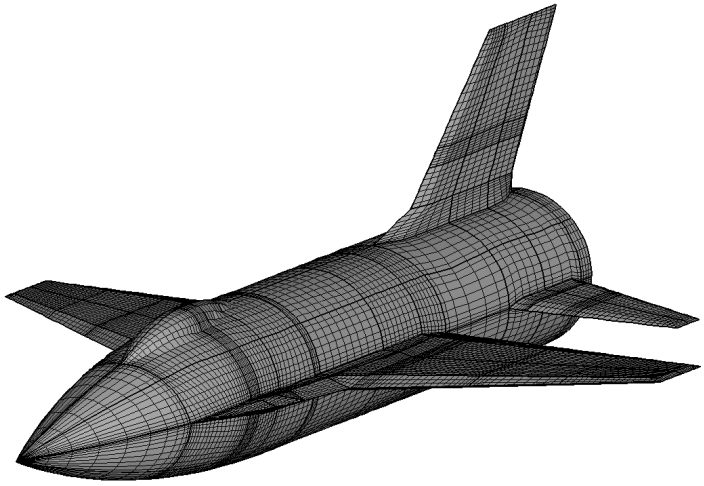

(b) Coarse, 0.7 million points

Figure 3.2: Surface grid for the SDM model geometry [131]

Parameter	Value
S	$0.1238\,m^2$
b	$0.6096\,m$
c	$0.2299\,m$
d	$0.9429\,m$

Table 3.1: Reference values of the SDM model geometry

3.2.2 Transonic CRuiser Wind Tunnel Model

The Transonic CRuiser (TCR) aircraft was designed, built and wind tunnel tested within the SimSAC project [80] to highlight the difficulties in using engineering methods for aircraft design in the transonic regime, see also Appendix A.1. A multi-block structured grid was generated at Liverpool for the half configuration with 8.5 million points. The main characteristics of the mesh are illustrated in Figs. 3.3 and 3.4. The mesh around the solid model and the symmetry plane are shown, with a high concentration of cells in the regions adjacent to the solid. The non-dimensional minimum spacing normal to the solid wall is 2.5×10^{-6} which allows flows with Reynolds numbers of around 2 million to be simulated. The tips of the wing and the canard of the TCR model are both blunt, for which the same block topology was chosen. Here, a diamond shaped block fits into the leading-edge and another at the trailing edge. The quality of the cells in these two areas is slightly compromised in order to allow the C-blocking around the wing.

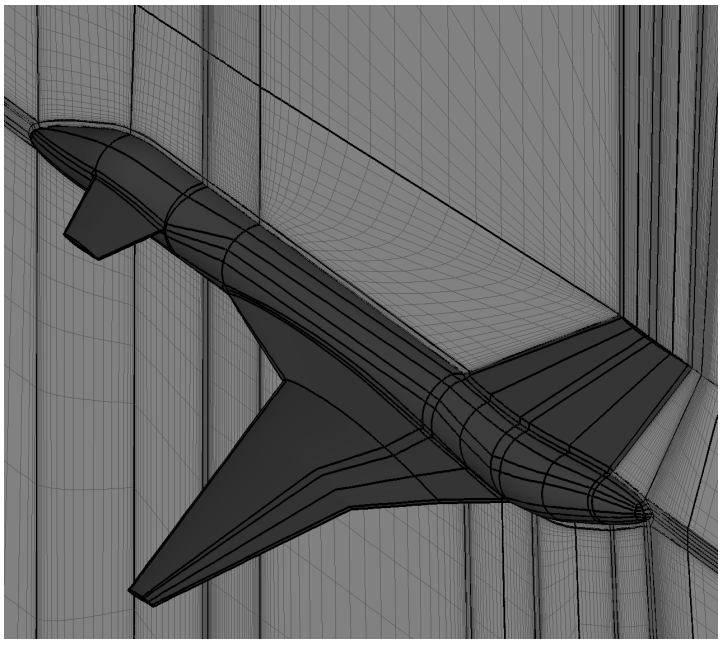

Figure 3.3: Viscous grid of TCR wind tunnel model [131]

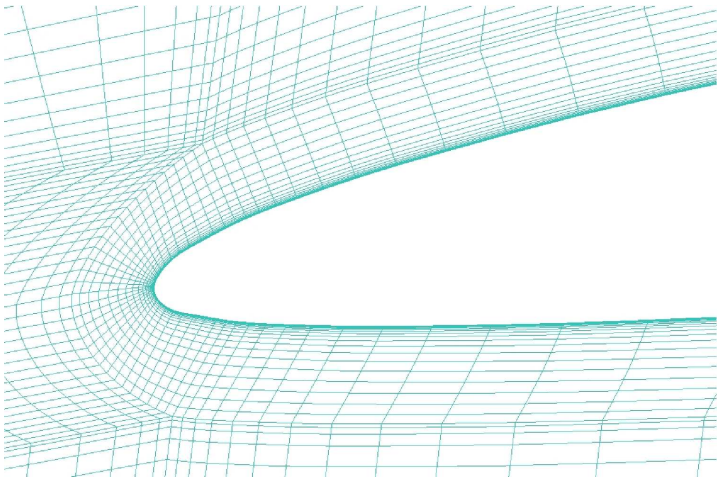

Figure 3.4: Chordwise grid section on the wing

Experimental investigations of the aerodynamic characteristics at low speed and up to 40° angle of attack were performed in the wind tunnel facilities at the Central Aerohydrodynamic Institute, TsAGI. The T–103 wind tunnel is used for investigations of unsteady aerodynamic characteristics in the low subsonic velocity range. The wind tunnel has an open jet working section, of the continuous type, with an elliptical cross section, $4.0 \times 2.33\,m$. Several configurations of the wind tunnel model were investigated to allow consideration of the influence of single components (vertical tail and canard wing on/off) on the overall performance. The approved test matrix contained a large set of experimental measurements to get insights of static aerodynamic characteristics, rotary and unsteady aerodynamic derivatives and unsteady non-linear aerodynamic characteristics during large amplitude oscillations. The normal and lateral forces and the moment coefficients from static and large amplitude oscillations were measured. The mean values, in-phase and out-of-phase components of the force and moment coefficients were measured from the rotary and oscillatory motions. Wind tunnel tests were run at a freestream speed of $40\,m/s$, which corresponds at sea level to a Mach number of 0.117, and a Reynolds number, based on the mean aerodynamic chord of the wind tunnel model, of 0.778 million. The moment reference point and the model centre of gravity are coincident and located at 54.78% of the fuselage length from the foremost point. Geometrical dimensions of the wind tunnel model are summarized in Table 3.2.

3.3 Numerical Results

Numerical results are presented for the SDM model geometry and TCR wind tunnel model. The flow is modelled using the Euler equations for the SDM. The unsteady aerodynamic loads arising from forced periodic motions converge to a steady harmonic

Parameter	Value
S	$0.3056\,m^2$
b	$1.12\,m$
c	$0.2943\,m$
d	$0.1596\,m$

Table 3.2: Reference values of the TCR wind tunnel model

response after the decay of the initial transient. The SDM has been investigated in previous studies. Benchmarking of steady aerodynamic coefficients can be found in Ghoreyshi et al [23]. A large set of results was computed and is presented for sinusoidal pitching motions in the current thesis. A comparison of lateral dynamic derivatives with experimental data is shown in reference [132]. For the TCR, dynamic derivatives are predicted from the RANS equations based on small amplitude oscillatory motions for several values of the reduced frequency up to high mean angles of attack. Large amplitude oscillatory motions were also numerically simulated to investigate non-linear effects of flow separation development at dynamic conditions. Then, the predicted dynamic derivatives from small amplitude oscillations are used in the traditional flight dynamics mathematical model to predict aerodynamic loads during large amplitude maneouvers.

3.3.1 Standard Dynamic Model Aircraft

Results presented are limited to forced sinusoidal motions in pitch. Several combinations of solver parameters were examined to find those needed for a numerically well converged solution. Several experimental [133, 134] and numerical [135] investigations were addressed to the determination of dynamic derivatives of the SDM geometry model throughout the transonic regime and at low speed up to high angles of incidence. Wind tunnel tests [136] were conducted to study the unsteady aerodynamic behaviour of an airfoil sinusoidally oscillating in plunge for a range of reduced frequencies. However, the range of motions performed in dynamic testing facilities is limited by wind tunnel walls, kinematic and vibrational restrictions. The mass and moments of inertia of a dynamic wind tunnel model must be as low as possible to achieve a favourable ratio between the aerodynamic forces of interest and the additional inerital forces. The elastic deformation of the tunnel model, on the other hand, must be as small as possible. A constraint in dynamic tests is that the first eigenfrequency of the model should be one order of magnitude above the excitation frequency (e.g., above $15Hz$) in order to avoid the excitation of higher frequencies in the model [137]. Explorative studies were undertaken to assess the variation of the dynamic derivatives with reduced frequency and amplitude of the applied motion. Each study focuses primarily on the effect of one motion parameter, as shown in Table 3.3.

Set 1	Set 2	Set 3	Set 4
M	α_0	k, (α_0)	α_A, (α_0, k)

Table 3.3: Description of the SDM test cases; terms in parentheses indicate secondary dependencies of the investigations

3.3.1.1 Mach Number

The dependency of the damping-in-pitch derivative on Mach number is evaluated in subsonic and high transonic regimes. The Mach number varies between 0.4 up to 1.1 with a finer step increment near the sonic region where a significant change in damping was experimentally observed [133, 134]. Results are for the coarse and half-fine grids. The reduced frequency is held constant. At high speeds ($M \sim 1$), the dimensional frequency of motion is an order larger than at low speeds ($M \sim 0.1$), with a significant impact on wind tunnel requirements. Numerical predictions are compared with results obtained in the large transonic wind tunnel at TsAGI [134] . With a flowfield featuring the formation of shock waves and their time-dependent motion, a time step study was undertaken to evaluate the influence of the time resolution on the flow solution. Two sets of unsteady calculations were performed. First, the numerical solution was computed at 20 time steps uniformly distributed in one harmonic period ($\Delta t^* = 3.18$) and 3 cycles were simulated. Then, the number of time steps per cycle was increased to 80 ($\Delta t^* = 0.796$), retaining the same number of cycles. Tests verified that an adequate convergence of the pseudo iterations was achieved at each physical time step. The influence of the time step is shown in Fig. 3.5 for the coarse grid, and shows that 20 time steps per pitching cycle are adequate for these cases. A similar conclusion holds valid for the fine grid.

The variation of the damping-in-pitch derivative with Mach number is shown in Fig. 3.6. Results for the two temporal resolutions were virtually identical and only one data set is herein included. Numerical results are in good agreement with experimental measurements. An increase in the damping is predicted for increasing Mach numbers, with the largest values in the sonic range. Beyond the transonic dip, where some mesh dependence is observed, the numerical results predict the reduction of the damping value.

At low speeds, variations of the pressure coefficient in the region of the wing leading-edge were in phase with the harmonic motion. Variations over the horizontal tailplane lag behind the angle of attack change because of the lever arm from the rotation axis and the finite time to convect downstream changes in the flowfield. At higher speeds, the periodic motion of the shock wave forming at the wing leading-edge is found to have a phase lag with respect to the forced motion. During the upstroke, the shock wave near the leading-edge bends toward the wing tip and its downstream location

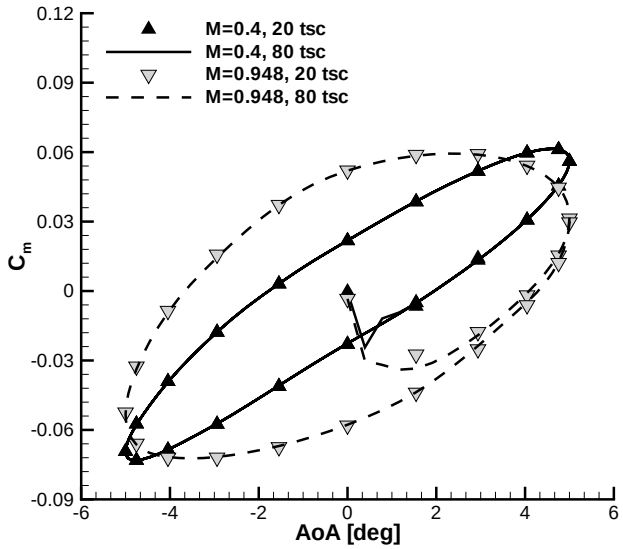

Figure 3.5: Pitching moment coefficient loops for the SDM model geometry at two values of Mach number; the term "tsc" indicates the number of physical time steps per cycle of unsteadiness

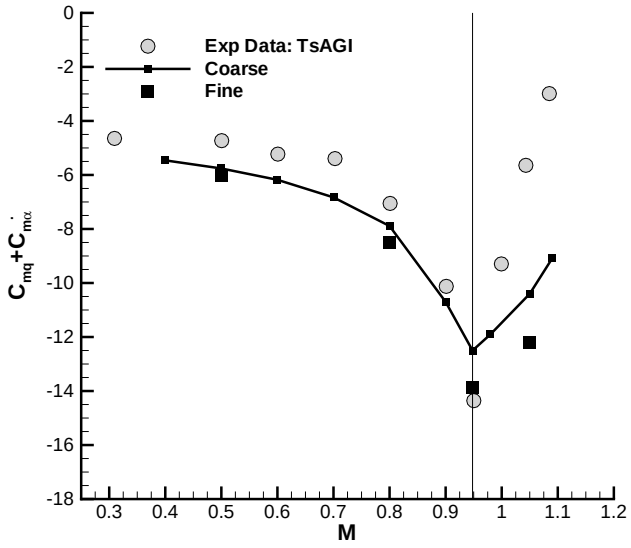

Figure 3.6: Influence of Mach number on the pitch damping derivative for the SDM model geometry; experimental data were obtained in TsAGI [134]

moves until 70–80% of the tip chord and, eventually, interacting with the shock wave at the trailing-edge. A similar pattern is observed on the lower side of the wing surface for decreasing angle. Moving from the wing tip inward, the strength of the shock wave forming at the leading-edge is reduced while an increase in strength is observed for the

shock wave at the trailing-edge. The low pressure region on the horizontal tailplane reaches its maximum downstream location up to about 50% of the local chord. Davari and Soltani [138] performed supersonic visualizations to measure the motion of shock waves generated from several components of the SDM geometry model in pitching oscillations, and found that a relationship exists between the shape of the hysteresis loop of the shock angle and that of the normal force coefficient. The effect of reduced frequency was observed to be similar in both shock wave and force coefficient hysteresis loops.

In the absence of boundary-layer separation, the motion of the shock wave is the essential feature that makes the unsteady transonic problem non-linear [139]. A non-linear system transfers energy to a range of frequencies higher than the frequency being forced by the harmonic change in the angle of attack. For low angles of incidence and amplitude, a linear or quasi-linear response is obtained in terms of integrated aerodynamic loads, as suggested in Fig. 3.5. The system response, quantified by the amplitude ratio and phase lag with respect to the input, can be determined by the transfer function of the input-output pair. For the pitching moment coefficient, this is

$$G\left(i\,\omega\right) \;=\; \frac{\mathscr{F}\left[C_m\left(t\right)\right]}{\mathscr{F}\left[\alpha\left(t\right)\right]} \;=\; R\left(\omega\right)\, e^{i\,\phi(\omega)} \tag{3.1}$$

where $R\left(\omega\right)$ and $\phi\left(\omega\right)$ are the amplitude ratio and phase lag, respectively, and defined as

$$R\left(\omega\right) \;=\; \frac{\|\tilde{C}_m\left(i\,\omega\right)\|}{\|\tilde{\alpha}\left(i\,\omega\right)\|} \tag{3.2}$$

$$\phi\left(\omega\right) \;=\; \angle\,\tilde{C}_m\left(i\,\omega\right) \;-\; \angle\,\tilde{\alpha}\left(i\,\omega\right) \tag{3.3}$$

The amplitude ratio is analogous to the steady-state pitching moment curve slope with respect to the angle of attack. The Fourier transform of the harmonic change in angle of attack, $\tilde{\alpha}\left(i\,\omega\right)$, has a non-zero component only at the corresponding forced oscillation, $\bar{\omega}$. It is then possible to quantify the variation of the transfer function at the oscillatory frequency of interest, $G\left(i\,\bar{\omega}\right)$, for several values of Mach number, as shown in Fig. 3.7. At low speeds, both amplitude ratio and phase angle are constant and the pitching moment lags behind the angle of attack change by about twenty degrees. Due to compressibility effects, the amplitude ratio increases continuously until a sudden drop is observed at the higher end of the Mach range. The variation in phase angle indicates that the pitching moment coefficient has an increasing phase lag with respect to the angle of attack. The phase lag appears to be nearly forty-five degrees at the Mach number which corresponds to the largest aerodynamic damping (see Fig. 3.6), and is indicated in figure by a vertical line. In case of free pitching oscillations, the free response would be highly damped.

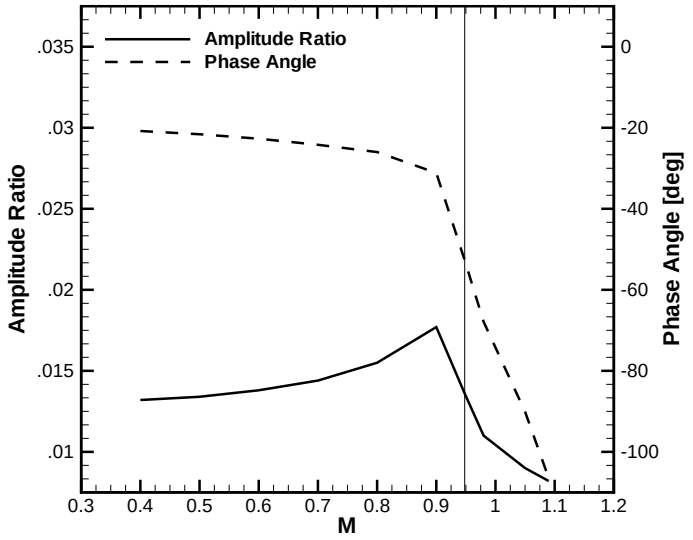

Figure 3.7: Amplitude ratio, $R(\bar{\omega})$, and phase angle, $\phi(\bar{\omega})$, between the fundamental harmonic of the angle of attack and the fundamental harmonic of pitching moment coefficient; $\bar{\omega}$ indicates the oscillatory frequency of the applied forced motion

3.3.1.2 Mean Angle of Incidence

Several independent experimental investigations [128,129] were conducted to assess the variation of the dynamic derivatives with the mean angle of incidence. Measurements were obtained in different wind tunnel facilities at low speed. To benchmark computed values, experimental data of the normal force damping derivative are taken from investigations conducted in the continuous, open circuit wind tunnel of the aerodynamic laboratory at IHU, Iran [128]. For damping-in-pitch, experimental data were collected in the low speed, closed circuit Ankara wind tunnel [129].

As the incidence is increased, a complex interaction of the strake and wing vortices develops, and this is shown in Fig. 3.8. The investigation was performed by the author and published in a previous work [23]. At ten degrees, the vortices form, remain coherent and do not interact over the airframe. At fifteen degrees, the two vortices wind around each other towards the trailing-edge of the wing and the breakdown location of the wing vortex moves closer to the trailing-edge. At twenty degrees, the wing vortex appears to breakdown quickly after formation, whereas the strake vortex is coherent for longer. Finally at thirty degrees there is no sign of coherent vortices. Consistent with a number of experimental investigations [140], the location of the vortex breakdown was found to fluctuate significantly when positioned over the wing. Unsteadiness in the axial location of the vortex breakdown impacts the aerodynamic loads, in particular the pitching moment, motivating in the current study the simulation of the unsteady flow around the aircraft model at fixed-attitude for several values of the angle of attack.

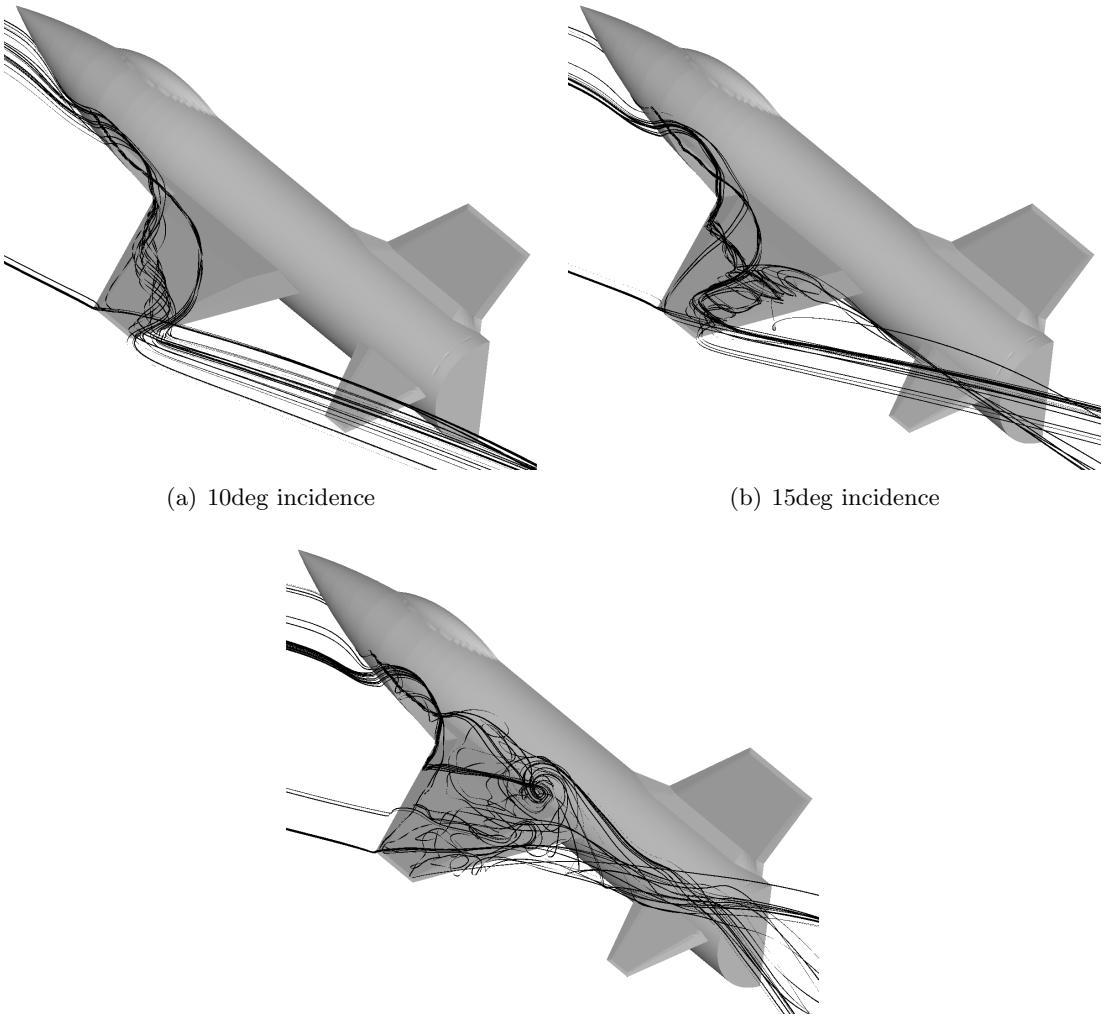

(a) 10deg incidence

(b) 15deg incidence

(c) 20deg incidence

Figure 3.8: Flow field visualization for the SDM model geometry at Mach number of 0.3

One of the most important factors in the execution of the unsteady calculations is the choice of the non-dimensional time step. The time step should be small enough to adequately resolve the unsteady fluctuations of the flow, but large enough not to increase excessively the required computational resources. Without any prior knowledge of the value of the important frequencies in the flow, three values of the non-dimensional time step were selected, equal to 0.01, 0.005 and 0.001. The unsteady calculations performed by the author used five thousand, ten thousand and fifty thousand real time steps for a non-dimensional time duration of fifty, which corresponds to about 1.7 seconds based on the mean aerodynamic chord and freestream speed. The vortices were observed to be highly unsteady with periodic fluctuations in the axial direction. The corresponding unsteadiness observed in the pitching moment is shown in Fig. 3.9 at twenty degrees incidence. Unsteadiness in the moment coefficient for the coarse grid is at a much lower amplitude than that for the half-fine grid, suggesting that the grid

density on the coarse grid above the wing might be not adequate to resolve the dynamics of the vortex breakdown at this angle. Results for the coarse grid are virtually identical for all temporal resolutions. High-frequency fluctuations at a primary non-dimensional frequency of 0.2 characterize the half-fine grid, due to the frequency of the vortex breakdown motion. However, high frequency variations due to the natural unsteadiness of the flow are at a lower amplitude than the variations due to the oscillatory motion. These can interact with each other in ways not predictable on the basis of linear or linearized theories at higher angles of incidence, and hence the importance of investigating the effect of varying the amplitude of the forced motion.

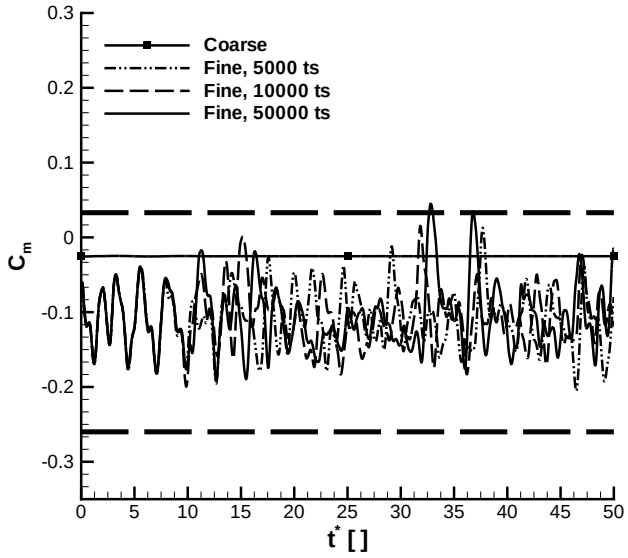

Figure 3.9: Fixed-geometry unsteady calculations for the SDM model geometry at a Mach number of 0.3 and angle of attack of twenty degrees; the term "ts" indicates the number of real time steps; horizontal thick lines mark the variation obtained in forced motion of five degrees amplitude for the half-fine grid

Figure 3.10 compares the CFD-based damping derivatives with selected wind tunnel data. Results are for the coarse and half-fine grids. Because measurements were obtained in different experimental facilities, and in different atmospheric and flow conditions, the flow conditions used in the CFD calculations can only approximate the experimental setup in each case. In this respect, the influence of different experimental setups was found to have a small impact and results compare favourably to measured quantities. A reasonable agreement is obtained between the two grids. The magnitude of the peak in the moment coefficient is mesh-dependent, which is not unexpected for Euler solutions which rely on numerical diffusion in the region of the leading edge for the generation of vorticity. Varying the level of grid refinement in the leading edge drastically alters the solution, as Newsome [130] documented. Numerical investiga-

tions [141,142] have analyzed the effect of grid resolution and topology when computing delta wing flows, and showed that for Euler simulations the solutions were dependent on both mesh topology and refinement. Therefore, a finer spatial discretization was not considered. The purpose of this study is the evaluation of unsteady aerodynamic derivatives and their dependence on several flow and motion parameters. These influence the values of computed dynamics derivatives, which in turn impact the aerodynamic loads computed using the traditional flight dynamics mathematical model. Of primary importance is to assess the scatter of aerodynamic loads for arbitrary unsteady motions due to the variability in dynamic derivatives, and the current study is adequate to investigate this point. A more accurate modelling of the flow physics in the presence of vortices breakdown calls for more expensive alternatives (RANS, Dettached Eddy simulations).

Below ten degrees, the pitch damping derivative continuously decreases as the angle of attack is increased (see Fig. 3.10(b)). Beyond an angle of attack of fifteen degrees, the reduction of dynamic stability is due to the breakdown location of the strake vortices decreasing the longitudinal stability. A time-lag in the response of the vortex flow was observed during the unsteady motion, which results in a temporarily delayed vortex formation at lower angles of attack and temporarily delayed vortex breakdown at higher angles. Hysteresis develops in the vortex flow behaviour with respect to the static case [143]. The inability of the flow to adapt to changes in the attitude and reach a fully developed size introduces a further level of complexity in the vortical flowfields. The unsteady flowfield of the model undergoing pitch oscillation is visualized in Fig. 3.11. The vortex is made visible by creating an isosurface of pressure, and is shown at the same instantaneous angle of attack for direction increasing and decreasing angles. The vortex breakdown is located somewhere over the wing during the upstroke motion. During the downstroke, the vortex core is expanded at the wing apex, and this is expected as the breakdown location moves downstream from the foremost position.

The hysteresis in pitching moment coefficient is illustrated in Fig. 3.12(a) at two values of the mean angle of attack, α_0. The aircraft model is statically unstable at low angles of incidence, recovering stability at larger angles. At the highest α_0, the angle of attack oscillates around a mean value that is of the order of the static stall and hysteresis develops in the aerodynamic responses [139]. This is supported by CFD calculations where the static stall is identified around twenty degrees [23]. In addition, the instantaneous aerodynamic damping can become positive during part of the oscillatory motion, as shown. If the net damping over a cycle is positive, the airframe extracts energy from the flow and the pitch oscillations will tend to increase in amplitude. An interesting feature is the cross-over point in the moment coefficient forming the characteristic shape of "eight", and caused by a switch in the lag and lead between the flowfield and the model attitude. The signal "1 Harmonic" is the corresponding time-domain response retaining the fundamental harmonic only and neglecting any other frequency compo-

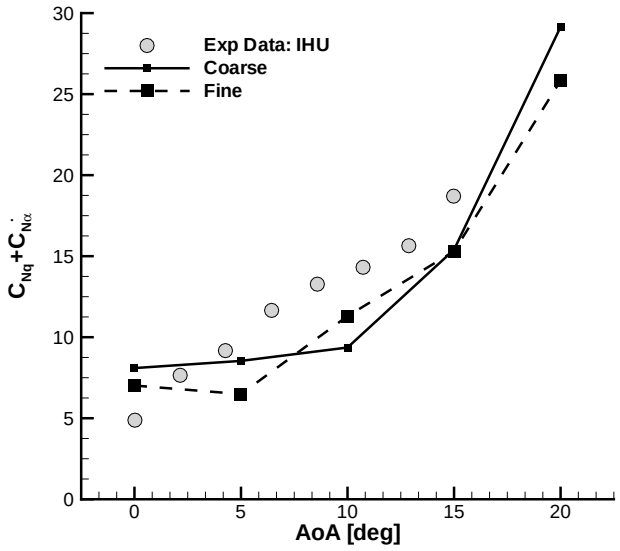

(a) Normal force coefficient damping

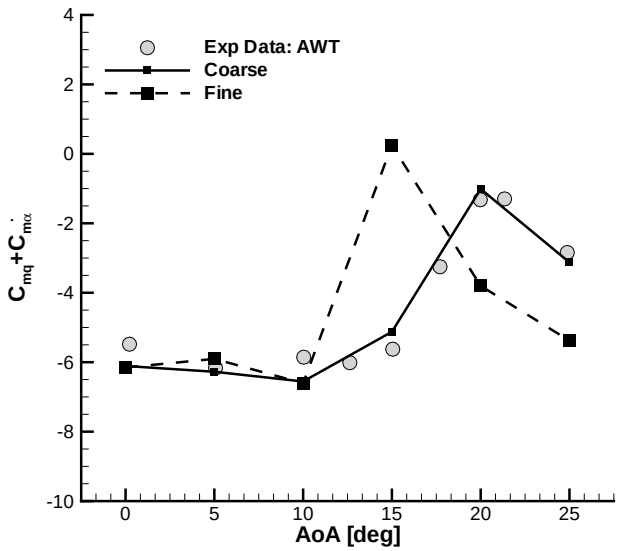

(b) Pitching moment coefficient damping

Figure 3.10: Influence of mean angle of attack on the damping derivatives for the SDM model geometry at Mach number 0.3; experimental data were obtained in IHU [128] and AWT [129]

nent. In the non-linear regime, aerodynamic modes are excited at higher frequencies than the frequency being forced by the applied motion. The frequency content of the moment coefficient was found to include important frequencies up to three times the prescribed frequency of motion, as shown in Fig. 3.12(b).

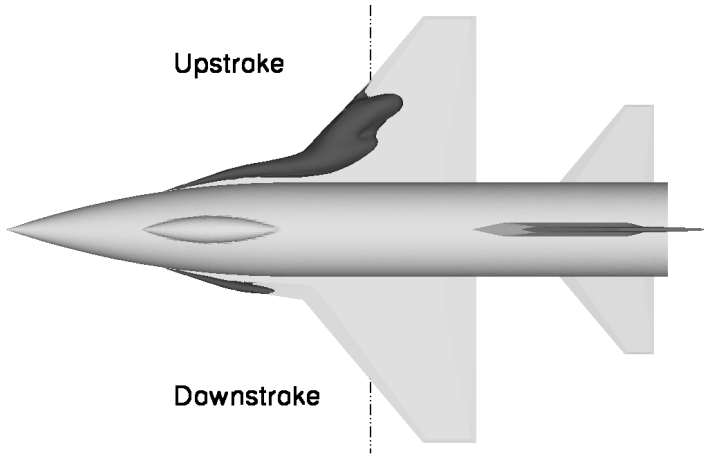

Figure 3.11: Isosurface of pressure at mean angle of attack of fifteen degrees for direction increasing and decreasing angle; the axis of rotation is illustrated

3.3.1.3 Reduced Frequency

Two sets of motions were generated. The first set is considered for a range of reduced frequencies ($k = 0.037$ to 0.090) representative of the reduced frequencies experienced by the main wing on high-performance aircraft. The second set is for a relatively large value of reduced frequency of 0.2. The pitching frequency, based on the freestream speed and mean aerodynamic chord, is $6\,Hz$.

As the reduced frequency increases, the hysteresis effect becomes larger at a given angle of attack (see Fig. 3.13(a)). The effect of reduced frequency is seen throughout most of the pitching cycle, and is dominant at the maximum and minimum values of the angular velocity during the upstroke and downstroke, respectively. The cross-over point forming the characteristic shape of "eight" was found in the slower motions only. For a two-dimensional configuration, the over- and undershoots in the unsteady aerodynamic loads relative to the static case have been explained resorting to the "moving-wall" effect, and this flow mechanism was found to play an equally prominent role in the case of three-dimensional unsteady separated flows on a manoeuvring combat aircraft [144]. The phase angle difference between the loads and the model position is shown in Fig. 3.13(b), as a function of the reduced frequency at ten degrees mean angle of attack. A near-linear relationship is observed between the phase angle of the normal force and the reduced frequency. As the reduced frequency increases, so does the phase lag. For the pitching moment, the phase angle is mostly constant for the range of reduced frequencies computed. The moment coefficient lags the pitching motion by nearly ninety degrees, which is expected as the extreme values of the moment are observed during the upstroke and downstroke motions when the angular velocity is maximum and minimum. The reason for the phase lag in aerodynamic loads is the existence of a phase lag in the vortex flow. LeMay et al. [145] presented results of an

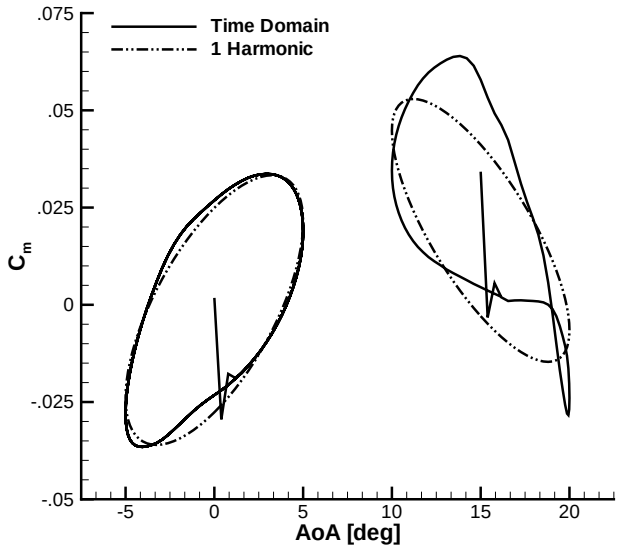

(a) Time histories

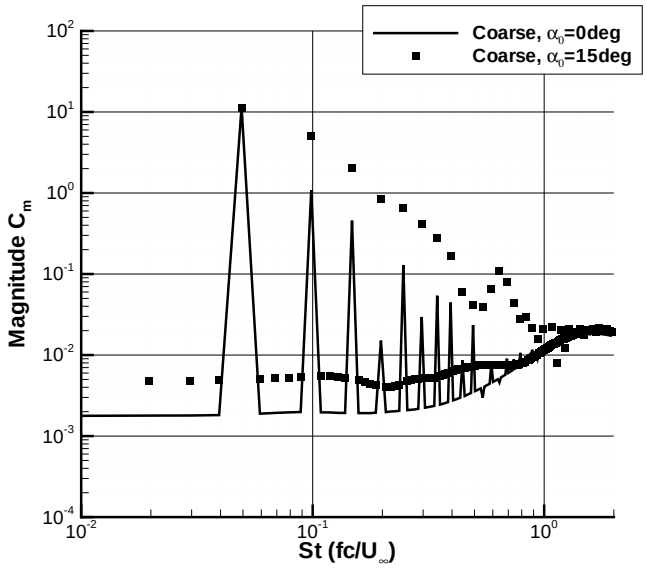

(b) Frequency spectra

Figure 3.12: Pitching moment coefficient for the SDM model geometry for the coarse grid at mean angle of attack of 0 and 15 degrees; in (a), the term "1 Harmonic" indicates a reconstructed signal with the fundamental frequency only; in (b), the magnitude is plotted as function of the Strouhal number, St

experimental investigation of vortex dynamics around a sharp leading edge 70deg delta wing. The phase lag difference of the chordwise breakdown location and the model motion was found to increase linearly with the reduced frequency. The similarity of

their findings with the linear relationship presented is noted.

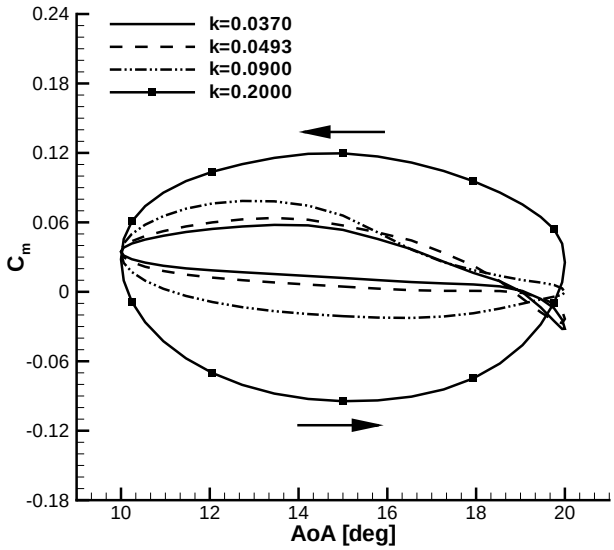

(a) Time history

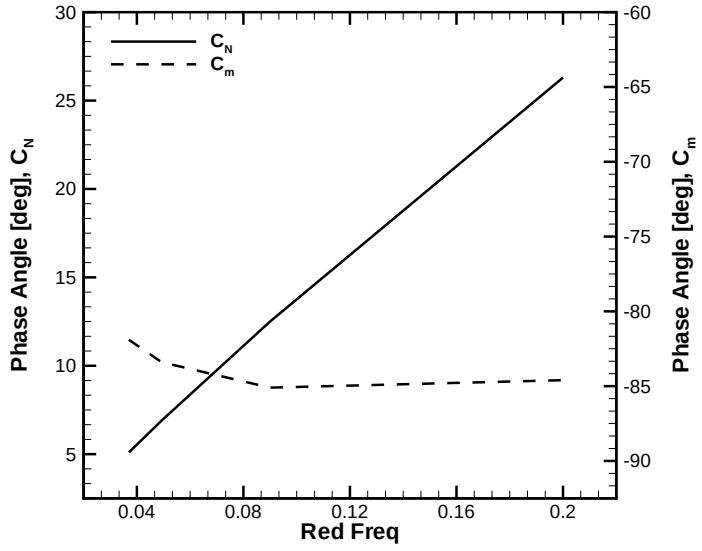

(b) Phase angle at ten degrees angle of attack

Figure 3.13: Time history of pitching moment coefficient and phase lag in aerodynamic loads as a function of the reduced frequency; in (a), $\alpha_0 = 15.0°$ and $\alpha_A = 5.0°$; in (b), the mean angle of attack is ten degrees

Dynamic derivatives are shown in Fig. 3.14 for several values of reduced frequency. Little variation was found at lower angles of incidence. The effect of reduced frequency is more dominant in the non-linear aerodynamic regime beyond fifteen degrees. The

dynamic derivatives computed for the lower values of reduced frequency are very similar, and indicate the same qualitative trends in both force and moment data. It should be noted that the damping-in-pitch is locally positive at twenty degrees angle of attack for a reduced frequency of 0.09. Lower values of force coefficient damping and a continuous decrease in the longitudinal dynamic stability were observed for the rapid motion.

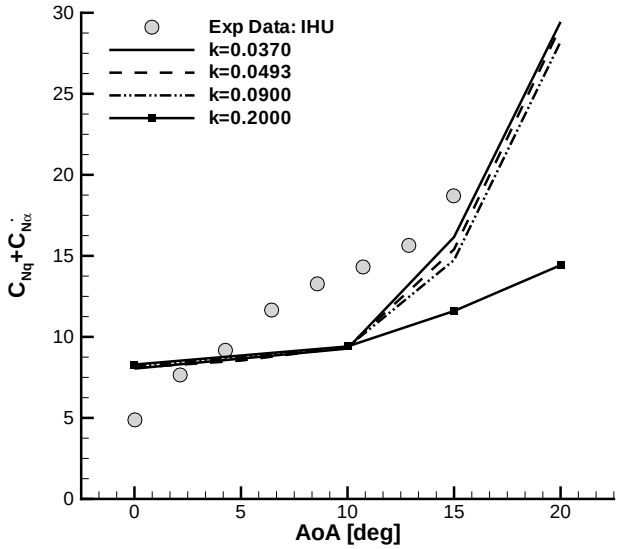

(a) Normal force coefficient damping

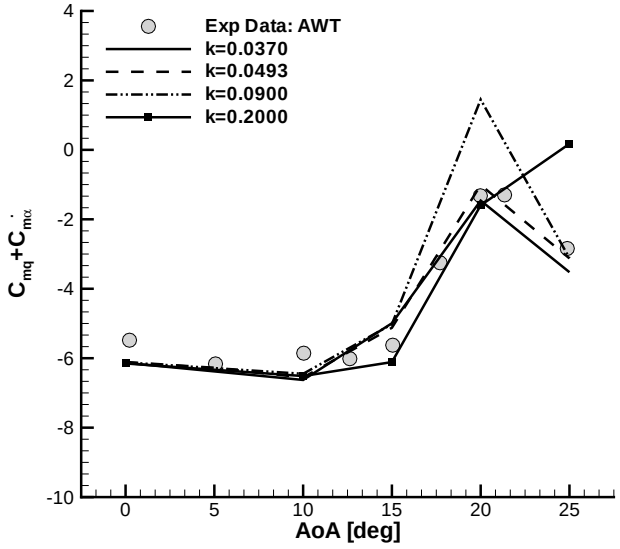

(b) Pitching moment coefficient damping

Figure 3.14: Influence of reduced frequency on the damping derivatives for the SDM geometry model at Mach number 0.3 ($\alpha_A = 5.0°$); experimental data were obtained in IHU [128] and AWT [129]

3.3.1.4 Oscillatory Amplitude

The oscillatory amplitude has a moderate influence on damping derivatives in the linear range of the normal force coefficient [129]. This is verified as long as the amplitude of motion is lower than five degrees and when separation is not the dominant flow feature. Computations were performed with both grids for a set of reduced frequencies of typical high-performance wings ($k = 0.037 \text{ to } 0.090$). Variations in aerodynamic loads due to the forced motion need to be larger than the natural unsteadiness of the flow. Tests were performed to identify the lower bound in amplitude to properly excitate the aerodynamics of interest. Values of amplitude presented are 2.0°, 3.5° and 5.0°, as shown in Fig. 3.15. The system is locally linear but, as the amplitude of the applied motion is further increased, the non-linear behaviour is the dominant feature. The instantaneous aerodynamic damping can become positive during part of the oscillatory motion, as shown for the largest amplitude. If the net damping over a cycle is positive, the airframe extracts energy from the flow and the pitch oscillations will tend to increase in amplitude. An interesting feature is the cross-over point in the moment coefficient forming the characteristic shape of "eight", and caused by a switch in the lag and lead between the flowfield and the model attitude.

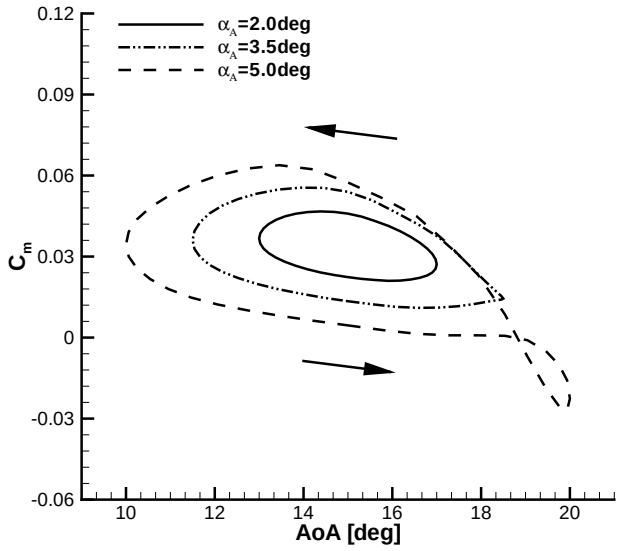

Figure 3.15: Pitching moment coefficient loop for the SDM geometry model for the coarse grid at Mach number 0.3 and several values of the amplitude of motion, α_A

Dynamic derivatives are shown in Fig. 3.16. The effect of varying the oscillation amplitude is small at low angles of attack but significant at higher incidences. Although defining similar trends in both force and moment data, values for the smallest amplitude correspond to higher longitudinal dynamic stability. This observation is valid for all

reduced frequencies tested.

Effects of varying the small amplitude of motion are similar to those observed varying the reduced frequency, that is a more dominant influence on dynamic derivatives is observed above fifteen degrees mean angle of attack. The question whether variations in dynamic derivatives due to amplitude or reduced frequency changes are the most significant in terms of aerodynamic loads, within a flight dynamics contest, is addressed in the next section.

3.3.1.5 Large Amplitude Motions

Dynamic derivatives were shown in the preceding subsections to depend upon several motion and flow parameters. Dependency on Mach number and angle of attack are in general included in a simulation mathematical model, with dynamic derivatives taken as a function of these states [81]. Further dependencies were observed for changes in small amplitude and reduced frequency of the forced motion. There is no general consensus or common guideline for prescribing the value of small amplitude to be used in forced motion tests, and commonly dynamic derivatives are used at the reduced frequency which is thought to be the most representative of the expected aircraft motions [146].

Results presented above are adequate for the assessment of the variations in aerodynamic loads using the conventional mathematical model based on aerodynamic stability derivatives. The approach in the current study consists of simulating an unsteady manoeuvre at moderately high mean angle of attack for large amplitude oscillations in pitch. The solution obtained using CFD is the reference solution because it is time-accurate. To improve the predictions of the linear model in Eq. (2.15), the aerodynamic model is reformulated to include non-linear dependencies of aerodynamic derivatives.

$$C_j \;=\; C_{j\,0}\,(\alpha, \dots) + \bar{C}_{j_q}\,(\alpha, \dots) \cdot \frac{c\,q}{2\,U_\infty} \qquad (3.4)$$
$$\text{for } \; j = L, D, \;\; \text{and } \; m$$

The main variable is the instantaneous angle of attack during the unsteady motion, α, and aerodynamic derivatives are then assumed to depend on this variable in combination with the reduced frequency and small amplitude, separately. The motion is simulated at constant subsonic speed, and no dependence on the Mach number is considered. The static terms depend non-linearly on the independent variables. The dynamic derivatives, while non-linear functions in the arguments, are linear with respect to the pitching angular rate. The manoeuvre is calculated at ten degrees mean angle of attack for an oscillatory amplitude of ten degrees, and the reduced frequency is 0.0493. This goes through the angle of attack range where variations in dynamic derivatives were observed.

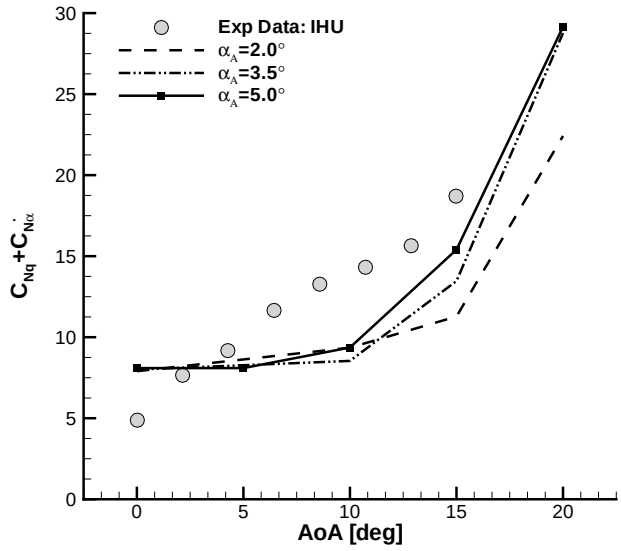

(a) Normal force coefficient damping

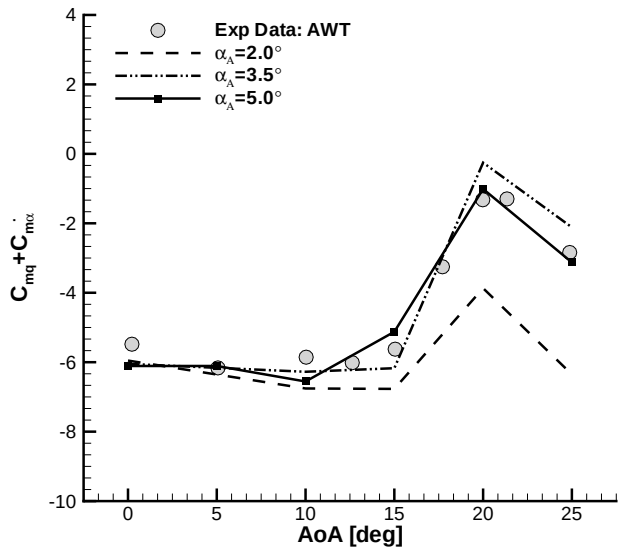

(b) Pitching moment coefficient damping

Figure 3.16: Influence of amplitude on the damping derivatives for the SDM geometry model at Mach number 0.3; experimental data were obtained in IHU [128] and AWT [129]

Simulation results are compared to the time-accurate solution in Fig. 3.17, and two situations arise. In the first scenario, aerodynamic derivatives are assumed a function of the angle of attack and forced oscillatory pitch amplitude ($\alpha_A = 2.0° \text{ to } 5.0°$), but estimated at the same reduced frequency ($k = 0.0493$) of the manoeuvre being simulated. This allows the isolation and exploration of the effect of small oscillatory

amplitude. In the second scenario, aerodynamic loads are computed from aerodynamic derivatives provided from a set of forced motions at several values of the reduced frequency ($k = 0.037\,\text{to}\,0.090$), and for a given amplitude ($\alpha_A = 5.0°$). Comparison between the model and the time-accurate solution is illustrated in Fig. 3.17. The non-linear model agrees with the time-accurate solution, and predicts some of the main features of the hysteresis loops. Dynamic force dependencies are correctly accounted for during most of the upstroke motion up to seventeen degrees incidence, and during part of the downstroke motion. With a loss of performance at the higher end of the angle of attack range, the model curve approaches the reference curve during the down-swing earlier under the first scenario. Two significant differences appear in the force loop when comparing the two scenarios. First, the scatter in the load is at much lower amplitude under the second scenario than under the first scenario, suggesting that the variability introduced by changes in oscillation amplitude is more important than that of the reduced frequency. However, results under the first scenario are more precise, and do have a higher degree of agreement with the time-accurate solution at higher angles of incidence. Dependencies on the reduced frequency shift the mean trend away from the time-accurate solution, degrading significantly the prediction of the moment coefficient in presence of non-linearities. This is not unexpected because static terms depend on the reduced frequency [146].

At twenty degrees, the angular rate vanishes and the model formulation reduces to include only the non-linear static term. This represents a time-averaged solution of the small amplitude forced motion, as opposed to the instantaneous representation of the flow realized in the time-accurate simulation. Without time-history effects, the time-averaged solution can only approximate the development of the flow solution. In particular, the surface vortex footprint was found in the time-accurate solution to be of larger intensity and located further downstream than in the time-averaged solution. Differences in local contributions to the normal force coefficient between the time-accurate and time-averaged solutions are displayed in Fig. 3.18. Black areas indicate that the time-accurate solution predicts larger force increments located upstream of the axis of rotation. This explains the larger force and moment coefficient values observed in the CFD-based than in the model-based results at the largest angles of attack.

3.3.2 Transonic CRuiser Wind Tunnel Model

Predictions of static aerodynamic characteristics of the TCR were compared using different CFD codes in a parallel work [147]. In this study, static results are briefly reviewed. The attention is then addressed to unsteady aerodynamics. Numerical results of aerodynamic derivatives for small oscillation amplitudes are first presented, followed by results for large amplitude motions. Dependencies of dynamic characteristics on mean angle of attack and reduced frequency were investigated both experimentally and

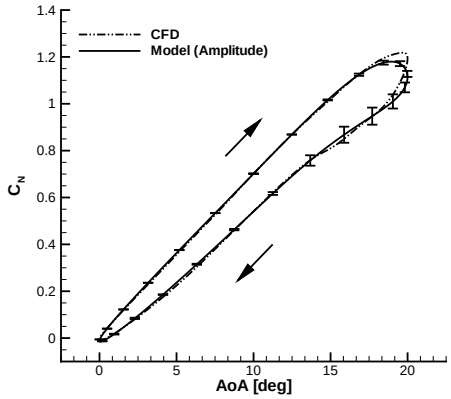

(a) Normal force coefficient (amplitude)

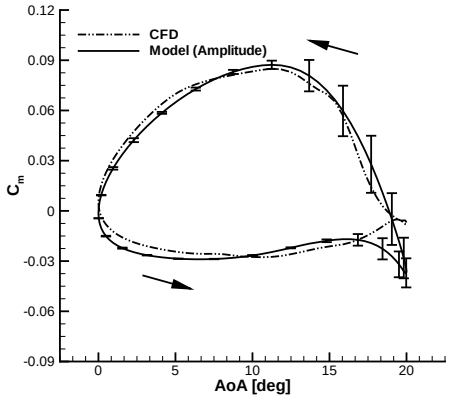

(b) Pitching moment coefficient (amplitude)

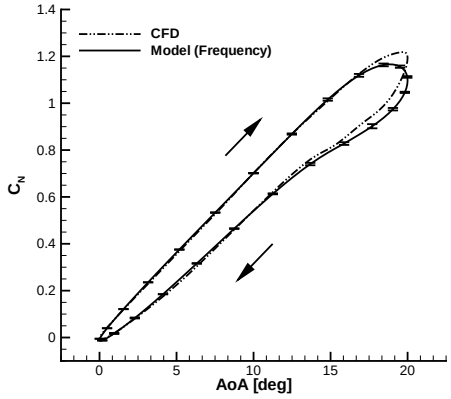

(c) Normal force coefficient (frequency)

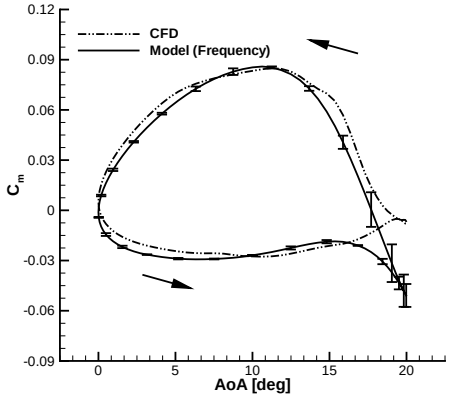

(d) Pitching moment coefficient (frequency)

Figure 3.17: Non-linear mathematical model and unsteady CFD for a large amplitude manoeuvre ($\alpha_0 = 10.0°$, $\alpha_A = 10.0°$ and $k = 0.0493$); (a) and (b) show the small amplitude effects on the stability derivatives; (c) and (d) show the frequency effects

numerically. In all cases presented, computations are for the wind tunnel model with vertical tail and undeflected canard wing.

The flow conditions at which experimental data from the TsAGI T–103 wind tunnel [148] are available are given in Table 3.4. The Mach number is 0.117 and the Reynolds number, based on the wing mean aerodynamic chord and freestream speed, is 0.778 million. The low Reynolds number at the operating wind tunnel conditions and the blunt leading-edge geometry of the TCR wind tunnel model make the prediction of the initial flow separation difficult. No transition tripping was used in the wind tunnel model. Without other information, all simulations assumed fully turbulent flow and were run at experimental conditions. In all cases computed, results are for zero sideslip angle and the influence of the rear sting was ignored.

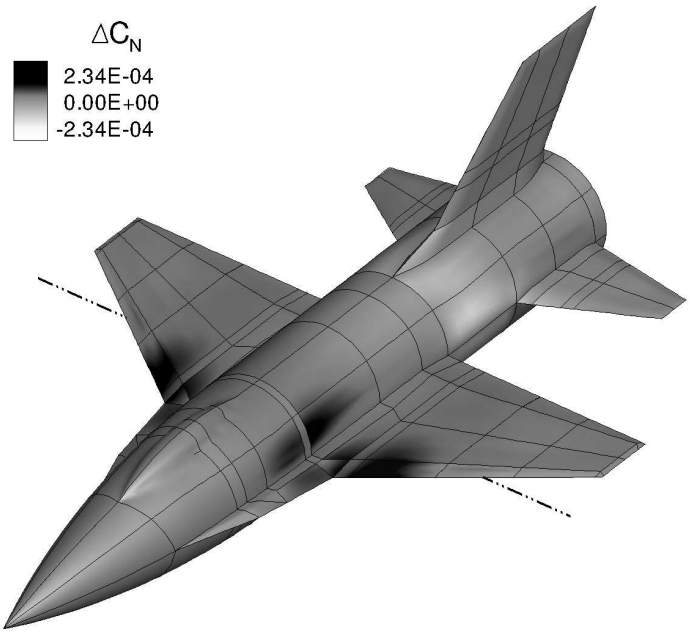

Figure 3.18: Differences between time-accurate and time-averaged solutions of local contributions to the normal force coefficient; the axis of rotation is illustrated

Parameter	Value
U_∞	$40\,m/s$
Re	0.778×10^6

Table 3.4: Experimental conditions for testing of the TCR wind tunnel model at TsAGI T–103 facility [148]

3.3.2.1 Static Cases

Tests were performed to guarantee well-converged results over the angle of incidence range from $-10.0°$ to $25.0°$. Two sets of steady-state calculations were generated. First, results were obtained after ten thousand pseudo iterations. At moderate angles of attack, the aerodynamic loads were unconverged, and calculations were then restarted from the previous solution and run for an additional thirty thousand pseudo iterations. In general, vortical structures were found to be more developed and located further downstream in the initial solutions, resulting in larger increments in the normal force coefficient and more negative values (pitch-down) for the pitching moment. To evaluate the convergence of these steady-state predictions, static results above ten degrees angle of attack were computed using time-accurate simulations. Static unsteady cases were run at a non-dimensional time step of 0.005 for a total of ten thousand time steps. Based on a preliminary study performed by the author with various time steps, the time step of 0.005 was considered adequate to resolve any flow unsteadiness. The steady-state converged solutions were in good agreement with static unsteady results for all cases

computed.

Figure 3.19 illustrates the static normal force and pitching moment coefficients. The moment curve exhibits two distinct breaks. The first discontinuity occurs at about eight degrees, followed by a reduction of the pitch-down authority up to the second break at twenty degrees. After a sudden drop, the moment continues to grow further with similar unstable characteristics. Simulation results compare well to wind tunnel data up to the first discontinuity point, with an offset being observed at the higher end of the angle of attack range. The discontinuity above twenty degrees is well reproduced. An explanation of the underlying mechanisms for the observed moment curve behaviour is found when looking at the contributions to the total integrated aerodynamic loads generated, separately, from the canard and the main wings [147]. The first break and subsequent slope in pitching moment originates from flow separation on the main wing. The second break and ensuing change of slope after twenty degrees angle of attack results from flow separation on the canard wing. Separation starts in a region confined to the tip and leading-edge, and increases with the angle of attack. At twenty degrees, there is a large separated area. The outer part of the main wing is dominated by separated flow, whereas the flow in the inner section is predominantly attached. Figure 3.20 conveys the flow development around the model for several angles of attack. Attached flow streamlines are observed at zero angle of attack. Leading-edge vortices on the canard and on the wing outer section form as the incidence is increased, with the appearance of an additional wing inboard vortex at higher angles. The outer vortex moves progressively inboard, followed by the coalescing of the dual vortex system.

3.3.2.2 Small Amplitude Motions

With the TCR wind tunnel model undergoing small amplitude oscillatory motions, stability characteristics were investigated at low speed. The oscillatory amplitude is three degrees and the forced motion is applied through the model centre of gravity. Considering pitch oscillations, the dependency of the aerodynamic derivatives on the mean angle of attack and reduced frequency were assessed, and compared to wind tunnel measurements. To conform to the experimental practice, a linear regression model was used to post-process time-domain data.

The dependency of measured and computed dynamic derivatives on the mean angle of attack is shown in Fig. 3.21. The variation of the dynamic derivatives measured from small amplitude motions at several values of the dimensional frequency, from 0.5 to $1.5\,Hz$, is evident. The force dynamic derivative increases with increasing mean angle of attack, with significant frequency effects. Small variations in the value of the damping-in-pitch, with a limited dependency on the frequency of motion, are observed up to fifteen degrees. A strong frequency dependence, with a significant change from the background trend, is seen in the region between sixteen and twenty-four degrees. The

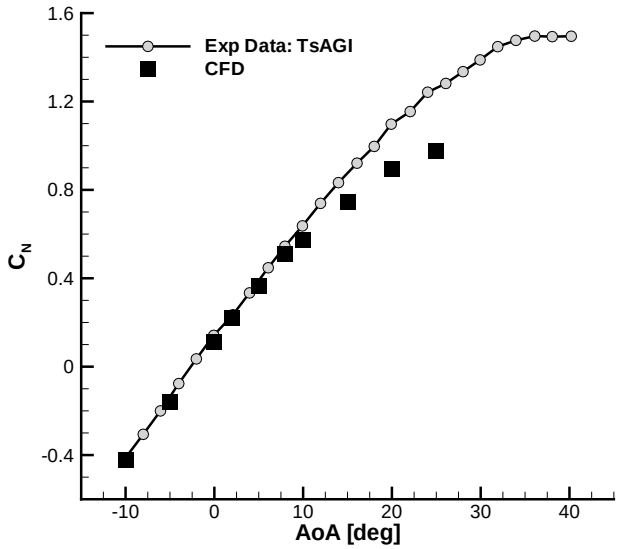

(a) Normal force coefficient

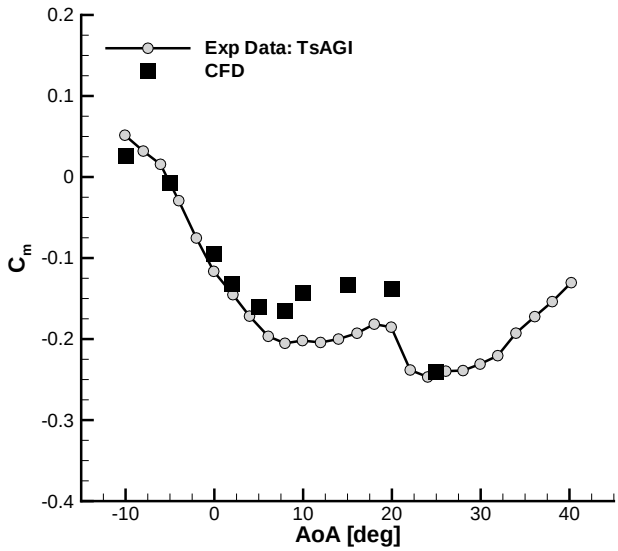

(b) Pitching moment coefficient

Figure 3.19: Static longitudinal aerodynamic characteristics for the TCR wind tunnel model ($M = 0.117$ and $Re = 0.778 \times 10^6$)

onset of flow separation on the canard wing was identified as the reason for the positive damping value. The extensive testing campaign revealed also that the magnitude and location of the positive damping spike depend on the deflection of the canard wing, and eventually the unstable characteristic disappears for the model without the canard wing.

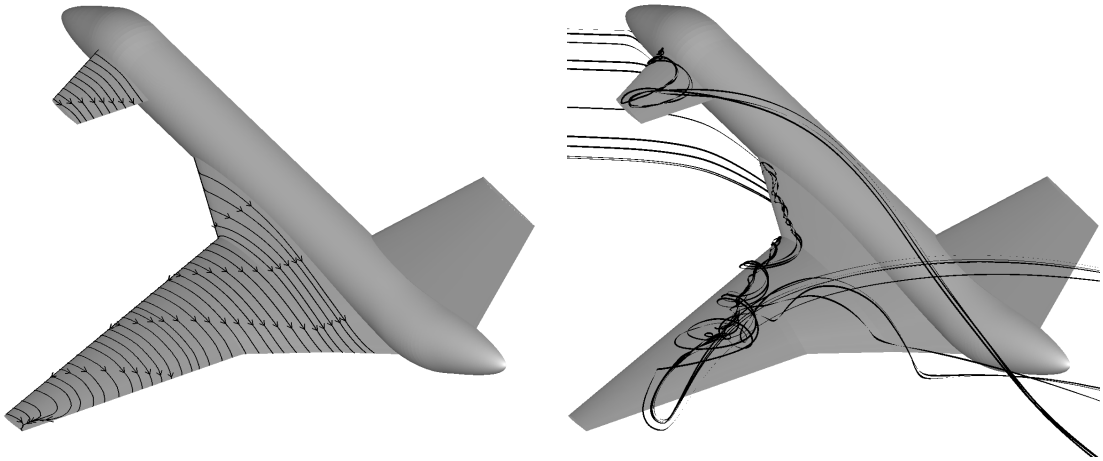

(a) 0deg incidence

(b) 18deg incidence

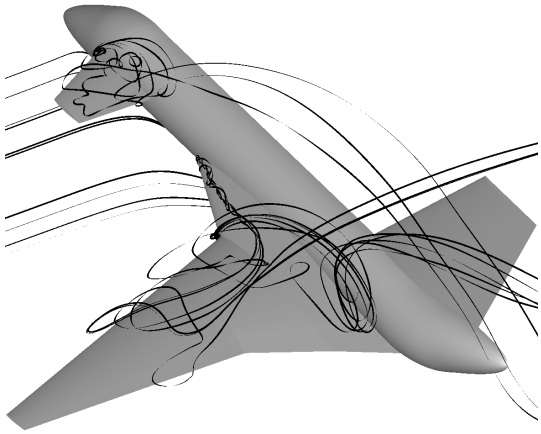

(c) 25deg incidence

Figure 3.20: Surface streamlines and flow field visualization of the TCR wind tunnel model at several angles of attack

Numerical results included in Fig. 3.21 were obtained for the model with the undeflected canard at a frequency of $1.0\,Hz$. To assess the convergence of the unsteady simulations, several tests were initially performed at mean angles of attack above ten degrees representative of difficult convergence from static cases. Three values of the number of time steps per cycle were used, four hundred, eight hundred and one thousand, corresponding to a non-dimensional time step of 0.33, 0.17 and 0.13, respectively. The non-dimensional period of an oscillatory motion at a frequency of $1.0\,Hz$ is $t^* = 68$. For the two smaller time steps, identical hysteresis loops resulted. The time step of 0.17 was then used for all numerical data presented. Predicted values of dynamic derivatives compare reasonably to the measured data, being within a five percent band of the maximum absolute value from the experimental curve for angles of attack between five and fifteen degrees. Two important observations can be made for the remaining computed

points. At zero degrees mean angle of attack, the magnitude of the damping values from simulation, e.g., the hysteresis in the aerodynamic loops, is under-predicted. A reason for this deficiency may be associated with the assumption of fully turbulent flow to model a fluid which is likely to be laminar at these conditions of low angle of attack and freestream speed. It would be interesting to determine, for the same flow conditions, the impact of the turbulence model used in the RANS modelling and the grid resolution. The second remark is that the simulation results fail to predict a positive damping-in-pitch at twenty degrees angle of attack, as observed in wind tunnel testing. The change in the sign of the measured aerodynamic damping has a significant impact on the accuracy of the moment coefficient, and resulted in a dramatic failure of the non-linear model, as shown in the next section. Pursuing the use of more advanced turbulence models to resolve turbulent eddies is not part of the current work, as the interest here is on the investigation of the sensitivity of the conventional mathematical model, using a set of measured and predicted aerodynamic coefficients, to reproduce dynamic loads for a large amplitude manoeuvre.

The dependency of the dynamic derivatives on the frequency is illustrated in Fig. 3.22 for a mean angle of attack of ten degrees. As the non-dimensional time step increases for decreasing frequency, tests verified that convergence was achieved at each physical time step for the motion at $0.5\,Hz$. The correlation of the numerical results with the experimental data improves significantly with increasing frequency, and the best agreement observed at the largest frequency of motion is not unexpected. The reduction of the hysteresis in the aerodynamic loads for small values of the frequency leads to a difficulty in the accurate prediction of damping terms, caused by the reduction of the ratio between the aerodynamic load increments being analyzed and random errors effecting the measurement process or numerical simulation [149]. This poses significant practical challenges for wind tunnel testing and for numerical simulations [150–152].

3.3.2.3 Large Amplitude Motions

A large amplitude motion was then used to assess the accuracy of the stability derivative model based on measured and predicted aerodynamic datasets. The manoeuvre was run at eight degrees mean angle of attack, with an oscillatory amplitude of ten degrees at a frequency of $1.0\,Hz$, for which measurements are available. Wind tunnel data were measured for sixteen periods of oscillations, in wind-on and wind-off conditions. Aerodynamic loads were smoothed with Butterworth digital filtering [153], and the average values of the aerodynamic coefficients were then calculated for one period. The same numerical parameters described above were used in the computations.

Figure 3.23 illustrates the force and moment dynamic dependencies, measured from experimental testing and obtained using time-accurate simulations. The overall shape

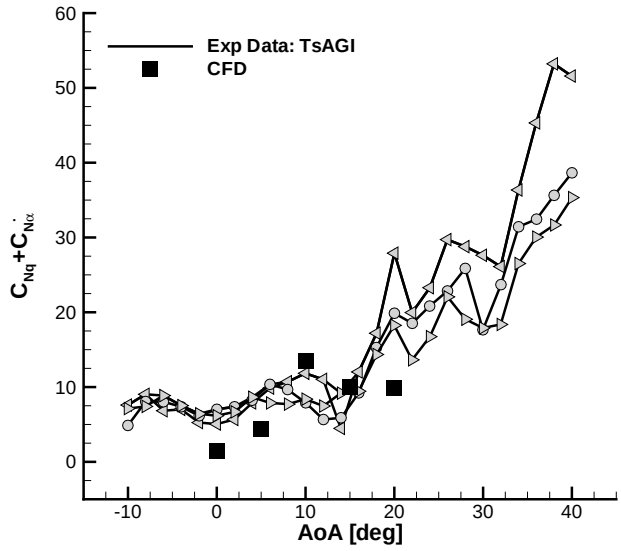

(a) Normal force coefficient damping

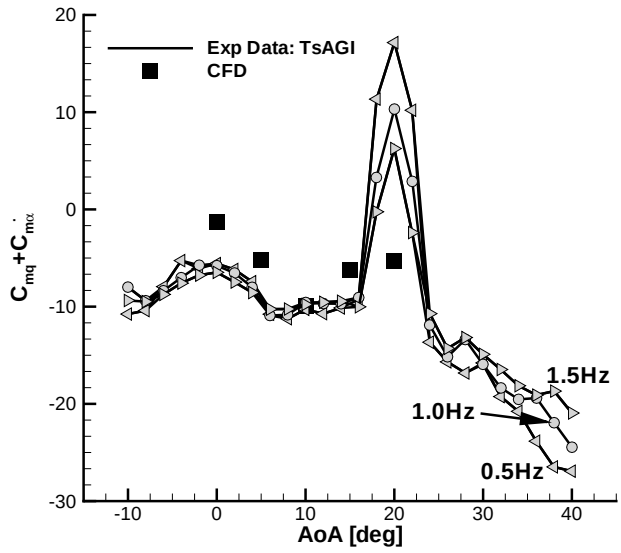

(b) Pitching moment coefficient damping

Figure 3.21: Damping derivatives for the TCR wind tunnel model ($\alpha_A = 3.0°$); (a) and (b) show the dependence on mean angle of attack (left triangles, $f = 0.5\,Hz$; circles, $f = 1.0\,Hz$; right triangles, $f = 1.5\,Hz$)

of the hysteresis curves is similar between the two sets of results. Consistent with the observations from the static cases, at the higher angles of attack the force coefficient is under-predicted and the moment coefficient has a constant offset. At low angles, the hysteresis in the numerical results has lower magnitude than in experimental data,

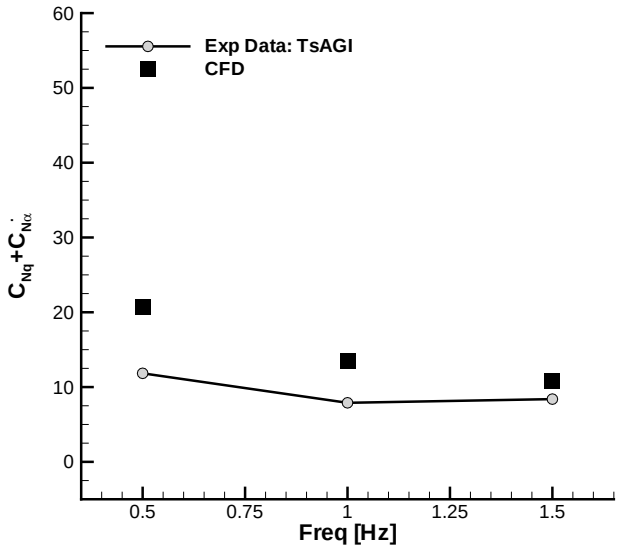

(a) Normal force coefficient damping

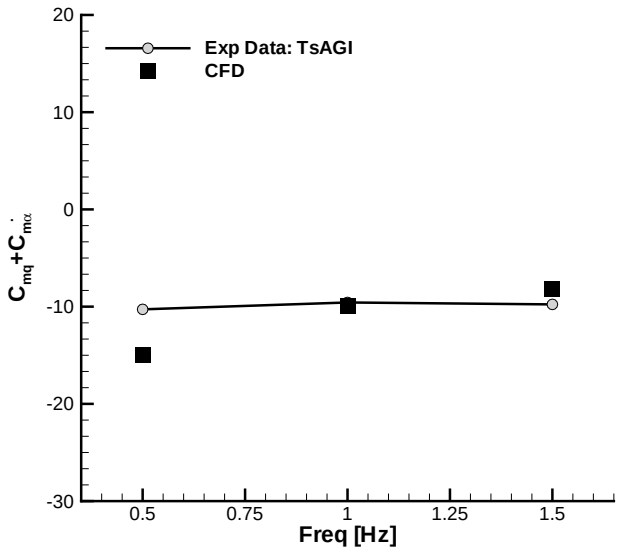

(b) Pitching moment coefficient damping

Figure 3.22: Influence of frequency on the damping derivatives for the TCR wind tunnel model at mean angle of attack of ten degrees

and this is consistent considering that the damping terms were under-predicted in magnitude, as shown in Fig. 3.21. In these figures, arrows indicate the time evolution. If the arrows are oriented in the clockwise direction, the contribution from the dynamic derivative is positive, and vice versa. Note the lack of any cross-over point in the moment data, as would be expected in the experimental curve due to the positive

damping-in-pitch measured above sixteen degrees (see Fig. 3.21(b)).

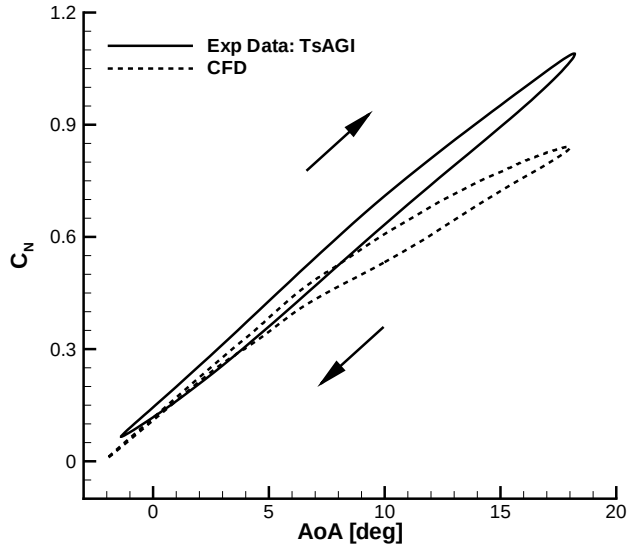

(a) Normal force coefficient

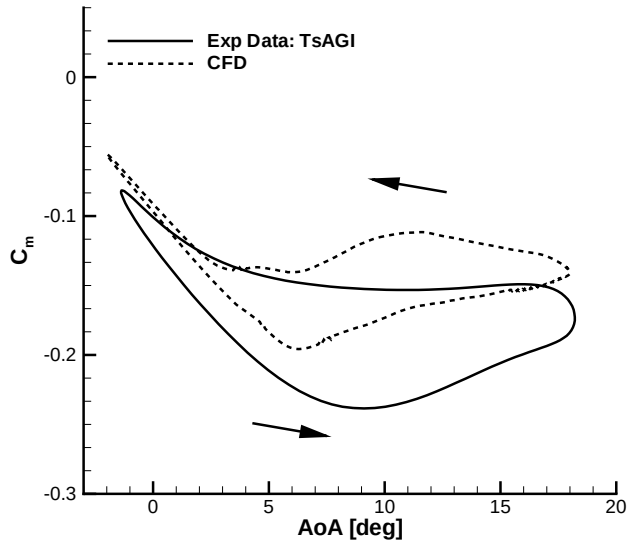

(b) Pitching moment coefficient

Figure 3.23: Dynamic dependencies for the TCR wind tunnel model for a large amplitude manoeuvre ($\alpha_0 = 8.0°$, $\alpha_A = 10.0°$ and $f = 1.0\,Hz$)

The force and moment dynamic dependencies for the large amplitude manoeuvre were reproduced in the upper portion of Fig. 3.24 using the model based on the aerodynamic stability derivatives. In this case, aerodynamic terms were assumed to vary with the angle of attack and frequency. At any given angle of attack, the prediction is

obtained as the sum of two contributions, that is, a non-linear static term, $C_{j\,0}\,(\alpha, f)$, and an increment due to the dynamic motion, $\bar{C}_{j_q}\,(\alpha, f)$. For the static terms, mean values of the aerodynamic coefficients obtained from small amplitude oscillations were used in place of the values from static cases. The former provided a closer correlation to the reference solution. The reason is that a small amplitude forced motion better approximates the effects of under- and overshoot in the force and moment loads, as experienced in dynamic motions, than any steady-state solution. The overall shape is well predicted for both force and moment coefficients, and the sensitivity of the model to variations in the frequency used to estimate the dynamic derivatives is limited throughout most of the oscillatory cycle. However, the model under-predicts the force dynamic dependency in Fig. 3.24(a), with increasing offset from the large amplitude data for increasing angles of attack. Up to sixteen degrees, a good agreement is also observed for the moment loop. Above this angle of attack, the model predicts a cross-over point as the upswing and downswing curves intersect, with a marked frequency dependence (see Fig. 3.24(b)). The change of the hysteresis direction from counter-clockwise to clockwise is attributable to the positive damping-in-pitch measured experimentally. This dramatic failure of the non-linear model in predicting the moment dynamic dependency has been consistently observed when analyzing several large amplitude manoeuvres available from tunnel testing passing through this critical range of incidence.

The model based on the aerodynamic stability derivatives obtained from small amplitude simulations is compared in the lower part of Fig. 3.24 with the time-accurate CFD simulation of the large amplitude manoeuvre. The model data points are plotted as symbols at increments of five degrees angle of attack. For the force coefficient, the model values correlate well to the reference data, laying upon the time-accurate solution. The agreement is also good for the moment coefficient loop. In all cases, the reduction of the predicted hysteresis at low angles of attack is well captured, and consistent with the reference solution in this case. The calculated damping-in-pitch was negative for all mean angles of attack, which guarantees that the model will correctly predict the hysteresis loop at the higher end of the angles of attack range.

At moderate angles of attack, the aerodynamic coefficients are not only non-linear but include effects of higher harmonics and time lags. In such conditions, the flow unsteadiness can significantly impact the results of dynamic derivative calculations, which assume steadiness and linearity of aerodynamic coefficients during the dynamic motion of the model. This is clearly illustrated comparing the model performance in the two cases above. To produce non-linearities in the aerodynamic coefficients, dynamic derivatives used were expressed as functions of motion variables. Albeit non-linear, this formulation is instantaneous. Each aerodynamic coefficient, $C_j(t)$, is only a function of the current time, t, and the formulation is then inadequate to predict dynamic manoeuvres when the flow is strongly unsteady and the loads are time dependent.

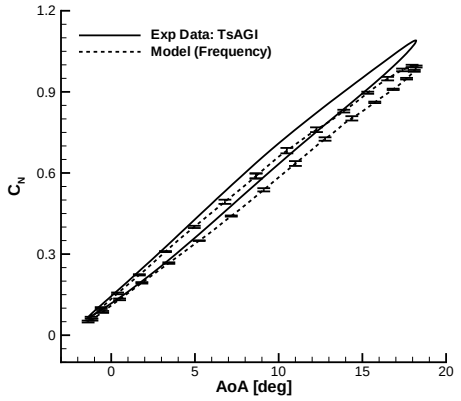

(a) Normal force coefficient (wind tunnel)

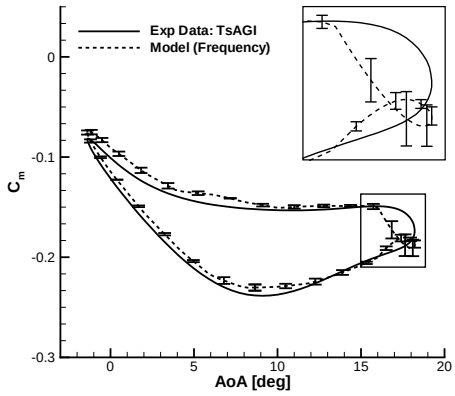

(b) Pitching moment coefficient (wind tunnel)

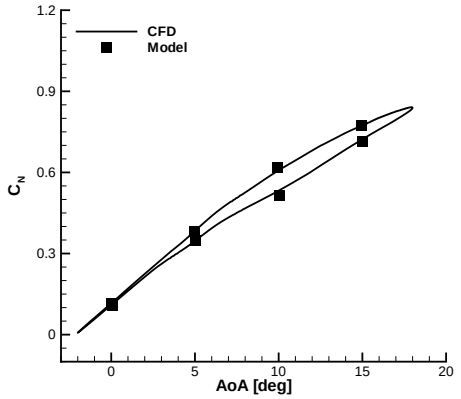

(c) Normal force coefficient (CFD)

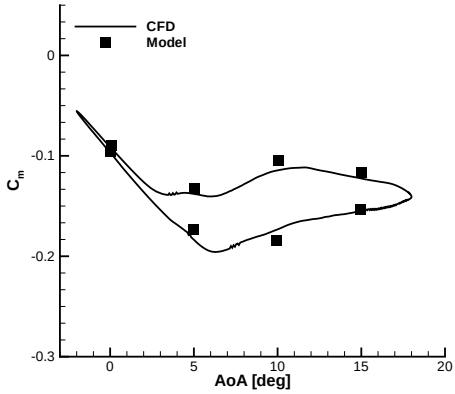

(d) Pitching moment coefficient (CFD)

Figure 3.24: Mathematical model based on aerodynamic stability derivatives from wind tunnel (top) and CFD (bottom) simulations for the prediction of a large amplitude manoeuvre ($\alpha_0 = 8.0°$, $\alpha_A = 10.0°$ and $f = 1.0\,Hz$)

3.4 Conclusions

A framework for the computation of dynamic derivatives using CFD was presented. Two techniques to post-process time-domain data were detailed. A step towards a more comprehensive investigation of the limitations of models based on stability derivatives for the prediction of the aerodynamics of manoeuvring aircraft was also made. For the SDM model, dynamic stability derivatives at low incidence and up to high-transonic speed, and at low speed and up to high angles of attack, compared well with tunnel measurements. Whilst no significant dependence was found in transonic conditions, a finer temporal discretization was required to resolve high-frequency fluctuations in aerodynamic loads due to vortex breakdown. In these conditions, a grid dependence was also observed. The effects of variations of reduced frequency and small amplitude on

dynamic derivatives were illustrated. To produce non-linearities in aerodynamic loads, dynamic derivatives were expressed as functions of motion variables. The main variable was taken to be the angle of attack, and aerodynamic derivatives were then assumed to depend on this variable in combination with the frequency and small amplitude, separately. As the sensitivity of the dynamic derivatives on parameters investigated fell into well defined bands, it was considered reasonable that it is only the general behaviour of these bands, rather than small and often irregular variations in the individual curves, that may be of practical interest for the flight dynamics simulation. The non-linear model compared best to the time-accurate solution when aerodynamic derivatives were estimated at the same frequency of the manoeuvre being analyzed. The scatter in the predictions was at lower amplitude for variations of aerodynamic derivatives with the frequency, but resulted in a larger offset at the higher angles of attack.

For the TCR wind tunnel model, dynamic derivatives computed for several values of the angle of attack were in agreement with measurements, but simulations failed to predict the positive damping-in-pitch at around twenty degrees observed in tunnel testing. The effect of frequency was addressed, and it was found that the higher the frequency, the better the correlation between measurements and simulations. A significant failure of the non-linear model in predicting the moment dependency was found using measured aerodynamic data. The model predicted a change in the hysteresis direction, from counter-clockwise to clockwise, associated with positive damping-in-pitch measured in small amplitude motion, but not observed in any large amplitude oscillation. This might have some implications when simulating the motion of a free-to-pitch aircraft. The non-linear formulation based on stability derivatives is instantaneous, that is, aerodynamic coefficients are only a function of the current time. The formulation is then not adequate in the case aerodynamic loads are dependent on the flow history and past motion. It was shown that, in these conditions, large amplitude data cannot be extrapolated from small amplitude tests and cannot be represented accurately by stability derivatives.

The major computational cost is the computation of time-accurate simulations in response to periodic motions. For the SDM, a typical calculation on 16 processors required about 10 hours of CPU time. For the TCR, a dynamic simulation performed on 128 processors required about 60 hours of CPU time. For the TCR test case, computer time was provided through the U.K. Applied Consortium under EPSRC grant EP/F005954/1. To overcome this practical issue, a concurrent work based on linear frequency domain and harmonic balance predictions of dynamic derivatives will be presented. Limiting assumptions of the aerodynamic derivative model motivates the need to address future research on the use of more advanced mathematical formulations.

Chapter 4

Dynamic Derivatives from Frequency-Domain Methods

4.1 Introduction

A common wind-tunnel testing technique for the prediction of dynamic derivatives relies on harmonic forced-oscillation tests. After the decay of initial transients, the nature of the aerodynamic loads becomes periodic. The objective of this chapter is to exploit the periodicity of the resulting aerodynamic system to significantly decrease the computational cost incurred by unsteady CFD simulations. A time-domain simulation of this problem requires significant computational effort, as described in Section 3.4. Several oscillatory cycles have to be simulated to obtain a harmonic aerodynamic response, and a time-accurate solution requires a small time-step increment to accurately capture the flow dynamics [131,151]. Time-domain calculations support a continuum of frequencies up to the frequency limits given by the temporal and spatial resolution, but dynamic derivatives are computed at the frequency of the applied sinusoidal motion. It is therefore worthwhile to consider a frequency-domain formulation to obtain a good estimate of the derivatives at reduced computational cost. The computational methods used in this thesis, the Harmonic Balance (HB) and the Linear Frequency Domain (LFD) methods, provide the ability to efficiently approximate the aerodynamics resulting from small, periodic and unsteady perturbations of the geometry of an aircraft configuration. By resolving only the frequencies of interest, the computational cost of dynamic derivatives is greatly reduced. Initially developed in the field of turbomachinery [154,155], the HB and LFD methods have been subsequently used for external aerodynamics applied to aircraft problems [156–158]. Murman [135] envisioned the exploitation of the periodicity to reduce the cost of computing dynamic derivatives. The concept of an adaptive HB method has also been put forward, with good success [159, 160]. A large amount of research has been devoted to applications of the HB and the LFD technologies to a broad spectrum of engineering disciplines. There is the question of the influence of

the approximations on the derivative predictions. The evaluation of the computational benefits and the predictive limitations are the subject of this chapter.

The chapter begins with a description of the HB and LFD methods. Results are then presented to compare the dynamic derivative predictions obtained from the time-domain and from the acceleration methods. Two test cases of increasing complexity are considered for transonic flows. One of the reasons for choosing flight conditions featuring compressibility effects is to substantiate the validity of these methods in providing cheap yet reasonable predictions for aircraft applications of practical interest. The accuracy of the acceleration methods is evaluated by comparing the predictions against the underlying time-accurate solver. Conclusions are then given.

4.1.1 Harmonic Balance Method

Reference [161] examined the unsteady viscous transonic flow in the front stage rotor of a high pressure compressor with the harmonic balance technique. The unsteady aerodynamic response of the rotor for a case where the aerofoils vibrate harmonically in pitch about their midchords with a reduced frequency of one and an interblade phase angle of 30° was considered. Pitch amplitudes of 0.01° and 1.0° were used. Note that, while these values are sufficiently large for aeroelastic investigations, the response to larger amplitudes is often required in studies of flight mechanics. For the small-amplitude case, the mean flow was found identical to the steady-state flow computed with no motion. This is not unexpected because in this case the unsteadiness is so small that non-linear effects are unimportant. For the larger-amplitude case, differences were observed comparing results obtained using various number of harmonics, however the solution converged rapidly as the number of harmonics was increased. The first harmonic of the unsteady pressure distribution was then investigated. This component is important because it contributes to the aerodynamic damping for harmonic pitching motion of the aerofoils, see also Sections 3.3.1.1 and 4.2.3 for further considerations. For the small-amplitude case, the first harmonic solution was identical to a time-linearized solution. For the larger-amplitude case, the pressure distributions computed with various number of harmonics were different, but converging rapidly for increasing number of harmonics. For the small amplitude, shock impulses associated with the unsteady motion of the shocks were observed. For increasing amplitude of the pitching vibration, these peaks are reduced and spread out because the shock motion is larger and the resulting shock impulse is spread over a larger chordwise extent. The real part of the pitching moment is important for aeroelastic stability and for the determination of the free-response, and accurately determining the damping-in-pitch term is a key factor. In the absence of mechanical damping, the rotor is stable only if the real part is less than zero for all interblade phase angles. For a value of 30°, the computed real component of the moment was positive (unstable) for small amplitude motions, and it

was found to cross the real axis at a pitching amplitude of about 0.7°. Thus, the blade is likely to vibrate in a stable limit cycle with this pitch amplitude. It was also found that three to five harmonics are adequate to obtain converged solutions for the zeroth and first harmonic components of the unsteady flow. The authors claimed that, even with seven harmonics, the cost of the harmonic balance technique is about ten times the cost of a steady-state flow solution. However, no direct comparison with the cost of an unsteady time-domain solution was provided

The study in Ref. [158] investigated the use of a linearized method, referred to as LUR, and an harmonic balance method over a range of pysical conditions for a two-dimensional aerofoil. The test case was the NACA 64A006 with an oscillating flap mounted at three quarter of the chord. The LUR and the HB methods were compared in terms of accuracy and efficiency to the unsteady time-domain solution. It was found that, for a subsonic case, the LUR method is the most efficient. In the transonic regime, the LUR remained the fastest approach, but with limited accuracy around shocks. On the other hand, a one-harmonic HB solution achieved a closer agreement with the reference solution. In the case of separation in the transonic regime, the LUR method did not converge, whereas the HB method was found more robust and accurate.

4.1.2 Small Disturbance Method

The small disturbance method was presented to illustrate the use of the Euler equations applied to several two-dimensional test cases and an initial extension to a three-dimensional case [162]. Beside the sub- and supersonic regime, the capabilities of the implemented approach were demonstrated in the transonic speed range for a NACA 64A010 aerofoil and LANN wing. The small disturbance Euler solution was compared to the underlying nonlinear Euler solution. For the aerofoil case, the first harmonic unsteady pressure coefficient distribution displayed a good agreement upstream and downstream of the shock region. Deviations were observed around the shock, with spikes detected in the small disturbance solution. Although differences in the shape of the shock impulse, the load contribution of the shock impulses can be considered equal, and the first harmonic lift coefficient compared well between the two data sets. This is quite remarkable because the shock moves up to 20% of the aerofoil chord depending on the reduced frequency. This asserts the validity of shock capturing in a perturbation method applied to the transonic regime, as originally introduced by Lindquist and Giles [163]. It is argued that the load contribution to the pitching moment coefficient is not considered, which typically exhibits higher nonlinearities than the force coefficient because of the leverage arm between the shock impulse and the reference point. With the use of different nonlinear Euler codes in addition to the underlying CFD code, the application of the LANN wing corroborates the capability of the small disturbance Euler equations for a more complex configuration. It is demonstrated that variations in

the unsteady pressure coefficient obtained using different CFD solvers are more significant than those detected between the small disturbance Euler code and the underlying nonlinear CFD code. This confirms the capabilities of the small disturbance Euler method to predict unsteady loads even with a complex shock structure as observed for the LANN wing.

A 53° low aspect ratio cropped delta wing was then tested in the transonic regime as a frequent high manoeuvrable aircraft wing [164]. The flow topology consists of leading-edge vortices forming at higher angle of attack and the application of the small disturbance Euler method was aimed to simulate unsteady aerodynamic loads due to rigid body, flap and elastic harmonic motions. The important concern to guarantee flap efficiency during the entire flight envelope calls for an accurate prediction of control derivatives, which was demonstrated to be possible with the small disturbance method. An aeroelastic-like example, using an equation with polynomial coefficients for the local amplitudes for the elastic eigenmode, provided an additional test of the Euler method. In all cases, a reduction of one order in computational time was achieved using the small disturbance method with respect to the nonlinear counterpart.

Inviscid methods reach their limitations with flows where viscous effects are a dominant feature (separation, shock/boundary layer interaction), and the extension of the small disturbance method to viscous flows is an attractive alternative to time marching the RANS equations. A small disturbance Navier-Stokes method was developed from the existing inviscid solver supplementing the viscous algorithms and incorporating turbulence models in an appropriate formulation [165]. Within a linearized framework, higher harmonics in the aerodynamic response are considered to be negligible. With the use of a triple decomposition of the flow development [166], an arbitrary instantaneous flow quantity is constructed as sum of a steady mean component, a periodic perturbation and a turbulent fluctuation. The simulation process consists, first, of a turbulent steady state solution on the reference grid using the nonlinear Navier-Stokes equations, which provide the prerequisite mean flow values contained in the source term and the convective flux Jacobian. Then, the small disturbance equations are solved for the complex amplitude of the unsteady flow solution. Two two-dimensional test cases were considered and the Spalart-Allmaras turbulence model used in all calculations. For the NACA 64A010 aerofoil featuring a weak shock, the viscous solutions are compared to the small disturbance Euler solution. The inviscid solution, not including the influence of the boundary layer in the shock formation, predicts a shock located further downstream with a stronger gradient, and an overextended recompression before merging into the pressure recovery curve close to the trailing edge. Varying the reduced frequency, the computational speedup of the small disturbance viscous solution over the underlying nonlinear viscous solution is between a factor of 5 and 28. The perturbation method requires more than three times the working memory computed with the time-accurate method. The second test case is the NLR 7301 aerofoil fea-

turing a strong shock. When including the viscous effects, the shock location in the zeroth harmonic component is in good agreement with experimental data whereas the inviscid solution predicts a shock situated 20% further downstream due to the neglect of the strong shock/boundary layer interaction. Furthermore, contribution of higher harmonics in the shock region was detected in the nonlinear solutions, resulting in a poor prediction of the unsteady pitching moment coefficient obtained using the small disturbance Navier-Stokes equations.

Derived from the wing of a supersonic transport aircraft configuration, the 50° NASA clipped delta wing was considered in conditions featuring varying shock strength and leading-edge vortex formation [157]. Inviscid and viscous solutions were compared to available experimental data. For the weak shock case, the experimental data of first harmonic unsteady pressure coefficient are best reproduced using the inviscid methods. Surprisingly, the small disturbance Euler method performs better in terms of unsteady aerodynamic loads than the nonlinear counterpart and, in particular, predicts the very similar damping term compared with the nonlinear Navier-Stokes calculations. The inclusion of the viscous effects has a significant and consistent improvement on the moment damping with respect to the inviscid methods, and is of paramount importance when free pitching oscillations are considered. The second case is a medium strength shock extending from the wing root to the tip featuring a leading edge vortex formation. The interaction of the shock with the vortical flow in the outer wing section close to the wing tip results in deviations between the two viscous solutions in the unsteady pressure distribution. The dynamic shock/vortex interaction introduces in this limited wing region higher harmonics into the flow solution, which are beyond the assumptions of the small disturbance method. A strong shock is then considered, extending beyond the wing tip. In these circumstances, the inclusion of the viscous terms improves the predictions of the small disturbance method compared to the inviscid counterpart. Depending on the flow conditions, the computational efficiency increase varied between a factor of 10 and 20 in all cases.

4.2 Frequency-Domain Methods

4.2.1 Harmonic Balance Method

As an alternative to time marching, the Harmonic Balance method [161] allows for a direct calculation of the periodic state. Write the semi-discrete form as a system of ordinary differential equations

$$\mathbf{I}(t) = \frac{d\mathbf{W}(t)}{dt} + \mathbf{R}(t) = 0 \tag{4.1}$$

Consider the solution vector $\mathbf{W}$ and residual $\mathbf{R}$ to be periodic in time and a function of ω,

$$\mathbf{W}(t) \approx \widehat{\mathbf{W}}_0 + \sum_{n=1}^{N_H} \left(\widehat{\mathbf{W}}_{a_n} \cos(\omega n t) + \widehat{\mathbf{W}}_{b_n} \sin(\omega n t) \right) \tag{4.2}$$

$$\mathbf{R}(t) \approx \widehat{\mathbf{R}}_0 + \sum_{n=1}^{N_H} \left(\widehat{\mathbf{R}}_{a_n} \cos(\omega n t) + \widehat{\mathbf{R}}_{b_n} \sin(\omega n t) \right) \tag{4.3}$$

giving a system of $N_T = 2N_H + 1$ equations in N_T unknown harmonic terms, which can be expressed as

$$\omega \mathbf{A} \widehat{\mathbf{W}} + \widehat{\mathbf{R}} = 0 \tag{4.4}$$

where $\mathbf{A}$ is a $N_T \times N_T$ matrix containing the entries $\mathbf{A}(n+1, N_H+n+1) = n$ and $\mathbf{A}(N_H+n+1, n+1) = -n$, and $\widehat{\mathbf{W}}$ and $\widehat{\mathbf{R}}$ are vectors of the Fourier coefficients.

The difficulty with solving Eq. (4.4) is in finding a relationship between $\widehat{\mathbf{R}}$ and $\widehat{\mathbf{W}}$. To avoid this problem, the system is converted back to the time domain. The solution is split into N_T discrete equally spaced sub-intervals over the period $T = 2\pi/\omega$

$$\mathbf{W}_{hb} = \begin{Bmatrix} \mathbf{W}(t_0 + \Delta t) \\ \mathbf{W}(t_0 + 2\Delta t) \\ \vdots \\ \mathbf{W}(t_0 + T) \end{Bmatrix} \qquad \mathbf{R}_{hb} = \begin{Bmatrix} \mathbf{R}(t_0 + \Delta t) \\ \mathbf{R}(t_0 + 2\Delta t) \\ \vdots \\ \mathbf{R}(t_0 + T) \end{Bmatrix} \tag{4.5}$$

where $\Delta t = 2\pi/(N_T \omega)$. Then there is a transformation matrix [167] which allows Eq. (4.4) to be written as

$$\omega \, \mathbf{D} \, \mathbf{W}_{hb} + \mathbf{R}_{hb} = 0 \tag{4.6}$$

where the components of $\mathbf{D}$ are defined by

$$D_{i,j} = \frac{2}{N_T} \sum_{k=1}^{N_H} k \sin(2\pi k (j-i)/N_T) \tag{4.7}$$

One can then apply pseudo-time marching to the harmonic balance equation

$$\frac{d\mathbf{W}_{hb}}{dt} + \omega \, \mathbf{D} \, \mathbf{W}_{hb} + \mathbf{R}_{hb} = 0 \tag{4.8}$$

The HB method was implemented within the structured PMB and COSA codes. The main difference between the PMB and COSA implementations of the HB method is that the former solves the equations with an implicit method [168], whereas the latter adopts an explicit multigrid integration [169]. Reference [169] presents a stabilization technique to handle the harmonic balance source term, $\omega \, \mathbf{D} \, \mathbf{W}_{hb}$, when using an explicit numerical integration process. Such a stabilization method can be viewed as the conterpart of that

reported in reference [170], which instead applies to the case of implicit integration. The parallelization of the COSA explicit multigrid HB solver is based on a hybrid distributed (MPI) and shared (OpenMP) architecture, which is reported in reference [171].

4.2.2 Linear Frequency Domain Method

The Linear Frequency Domain (LFD) method [172] is obtained by linearizing Eq. (4.4), in which the residual $\widehat{\mathbf{R}}$ is considered as a function of the grid point locations, $\mathbf{x}$, the grid point velocities, $\dot{\mathbf{x}}$, and flow solution, $\mathbf{W}$. Assuming an unsteady motion with a small amplitude, the unsteady terms can be expressed as a superposition of a steady mean state and a perturbation, which is expressed by a Fourier series

$$\begin{aligned} \mathbf{W}(t) &\approx \widehat{\mathbf{W}}_0 + \widetilde{\mathbf{W}}(t), & \|\widetilde{\mathbf{W}}\| &\ll \|\widehat{\mathbf{W}}_0\| \\ \mathbf{x}(t) &\approx \widehat{\mathbf{x}}_0 + \widetilde{\mathbf{x}}(t), & \|\widetilde{\mathbf{x}}\| &\ll \|\widehat{\mathbf{x}}_0\| \\ \dot{\mathbf{x}}(t) &\approx \dot{\widetilde{\mathbf{x}}}(t) \end{aligned}$$

When linearizing about the steady mean state, Eq. (4.4) results in the following complex-valued linear system of equations for the n-th mode index

$$\begin{bmatrix} \partial\mathbf{R}/\partial\mathbf{W} & \omega\, n\, \mathbf{I} \\ -\omega\, n\, \mathbf{I} & \partial\mathbf{R}/\partial\mathbf{W} \end{bmatrix} \begin{Bmatrix} \widehat{\mathbf{W}}_{a_n} \\ \widehat{\mathbf{W}}_{b_n} \end{Bmatrix} = - \begin{bmatrix} \partial\mathbf{R}/\partial\mathbf{x} & \omega\, n\, \partial\mathbf{R}/\partial\dot{\mathbf{x}} \\ -\omega\, n\, \partial\mathbf{R}/\partial\dot{\mathbf{x}} & \partial\mathbf{R}/\partial\mathbf{x} \end{bmatrix} \begin{Bmatrix} \widehat{\mathbf{X}}_{a_n} \\ \widehat{\mathbf{X}}_{b_n} \end{Bmatrix} \tag{4.9}$$

Derivatives of the residual are all evaluated at the steady mean state $(\widehat{\mathbf{W}}_0, \widehat{\mathbf{x}}_0)$. This system of equations can be written in the form of a linear equation, $\mathbf{A}\,\mathbf{x} = \mathbf{b}$. The accuracy of the result will depend on the degree to which the dual assumptions of small perturbations and linearity are satisfied.

The Jacobian $\partial\mathbf{R}/\partial\mathbf{W}$ has been obtained previously in the context of the discrete adjoint method by analytic differentiation of the flow solver. Considerable attention has been given to ensure that the evaluation of the Jacobian and matrix-vector products involving the Jacobian are efficient in terms of memory and time, and requires no more than four times the memory requirements of the non-linear code. The frequency domain residual however requires two products of a vector with the Jacobian, and hence a single evaluation is approximately 20 to 60% more expensive than a non-linear residual on the same case.

The terms $\partial\mathbf{R}/\partial\mathbf{x}$ and $\partial\mathbf{R}/\partial\dot{\mathbf{x}}$, which arise from the prescribed periodic deformation of the grid, are evaluated using central finite differences

$$\frac{\partial\mathbf{R}}{\partial\mathbf{x}}\,\widetilde{\mathbf{x}} \approx \frac{\mathbf{R}\left(\widehat{\mathbf{W}}_0\,,\,\widehat{\mathbf{x}}_0 + \epsilon\,\widetilde{\mathbf{x}}\,,\,0\right) - \mathbf{R}\left(\widehat{\mathbf{W}}_0\,,\,\widehat{\mathbf{x}}_0 - \epsilon\,\widetilde{\mathbf{x}}\,,\,0\right)}{2\,\epsilon} \tag{4.10}$$

$$\frac{\partial\mathbf{R}}{\partial\dot{\mathbf{x}}}\,\dot{\widetilde{\mathbf{x}}} \approx \frac{\mathbf{R}\left(\widehat{\mathbf{W}}_0\,,\,\widehat{\mathbf{x}}_0\,,\,\epsilon\,\dot{\widetilde{\mathbf{x}}}\right) - \mathbf{R}\left(\widehat{\mathbf{W}}_0\,,\,\widehat{\mathbf{x}}_0\,,\,-\epsilon\,\dot{\widetilde{\mathbf{x}}}\right)}{2\,\epsilon} \tag{4.11}$$

where ϵ is a small number chosen to balance truncation and rounding errors.

4.2.3 Method of Data Analysis

The dynamic derivatives from the time-domain solutions and the LFD method were obtained using the techniques described in Chapter 2.6. A different approach was adopted for the HB solver, whose solution is computed at $N_T = 2\,N_H + 1$ equally spaced points in time over one cycle. Then

$$\mathbf{W}\,(x,\,y,\,z,\,t) \approx \widehat{\mathbf{W}}_0\,(x,\,y,\,z) + \sum_{n=1}^{N_H} \left(\widehat{\mathbf{W}}_{a_n}\,(x,\,y,\,z)\,\cos\left(\omega\,n\,t\right) + \widehat{\mathbf{W}}_{b_n}\,(x,\,y,\,z)\,\sin\left(\omega\,n\,t\right) \right) \tag{4.12}$$

where $\widehat{\mathbf{W}}_0$, $\widehat{\mathbf{W}}_{a_n}$ and $\widehat{\mathbf{W}}_{b_n}$ are the Fourier coefficients of a flow variable, $\mathbf{W}\,(x,\,y,\,z,\,t)$. This expression is easily re-written in matrix form as [170]

$$\underbrace{\begin{Bmatrix} \mathbf{W}_1 \\ \mathbf{W}_2 \\ \vdots \\ \mathbf{W}_{N_T} \end{Bmatrix}}_{\mathbf{W}^*} = \underbrace{\begin{bmatrix} 1 & \cos\left(\omega\,t_1\right) & \sin\left(\omega\,t_1\right) & \dots & \cos\left(N_H\,\omega\,t_1\right) & \sin\left(N_H\,\omega\,t_1\right) \\ 1 & \cos\left(\omega\,t_2\right) & \sin\left(\omega\,t_2\right) & \dots & \cos\left(N_H\,\omega\,t_2\right) & \sin\left(N_H\,\omega\,t_2\right) \\ \vdots & \vdots & \vdots & \ddots & \vdots & \vdots \\ 1 & \cos\left(\omega\,t_{N_T}\right) & \sin\left(\omega\,t_{N_T}\right) & \dots & \cos\left(N_H\,\omega\,t_{N_T}\right) & \sin\left(N_H\,\omega\,t_{N_T}\right) \end{bmatrix}}_{\mathbf{E}^{-1}} \underbrace{\begin{Bmatrix} \widehat{\mathbf{W}}_0 \\ \widehat{\mathbf{W}}_{a_1} \\ \widehat{\mathbf{W}}_{b_1} \\ \vdots \\ \widehat{\mathbf{W}}_{a_{N_H}} \\ \widehat{\mathbf{W}}_{b_{N_H}} \end{Bmatrix}}_{\widetilde{\mathbf{W}}} \tag{4.13}$$

where $\mathbf{W}^*$ is the vector of the flow variable at $2\,N_H+1$ equally spaced points in time over one period and $\mathbf{E}^{-1}$ is the matrix that is the inverse discrete Fourier transform operator. The time instances at which the HB solution is known are denoted by $t_i = t_0 + i\,\Delta\,t$, $i = 1,\,2,\,\dots,\,N_T$. The Fourier coefficients of the flow variable are computed as

$$\widetilde{\mathbf{W}} = \mathbf{E}\,\mathbf{W}^* \tag{4.14}$$

Dynamic derivatives, as well as the real and imaginary parts of the flow variable, are determined directly from the Fourier coefficients without any additional transformation in the time domain.

To determine the stability behaviour of the free-to-pitch oscillations, the work done by the fluid on the airframe over one single period can be expressed as

$$\begin{aligned} E &= \int_{\alpha(0)}^{\alpha(T)} \Delta\,C_m\,(\alpha)\;d\alpha \\ &= \alpha_A\,\omega \int_{t_0}^{t_0+T} \left(\widehat{C}_{m\,a_1}\,\cos\left(\omega\,t\right) + \widehat{C}_{m\,b_1}\,\sin\left(\omega\,t\right) \right) \cos\left(\omega\,t\right)\;dt \\ &= 2\,\pi\,\alpha_A\,\widehat{C}_{m\,a_1} \end{aligned} \tag{4.15}$$

Parameter	Value
M	0.755
α_0	0.016°
α_A	2.51°
k	0.0814

Table 4.1: Description of the AGARD CT5 conditions for the NACA 0012 aerofoil [173]

The second equality follows by assuming a Fourier series for the pitching moment and, recalling the orthogonality properties of the trigonometric series, it is apparent that the energy transfer is proportional to the imaginary part of the aerodynamic moment. It is shown that $\widehat{C}_{m\,a_1}$ is proportional to the damping term in Eq. (2.21). Hence, for $\alpha_A > 0$, the free pitching oscillation can be classified as unstable if $\widehat{C}_{m\,a_1} > 0$ (equivalently, $\bar{C}_{m_q} > 0$), or stable if $\widehat{C}_{m\,a_1} < 0$ (equivalently, $\bar{C}_{m_q} < 0$).

4.3 Two-Dimensional Case

Experimental data for the NACA 0012 aerofoil undergoing oscillatory pitch motions are available [173]. Measured quantities include the pressure at 30 locations distributed on the aerofoil surface. These data were collected at several time intervals. No transition tripping was applied in the experiments, and corrections corresponding to a steady interference have been applied to the measured quantities. There were some questions about unsteady interference effects on the experimental data. However, the deviation between numerical and experimental data is not the emphasis of the present work which is instead on the quality of the HB and LFD results compared to the time-domain predictions.

This thesis focuses on the AGARD CT5 case because it is transonic with strong non-linearities in the aerodynamic loops arising from shock wave motions. The flow conditions for the case CT5 are summarized in Table 4.1.

4.3.1 Numerical Setup

A preliminary study was made to test that solutions presented are independent of the grid used. Three sets of grids were generated. The two-dimensional domain extends fifty chords from the solid wall to the farfield. The coarsest grid had a total number of 13068 points, with 132 nodes on the aerofoil, and 36 in the normal direction. The wake behind the aerofoil was discretized using 36 points in the streamwise direction. A medium grid consisted of 32028 grid points, 212 nodes were distributed on the aerofoil, 51 points were used in the normal direction and along the streamwise direction for the wake (see Fig. 4.1). The finest grid was obtained with a total of 37180 grid points. The

	$C_{N\,0}$	C_{N_α}	C_{N_q}	$C_{m\,0}$	C_{m_α}	C_{m_q}
Coarse	$3.51\cdot 10^{-3}$	7.66	$-3.71\cdot 10^{1}$	$-7.58\cdot 10^{-5}$	$-1.10\cdot 10^{-1}$	-3.07
Medium	$3.51\cdot 10^{-3}$	7.66	$-3.72\cdot 10^{1}$	$-6.98\cdot 10^{-5}$	$-1.03\cdot 10^{-1}$	-3.14
Fine	$3.51\cdot 10^{-3}$	7.66	$-3.72\cdot 10^{1}$	$-7.15\cdot 10^{-5}$	$-1.03\cdot 10^{-1}$	-3.14

Table 4.2: NACA 0012: grid influence on static and dynamic derivatives obtained from the time-domain PMB solution for the AGARD CT5 conditions

structured grids consisted of six blocks, and were converted to an unstructured format for use with the unstructured solver TAU.

Note that the three grids were used in combination with each time-domain solver, and numerical results were compared with tunnel measurements under static [174] and unsteady conditions. Table 4.2 conveys the grid influence on the dynamic derivatives of the normal force and moment coefficients. Aerodynamic data of the force coefficient show little sensitivity to the grid used. Values of $C_{m\,0}$ can be considered numerically nil and thus grid invariant. For the computations on the medium grid, dynamic derivatives of the moment coefficient are observed to be identical to the respective values obtained using the finest grid. Some deviations are identified in the case of the coarsest grid. Based on this comparison, results presented hereafter are for the medium grid.

Unsteady simulations were run for three periods using 128 time-steps per cycle. A time-step study was also performed for the unsteady PMB solver, and details are given in Section 4.3.4. The choice of the numerical parameters led to well converged solutions in all cases. For TAU, the CFL number used was 1.5 in combination with a "4w" multigrid cycle. For the LFD, the LU-SGS scheme with multigrid was used. The COSA pair used three multigrid levels, performing 10 smoothed Runge-Kutta cycles on the coarsest level, and 3 on the finest levels. The CFL number was 4 for both the time-domain and the harmonic balance solver. The implicit CFL number for the PMB solver was 500. A Block Incomplete Lower Upper (BILU) factorization was used with no fill-in for the linear solver preconditioner.

4.3.2 Validation

The Euler solutions presented are for the medium grid, shown in Fig. 4.1. The flow for the AGARD CT5 conditions is non-linear, with a shock appearing in the leading edge region and moving downstream for increasing angle of attack. The shock continues downstream until approximately forty-five per cent of the chord. Then the shock returns upstream close to the leading edge. The same pattern is repeated on the opposite side of the aerofoil. The flow remains attached throughout the cycle of unsteadiness. Since this case features a strong shock on the upper and lower surface, the question is whether the presence of the dynamic shock has a negative impact on the accuracy of the frequency-domain solvers. First, a validation study of the unsteady time-accurate

solutions was performed before attempting to compare the spectral methods to the underlying CFD solvers. Figure 4.2 illustrates the comparison of numerical predictions of integrated aerodynamic loads with experimental data. The initial transient was removed from the numerical solutions, and two arrows indicate the time evolution. If the arrows are oriented in the counter-clockwise direction, the contribution from the dynamic derivative is negative, and vice versa. Results compare well for all time-accurate solutions. It is seen that the force coefficient is harmonic with a phase lag with respect to the forced motion. No contribution from higher harmonics can be detected. The moment coefficient is influenced by the instantaneous location of the moving shock wave due to its moment arm with respect to the reference point. A favourable agreement between the tunnel measurements and the numerical solutions is observed.

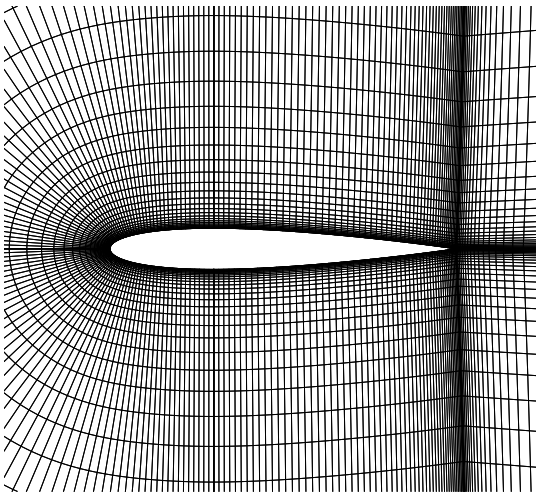

Figure 4.1: Grid used for the NACA 0012 aerofoil, medium grid (212×51)

Measurements of the instantaneous pressure coefficient distribution were taken at several time instances in one cycle of unsteadiness, and the nearest angle at which numerical results were computed was used for comparison. Numerical solutions are compared with tunnel measurements in Figs. 4.3 and 4.4. The numerical solutions agree well with each other, with minor deviations around the shock wave. The overall performance and systematic variations from measurements are in line with other independent numerical investigations, e.g., Batina [175] and Marques et al. [176].

For the range of test cases computed in Da Ronch et al. [131], the dependence of dynamic derivatives on motion and flow conditions was reported. In the present study, the influence of the amplitude of the forced-motion, α_A, was examined for the conditions given in Table 4.1. Values of amplitude presented are between 0.01° and 2.81°. The

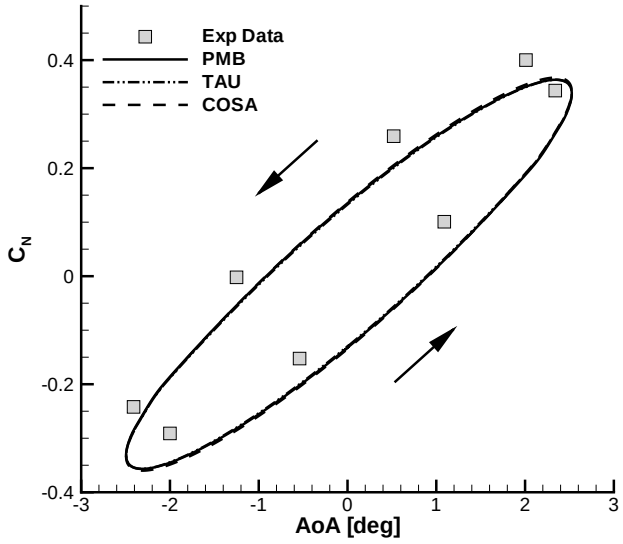

(a) Normal force coefficient

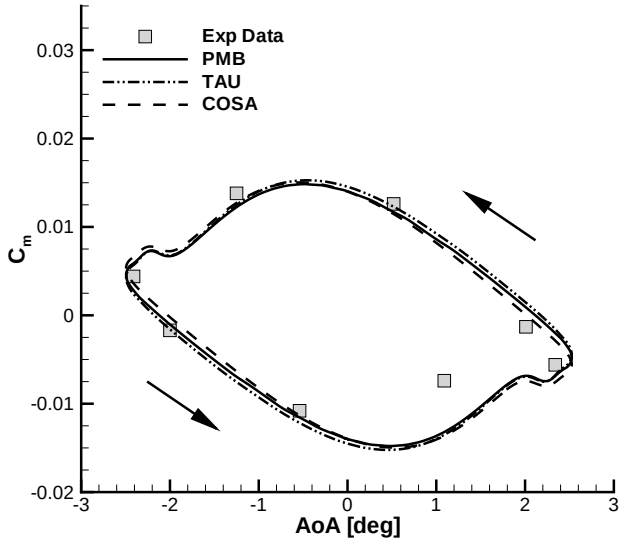

(b) Pitching moment coefficient

Figure 4.2: NACA 0012: predictions of unsteady time-accurate Euler solutions ($M = 0.755$, $\alpha_0 = 0.016°$, $\alpha_A = 2.51°$, and $k = 0.0814$); experimental data from Landon [173]

variation of the pitching moment coefficient dynamic derivatives is shown in Fig. 4.5. Dynamic derivatives are nearly constant for small values of oscillatory amplitude, and exhibit a significant variation for values of amplitude larger than approximately 1.0°. Predictions obtained using the LFD solver are included in the figure as a dotted line, and are closer to the results obtained using time-domain calculations for small amplitude

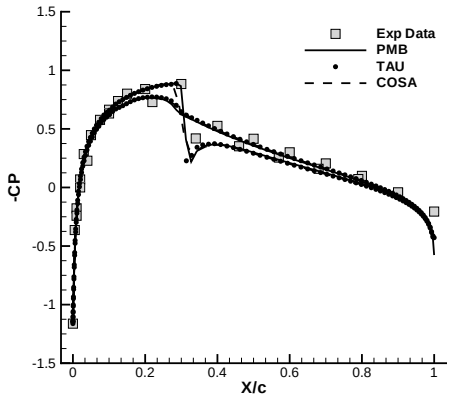

(a) $\alpha = 1.09^\circ$ (up)

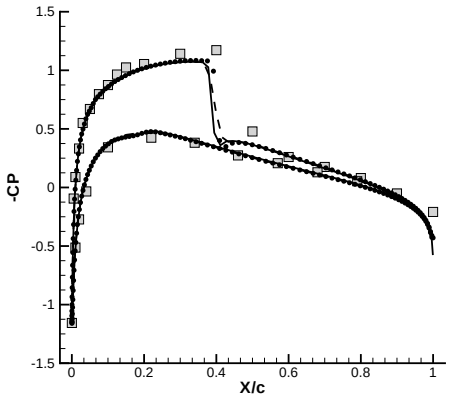

(b) $\alpha = 2.34^\circ$ (up)

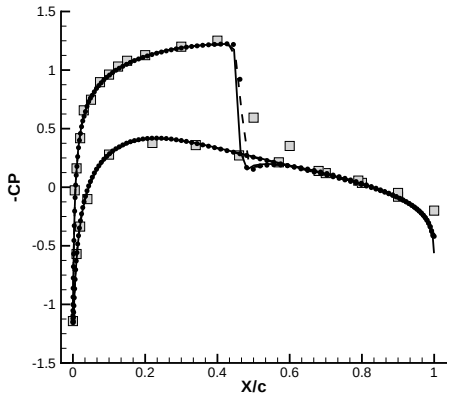

(c) $\alpha = 2.01^\circ$ (down)

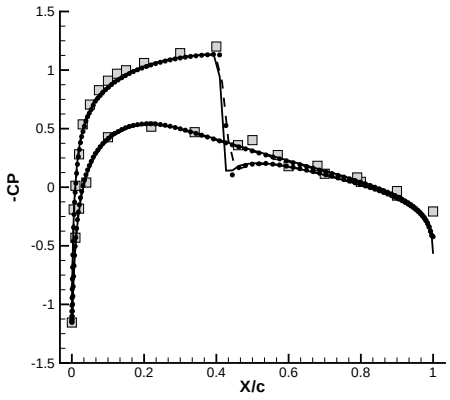

(d) $\alpha = 0.52^\circ$ (down)

Figure 4.3: Instantaneous pressure coefficient distribution compared to experimental data of Landon [173]; the terms up and down in parenthesis indicate the direction increasing and decreasing angle, respectively (continued)

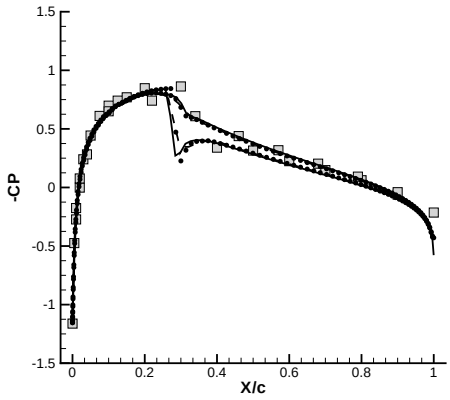

(a) $\alpha = -1.25°$ (down)

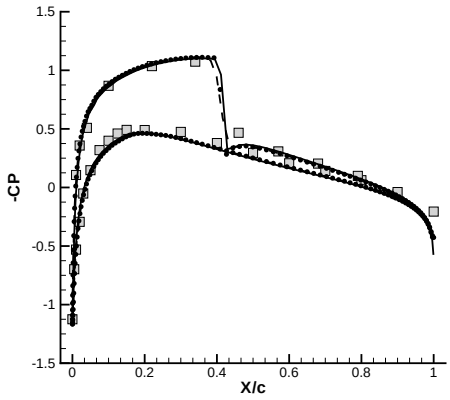

(b) $\alpha = -2.41°$ (down)

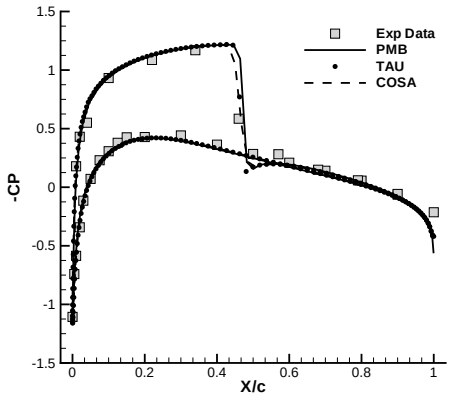

(c) $\alpha = -2.00°$ (up)

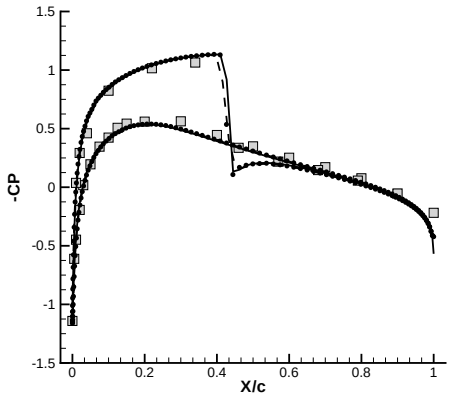

(d) $\alpha = -0.54°$ (up)

Figure 4.4: Instantaneous pressure coefficient distribution compared to experimental data of Landon [173]; the terms up and down in parenthesis indicate the direction increasing and decreasing angle, respectively (concluded)

values. Increasing the oscillatory amplitude of the forced-motion above 1.0° causes the periodic appearance and disappearance of the shock wave on the aerofoil surface, with a considerable impact on dynamic derivatives. Numerical predictions representative of a one-mode harmonic balance solution were computed for several values of the oscillatory ampliude. It is recognized that the harmonic balance solution closely approximates the time-domain solution in all cases. Note that dynamic derivatives computed at the nominal conditions of the AGARD CT5 are also included in the figure.

4.3.3 Frequency-Domain Results

To demonstrate the convergence of the HB method to the unsteady solution, cases were run using up to 7 harmonics. Figure 4.6 shows the loops of the integrated loads against the instantaneous angle of attack. The time evolution in the force coefficient was observed to be linear and harmonic with the forced variation in the motion variable. This reflects the satisfactory agreement achieved by the frequency-domain methods using one Fourier harmonic, as illustrated in Fig. 4.6(a). It also suggests that the motion of the shock wave is harmonic and lags behind the angle of attack change. Increasing the number of Fourier modes in the HB solution had little effect on the result, as most of the energy is at the frequency of the applied motion. The moment coefficient is illustrated in the remaining figures for each solver pair, separately. Comparing the harmonic balance solutions obtained using the PMB-HB and COSA-HB highlights the similarity in the results from the two solvers, as shown in Figs. 4.6(b) and 4.6(c). Observe that including the third Fourier mode in the HB solution has a far larger impact on improving the correlation to the reference solution than adding the second mode. This reflects the frequency spectrum of the moment coefficient, due to the flow conditions and symmetry in the aerofoil geometry, as described below. Higher modes are not included, but they closely overlap the reference solution. The LFD solution is illustrated in Fig. 4.6(d), and indicates a degraded prediction of the moment dynamic dependence. Consistent with the other data, the LFD predicts a large hysteresis but the loop is rotated in the opposite direction. This is quantified calculating the system response between the prescribed angle of attack and the aerodynamic loads. Let us denote x and y, respectively, the input and the output of interest. Then, the system response is

$$G\left(j\,\omega\right) \;=\; \frac{\mathscr{F}\left[y\left(t\right)\right]}{\mathscr{F}\left[x\left(t\right)\right]} \;=\; R\left(\omega\right)\, e^{j\,\phi(\omega)} \tag{4.16}$$

where $R\left(\omega\right)$ and $\phi\left(\omega\right)$ indicate, respectively, the amplitude ratio and the phase lag, and are defined as

$$R\left(\omega\right) \;=\; \frac{\|\tilde{y}\left(j\,\omega\right)\|}{\|\tilde{x}\left(j\,\omega\right)\|} \tag{4.17}$$

$$\phi\left(\omega\right) \;=\; \angle\,\tilde{y}\left(j\,\omega\right) \;-\; \angle\,\tilde{x}\left(j\,\omega\right) \tag{4.18}$$

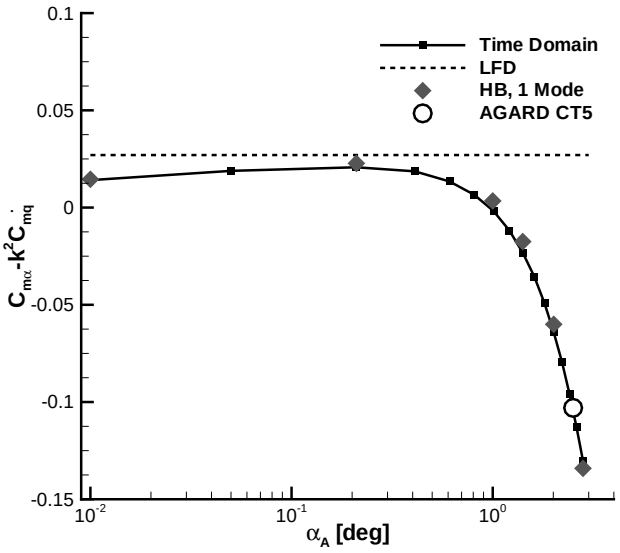

(a) In-phase component, $\bar{C}_{m_\alpha}$

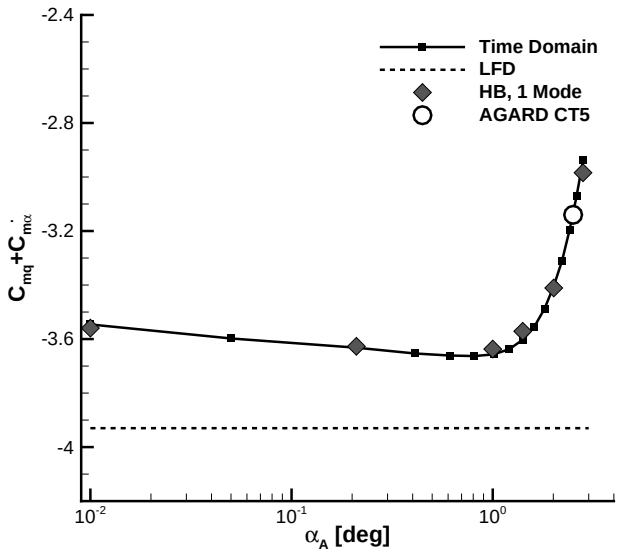

(b) Out-of-phase component, $\bar{C}_{m_q}$

Figure 4.5: NACA 0012: influence of amplitude of oscillatory motion, α_A, on the pitching moment coefficient dynamic derivatives ($M = 0.755$, $\alpha_0 = 0.016°$, and $k = 0.0814$)

Values from the one-mode HB and the LFD solutions are summarized in Table 4.3, along with the reference solution. In the table, the subscript and superscript indicate, respectively, the input and the output, and the phase angle is measured in degrees. Apart from the satisfactory agreement observed for the force data, a discrepancy is detected in the phase angle of the moment coefficient. For a sinusoidally varying input,

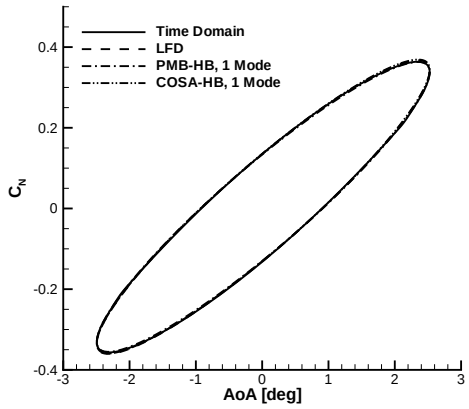

(a) Normal force coefficient

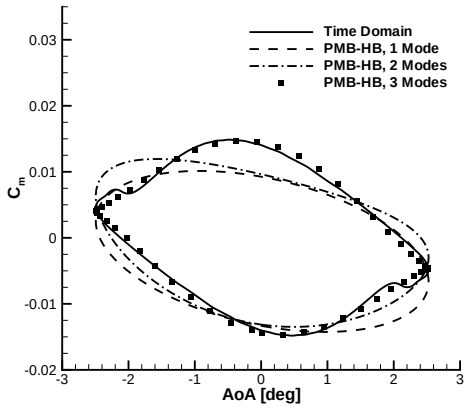

(b) Pitching moment coefficient, PMB-HB

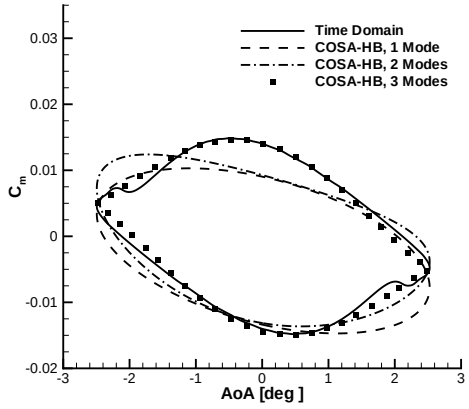

(c) Pitching moment coefficient, COSA-HB

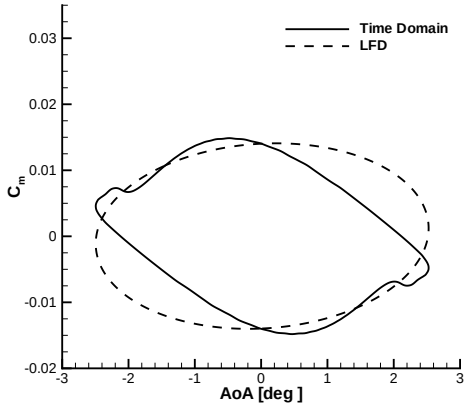

(d) Pitching moment coefficient, LFD

Figure 4.6: NACA 0012: normal force and pitching moment coefficients dynamic dependence ($M = 0.755$, $\alpha_0 = 0.016°$, $\alpha_A = 2.51°$, and $k = 0.0814$)

a phase angle of $-90°$ corresponds to shifting the response to a cosine function. The positive mean curve slope of the LFD solution in Fig. 4.6(d) reflects a phase lag in the moment dynamic dependence greater than $-90°$. On the contrary, a larger phase angle, in absolute value, reflects a negative mean curve slope, consistent with the one-mode HB solution.

To get further insights on the performance of the frequency-domain methods, the first harmonic unsteady surface pressure coefficient distribution is presented in Fig. 4.7. Results on the left side of the figure are for the one-mode HB and the LFD solutions, and the axis of rotation is also illustrated, while the right side illustrates the effect of retaining higher Fourier modes. Due to the similarity with the trends defined by the PMB-HB results, the COSA-HB solutions presented include only one Fourier mode. Figure 4.7(a) shows the zeroth harmonic, that is, the average value of the pressure

	$R_\alpha^{C_N}$	$\phi_\alpha^{C_N}$	$R_\alpha^{C_m}$	$\phi_\alpha^{C_m}$
Time Domain	0.144	-21.6	$4.80 \cdot 10^{-3}$	-112.1
PMB-HB, 1 Mode	0.143	-21.5	$4.86 \cdot 10^{-3}$	-112.1
COSA-HB, 1 Mode	0.145	-21.4	$4.98 \cdot 10^{-3}$	-116.3
LFD	0.145	-21.5	$5.60 \cdot 10^{-3}$	-85.2

Table 4.3: NACA 0012: amplitude ratio and phase angle of the fundamental harmonic between the input, α, and the outputs, C_N and C_m

coefficient through a cycle of unsteadiness. The HB solutions are identical for the two solvers, and are significantly different from the LFD solution. The asymmetric shock pattern on the lower and upper surfaces is attributable to the use of one Fourier mode and the actual location of the three time instances computed, which form a solution base sampled at uniformly spaced temporal intervals. Note that two snapshots feature a shock wave on the lower side, and on the upper surface for one snapshot, giving the over-prediction of the shock strength on the lower side and the under-prediction on the upper surface, in combination with a more upstream and downstream location, respectively. The mean solution of the LFD method corresponds to a steady-state analysis, and shows a good agreement away from the reference shock location. The dynamic conditions of the prescribed forced motion moves the averaged shock position backward from its static position, determined at the mean angle of attack, by nearly twenty per cent of the aerofoil chord. Convergence to the time-accurate solution is obtained when increasing the number of modes in the HB method, as shown in Fig. 4.7(b). The real and imaginary parts, shown in Figs. 4.7(c) and 4.7(e), respectively, exhibit the already mentioned asymmetric pattern of the one-mode HB solution. Large spikes in the LFD solution are located around the steady-state shock position, and indicate a linear harmonic motion of the shock wave. The results for increasing number of harmonics are illustrated in Figs. 4.7(d) and 4.7(f). Note the different vertical scales used with respect to the prior set of corresponding figures. While consistently converging to the time-accurate solution, the rate of convergence is hindered by oscillations around the shock. Considering that three modes were adequate to approximate the moment dynamic dependence, this case illustrates the greater difficulty in converging a local quantity than an integrated one.

Table 4.4 summarizes the dynamic derivatives for the force and moment coefficients. A satisfactory agreement for the force dynamic derivatives is noted. For the moment values, the PMB-HB results illustrate that the one-mode solution provides a good estimation of the information needed for flight dynamics. The predictions of the LFD are reasonable for the aerodynamic damping term, while the in-phase component features a large inaccuracy. The contrasting sign reflects the observation that the moment loop was rotated in the opposite direction, indicating an unstable longitudinal static stability. A consideration is that the steady-state shock wave, shown in Fig. 4.7(a),

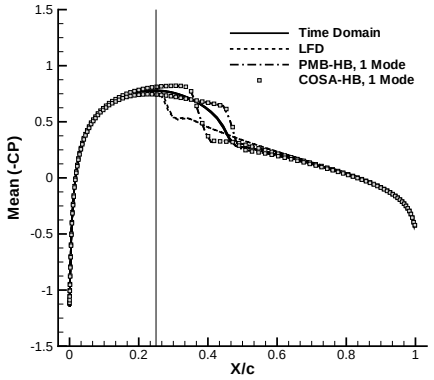

(a) Mean value

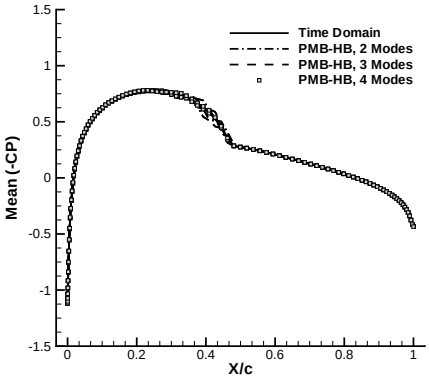

(b) Mean value, higher modes

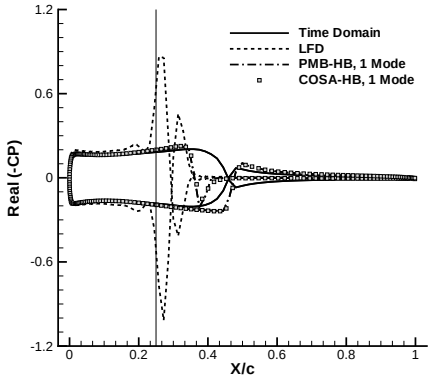

(c) Real part

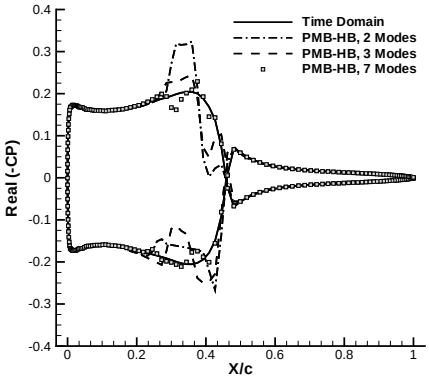

(d) Real part, higher modes

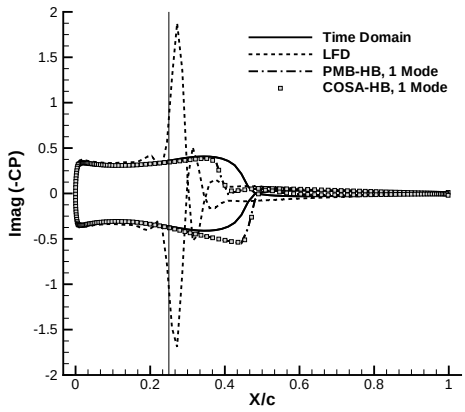

(e) Imaginary part

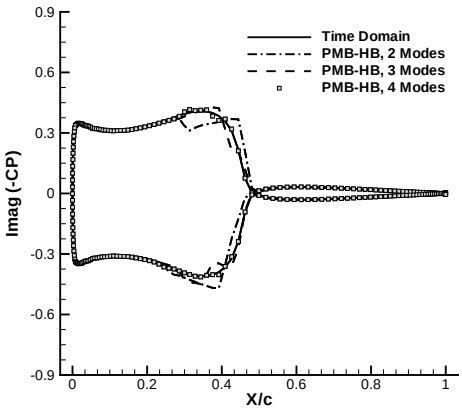

(f) Imaginary part, higher modes

Figure 4.7: NACA 0012: zeroth and first harmonic unsteady surface pressure coefficient distribution ($M = 0.755$, $\alpha_0 = 0.016°$, $\alpha_A = 2.51°$, and $k = 0.0814$)

is located near the reference point at one quarter of the chord, and makes the mo-

	C_{N_α}	C_{N_q}	C_{m_α}	C_{m_q}
Time Domain	7.66	$-3.72\cdot 10^{1}$	$-1.03\cdot 10^{-1}$	-3.14
PMB-HB, 1 Mode	7.63	$-3.70\cdot 10^{1}$	$-1.04\cdot 10^{-1}$	-3.17
PMB-HB, 2 Modes	7.63	$-3.72\cdot 10^{1}$	$-1.06\cdot 10^{-1}$	-3.19
PMB-HB, 3 Modes	7.64	$-3.72\cdot 10^{1}$	$-1.02\cdot 10^{-1}$	-3.14
PMB-HB, 4 Modes	7.65	$-3.72\cdot 10^{1}$	$-1.04\cdot 10^{-1}$	-3.15
PMB-HB, 5 Modes	7.65	$-3.72\cdot 10^{1}$	$-1.03\cdot 10^{-1}$	-3.14
PMB-HB, 6 Modes	7.65	$-3.72\cdot 10^{1}$	$-1.03\cdot 10^{-1}$	-3.14
PMB-HB, 7 Modes	7.65	$-3.72\cdot 10^{1}$	$-1.03\cdot 10^{-1}$	-3.14
LFD	7.73	$-3.73\cdot 10^{1}$	$0.27\cdot 10^{-1}$	-3.93

Table 4.4: NACA 0012: normal force and pitching moment coefficient dynamic derivatives ($M = 0.755$, $\alpha_0 = 0.016°$, $\alpha_A = 2.51°$, and $k = 0.0814$)

ment data sensitive to any upstream or downstream variation of the resulting centre of pressure.

The frequency spectrum of the moment coefficient is presented in Fig. 4.8. Data for the time-domain solution are shown up to the seventh harmonic component. The LFD and the one-mode HB solutions show a good agreement for the magnitude term. The phase angle of the LFD solution differs by about thirty degrees from the HB counterpart. For the frequency range included, the amplitude of any odd harmonic is lower than the amplitude of the accompanying even harmonic. This arises from the symmetry of the aerofoil section and the nearly zero mean angle of attack.

4.3.4 Computational Efficiency

Figure 4.9 conveys the computational efficiency of the spectral methods with respect to the underlying time-domain simulation. For the comparison, the solutions were obtained using 128 time-steps per cycle and were simulated for 3 periods. In this case, the LFD solution was obtained in about 5% of the time of the corresponding time-domain solver. While achieving the largest computational saving time, a loss in accuracy was observed in the LFD-based predictions of dynamic derivatives. With a performance similar to the LFD solver, the HB formulation was seen to be adequate for the prediction of stability characteristics and local flow variables. By retaining more Fourier modes, the HB method rapidly loses favor relative to solving the time-dependent equations. It is observed, however, that the computational efficiency of the HB method is solver-dependent.

A detailed quantification of the computational efficiency of the HB method compared with the underlying unsteady solution was undertaken for the PMB solver pair, and following the procedure outlined in reference [177]. To assess the sensitivity of the temporal discretization used, unsteady solutions were obtained using 8, 16, 32, 64, 128, 256, 512 and 1024 time-steps per oscillatory cycle. All cases were run using the same

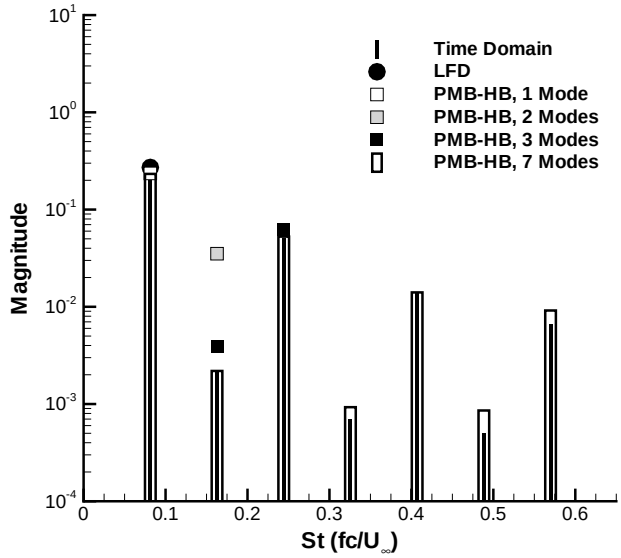

(a) Magnitude

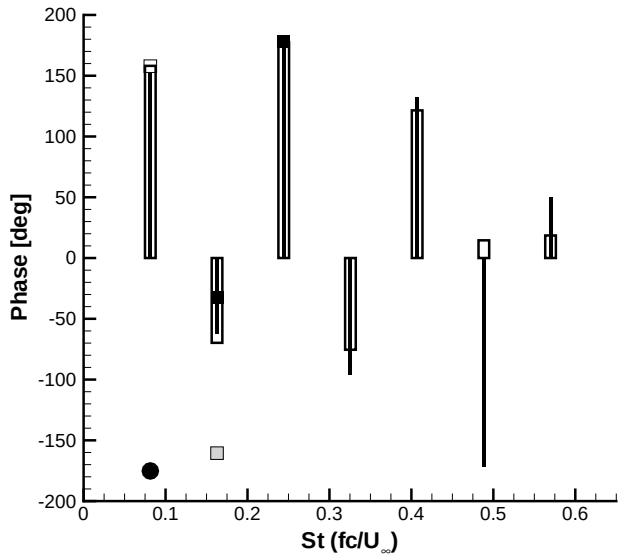

(b) Phase

Figure 4.8: NACA 0012: magnitude and phase of pitching moment coefficient ($M = 0.755$, $\alpha_0 = 0.016°$, $\alpha_A = 2.51°$, and $k = 0.0814$)

solver parameters. To reduce the effects of the initial transient on the solution, eleven cycles were simulated. The damping-in-pitch term was taken as the figure of merit, which is of interest for this work. For each time step, the dynamic term was determined from the last cycle of the solution computed, and compared with the reference value obtained from the most accurate simulation, that is, using 1024 time-steps. The

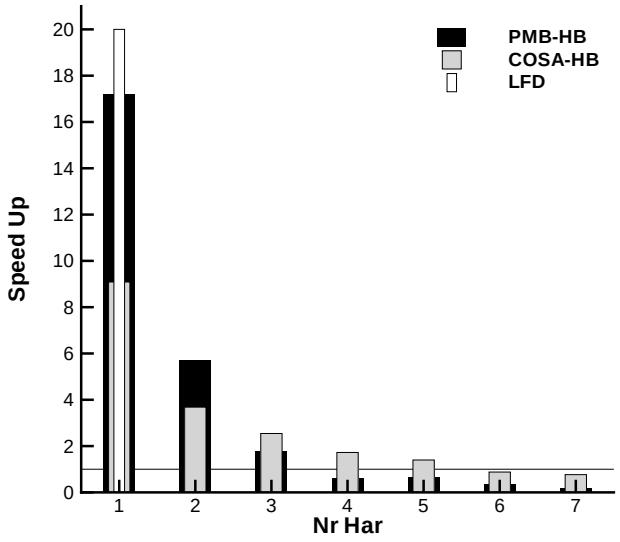

Figure 4.9: NACA 0012: CPU time speed up of the frequency-domain methods with respect to the underlying time-domain method; "Nr Har" indicates the number of harmonics

norm

$$E_n = |\bar{C}^n_{m_q} - \bar{C}^{1024}_{m_q}| \,/\, |\bar{C}^{1024}_{m_q}| \tag{4.19}$$

indicates the temporal error. The procedure was also adopted for the PMB-HB results, and the seven-mode solution was assumed the reference solution. Figure 4.10(a) shows the error levels for the two solvers. The intersection of the PMB-HB lines with the PMB curve indicates the temporal resolution needed in the unsteady simulation to achieve an equivalent error level. To match the error level defined by the one-mode PMB-HB solution, 50 time-steps per oscillation are required for the time-domain simulation, increasing to 90 to guarantee a similar error level as for the three-mode HB solution. A convergence study was then performed to identify the number of oscillatory cycles needed to obtain asymptotic convergence. Results for the two time-steps are shown in Fig. 4.10(b). The curves converge to an error level representing the minimum error achievable using the corresponding time-step size. Convergence is observed after 3 oscillatory cycles for the larger time-step size, increasing to 6 in combination with the finer step increment. Data are summarized in Table 4.5. It was found that the execution time of the HB solution using one-mode is about 11 times faster than the time required for the unsteady results. The time saving decreases to less than 3 times when three-modes are retained in the solution. Increased work associated with the linear solver as the number of modes is increased contributes to increased cost.

The memory cost of the PMB-HB method to store the linear system scales as

$(4N_H^2 + 16N_H + 7)/7$ [168]. The memory is expressed as a fraction of the memory required by the implicit steady state solver on the same grid. The memory requirements grow quickly and become significant above a small number of harmonics.

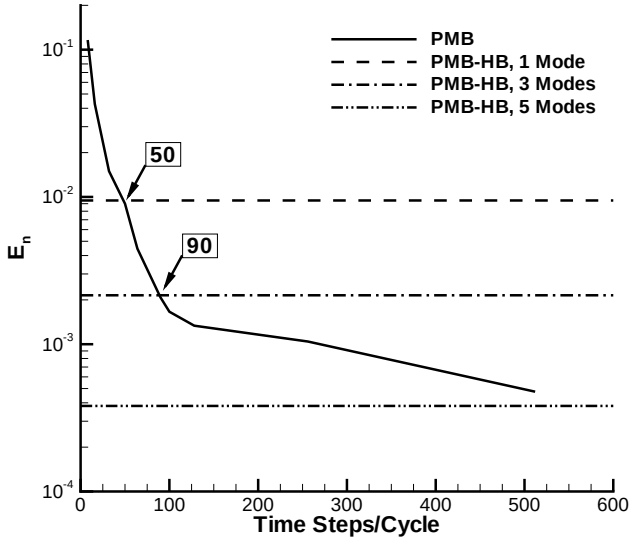

(a) Estimating the number of time-steps per cycle

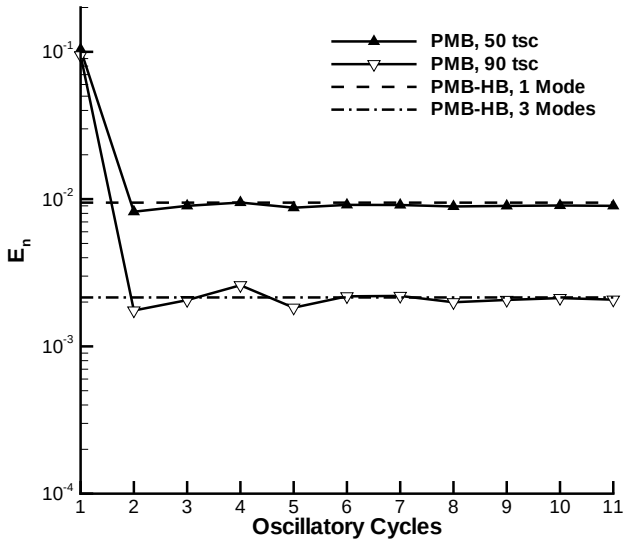

(b) Estimating the number of cycles

Figure 4.10: NACA 0012: error norm in the prediction of the damping-in-pitch obtained using the PMB solver pair; in (b), the term tsc indicates the number of time steps per cycle

PMB-HB	PMB ($tsc \times n_c$)	Speed-Up
1 Mode	50×3	10.9
3 Modes	90×6	2.6

Table 4.5: NACA 0012: time reduction of the PMB-HB solution compared to unsteady PMB solution using the damping-in-pitch as the figure of merit; the terms tsc and n_c indicate, respectively, the number of time-steps per cycle and the number of oscillatory cycles

4.4 Three-Dimensional Case

The second test case is for a civil passenger transport aircraft tested at the German Aerospace Center (DLR), and referred to as the DLR-F12 model. Extensive tunnel investigations and numerical simulations focused on the linear aerodynamics range, that is, at low speed and at low angles of attack [137, 150, 172, 178–180]. The emphasis in the current work is for a transonic cruise condition, which has been investigated in a previous study [181].

4.4.1 Numerical Setup

Two Euler grids for the half-configuration of the wind tunnel model were used for the PMB and TAU pairs, shown in Fig. 4.11. A structured grid including 300 blocks was generated with around 2 million grid points, and 1.8 million points were used for the unstructured grid. A detailed comparison of the structured and unstructured grids can be found, for example, in Mialon et al. [178].

Calculations presented in this thesis are for a cruise condition at an altitude of $6000\,m$, Mach number of 0.73 and trim angle of attack of $0.7°$. The analysis is performed on the clean configuration with undeflected control surfaces. This was considered a reasonable simplification because the required trim elevator deflection is lower than one degree and, consistent with the traditional mathematical formulation, forces and moments are expanded in a Taylor series around the equilibrium level flight condition to obtain the stability and control derivatives. Data for the oscillatory pitching motion are summarized in Table 4.6. The mean aerodynamic chord of the wind tunnel model is $c = 0.2526\,m$. The rotation point and the model centre of gravity are coincident and located at 46.7% of the fuselage length from the foremost point. The moment reference point is set at the aircraft nose.

Unsteady simulations were run for three periods using 128 time-steps per cycle. Note that all time-domain calculations were repeated for a smaller time-step that has twice the number of points per cycle, with identical results obtained. For the TAU solver, a GMRES Krylov solver was used in combination with a "3v" multigrid cycle as preconditioner at a CFL number of 10. The PMB calculations were also run at a constant CFL number of 10. The HB method was run with one Fourier mode only

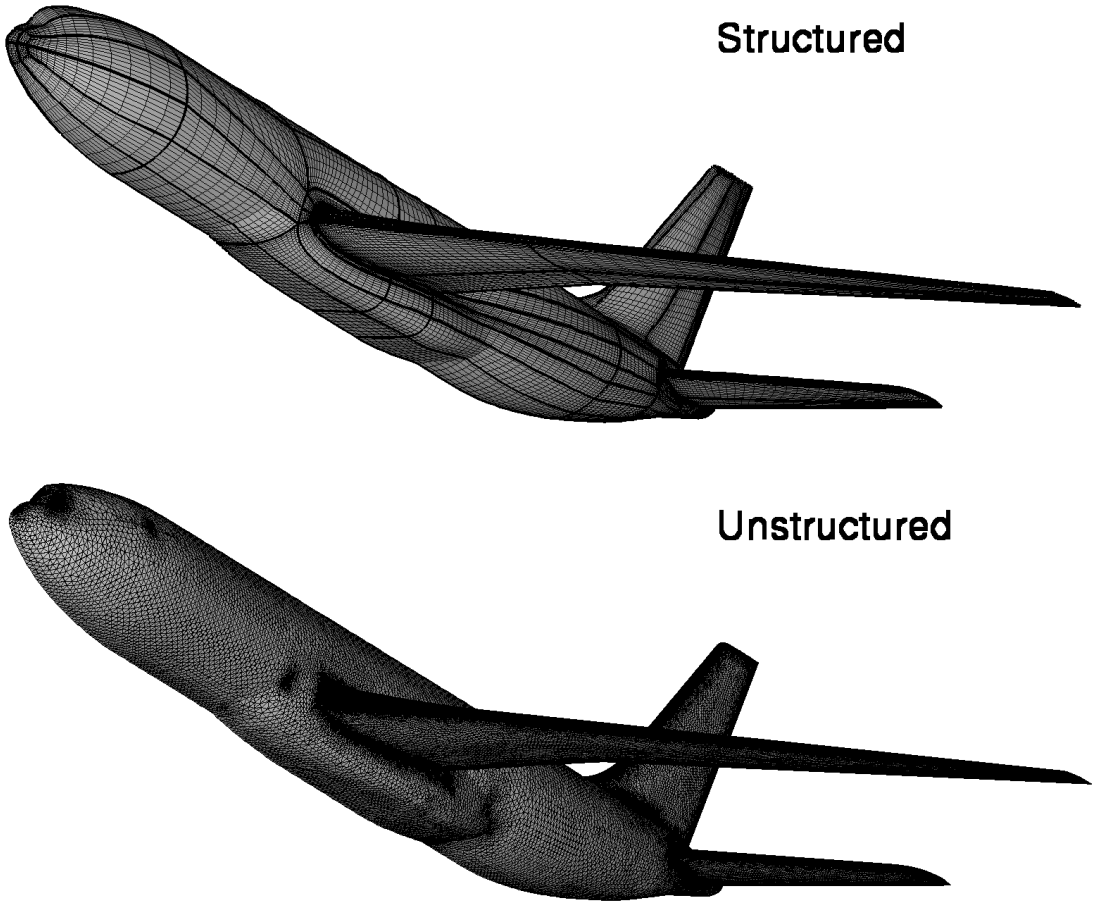

Figure 4.11: Structured and unstructured grids for the DLR-F12 model [182]

due to memory requirements. The COSA solver is under development and a three-dimensional version of the code is not available at the time of writing. Therefore, it was not used for the current configuration.

4.4.2 Results

Results obtained using the PMB and TAU solvers are illustrated in Fig. 4.12. Aerodynamic loops are similar in shape, and in this case the shock motion does not introduce a large distortion from a harmonic time response, when compared with the aerofoil case. For the pitching moment, the contribution from the dynamic derivative is negative, and the slope is also negative. This guarantees that the aircraft is statically and dynamically stable in the longitudinal plane. When comparing Figs. 4.12(b) and 4.12(d), a deviation in the values of the pitching moment at the lower end of the angle of attack range can be detected, indicating some grid dependence in the solutions.

Frequency-domain calculations are illustrated for comparison to the underlying CFD solver in Fig. 4.12. It is observed that the HB solution reproduces the force and mo-

Parameter	Value
M	0.73
α_0	$0.70°$
α_A	$0.50°$
k	0.034
h	$6000\,m$

Table 4.6: Description of the conditions for the DLR-F12 aircraft model

ment dynamic dependence well, whereas the LFD solution underpredicts the hysteresis in the moment data. As shown below, this deficiency of the LFD is attributable to underpredicting the real part of the first harmonic pressure coefficient distribution on the horizontal tail.

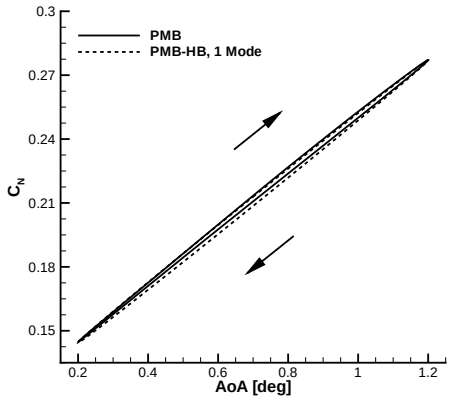

(a) Normal force coefficient, PMB-HB

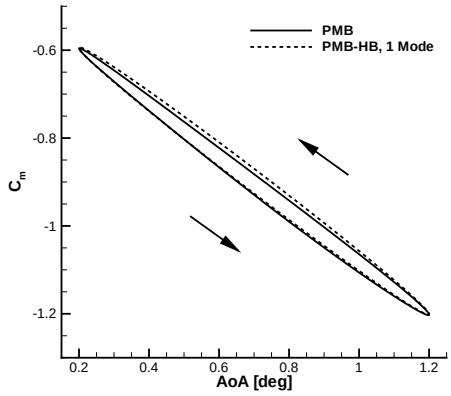

(b) Pitching moment coefficient, PMB-HB

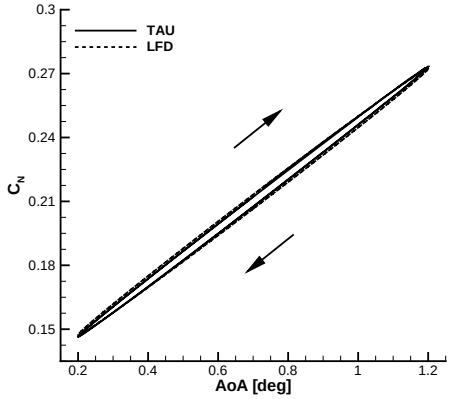

(c) Normal force coefficient, LFD

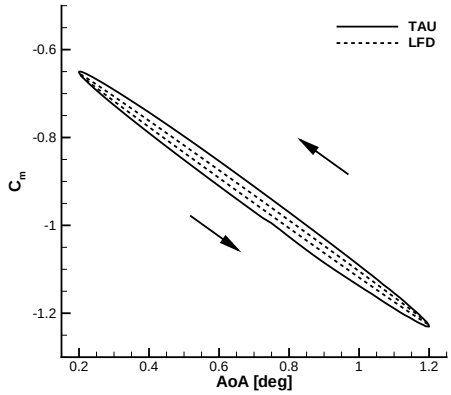

(d) Pitching moment coefficient, LFD

Figure 4.12: DLR-F12 model: normal force and pitching moment coefficients dynamic dependence ($M = 0.73$, $\alpha_0 = 0.70°$, $\alpha_A = 0.50°$, $k = 0.034$, and $h = 6000\,m$)

Stability characteristics relative to the nominal flight conditions are summarized in

	$C_{N\,0}$	C_{N_α}	C_{N_q}	$C_{m\,0}$	C_{m_α}	C_{m_q}
PMB	$2.11\cdot 10^{-1}$	7.59	1.17	$-9.00\cdot 10^{-1}$	-34.7	-20.1
PMB-HB, 1 Mode	$2.11\cdot 10^{-1}$	7.60	1.65	$-8.99\cdot 10^{-1}$	-34.7	-21.6
TAU	$2.10\cdot 10^{-1}$	7.16	2.80	$-9.41\cdot 10^{-1}$	-32.7	-28.1
LFD	$2.10\cdot 10^{-1}$	7.26	3.28	$-9.41\cdot 10^{-1}$	-33.1	-17.7

Table 4.7: DLR-F12 model: normal force and pitching moment coefficient dynamic derivatives ($M = 0.73$, $\alpha_0 = 0.70°$, $\alpha_A = 0.50°$, $k = 0.034$, and $h = 6000\,m$)

Table 4.7, which includes static and dynamic derivatives. Frequency-domain results are in agreement with the respective time-domain results, with the exception of the LFD method in the prediction of the damping-in-pitch term. However, the HB solution performs well, with deviations within 7% of the reference values. While reducing substantially the computational cost compared to a time-accurate solution, one single calculation with a frequency-domain method provides both static and dynamic derivative information. In this case, the frequency-domain solutions based on the HB and LFD methods were obtained in approximately 3% of the time required for a time-accurate simulation. This corresponds to a speed up of about 30. Due to the computational cost of the time-accurate method, an objective evaluation of the computational efficiency of the frequency-domain methods, similar to that outlined for the aerofoil case, was not performed.

Again, the zeroth and first harmonic of the pressure coefficient distribution at a spanwise section $Y/s = 0.148$ is shown in detail in Fig. 4.13. The selected spanwise section intersects both wing and horizontal tail, and features the periodically moving shock wave on the wing. The left and right side of the figure illustrates, respectively, the wing and horizontal tail station. The steady-state solution based on the LFD solver and the time-averaged solution are in good agreement, as seen in Figs. 4.13(a) and 4.13(b). This is indicative of less significant dynamic effects due to the limited oscillatory amplitude. Two considerations are noted for the real part of the first harmonic, shown in Figs. 4.13(c) and 4.13(d). The contribution from the wing is much smaller than the contribution which originates from the horizontal tail. This is expected because of the finite time to convect downstream changes in aircraft attitude. On the horizontal tail, a difference between time-accurate solutions occurs around the suction peak, where the formation of a shock wave of limited extent was observed during part of the sinusoidal cycle. At this section, the LFD solution differs substantially from the reference solution, and this causes the underprediction of the hysteresis in the moment loop observed in Fig. 4.12(d). This shows the limitations of the LFD method in cases featuring dynamic non-linearities not present in the steady-state reference solution. A better correlation of the frequency-domain methods to the underlying method is observed for the imaginary part. As expected, the response on the wing is larger in this case when compared to the real part of the pressure distribution.

Figure 4.13(d) clearly shows that the variations in the computational results due to numerical modelling (PMB and TAU solvers) are more significant than the differences obtained using the PMB-HB and the PMB solver. The HB method is therefore appropriate for the description of periodic unsteady flows. Variations between PMB and TAU results may be attributed to different grids used.

4.5 Conclusions

The current work explored the capabilities and limitations of the Harmonic Balance and Linear Frequency Domain methods in predicting aircraft stability characteristics in a computationally efficient way. Two test cases were presented, a NACA 0012 aerofoil and a wind tunnel aircraft configuration based on the DLR-F12 wind tunnel model. To stress the potential of the frequency-domain methods in conditions of practical interest for aircraft applications, flow conditions were in the transonic regime. For the formation of moving shock waves, the energy of aerodynamic modes redistribute at higher frequencies than the predescribed frequency of motion. While a time-domain calculation supports a continuum of frequencies up to the frequency limits given by the temporal and spatial resolution, the Harmonic Balance and Linear Frequency Domain methods resolve only a small subset of frequencies typically restricted to include one Fourier mode at the frequency at which dynamic derivatives are desired.

For the aerofoil case, it was noted that the Harmonic Balance method was able to predict dynamic derivatives very accurately. For the Linear Frequency Domain method, a loss in accuracy may be experienced whenever amplitudes increase and moving shocks appear. In terms of pressure distribution, convergence to time-accurate results was assessed for an increasing number of Fourier modes in the Harmonic Balance solution. It was demonstrated that the dynamic conditions of the prescribed forced motion moves the average shock position downstream from its static position by nearly twenty per cent of the aerofoil chord. In this case, a loss in accuracy of the Linear Frequency Domain method is expected. Numerical experiments for these cases demonstrate that the Harmonic Balance and Linear Frequency Domain methods are an order of magnitude more efficient than time-accurate methods.

Similar considerations were noted for a three-dimensional configuration based on the DLR-F12 wind tunnel model, for which a comparison of static and dynamic stability derivatives was presented. It was shown that frequency-domain methods are not intended to simply augment static calculations, but rather to complement and replace the static steady-state flow solver for flight and configuration conditions in which stability characteristics are desired. One single calculation with a frequency-domain method provides both static and dynamic derivative information at a fraction of the calculation time of a time-accurate simulation. In this case, the cost of the frequency-domain method was approximately 3% of the unsteady counterpart.

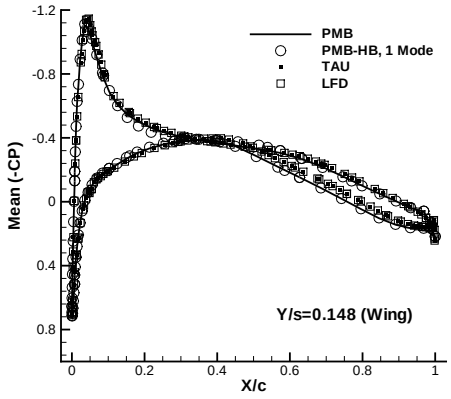

(a) Mean value (wing)

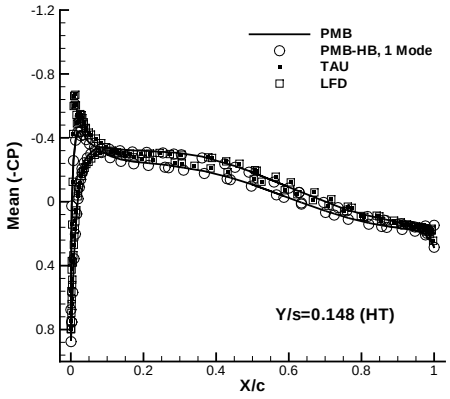

(b) Mean value (horizontal tail)

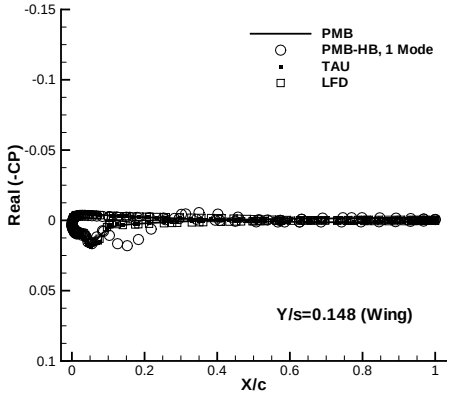

(c) Real part (wing)

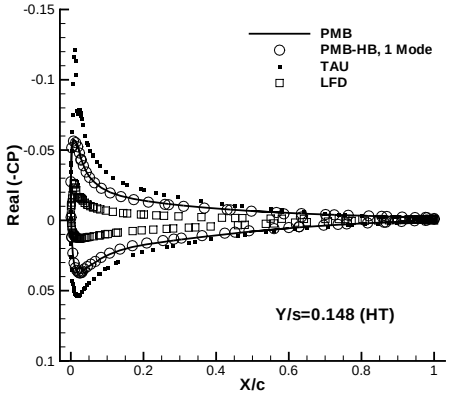

(d) Real part (horizontal tail)

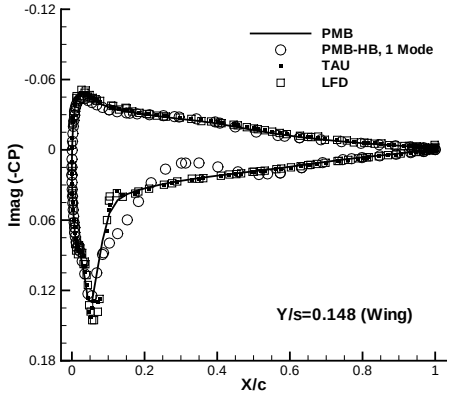

(e) Imaginary part (wing)

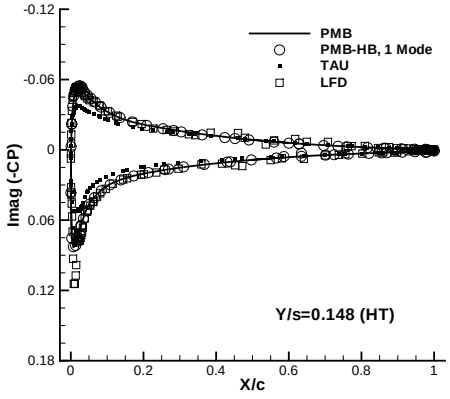

(f) Imaginary part (horizontal tail)

Figure 4.13: DLR-F12 model: zeroth and first harmonic unsteady surface pressure coefficient distribution at $Y/s = 0.148$ ($M = 0.73, \alpha_0 = 0.70°, \alpha_A = 0.50°, k = 0.034$, and $h = 6000\,m$)

This work demonstrates that the Harmonic Balance method is more robust than the Linear Frequency Domain method for cases featuring non-linear flow conditions. In addition to transonic cases herein presented, this was also observed for vortical flows at high angle of attack.

Chapter 5

Reduced Models for Flight Dynamics

5.1 Introduction

Previous work [23,183] substantiated the limitations of tabular models when comparing the predictions to CFD and flight test data, and this motivates the study detailed in this chapter. The objective is to evaluate various reduced models for the representation of non-linear unsteady aerodynamic loads. There are two approaches to model reduction. System identification methods take the response of the system to known inputs, and use this information to build a low-order model. The second approach is to manipulate the full-order system to reduce the cost of calculations. Because the model based on aerodynamic derivatives uses an input/output relationship, in this chapter the focus is on the first approach. This is a sensible choice because the assessment of various reduced models, within the same general class of identification-based methods, can be made. While in Chapter 4 two methods, based on a harmonic balance technique and a linearized solution in the frequency domain, were investigated for the prediction of dynamic derivatives, there is a need for a more general formulation to enhance the current practice in flight dynamics. The manipulation of the full-order residual to create a non-linear reduced order model is being investigated in non-linear aeroelasticity and control of flexible systems [1]. Based on the results presented in [184], the methodology has the potential to be applied to problems of flight dynamics.

In [185], CFD is combined with predictive modelling methods of low complexity to allow efficient and accurate predictions of the stability and control characteristics. The question whether the conventional model based on the concept of aerodynamic derivatives retains sufficient accuracy in predicting unsteady non-linear phenomena to

[1]The work is performed within the EPSRC project entitiled "Nonlinear Flexibility Effects on Flight Dynamics and Control of Next-Generation Aircraft".

pay off the significant initial cost incurred in generating the aerodynamic database will be assessed in this chapter.

The generality realized in a CFD simulation comes at the expense of computational cost. Routine use of high-fidelity CFD simulations can be hindered by the cost of calculations. The analysis of unsteady flows, in particular, is a computational challenge due to the time-step size used to accurately simulate the flow dynamics and the duration time of the simulation. This point motivates the need to assess the benefits and limitations in using low-order models for the prediction of non-linear unsteady aerodynamic loads. A two-dimensional aerofoil is the test case used in this chapter. While retaining complex flow features due to shock-induced phenomena, the time required for the unsteady time-domain simulations is drastically reduced when compared to three-dimensional cases. It is assumed that any consideration on the readiness of the mathematical models can be transferred to the analysis of more complex geometries. Future studies will be performed to demonstrate this point. Low-order mathematical models are used as computationally efficient approximations in place of the non-linear system of equations governing the flow physics. However, the success of a low-order model depends on appropriate information to be generated using unsteady time-domain calculations. The cost for the generation of suitable aerodynamic data and for the selection of appropriate training inputs will be considered.

The chapter continues with a description of the test case and various reduced models are formulated. Model predictions are then compared to the time-accurate solution for a manoeuvre dominated by significant non-linearities. Conclusions are then given.

5.2 Two-Dimensional Case

5.2.1 Numerical Setup

Unsteady time-domain viscous calculations were computed using the PMB and Cobalt (see Section 2.5.4) solvers. For the PMB solver, a refinement study was performed by the author to test that solutions presented were independent of the grid used. Three sets of grids were generated. In all cases, the two-dimensional domain extends fifty chords from the solid wall to the farfield. The coarsest grid had a total number of 50142 points, with 293 nodes on the aerofoil, and 61 in the normal direction. The wake behind the aerofoil was discretized using 59 points in the streamwise direction. A medium grid consisted of 96660 grid points, 377 nodes were distributed on the aerofoil, 90 points were used in the normal direction and 80 along the streamwise direction for the wake. The finest grid was obtained with a total of 125460 grid points. The grids were clustered at the aerofoil surface and the non-dimensional distance y^+ of the first grid point off the wall is less than unity. A time-step refinement study was also performed in combination with each grid using various numbers of time steps per oscillatory cycle, from 16 up

to 1024. Tests verified that convergent solutions were obtained on the medium grid, Fig. 5.1(a), and that 128 time steps per cycle were adequate for temporal accuracy. The viscous grid for use with Cobalt has a rectangular computational domain with the aerofoil geometry centrally located. The farfield is located twenty chords from the solid wall. The unstructured mesh shown in Fig. 5.1(b) has prisms in the boundary layer and tetrahedra elsewhere. This grid has been used in previous work, and further considerations on refinement studies can be found in Ref. [52].

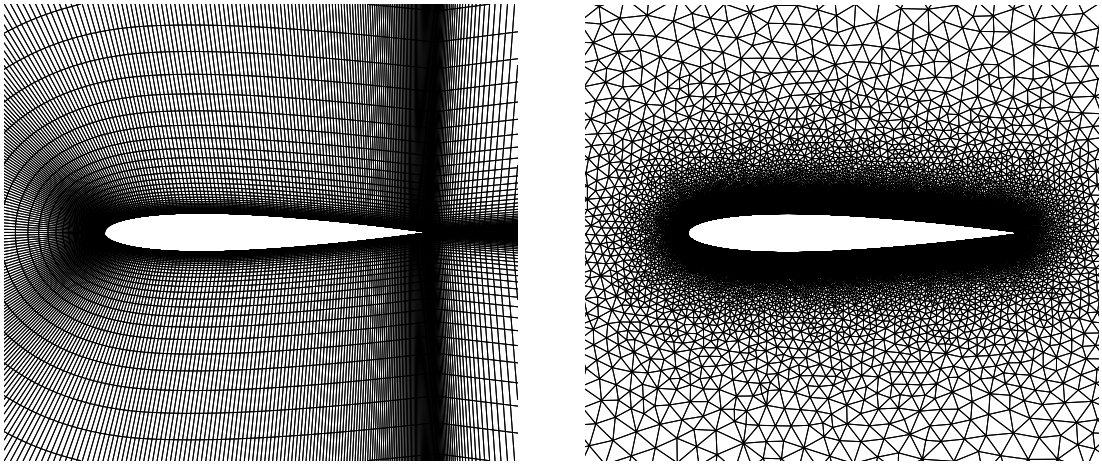

(a) Structured grid, 377×90 (PMB) (b) Unstructured grid (Cobalt)

Figure 5.1: Viscous grids used for the NACA 0012 aerofoil

5.2.2 Validation

Numerical simulations were compared to experimental data of Landon [173] for the AGARD CT2 test case. The corresponding flow conditions are summarized in Table 5.1. In this case, the Mach number is lower than for the AGARD CT5 case (see Table 4.1). The reason to consider the CT2 case for validation is that the aerofoil is forced to oscillate at higher angles of attack, where viscous contributions are more important. Figure 5.2 conveys predictions and measurements of the normal force and pitching moment coefficient. The $k-\omega$ turbulence model was used for the PMB results, whereas the Spalart-Allmaras was used in combination with Cobalt. In all cases, the flow was assumed fully turbulent. There are some variations in the numerical results, which are more evident for the moment case. This is likely because of the use of different turbulence models. Preliminary tests were made with PMB to assess the effects of grid resolution and turbulence modelling on the numerical solutions. It was found that varying the turbulence closures had a larger impact on the solutions than changing the grid resolution. However, the evaluation of differences between numerical simulations is not the objective of this work, which is instead on evaluating the readiness of reduced models.

Parameter	Value
M	0.6
α_0	3.16°
α_A	4.59°
k	0.0811
Re	4.8×10^6

Table 5.1: Description of the AGARD CT2 conditions for the NACA 0012 aerofoil [173]

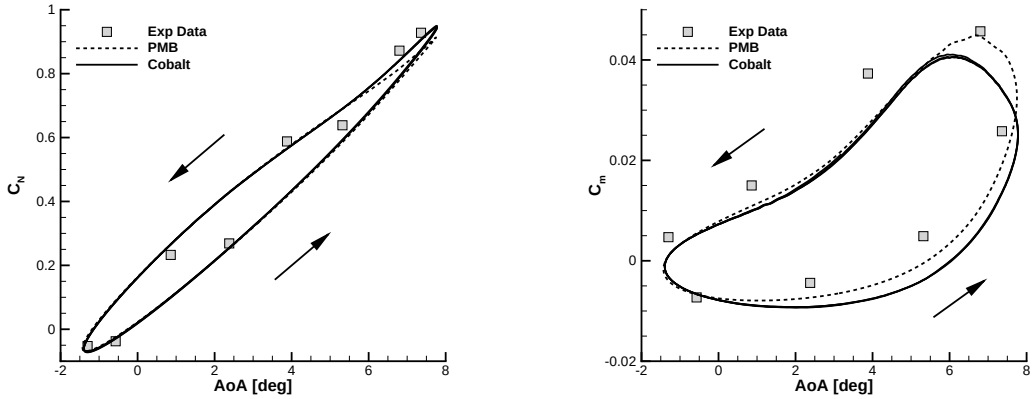

(a) Normal force coefficient

(b) Pitching moment coefficient

Figure 5.2: NACA 0012: predictions of unsteady time-accurate viscous solutions ($M = 0.6$, $\alpha_0 = 3.16°$, $\alpha_A = 4.59°$, $k = 0.0811$, and $Re = 4.8 \times 10^6$); experimental data from Landon [173]

5.2.3 Large Amplitude Manoeuvre

The training data for the generation of reduced models were obtained before the manoeuvre to be predicted was made. A pitching case was considered around zero degrees angle of attack, $\alpha_0 = 0.0°$, at Mach number of 0.764 and reduced frequency $k = 0.10$. A Reynolds number of 3 million was assumed. The oscillatory amplitude, α_A, was taken to vary between 0° and 10°, and represents the independent parameter of the problem. These conditions correspond to a popular modelling case described in the literature, see for example Refs. [17, 186], but experimental data are not available. Once reduced models were constructed, the test case used to compare the model predictions to the time-accurate solution was defined. Results presented are for an oscillatory amplitude of 8.5°.

Shown in Figs. 5.3(a) and 5.3(b) is the normal force and pitching moment dynamic dependence computed using a time-accurate solution, which is the reference solution for the reduced models. The initial transient was removed from the numerical solutions, and two arrows indicate the time evolution. The flow on the upper surface of the aerofoil is dominated by a shock which moves downstream for increasing angles. The

shock wave becomes stronger and interacts with the boundary layer. The boundary layer immediately after the shock separates, and this condition is shown in Fig. 5.3(c) as the separation becomes visible. At the largest angle of attack, there is a large separated area extending from the shock to the trailing edge, Fig. 5.3(d). During the downstroke motion, the flow reattaches and the same pattern is repeated on the opposite side of the aerofoil. It was found that changes in sign of the instantaneous value of C_{m_α} during the oscillatory motion are related to the appearance/disappearance of flow separation.

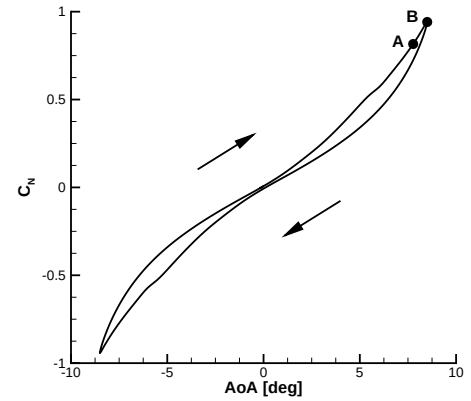

(a) Normal force coefficient

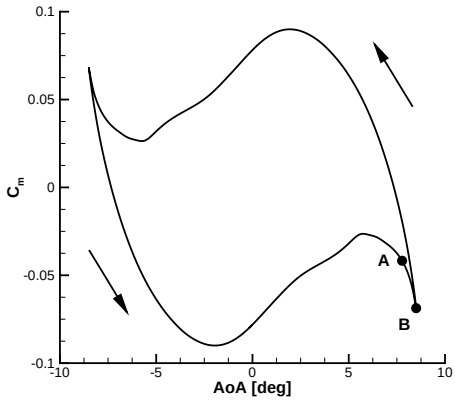

(b) Pitching moment coefficient

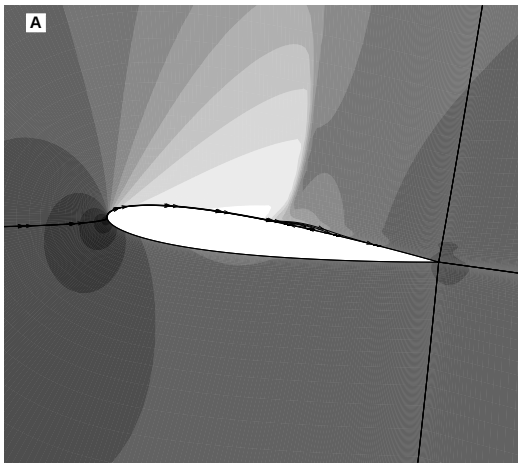

(c) $\alpha = 7.8°$

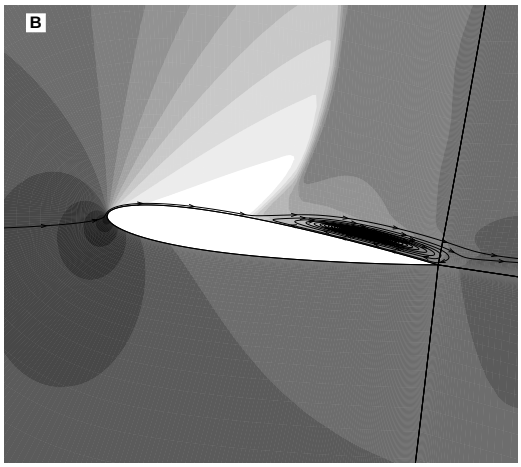

(d) $\alpha = 8.5°$

Figure 5.3: NACA 0012: unsteady time-accurate viscous solutions for the manoeuvre to be predicted ($M = 0.764$, $\alpha_0 = 0.0°$, $\alpha_A = 8.5°$, $k = 0.0811$, and $Re = 3.0 \times 10^6$); in (c) and (d), pressure contour

5.3 Model Formulation

Various low-order models are now introduced. For a description of the aerodynamic model based on aerodynamic derivatives, which represents the reference formulation

used in flight dynamics, the reader is referred to Section 2.2.

5.3.1 Volterra Series

The Volterra theory is well-known in the theory of non-linear systems [187], and it has been applied to systems involving transonic aerodynamics [188]. A brief overview on the applications of the Volterra theory can be found in Section 1.2.4.

For convenience, denote each aerodynamic coefficient, $y = C_i$ for $i = L, D, m$. The output of a continuous-time, casual, time-invariant, fading memory system in response to an input, $x(t)$, is formulated as

$$y(t) = \Psi(x(t)) = \sum_{i=1}^{p} \mathbb{H}_i(x(t)) \tag{5.1}$$

The output response, $y(t)$, is modeled using the p-th order Volterra series. The term $\mathbb{H}_i$ represents the i-th order Volterra operator, which is defined as an i-fold convolution between the input, $x(t)$, and the i-th order Volterra kernel, H_i.

$$\mathbb{H}_i(x(t)) = \int_{-\infty}^{t} \dots \int_{-\infty}^{t} H_i(t - \tau_1, t - \tau_2, \dots, t - \tau_i) \prod_{n=1}^{i} x(\tau_n)\, d\tau_n \tag{5.2}$$

For incompressible flow, unsteady aerodynamic loads are often expressed as a function of the angle of attack and its time derivatives [189]. Based on this consideration, the single-input Volterra model in Eq. (5.1) may be inadequate even for the representation of loads in the linear aerodynamic regime. For oscillations about the pitch axis, the relevant external inputs are

$$\mathbf{x}(t) = \big(\alpha(t), \dot{\alpha}(t), \ddot{\alpha}(t)\big) \tag{5.3}$$

A multi-input Volterra series is then formulated as

$$y(t) = \Psi\big(x_1(t), x_2(t), \dots, x_m(t)\big) = \sum_{i=1}^{p} \mathbb{H}_i^m \tag{5.4}$$

The term $\mathbb{H}_i^m$ is the multi-input Volterra operator defined as a m^p-fold summation of p-fold convolution integrals between the inputs and the p-th order multi-input Volterra

kernels [58]. The output response up to second order is rewritten as

$$y(t) = \sum_{j=1}^{m} \int_{-\infty}^{t} H_1^{x_j}(t-\tau)\, x_j(\tau)\, d\tau + \sum_{j_1=1}^{m} \sum_{j_2=1}^{m} \int_{-\infty}^{t} \int_{-\infty}^{t} H_2^{x_{j_1}, x_{j_2}}(t-\tau_1,\, t-\tau_2)\, x_{j_1}(\tau_1)\, x_{j_2}(\tau_2)\, d\tau_1\, d\tau_2 + \mathcal{O}\left(|x|^3\right) \tag{5.5}$$

Note that the superscripts in Eq. (5.5) identify to which inputs the kernel corresponds. Consider, for example, the second-order kernel $H_2^{x_{j_1}, x_{j_3}}$, which correlates the inputs x_{j_1} and x_{j_3}. Note that the second and higher-order kernels are symmetric with respect to the arguments, $H_2^{x_{j_1}, x_{j_3}} = H_2^{x_{j_3}, x_{j_1}}$.

The identification of the Volterra kernels is performed using an unsteady time-domain simulation as the source of the data. The CFD solution is discrete in time, and the time-step is indicated by Δt^*. Denote $x[n] = x(n\,\Delta t^*) = x(t)$. The discrete-time representation of Eq. (5.5) is

$$y[n] = \sum_{j=1}^{m} \times \sum_{k=0}^{n} H_1^{x_j}[n-k]\, x_j[k] + \sum_{j_1=1}^{m} \sum_{j_2=1}^{m} \times \sum_{k_1=0}^{n} \sum_{k_2=0}^{n} H_2^{x_{j_1}, x_{j_2}}[n-k_1,\, n-k_2]\, x_{j_1}[k_1]\, x_{j_2}[k_2] + \mathcal{O}\left(|x|^3\right) \tag{5.6}$$

The identification of discrete-time Volterra kernels involves the resolution of an overdetermined system. Values of aerodynamic coefficients and the time-history of the motion variables are known from the CFD simulation used as training input. Let $\mathbf{y} = (y[0],\, y[1],\, \ldots,\, y[n])^T$ denote each aerodynamic load computed using CFD, and let $\mathbf{A}$ contain the permutations of input parameters relevant to the unsteady motion. Equation (5.6) can be recast in the form

$$\mathbf{y} = \mathbf{A}\,\mathbf{b} \tag{5.7}$$

where the vector $\mathbf{b}$ contains the unknown Volterra kernels. The matrix $\mathbf{A}$ is in general non-square, with more rows than columns. Several numerical methods are available to solve least squares problems, e.g., direct inversion of $\mathbf{A}^T\mathbf{A}$, Gauss elimination, Moore-Penrose generalized inverse approach and the QR factorization. However, the Moore-Penrose approach and the QR factorization are more accurate than the Gaussian elimination and the direct inversion solutions. The cost of the QR factorization is $\mathcal{O}\left(n^2\right)$, and the Moore-Penrose inversion involves $\mathcal{O}\left(n^3\right)$ operations. Note that computational resources attributable to the identification of the Volterra kernels grow exponentially

with order. Increasing the order of the Volterra series introduces a requirement for a training manoeuvre of sufficient duration. A remedy to this is the use of a simplified form of the kernel parametric structure. Following, for example, Ref. [59]

$$H_p^{x_{j_1}, x_{j_2}, \ldots, x_{j_p}} [n - k_1, n - k_2, \ldots, n - k_p] = 0 \qquad (5.8)$$
$$\text{for } k_1 \neq k_2 \neq \ldots \neq k_p$$

all off-diagonal terms of the kernel are set to zero. Note that the above form of the Volterra series, with an attendant loss of generality, was not used for the results presented.

The Volterra kernels are first identified from Eq. (5.7) solving for $\mathbf{b}$, with $\mathbf{y}$ and $\mathbf{A}$ being known for a training manoeuvre. The matrix $\mathbf{A}$ is then recomputed for a novel manoeuvre, and the low-order model in Eq. (5.7) is used to predict the resulting unsteady aerodynamic loads in place of the full-order system.

5.3.2 Surrogate-Based Recurrence-Framework

The set of non-linear equations describing the CFD system can be interpreted as a general representation of a non-linear time-invariant discrete-time dynamical system. The state vector consists of the conservative variables, $\mathbf{W}$, and its size is proportional to the number of grid points. In this study, the aerodynamic loads form the vector of outputs, which are not only a function of the instantaneous values of the inputs, but also a function of the time history of the inputs.

To generate a computationally efficient approximation of the unsteady aerodynamic loads without solving the expensive CFD equations, the form of a dynamical system is assumed [17]. When the state vector of the full-order system is finite in dimension, the following non-linear system is equivalent to the unsteady CFD equations

$$y(t) = \Phi\big(\mathbf{x}(t), \mathbf{x}(t - \Delta t), \ldots, \mathbf{x}(t - m\,\Delta t), y(t - \Delta t), \ldots, y(t - n\,\Delta t)\big) \qquad (5.9)$$

where $\mathbf{x}$ takes the form of Eq. (5.3). The function Φ maps the inputs to the outputs. The terms m and n represent the number of previous values of the external inputs and outputs, respectively, influencing the output at the current time instant. These parameters account for time-history effects and phase-lag in the flow development.

Central to the generation of the reduced-order model is the computation of the function Φ. Without a closed-form analytical expression, a numerical approximation of Φ is constructed using a number of CFD solutions. For the pitching aerofoil case, see Eq. (2.16), any motion can be expressed as function of three parameters, e.g., α_0, α_A, and k. These independent variables form a parameter space, which represents the envelope of all possible flow conditions in which the aerofoil configuration is expected to operate. To generate a consistent set of unsteady aerodynamic loads in response

to a given aerofoil motion time history, the training cases at which CFD solutions are calculated should be representative of the expected flow conditions. Several design of experiment methods are available in the literature. A description of the kriging-based framework used in this study is detailed in Ref. [81]. Let N_T be the number of training cases at which CFD solutions are available. Each training case consists of different combinations of the independent parameters,

$$\mathbf{x}_i = \left(\alpha_i(t), \dot{\alpha}_i(t), \ddot{\alpha}_i(t)\right) \qquad \text{for } i = 1, \ldots, N_T \tag{5.10}$$

and the corresponding aerodynamic loads are indicated by $y_i(t)$. The approximation of the function Φ is obtained by interpolating the sampled data in the form of an input/output relationship. Several interpolation methods are available in the literature, and two of these have been used in the present study. Kriging interpolation is a common choice, see Section 2.3, but for increasing number of independent parameters the problem can result to be ill-conditioned. An alternative approach is the multi-linear interpolation technique, see Appendix C, which is in general faster than the kriging interpolation.

5.3.3 Indicial Function

The buildup in the aerodynamic loads in response to a unit step in one of the inputs can be evaluated by convolution. Let $H(t)$ indicate the Heaviside step function, or the unit step function, defined as

$$H(t) = \begin{cases} 1.0 & \text{for} \quad t \geq 0 \\ 0.0 & \text{for} \quad t < 0 \end{cases} \tag{5.11}$$

The unit response, or indicial admittance, is denoted by $\mathcal{A}(t)$. Assuming a linear relationship between the forcing function and the output, the airloads are defined as the convolution or Durhamel's superposition [190] of the indicial response with the derivative of the forcing function, $f(t)$.

$$y(t) = f(0)\,\mathcal{A}(t) + \int_0^t \frac{d\,f(\tau)}{d\tau}\,\mathcal{A}(t-\tau)\,d\tau \tag{5.12}$$

This model can approximate any finite-memory, time-invariant, single input/single output and continuous linear system [191]. The indicial response functions are used as a fundamental approach to represent the unsteady aerodynamic loads [37, 38]. Let C_{j_α} and C_{j_q} be the time response in the unsteady aerodynamic loads due to a step change in the angle of attack, α, and angular velocity, q. If these functions are known, then

the unsteady airloads at time t can be obtained as

$$C_i(t) = C_{i0} + \int_0^t \frac{d\alpha(\tau)}{d\tau} C_{i_\alpha}(t-\tau)\, d\tau + \int_0^t \frac{dq(\tau)}{d\tau} C_{i_q}(t-\tau)\, d\tau \qquad (5.13)$$
$$\text{for } i = L, D, \text{ and } m$$

These models approximate the unsteady lift and pitching-moment in the linear regimes of the flight envelope. For non-linear aerodynamics, the indicial response is computed at several values of the angle of attack, and this adds a considerable computational cost to the construction of the model. Linear indicial functions were used in the results presented. Further details on linear indicial aerodynamics can be found in Appendix B, where the calculation of the indicial response to a step change in any motion parameter and for the penetration into an arbitrary gust field are also discussed. Being a mathematical concept, experimental measurements of the step response are practically non-existent, and a modification to an existing CFD code is required for a correct determination of the indicial response. The author implemented a new functionality in the University of Liverpool PMB solver to calculate the indicial response to motion inputs and gust perturbations. More details are given in Appendix B.

5.3.4 Radial Basis Function

In this approach, the unsteady aerodynamic loads are approximated by learning an input-output mapping from a set of training data [192].The reconstructed state space model is presented in Eq. (5.9). The term Φ is a vector-valued non-linear function that maps the inputs to the output. The terms m and n are integers representing the past values in the output and input, respectively. The mapping function, Φ, is learned by a Radial Basis Function Neural Network (RBFNN). The remaining problem is how to choose $n = m$ such that the reconstructed model accurately represents the state-space model. For the results presented, the value of n is selected using "trial and error" attempts. Design of experiments are often used to select N_T combinations of these variables for training purposes. However, such an approach often needs a large value of N_T to cover the important regimes of the regressor space of the input variables. Ghoreyshi et al. [192] reduced the number of manoeuvre simulations using the design of new training manoeuvres. This approach was also used in this study.

5.4 Numerical Results

The model based on aerodynamic derivatives, the Volterra model, and the surrogate-based recurrence-framework model were generated using the PMB solver. The generation of models based on the indicial and radial basis function was made with Cobalt.

Predictions are compared to the time-accurate solution of the CFD solver used to create the model.

5.4.1 Model based on Aerodynamic Derivatives

Dynamic derivatives are illustrated in the upper part of Fig. 5.4 at the reduced frequency of the manoeuvre to be simulated, $k = 0.10$, and for several values of the oscillatory amplitude, α_A. Values of amplitude of the forced motion are 0.1°, 0.5°, 3.0°, and 5.0°. The force data, shown in Fig. 5.4(a), are negative for small values of the angle of attack, and become positive for larger values. The change in sign is observed to occur between 2° and 4° in all cases. At the lower and higher ends of the angle of attack range dynamic derivatives are similar in value independently of the amplitude α_A. This is attributed to the flow features at these conditions. For a small mean angle of attack, the flow is attached and the shock motion is the dominant non-linear effect. For a larger mean value, the flow is likely to be separated, and the separation is now the dominant effect. The largest differences in the results presented are found at intermediate values of the mean angle of attack, where shock-induced separation is observed. The damping-in-pitch, shown in Fig. 5.4(b), is negative throughout the angle of attack range. However, for the small amplitude case, dynamic derivatives have an erratic behaviour and show an increase in damping about a mean angle of 2°.

Based on this comparison, dynamic derivatives present a dependence on the oscillatory amplitude of the forced motion. For smaller amplitudes, spikes are found at median values of the angle of attack, whereas for the larger amplitude case, a continuous decrease/increase is noted. This is further investigated in Fig. 5.4, where results for the smallest and largest values of the oscillatory amplitude are presented for several values of the reduced frequency ($k = 0.05$, 0.10, and 0.15). For the smallest amplitude ($\alpha_A = 0.1°$), a change in sign in the force damping derivative shown in Fig. 5.4(c) is noted between 2° and 4°. The force data largely depend on the reduced frequency at small values of the mean angle of attack. In fact, increasing the reduced frequency primarily affects the mean slope of the force data (not shown), with a negligible effect on the hysteresis. At larger values of the angle of attack, the values are positive and similar for all reduced frequencies. In the case of the damping-in-pitch, shown in Fig. 5.4(d), the results computed for various values of the reduced frequency are similar. Next, the aerodynamic derivatives for the case in which the aerofoil oscillates with pitch amplitude of 5.0° are presented in Figs. 5.4(e) and 5.4(f). For the force data, a continuous increase is seen throughout the angle of attack range, whereas the moment data continuously decrease.

The aerodynamic information presented above were used in combination with the non-linear quasi-steady aerodynamic model in Eq. (2.2) to predict the unsteady loads for the manoeuvre selected. The dynamic dependence of the force and moment coef-

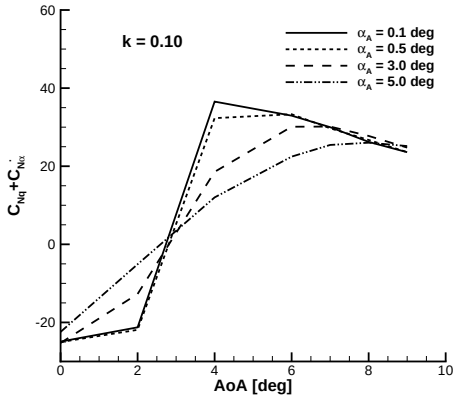

(a) Normal force coefficient damping

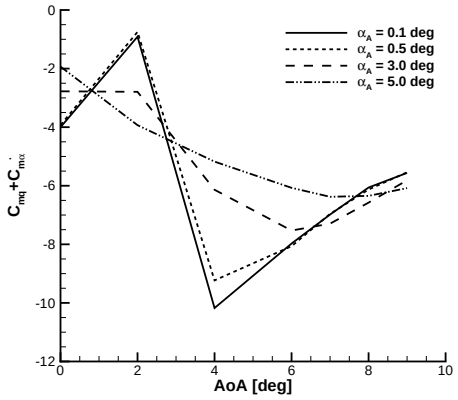

(b) Pitching moment damping coefficient

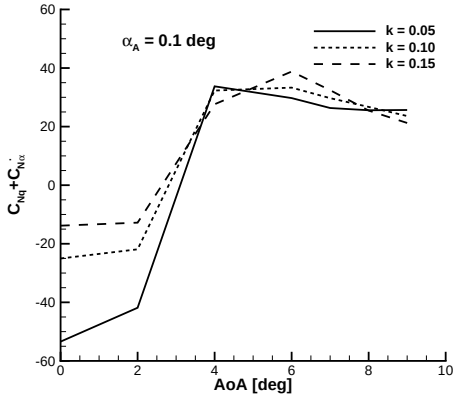

(c) Normal force coefficient damping

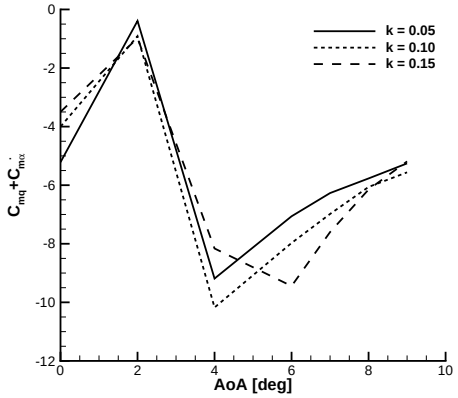

(d) Pitching moment damping coefficient

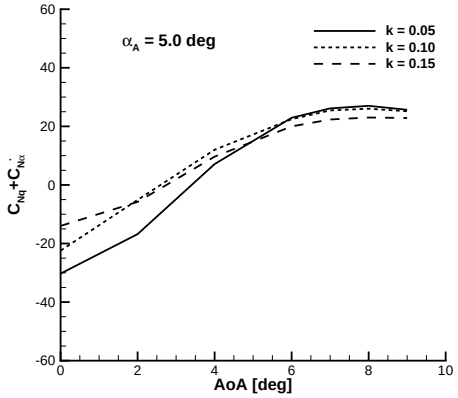

(e) Normal force coefficient damping

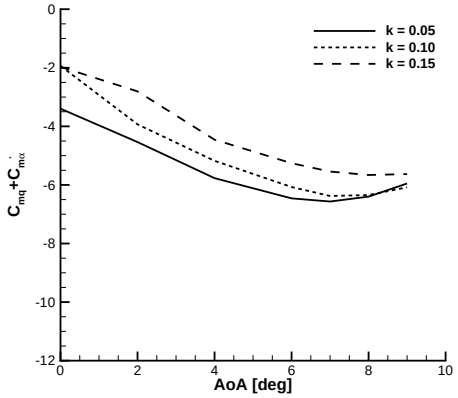

(f) Pitching moment damping coefficient

Figure 5.4: Dynamic derivatives for the NACA 0012 aerofoil ($M = 0.764$ and $\alpha_0 = 0.0°$); in (a)-(b), $k = 0.10$ and several values of amplitude; in (c)-(d), $\alpha_A = 0.1°$ and several values of reduced frequency; in (e)-(d), $\alpha_A = 5.0°$ and several values of reduced frequency

ficients shown in the upper part of Fig. 5.5 were computed using aerodynamic data estimated at the same reduced frequency of the manoeuvre, $k = 0.10$. In this case, the scatter indicates variations attributed to varying the amplitude of the forced motion. A cross-over point is detected in the force dynamic dependence at an angle of attack of about 3°, however not observed in the time-accurate solution. However, the model provides misleading results, and the agreement is poor for both force and moment data throughout the oscillatory cycle. The unsteady responses in the remaining figures illustrate the effects of varying the oscillatory amplitude at which dynamic derivatives were estimated. The results were obtained, respectively, for an amplitude of 0.1° and 5.0°. In both cases, the scatter is representative of variations attributable to reduced frequency effects. For the smallest amplitude case, see Figs 5.5(c) and 5.5(d), the agreement is poor and the force data exhibit a large dependence on the reduced frequency. Increasing the oscillatory amplitude has a positive effect of moving the model predictions closer to the reference solution, see Figs 5.5(e) and 5.5(f). Reduced frequency effects are moderate in this case but in all cases predictions are not representative of the time-accurate solution.

While for a two-dimensional aerofoil a systematic study on the dependencies of dynamic derivatives can be made, results demonstrate that the model predictions may be misleading. A point to consider is that aerodynamic data obtained from forced motions at a small amplitude do not necessarily provide a better agreement to the unsteady CFD solution than using aerodynamic information obtained for a larger amplitude case. In fact, the solution computed for a small amplitude is similar to a time-linearized solution which capture the flow behaviour near the point at which the calculation is done. This is in general inadequate for studies of flight dynamics because the aircraft may experience large excursions from the reference point. Performing a forced motion at a larger amplitude exposes the flow to some non-linearities, and this may improve somewhat the predictions. These observations are in agreement with the conclusions given in Chapter 4, where the predictive limitations of a linearized technique were discussed.

5.4.2 Volterra Series

For the identification of the Volterra kernels, a training case was run at the reduced frequency of the manoeuvre to be simulated. The oscillatory amplitude, being an independent parameter, was varied linearly from 0° up to 10°, and back to 0°. The duration time of the training data was equivalent to six periods. Kernels up to third order were retained in the model. However, not all kernels need to be identified because the resulting aerodynamic loads, for a symmetric aerofoil forced to oscillate around zero degrees mean angle of attack, are odd functions of the angle of attack change. For the

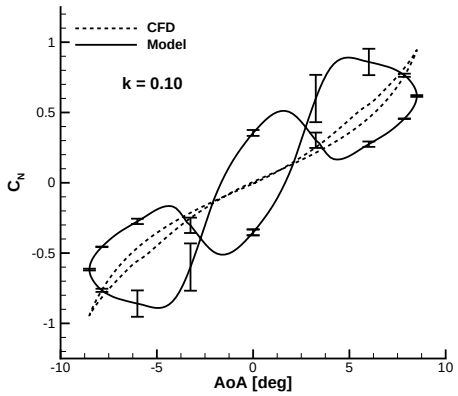

(a) Normal force coefficient

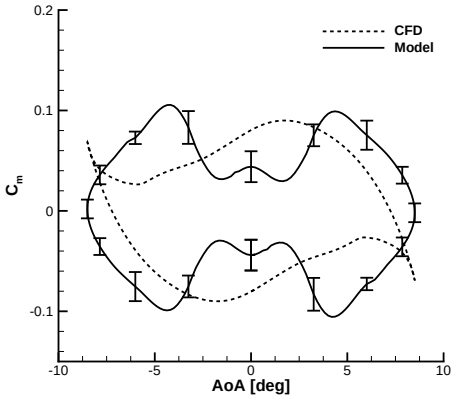

(b) Pitching moment coefficient

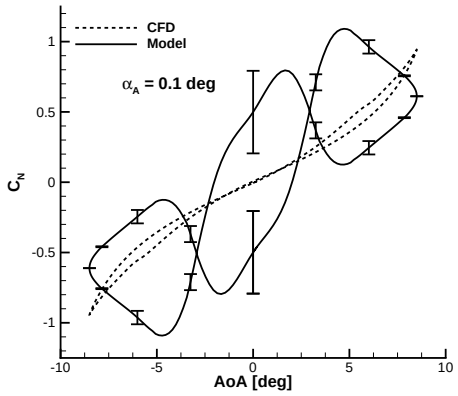

(c) Normal force coefficient

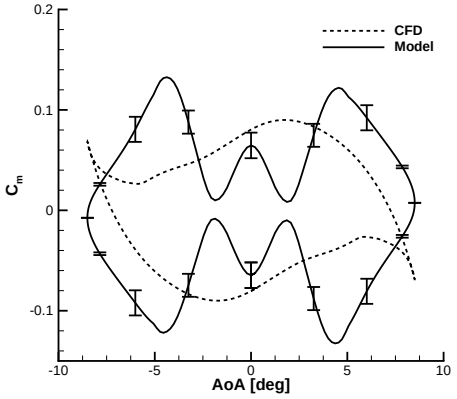

(d) Pitching moment coefficient

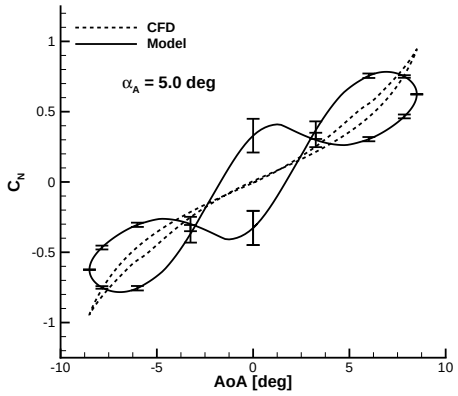

(e) Normal force coefficient

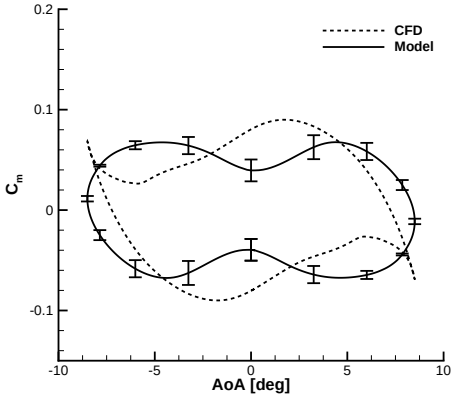

(f) Pitching moment coefficient

Figure 5.5: Non-linear mathematical model and unsteady CFD for a large amplitude manoeuvre ($M = 0.764$, $\alpha_0 = 0.0°$, $\alpha_A = 8.5°$, and $k = 0.10$); in (a)-(b), dependence on the oscillatory amplitude at reduced frequency $k = 0.10$; in (c)-(d), dependence on the reduced frequency at oscillatory amplitude $\alpha_A = 0.1°$; in (e)-(f), dependence on the reduced frequency at oscillatory amplitude $\alpha_A = 5.0°$

flow conditions considered in this chapter, the following kernels were retained

$$\begin{array}{llll} H_1^{\alpha} & H_1^{\ddot{\alpha}} & & \\ H_2^{\alpha,\dot{\alpha}} & H_2^{\dot{\alpha},\ddot{\alpha}} & & \\ H_3^{\alpha,\alpha,\alpha} & H_3^{\alpha,\dot{\alpha},\dot{\alpha}} & H_3^{\dot{\alpha},\dot{\alpha},\ddot{\alpha}} & H_3^{\alpha,\alpha,\ddot{\alpha}} \end{array} \tag{5.14}$$

The term k in Eq. (5.6) approximates time-history effects. For the kernel H_1^{α}, $k = 3$, whereas for the remaining first order kernels it was set to 2. For the second order kernel relating the angle of attack to its time derivative, $k = 1$. The value $k = 0$ was set for all of the order kernels shown in Eq. 5.14.

Figure 5.6 compares the aerodynamic coefficients from the time-accurate solution and from the Volterra model. For the force data, the model predicts a virtually linear response despite kernels up to third order were retained. While there are differences for the moment coefficient, the model prediction provides a reasonable approximation to the reference solution. The value of k for each kernel was optimum in the sense that, for a given model, the error norm was minimized.

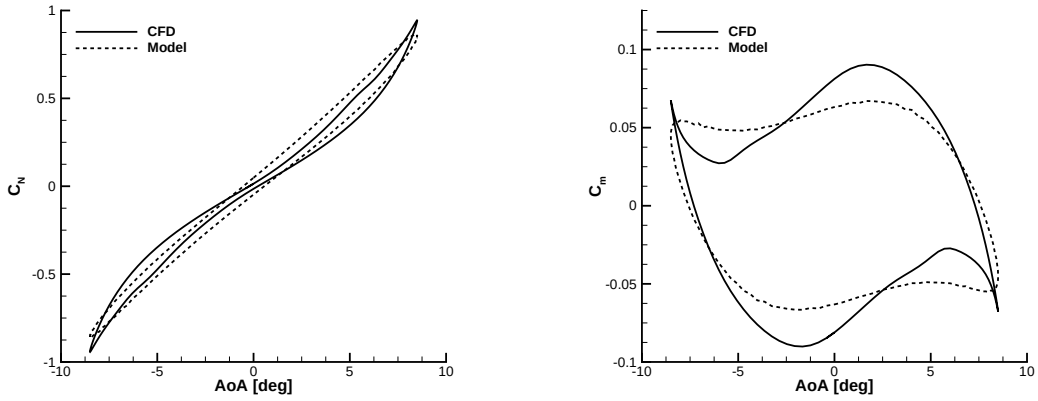

(a) Normal force coefficient

(b) Pitching moment coefficient

Figure 5.6: NACA 0012: predictions of pitching moment dynamic dependence ($M = 0.764$, $\alpha_0 = 0.0°$, $\alpha_A = 8.5°$, and $k = 0.10$); "Model" refers to the discrete-time multi-input Volterra model

For the case presented, the Volterra model was found to perform better than the model based on aerodynamic derivatives. The robustness of the model is however a crucial question which needs further investigations. A key point in the model identification is the selection of an appropriate training motion. In general, a suitable training manoeuvre is designed to allow sufficient representative data to create a low-order model with predictive capabilities within a desired parameter space. Previous research focused on training manoeuvres development [51, 57], but it was argued that an appropriate manoeuvre used to predict stability and control characteristics is not primarily given

by its frequency content or power density spectra [52]. As the low-order model is used to predict the aerodynamic behaviour within certain flight and control states, a sufficient coverage of the parameter space should be realized by the design manoeuvre to be effective. The downside of this consideration is the likely non-physical nature of the training input used for generation of the Volterra model, which limits the applicability of the model to numerical simulations.

5.4.3 Surrogate-Based Recurrence-Framework

Shown in Fig. 5.7 is the time evolution of the aerodynamic coefficients for several values of the oscillatory amplitude. The parameter space, in this case, is one-dimensional and varies between 0° and 10° with a step increment of 0.25°. The response surfaces were obtained using 10 CFD solutions, and the remainder of the parameter space was filled out with the use of kriging interpolation. A first CFD calculation was made for the largest value of the amplitude, and successive calculations were sampled according to the RMS criterion. The trivial solution corresponding to a null amplitude with no aerofoil motion was not run, and to avoid extrapolation, aerodynamic coefficients were set to zero. Increasing variations in the aerodynamic coefficients for increasing oscillatory amplitude are noted. However, the degree of non-linearity of the unsteady loads with respect to the applied sinusoidal motion is not attainable from the surface responses.

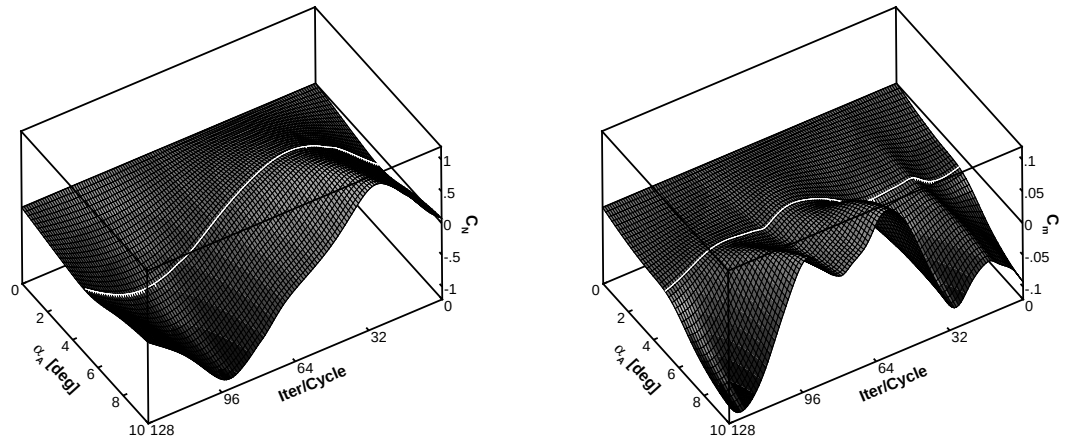

(a) Normal force coefficient

(b) Pitching moment coefficient

Figure 5.7: Response surfaces of the time evolution of aerodynamic coefficients throughout the parameter space of oscillatory amplitude, α_A ($M = 0.764$, $\alpha_0 = 0.0°$, and $k = 0.10$); the solid curve indicates the solution at an amplitude of 5 deg

To demonstrate the appearance of non-linearities, Fig. 5.8 conveys the dynamic dependence of the aerodynamic coefficients as a function of the instantaneous angle of attack. For clarity, curves are plotted for a one-degree increment in the oscillatory

amplitude. Linear behaviour is found in the force data up to 6°, whereas for larger amplitude values the loops become distorted from the shape of an ellipse. Note also that, in contrast with other results, the force loop for an oscillatory amplitude of 8° has a vanishing hysteresis and this is likely to impact the model prediction when reducing the number of training cases, as shown below. For the moment dynamic dependence, a localized non-linearity at both ends of the amplitude range is first noted, which is similar in shape to that computed for the AGARD CT5 conditions in Fig. 4.2. The upswing and downswing curves intersect each other for values of amplitude between 5° and 7°, and for larger values the cross-over points disappear. These features are indicative of a flow around an aerofoil which experiences various physical conditions.

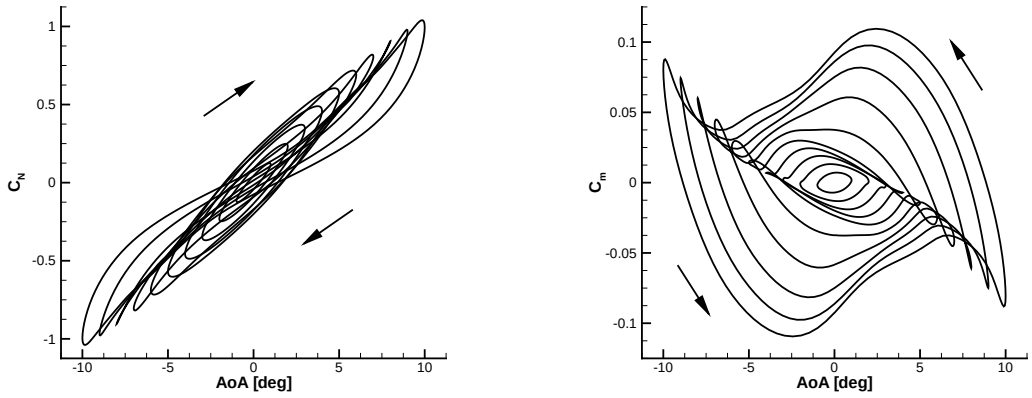

(a) Normal force coefficient

(b) Pitching moment coefficient

Figure 5.8: Aerodynamic coefficients dynamic dependence for several value of oscillatory amplitude ($M = 0.764$, $\alpha_0 = 0.0°$, and $k = 0.10$); curves are plotted every one-degree increment in amplitude

Figure 5.9 compares the dynamic dependencies obtained using the time-accurate solution and the predictive model. Models were created retaining various numbers of training cases. For the model based on 10 training cases, predictions are virtually identical to the unsteady solution. The dependence of the solution when varying the values of m and n appearing in Eq. (5.9) was first investigated. The value of n was found to have the largest effect on the solution and, for a given value of m, predictions degraded for $m \leq n$ in all cases. For the results presented, $m = 4$ and $n = 2$ proved adequate to approximate time-history effects. Next, a new model was generated recursively by removing the last training case included in the existing model. As shown in figure, a model created using 5 training cases is a good approximation to the reference solution. It can be argued, however, that the quality of the prediction depends on the location of sample points within the parameter space. In this case, three samples were located at the minimum, median and maximum values of the amplitude, and the

remaining two points were in the lower- and upper-half of the parameter range. For a more objective evaluation of the model predictions, a model was created using the three samples at the minimum, median and maximum values of the amplitude. The sample at zero amplitude has little or no effect on the prediction, being the furthest from the amplitude at which the manoeuvre is simulated. For the moment case, the model reproduces well the time-accurate solution. Differences in the force data are seen during part of the cycle and are indicative of the appearance of non-linearities for amplitudes larger than 5° (see Fig. 5.8). A consideration is that the validity of a predictive model, without any physical mechanism governing the flow development, is limited to the training dataset used to create it. Because the input data are reformatted when creating the prediction, the amount of information is critical.

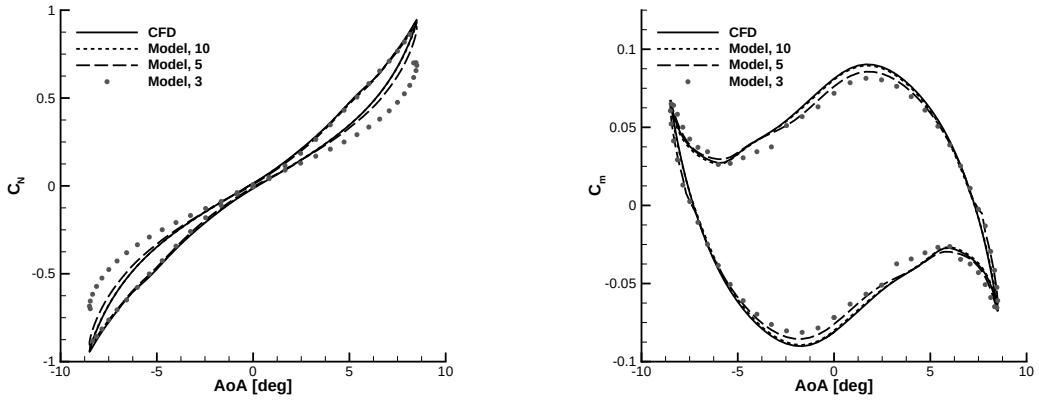

(a) Normal force coefficient

(b) Pitching moment coefficient

Figure 5.9: Model predictions and unsteady CFD for a large amplitude manoeuvre ($M = 0.764$, $\alpha_0 = 0.0°$, $\alpha_A = 8.5°$, and $k = 0.10$); "Model" refers to the surrogate-based recurrence-framework

Good predictions presented above should be confirmed by results for a higher-dimensional problem. The extension to include the dependencies on the reduced frequency and mean angle of attack is an interesting option.

5.4.4 Indicial Function and Radial Basis Function

The indicial responses of the aerofoil for a step change in angle of the attack and for a step change in pitch rate are shown in Fig. 5.10. The lift responses have an initial peak followed by a falling trend, see for example Appendix B. This can be explained based on the energy of the acoustic wave system created by the initial perturbation [190]. The initial peak becomes smaller as the Mach number increases. It was found that the translation of the grid (angle of attack response) has larger effects on the lift changes compared with rotating the grid. Note that the pitching moment has a negative peak

as the grid starts to move. The computational cost for each response is around the cost of 10 steady-state calculations.

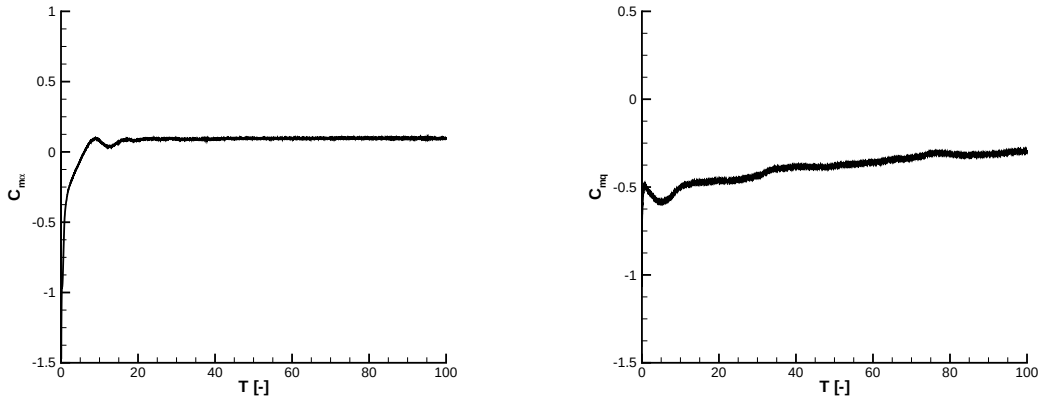

(a) Step change in angle of attack

(b) Step change in pitch rate

Figure 5.10: NACA 0012: indicial responses of pitching moment coefficient to step change in angle of attack and in pitch rate ($M = 0.764$ and $Re = 3.0 \times 10^6$)

The design of a new manoeuvre allows a reduction in the number of training motions. The training manoeuvre used in this study is a spiral manoeuvre which consists of a sweep in the amplitude

$$\alpha(t) = \alpha_A t^* \sin(2 k t^*) \tag{5.15}$$

The spiral motion eliminates the need for repeating motions for different values of amplitude. However, for reduced frequency effects, the motion with different values of k needs to be considered. In this study, a spiral motion was defined starting from zero degrees angle of attack at a reduced frequency of 0.10. The simulation was run for 35 oscillatory cycles. For RBFNN training, the amount of calculated data was reduced on the order of thousands using an interpolation scheme. This allows a faster network training and avoids any out-of-memory error. The reduced spiral data were rearranged according to Eq. (5.9) and then the network performance was tested for different values of n. Results showed that using $n = 2$ and $n = 4$ is sufficient for modelling the lift and the pitching moment, respectively.

A reduced model based on indicial functions was created using Eq. (5.9). The networks were also trained using training data in the same form. The validity of the models was tested for the manoeuvre to be simulated. Figure 5.11 conveys the non-linear results for the large amplitude pitch oscillation. The results show that the model based on indicial functions provides misleading results because the model formulation stems from the concept of linearity. On the other hand, the RBFNN predicts the overall trend of the pitching moment.

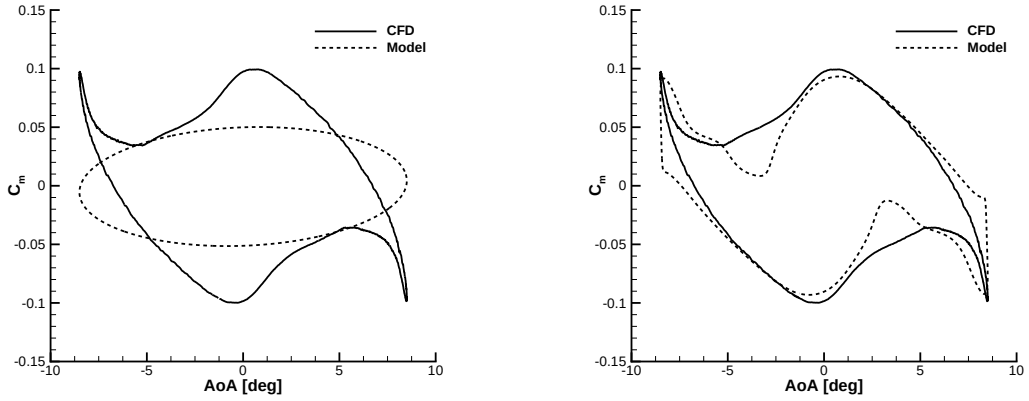

(a) Linear indicial functions

(b) Radial basis functions

Figure 5.11: NACA 0012: predictions of pitching moment dynamic dependence ($M = 0.764$, $\alpha_0 = 0.0°$, $\alpha_A = 8.5°$, $k = 0.10$, and $Re = 3.0 \times 10^6$); in (a), "Model" refers to the linear indicial functions, and in (b) to radial basis functions

5.5 Model Evaluation

For a thorough evaluation of the reduced models, relevant aspects are the accuracy in the predictions and the cost for model generation. To quantify the error between the time-accurate solution and the model prediction, the following error norm was introduced

$$E = \frac{1}{N} \frac{\sum_{i=1}^{N} | \, y^{\text{cfd}}[i] - y^{\text{rom}}[i] \, |}{y_{max}^{\text{cfd}} - y_{min}^{\text{cfd}}} \times 100 \tag{5.16}$$

which represents the average error in the models relative to the range of the reference solution. The term N is the total number of time-steps used in the CFD simulation, and the superscripts cfd and rom indicate the full- and the reduced-order models, respectively. The cost for model generation was normalized by the cost for the simulation of three oscillatory cycles. Table 5.2 summarizes the errors in the moment predictions and the cost for the models considered. Similar conclusions were found when considering the error norm in the force coefficient.

For the conventional model, aerodynamic data were computed at seven values of the angle of attack, and each calculation was run for three oscillatory cycles. The error is representative of the mean value of the predictions, shown in Fig. 5.5(f), and it does not account for the variations to changes in reduced frequency. It is found that the conventional model has the largest error in the predictions and is the most expensive to generate. The accuracy and the cost of the model based on linear indicial functions are similar to the values obtained for the conventional model. Improved predictions were achieved by the three remaining models. While similar in accuracy, the cost for the

	Error, C_m	Cost
DynDer	23.3	7
Volterra	7.8	2
SBRF	5.4	2
LIF	18.3	5
RBFNN	7.7	6

Table 5.2: Error norm in the model predictions of pitching moment coefficient and related cost for model generation

generation of the Volterra model was lower than for the generation of the model based on radial basis functions trained with neural networks. For the conditions presented, the surrogate-based recurrence-framework model resulted in the smallest error at a favourable cost. As explained above, for the surrogate-based recurrence-framework model the trivial solution corresponding to a null amplitude was not run.

5.6 Conclusions

Previous work demonstrated that the conventional model formulation of aerodynamic loads based on aerodynamic derivatives may experience a loss in accuracy for flow conditions of practical interest. The present chapter addresses the demand to explore alternative reduced-model formulations for the prediction of non-linear unsteady airloads. To allow a fast turn-around time of the investigations, the test case is the NACA 0012 aerofoil. The purpose of considering a pitching aerofoil at transonic conditions is to establish the effectiveness of the reduced-order models in a non-linear regime of the flow envelope. The non-linearities are attributable to shock motion and shock-induced separation.

Several modelling formulations were presented. A non-linear model based on aerodynamic derivatives, a multi-input discrete-time Volterra model, a surrogate-based recurrence-framework model, linear indicial functions and radial basis functions trained with neural networks were considered. To assess the predictions, reduced models were compared to unsteady time-domain CFD simulations for oscillatory pitching motions. The model based on aerodynamic derivatives exhibited large deviations from the reference solution. While retaining higher order Volterra kernels, the multi-input discrete-time model achieved a reasonable agreement. For the flow conditions presented, the loss of accuracy shown for the model based on indicial functions was expected. The remaining two models, e.g., surrogate-based recurrence-framework and radial basis functions trained with neural networks, achieved a good agreement with the CFD solution. The point to highlight is that these models, while providing good approximations for both force and moment data, were generated with no more computational resources than required for the conventional model. The application to more complex geometries should

verify these conclusions. The generation of a stability and control database will then be considered to assess the readiness of the reduced-models.

Chapter 6

Conclusions and Outlook

In this thesis, the exploitation of computational fluid dynamics (CFD) for the generation of flight simulation models was investigated. A tabular model based on aerodynamic derivatives was considered because commonly used by flight dynamicists. CFD was used as source of the aerodynamic information. In the model formulation, steady-state predictions are supplemented using dynamic derivatives to account for the aircraft motion. While the calculation of steady-state dependencies by a CFD solver is made in a routine manner, the numerical simulation of dynamic derivatives is a computationally expensive task. These terms are obtained in small-amplitude oscillatory tests, which involve the accurate prediction of the flow development around a moving airframe.

Dynamic derivatives computed using unsteady time-domain calculations were in agreement with available experimental data for two configurations. For a generic fighter model, a systematic study on the investigation of the dependencies of dynamic derivatives was presented. For a transonic cruiser wind tunnel model, a database of static and dynamic dependencies was created. In the presence of aerodynamic non-linearities, mainly due to three dimensional separated flow and concentrated vortices, dynamic derivatives were found to depend on motion and flow parameters. These dependencies are not reconcilable with the model formulation, which is based on a Taylor series expansion. However, as the sensitivity of dynamic derivatives on parameters investigated fell into well defined bands, it was considered reasonable that it is only the general behaviour of these bands, rather than small and often irregular variations in the individual curves, that may be of practical interest for flight dynamics simulations.

An approach to evaluate the sensitivity of the non-linear flight simulation model to variations in dynamic derivatives was introduced. The model predictions compared best to the time-accurate solution when aerodynamic information was estimated at the same frequency as the manoeuvre being simulated. This, however, introduces the question on how to determine the frequencies of interest prior to the manoeuvre being executed. For the transonic cruiser wind tunnel model, the model predictions for a large amplitude manoeuvre in the presence of flow separation were found misleading

and must be carefully interpreted. It was recognized that the non-linear formulation based on stability derivatives is instantaneous, that is, aerodynamic coefficients are only a function of the current time. The formulation is then not adequate in the case aerodynamic loads are dependent on the flow history and past motion. It was shown that, in these conditions, large amplitude data cannot be extrapolated from small amplitude tests and cannot be represented accurately by stability derivatives.

As the calculation of dynamic derivatives is the most expensive task, various reduced models for the fast computation of these terms were investigated. Reduced models were based on the manipulation of the full-order model to reduce the cost of calculations. The underlying idea is to exploit the periodicity of the aerodynamic system for oscillatory motions to significantly decrease the computational cost of unsteady time-accurate simulations. In fact, a time-domain calculation supports a continuum of frequencies up to the frequency limits given by the temporal and spatial resolution. It is therefore worthwhile to consider a frequency-domain formulation to obtain a good estimate of the derivatives at reduced cost.

A linearized solution of the unsteady problem, with an attendant loss of generality, was found inadequate to provide good predictions for the parameters at which dynamic derivatives are required. The reason is that a linearized solution captures the flow behaviour near the point at which the calculation is done, and the extrapolation of these information in presence of non-linearities may be misleading. It was recognized that this method is inadequate for studies of flight dynamics because the aircraft may experience large excursions from the reference point. These considerations were corroborated by additional findings, as explained below.

A harmonic balance technique, which approximate the flow solution in a Fourier series sense, retains a more general validity. While resolving a small subset of frequencies typically restricted to include one Fourier mode at the frequency at which dynamic derivatives are desired, the harmonic balance technique achieved good predictions of dynamic derivatives at a fraction of the cost for solving the original unsteady problems. Investigations demonstrated that a reduced model is not intended to simply augment static calculations, but rather complement and replace the static steady-state flow solver for flight and configuration conditions in which stability characteristics are desired. One single calculation with the two methods investigated provides both static and dynamic derivative information at an equivalent cost of few steady-state runs. Two- and three-dimensional test cases in the transonic regime were analyzed.

While the application of reduced models was successful for the fast computation of dynamic derivatives, the range of test cases considered exposed the limitations and shortcomings of the conventional model used by flight dynamicists. The limitations are due to the neglect of time history and unsteady effects, and other assumptions on dynamic derivatives. To address the need for models of more realism to be used in flight dynamics, enabling the aircraft design for extended flight envelopes, various

reduced models based on system identification methods were assessed. To allow a fast turn-around time of the investigations, a two-dimensional aerofoil is the test case. It was assumed that any consideration on the readiness of the models can be transferred to the analysis of more complex geometries. Tests on aircraft gemetries should verify this point. For the flow conditions considered, the dynamic shock motion and the shock-induced separation were the sources of strong non-linearities in the unsteady aerodynamic loads.

In addition to the conventional model, four model formulations were described. Compared to the unsteady time-domain results, the model based on aerodynamic derivatives was the least accurate. Dependencies of aerodynamic information were investigated for several parameters. It was recognized that aerodynamic data obtained from forced motions at a small amplitude do not necessarily provide a better agreement to the unsteady CFD solution than using aerodynamic information obtained for a larger amplitude case. The solution computed for a small amplitude is similar to a time-linearized solution which capture the flow behaviour near the point at which the calculation is done. This is in general inadequate for studies of flight dynamics because the aircraft may experience large excursions from the reference point. Performing a forced motion at a larger amplitude exposes the flow to some non-linearities, and this may improve somewhat the predictions.

While requiring similar computational resources than needed for the conventional model, improved predictions were achieved using the remaining non-linear models investigated. These results should be extended to more complex configurations and applied to the routine generation of aerodynamic models. There is, however, the question of appropriate training data to be generated, and the issue of model robustness. The development of reduced models based on the manipulation of the full-order residual is an appealing option, which is currently investigated by the author for flexible aircraft control design. The application of this methodology is a research question.

A framework for the automated generation of tabular aerodynamic data using CFD was described. Applications to the areas of flight handling qualities, stability and control characteristics and manoeuvring aircraft were considered for six test cases. Emphasis on the crucial question of how to keep down the computational cost incurred to generate the aerodynamic database was addressed. The framework presented is based on a kriging-based surrogate model. The kriging model is used as a multi-dimensional interpolation to efficiently predict aerodynamic information at untried flight conditions from a set of initial calculations. The number and location of computed flight conditions and the fidelity of the data are fundamental aspects for a robust and accurate kriging-based aerodynamic model. Many low-fidelity computationally cheap estimates are typically augmented by a few high-quality data, which are made available at a later time during the design refinement. Data fusion combines the two datasets into one single database, which is more accurate than the two databases separately.

During the design process, the aircraft geometry iteratively changes as undesired characteristics are discovered and in order to screen alternative configurations. An attractive feature of the framework presented is the flexibility offered in such cases. It was demonstrated that an existing high-quality database, for a given aircraft geometry being iteratively modified, can be updated to be representative of the incremented geometry at the cost of a few high-fidelity calculations. This is illustrative of the role played by CFD simulations and the potential impact that high-fidelity analyses might have to reduce overall costs and design cycle time. Two criteria to automate the selection of candidate sample points to strengthen and verify the readiness of the surrogate model were used. However, they can capture only global non-linear features. This motivates the need to address further research at the development of a methodology to efficiently identify local minima/maxima and changes in curvature in the aerodynamic loads.

The major computational cost is the computation of CFD analyses at points in non-linear regions of the flight envelope. Once constructed, the surrogate-based model is used in place of the expensive simulation process to calculate, at a negligible cost, the aerodynamic loads at any flight point. The tabular model is consistent with a non-linear quasi-steady representation of the aerodynamics and can be used in real-time to fly an aircraft through the database. This gives the opportunity to establish the limitations of the tabular model due to the neglect of time history and unsteady effects, and to assess other limitations related to sampling and assumptions on dynamic derivatives.

The simulation of manoeuvring aircraft involves costly time-accurate analyses, which were confronted with solutions obtained from the tabular data for several manoeuvres and different model configurations. It was recognized that the tabular solution was adequate in representing time histories of the forces and moments in benign conditions. In these cases, the inclusion of dynamic stability derivatives had a significant impact in improving the correlation to the reference solution. However, simplifying assumptions pertaining to the flow physics restrict the validity of the tabular model, and there is a demand for more advanced model formulations for non-linear aerodynamics.

Future work will evaluate the benefits and limitations of reduced-order models for complex configurations. The routine use of these aerodynamic models for manoeuvring aircraft will be investigated and compared to the unsteady time-domain CFD simulation or experimental data.

To briefly summarize, the main points of the work presented in this thesis are

1. exploitation of CFD for the generation of flight simulation models; physics-based simulations can now be used early in the aircraft design process for extended flight envelopes; a range of applications demonstrated the potential of CFD to reduce overall design cycle costs and time

2. different strategies to create CFD-derived simulation models across the flight envelope were assessed, ranging from a hierarchy of aerodynamic models to reduced-order modelling; the limitations and shortcomings of the conventional model based on aerodynamic stability derivatives were investigated

3. the level of accuracy and sensitivity of various flight simulation models compared to unsteady CFD solution were evaluated; predictions using the conventional model were found misleading when considering conditions of practical interest; the development of robust CFD-based reduced models applicable to transonic speeds and high angles of attack is a research question currently under investigation.

Bibliography

[1] Chambers, J. R. and Hall, R. M., "Historical Review of Uncommanded Lateral-Directional Motions at Transonic Conditions," *Journal of Aircraft*, Vol. 41, No. 3, 2004, pp. 436–447.

[2] Woodson, S. H., Green, B. E., Chung, J. J., Grove, D. V., Parikh, P. C., and Forsythe, J. R., "Understanding Abrupt Wing Stall with Computational Fluid Dynamics," *Journal of Aircraft*, Vol. 42, No. 3, 2005, pp. 578–585.

[3] Forsythe, J. R., Fremaux, C. M., and Hall, R. M., "Calculation of Static and Dynamic Stability Derivatives of the F/A-18E in Abrupt Wing Stall Using RANS and DES," *Computational Fluid Dynamics 2004*, edited by C. Groth and D. W. Zingg, Springer Berlin Heidelberg, 2006, pp. 537–542, doi: 10.1007/3-540-31801-1_76.

[4] Kimberlin, R. D., *Flight Testing of Fixed-Wing Aircraft*, AIAA Educational Series, Reston, Virginia, USA, 2003.

[5] Barlow, J. B., William, H. R., and Pope, A., *Low-Speed Wind Tunnel Testing*, Third Edition, John Wiley & Sons, Inc., 1999.

[6] Williams, J. E. and Vukelich, S. R., "The USAF Stability and Control Digital DATCOM," McDonnell Douglas Astronautics Company - St Louis Division, St Louis, Missouri 63166, 1979, AFFDL-TR-79-3032.

[7] Raymer, D. P., *Aircraft Design: A Conceptual Approach*, 2006, 4th ed, AIAA Education Series, Reston, VA, USA.

[8] Roskam, J., "Airplane Design," 1990, Roskam Aviation and Engineering Corporation, Kansas, USA.

[9] Boelens, O. J., Badcock, K. J., Elmilgui, A., Abdol-Hamid, K. S., and Massay, S. J., "Comparison of Measured and Block Structured Simulation Results for the F-16XL Aircraft," *Journal of Aircraft*, Vol. 46, No. 2, 2009, pp. 377–384.

[10] Bellman, R. E., *Dynamic Programming*, Courier Dover Publications, 2003.

[11] Giunta, A. A., Balabanov, V., Haim, D., Grossman, B., Mason, W. H., Watson, L. T., and Haftka, R. T., "Multidisciplinary Optimisation of a Supersonic Transport Using Design of Experiments Theory and Response Surface Modelling," *Aeronautical Journal*, Vol. 101, No. 1008, 1997, pp. 347–356.

[12] Schuster, D. M., Liu, D., and Huttsell, L. J., "Computational Aeroelasticity: Success, Progress, Challenge," *Journal of Aircraft*, Vol. 40, No. 5, 2003, pp. 843–856.

[13] Rogers, S. E., Aftomis, M. J., Pandya, S. A., Chaderjian, N. M., Tejnil, E. T., and Ahmad, J. U., "Automated CFD Parameter Studies on Distributed Parallel Computers," AIAA Paper 2003-4229, 2003.

[14] Ghoreyshi, M., Badcock, K. J., and Woodgate, M. A., "Accelerating the Numerical Generation of Aerodynamic Models for Flight Simulation," *Journal of Aircraft*, Vol. 46, No. 3, 2009, pp. 972–980.

[15] Sacks, J., Welch, W. J., Mitchell, T. J., and Wynn, H. P., "Design and Analysis of Computer Experiments," *Statistical Science*, Vol. 4, No. 4, 1989, pp. 409–435.

[16] Martin, J. D. and Simpson, T. W., "Use of Kriging Models to Approximate Deterministic Computer Models," *AIAA Journal*, Vol. 43, No. 4, 2005, pp. 853–863.

[17] Glaz, B., Liu, L., and Friedmann, P. P., "Reduced-Order Nonlinear Unsteady Aerodynamic Modeling Using a Surrogate-Based Recurrence Framework," *AIAA Journal*, Vol. 48, No. 10, 2010, pp. 2418–2429.

[18] Laurenceau, J. and Sagaut, P., "Building Efficient Response Surfaces of Aerodynamic Functions with Kriging and Cokriging," *AIAA Journal*, Vol. 46, No. 2, 2008, pp. 498–507.

[19] Bryan, G. H., "Stability in Aviation," MacMillan, London, 1911.

[20] Cowley, W. L. and Glauert, H., "The Effect of the Lag of the Downwash on the Longitudinal Stability of an Airplane and on the Rotary Derivative," Reports and Memoranda No. 718, February 1921.

[21] Tobak, M. and Schiff, L. B., "On the Formulation of the Aerodynamic Characteristics in Aircraft Dynamics," NACA TR R–456, 1976.

[22] Goman, M. G. and Khrabrov, A. N., "State-Space Representation of Aerodynamic Characteristics of an Aircraft at High Angles of Attack," *Journal of Aircraft*, Vol. 31, No. 5, 1994, pp. 1109–1115.

[23] Ghoreyshi, M., Badcock, K. J., Da Ronch, A., Marques, S., Swift, A., and Ames, N., "Framework for Establishing the Limits of Tabular Aerodynamic Models for Flight Dynamics Analysis," *Journal of Aircraft*, Vol. 48, No. 1, 2011, pp. 42–55, doi: 10.2514/1.C001003.

[24] Chaderjian, N. M., Pandya, S. A., Ahmad, J. U., and Murman, S. M., "Progress Toward Generation of a Navier-Stokes Database for a Harrier in Ground Effect," *2nd Biennial International Powered Lift Conference and Exhibit*, AIAA–2002–5966, Williamsburg, Virginia, 2002.

[25] Butland, J. and Fritsch, F. N., "A Method for Constructing Local Monotone Piecewise Cubic Interpolants," *SIAM Journal on Scientific and Statistical Computing*, Vol. 5, June 1984, pp. 300–304.

[26] Chaderjian, N. M., Pandya, S. A., Ahmad, J. U., and Murman, S. M., "Parametric Time-Dependent Navier-Stokes Computations for a YAV-8B Harrier in Ground Effect," *AIAA Paper 2002-0950*, 2002.

[27] Jacob, B., Ferreira, L., Bieberstein, N., Gilzean, C., Girard, J., Strachowski, R., and Yu, S., "Enabling applications for Grid Computing with Globus," Redbook, IBM, March 2003.

[28] Chaderjian, N. M., Rogers, S. E., Aftosmis, M. J., Pandya, S. A., Ahmad, J. U., and Tejnil, E., "Automated CFD Database Generation for a 2^{nd} Generation Glide-Back Booster," *21th AIAA Applied Aerodynamic Conference*, AIAA–2003–3788, Orlando, FL, 2003.

[29] Murman, S. M., Aftosmis, M. J., and Nemec, M., "Automated Parameter Studies Using a Cartesian Method," *22th AIAA Applied Aerodynamic Conference*, AIAA–2004–5076, Providence, RI, 2004.

[30] Simos, T. E., "A Runge-Kutta Fehlberg method with phase-lag of order infinity for initial-value problems with oscillating solution," *Computers & Mathematics with Applications*, Vol. 25, No. 6, 1993, pp. 95–101.

[31] Emerson, D. R., Sunderland, A. J., Ashworth, M., and Badcock, K. J., "High Performance Computing and Computational Aerodynamics in the UK," *Aeronautical Journal*, Vol. 111, No. 1117, 2007, pp. 125–131.

[32] Vallespin, D., Badcock, K. J., Da Ronch, A., White, M., Perfect, P., and Ghoreyshi, M., "Computational Fluid Dynamics Framework for Aerodynamic Model Assessment," to appear in Progress in Aerospace Sciences, 2012.

[33] Leishman, J. G., "Subsonic Unsteady Aerodynamics Caused by Gusts Using the Indicial Method," *Journal of Aircraft*, Vol. 33, No. 5, 1996, pp. 869–879.

[34] Parameswaran, V. and Baeder, J. D., "Indicial Aerodynamics in Compressible Flow - Direct Computational Fluid Dynamic Calculations," *Journal of Aircraft*, Vol. 34, No. 1, 1997, pp. 131–133.

[35] Sitaraman, J. and Baeder, J. D., "Computational-Fluid-Dynamics-Based Enhanced Indicial Aerodynamic Models," *Journal of Aircraft*, Vol. 41, No. 4, 2004, pp. 798–810.

[36] Lesieutre, D. J., Reisenthel, P. H., and Dillenius, M. F. E., "A Practical Approach for Calculating Aerodynamic Indicial Functions with a Navier-Stokes Solver," AIAA Paper 1994–0059, January 1994.

[37] Tobak, M., Chapman, G. T., and Schiff, L. B., "Mathematical Modeling of the Aerodynamic Characteristics in Flight Dynamics," NACA TN–85880, 1984.

[38] Tobak, M. and Chapman, G. T., "Nonlinear Problems in Flight Dynamics Involving Aerodynamic Bifurcations," NACA TN–86706, 1985.

[39] Reisenthel, P. H., "Development of a Nonlinear Indicial Model for Maneuvering Fighter Aircraft," AIAA Paper 1996–0896, 1996.

[40] Reisenthel, P. H., "Application of Nonlinear Indicial Modeling to the Prediction of a Dynamically Stalling Wing," AIAA Paper 1996–2493, 1996.

[41] Reisenthel, P. H. and Bettencourt, M. T., "Data-Based Aerodynamic Modeling Using Nonlinear Indicial Theory," AIAA Paper 1999–0763, 1999.

[42] Morton, S., Forsythe, J., McDaniel, D., Bergeron, K., Cummings, R., Göertz, S., Seidel, J., and Squires, K., "High Resolution Simulation of Full Aircraft Control at Flight Reynolds Numbers," HPCMP Users Group Conference, pp. 41-47, 2007 DoD High Performance Computing Modernization Program Users Group Conference, 2007.

[43] McDaniel, D. R., Cummings, R. M., Bergeron, K., Morton, S. A., and Dean, J. P., "Comparisons of Computational Fluid Dynamics Solutions of Static and Manoeuvring Fighter Aircraft with Flight Test Data," *Proceedings of the Institution of Mechanical Engineers, Part G: Journal of Aerospace Engineering*, Vol. 223, No. 4, 2009, pp. 323–340.

[44] Jeans, T. L., McDaniel, D. R., Cummings, R. M., and Bergeron, K., "Lower-Order Aerodynamic Loads Modeling of a Maneuvering Generic Fighter Using DDES Simulations," *7th AIAA Aerospace Sciences Meeting*, AIAA–2009–0094, Orlando, FL, 2009.

[45] Dean, J. P., Clifton, J. D., Bodkin, D. J., and Ratcliff, C. J., "High Resolution CFD Simulations of Maneuvering Aircraft Using the CREATE-AV/Kestrel Solver," *49th AIAA Aerospace Sciences Meeting*, AIAA–2011-1109, Orlando, Florida, 2011.

[46] Rao, D. M. and Bhat, M. K., "A Low-Speed Wind Tunnel Study of Vortex Interaction Control Techniques on a Chine-Forebody/Delta-Wing Configuration," NACA CR–189616, March 1992.

[47] Klein, V. and Morelli, E. A., *Aircraft System Identification: Theory and Practice*, AIAA Education Series, Reston, VA, 2006.

[48] Morelli, E. A., "System IDentification Programs for AirCraft (SIDPAC)," AIAA Paper 2022–4704, 2002.

[49] Görtz, S., McDaniel, D. R., and Morton, S. A., "Towards an Efficient Aircraft Stability and Control Analysis Capability using High-Fidelity CFD," *45th AIAA Aerospace Sciences Meeting*, AIAA–2007-1052, Reno, Nevada, 2007.

[50] Young, P. and Patton, R. J., "Comparison of Test Signals for Aircraft Frequency Domain Identification," *Journal of Guidance, Control, and Dynamics*, Vol. 13, No. 3, 1990, pp. 430–438.

[51] O'Neill, C. R. and Arena Jr., A. S., "Time-Domain Training Signals Comparison for Computational Fluid Dynamics Based Aerodynamic Identification," *Journal of Aircraft*, Vol. 42, No. 2, 2005, pp. 421–428.

[52] Jirasek, A., Jeans, T. L., Martenson, M., Cummings, R. M., and Bergeron, K., "Improved Methodologies for Maneuver Design of Aircraft Stability and Control

Simulations," *48th AIAA Aerospace Sciences Meeting Including the New Horizons Forum and Aerospace Exposition*, Orlando, FL, 2010.

[53] Hardy, R. L., "Multiquadratic Equations of Topography and Other Irregular Surfaces," *Journal of Geophysical Research*, Vol. 76, 1971, pp. 1905–1915.

[54] Silva, W. A., "Discrete-Time Linear and Nonlinear Aerodynamic Impulse Responses for Efficient CFD Analysis," PhD Dissertation, Faculty of the Department of Applied Science, The College of William and Mary in Virginia, VA, September 1997.

[55] Beran, P. S., Lucia, D. J., and Pettit, C. L., "Reduced-Order Modelling of Limit-Cycle Oscillation for Aeroelastic Systems," *Journal of Fluids and Structures*, Vol. 19, No. 5, 2004, pp. 575–590.

[56] Silva, W., "Identification of Nonlinear Aeroelastic Systems Based on the Volterra Theory: Progress and Opportunities," *Nonlinear Dynamics*, Vol. 39, No. 1-2, 2005, pp. 25–62.

[57] Jirasek, A. and Cummings, R. M., "Application of Volterra Functions to X-31 Aircraft Model Motion," *27th AIAA Applied Aerodynamics Conference*, AIAA–2009–3629, San Antonio, TX, 2009.

[58] Balajewicz, M., Nitzsche, F., and Feszty, D., "Application of Multi-Input Volterra Theory to Nonlinear Multi-Degree-of-Freedom Aerodynamic Systems," *AIAA Journal*, Vol. 48, No. 1, 2010, pp. 56–62.

[59] Balajewicz, M., Nitzsche, F., and Feszty, D., "Reduced Order Modeling of Nonlinear Transonic Aerodynamics Using a Pruned Volterra Series," *50th AIAA/ASME/ASCE/AHS/ASC Structures, Structural Dynamics and Materials Conference*, Palm Springs, CA 2009.

[60] Balajewicz, M., "Reduced Order Modeling of Transonic Flutter and Limit Cycle Oscillations Using the Pruned Volterra Series," *51st AIAA/ASME/ASCE/AHS/ASC Structures, Structural Dynamics and Materials Conference*, 2010.

[61] Loève, M., "Probability Theory," D. Van Nostrand, New York, 1955.

[62] Holmes, P., Lumley, J. L., and Berkooz, G., "Turbulence, Coherent Structures, Dynamical Systems and Symmetry," Cambridge Univerity Press, Cambridge, England, UK, 1996.

[63] Hall, K. C., Thomas, J. P., and Dowell, E. H., "Proper Orthogonal Decomposition Technique for Transonic Unsteady Aerodynamic Flows," *AIAA journal*, Vol. 38, No. 10, 2000, pp. 1853–1862.

[64] Lillian, C. S., Morton, S. A., and McDaniel, D. R., "Aircraft Loads Characteristics Determined by System Identification and Proper Orthogonal Decomposition of CFD Simulations," *28th AIAA Applied Aerodynamic Conference*, AIAA–2010–4368, Chicago, IL, 2010.

[65] Lillian, C. S., McDaniel, D. R., and Morton, S. A., "An Efficient Method of Computing Maneuvering Aircraft Surface Loads Using CFD, Proper Orthogonal Decomposition, and System Identification," *49th AIAA Aerospace Sciences Meeting*, AIAA–2011–1177, Orlando, FL, 2011.

[66] Tang, C. Y., Gee, K., and Lawrence, S. L., "Generation of Aerodynamic Data using a Design of Experiment and Data Fusion Approach," *43th AIAA Aerospace Sciences Meeting*, AIAA–2005-1137, Reno, Nevada, 2005.

[67] Simpson, T. W., Peplinski, J. D., Koch, P. N., and Allen, J. K., "Metamodels for Computer-Based Engineering Design: Survey and Recommendations," *Engineering with Computers*, Vol. 17, No. 2, 2001, pp. 129–150.

[68] Queipo, N. V., Haftka, R. T., Shyy, W., Goel, T., Vaidyanathan, R., and Kevin Tucker, P., "Surrogate-Based Analysis and Optimization," *Progress in Aerospace Sciences*, Vol. 41, No. 1, 2005, pp. 1–28, Aerospace systems;Data sets;Optimal design;Surrogate-based analysis;.

[69] Han, Z., Görtz, S., and Hain, R., "A Variable-Fidelity Modeling Method for Aero-Loads Prediction," *New Results in Numerical and Experimental Fluid Mechanics VII*, edited by A. Dillmann, G. Heller, M. Klaas, H.-P. Kreplin, W. Nitsche, and W. Schröder, Vol. 112 of *Notes on Numerical Fluid Mechanics and Multidisciplinary Design*, Springer Berlin / Heidelberg, 2010, pp. 17–25, doi: 10.1007/978-3-642-14243-7_3.

[70] Greenwell, D. I., "Frequency Effects on Dynamic Stability Derivatives Obtained from Small-Amplitude Oscillatory Testing," *Journal of Aircraft*, Vol. 35, No. 5, 1998, pp. 776–783.

[71] Nguyen, L. T., "Evaluation of Importance of Lateral Acceleration Derivatives in Extraction of Lateral-Directional Derivatives at High Angles of Attack," NASA TN D–7739, October, 1974.

[72] Wagner, H., "Üeber die Entstehung des dynamischen Auftriebes von Tragflügeln," Zeitschrift für angewandte Mathematik und Mechanik, Vol 1, Book 1, 1925, pp. 17–35.

[73] Küssner, H. G. K., "Stresses Produced in Airplane Wings by Gusts," NASA TM 654, January, 1932.

[74] Sears, W. R., "Some Aspects of Non-Stationary Airfoil Theory and Its Practical Application," *Journal of the Aeronautical Sciences*, Vol. 8, No. 5, 1941, pp. 104–108.

[75] Jones, R. T. and Fehlner, L. F., "Transient Effects of the Wing Wake on the Horizontal Tail," NACA TN 771, 1940.

[76] Tobak, M., "On the Use of the Indicial Function Concept in the Analysis of Unsteady Motions of Wings and Wing-Tail Combinations," NACA Report 1188, 1954.

[77] Volterra, V., *Theory of Functionals and of Integral and Integro-Differential Equations*, Dover Pub., Inc., New York, 1966.

[78] Goman, M. G., Stolyarov, G. I., Tyrtyshnikov, S. L., Useltsev, S. P., and Khrabrov, A. N., "Mathematical Description of Aircraft Longitudinal Aerodynamic Characteristics at High Angle of Attack Accounting for Dynamic Effects of Separated Flow," TsAGI Preprint No. 9, 1990.

[79] Khrabrov, A., Kolinko, K., Miatov, O., Vinogradov, J., and Zhuk, A., "Using of Oscillatory Conning Experimental Rig for Separation of Rotary and Unsteady Aerodynamic Derivatives," *18th International Congress on Instrumentation in Aerospace Simulation Facilities*, 1999, pp. 37/1–37/9.

[80] Rizzi, A., "Modeling and Simulating Aircraft Stability & Control – The SimSAC Project," *Progress in Aerospace Sciences*, Vol. 47, 2011, pp. 573–588, doi: 10.1016/j.paerosci.2011.08.004.

[81] Da Ronch, A., Ghoreyshi, M., and Badcock, K. J., "On the Generation of Flight Dynamics Aerodynamic Tables by Computational Fluid Dynamics," *Progress in Aerospace Sciences*, Vol. 47, No. 8, 2011, pp. 597–620, doi: 10.1016/j.paerosci.2011.09.001.

[82] Smith, B. C. and Malcolm, G. N., "Determination of Non-Linear Dynamic Aerodynamic Coefficients for Aircraft," Eidetics Corporation, TR97-001, January 1997.

[83] Greenberg, H., "Determination of Stability Derivatives from Flight Data," *Journal of the Aeronautical Sciences*, Vol. 16, No. 1, 1949.

[84] Greenberg, H., "A Survey of Methods for Determining Stability Parameters of an Airplane from Dynamic Flight Measurements," NACA TN–2340, 1951.

[85] Da Ronch, A., Vallespin, D., Ghoreyshi, M., and Badcock, K. J., "Computation of Dynamic Derivatives Using CFD," *28th AIAA Applied Aerodynamics Conference*, AIAA–2010–4817, Chicago, IL, 2010.

[86] Lophaven, S. N., Nielsen, H. B., and Søndergaard, J., "DACE, A Matlab Kriging Toolbox. Version 2.0," Technical Report IMM-TR-2002-12, Technical University of Denmark, August 1, 2002.

[87] Lophaven, S. N., Nielsen, H. B., and Søndergaard, J., "Aspects of the Matlab Toolbox DACE," Technical Report IMM-REP-2002-12. Technical University of Denmark, August 1, 2002.

[88] Chaloner, K. and Verinelli, I., "Bayesian Experimental Design: A Review," *Statistical Science*, Vol. 10, No. 3, 1995, pp. 273–304.

[89] Metropolis, N. and Ulam, S., "The Monte Carlo Method," *ACM Transactions on Mathematical Software*, Vol. 44, No. 247, 1949, pp. 335–341.

[90] McKay, M. D., Beckman, R. J., and Conover, W. J., "A Comparison of Three Methods for Selecting Values of Input Variables in the Analysis of Output from a Computer Code," *Technometrics*, Vol. 21, No. 2, May 1979, pp. 239–245.

[91] Kocis, L. and Withen, W. J., "Computational Investigations of Low-Discrepancy Sequences," *ACM Transactions on Mathematical Software*, Vol. 23, No. 2, 1997, pp. 266–294.

[92] Morris, M. D. and Mitchell, T. J., "Exploratory Designs for Computational Experiments," *Journal of Statistical Planning and Inference*, Vol. 43, 1995, pp. 381–402.

[93] Isaaks, E. H. and Srivastava, R. M., *An Introduction to Applied Geostatistics*, Oxford University Press, New York, USA, 1989.

[94] Jones, D. R., Schonlau, M., and Welch, W. J., "Efficient Global Optimization of Expensive Black-Box Functions," *Journal of Global Optimization*, Vol. 13, No. 4, 1998, pp. 455–492.

[95] Razgonyaev, V. and Mason, W. H., "An Evaluation of Aerodynamic Prediction Methods Applied to the XB-70 for Use in High Speed Aircraft Stability and Control System Design," 33rd Aerospace Sciences Meeting and Exhibit, AIAA95-0759, Reno, Nevada, 1995.

[96] Anderson, J. D., "Modern Compressible Flow," McGraw Hill, 1990.

[97] Munk, M., "The Aerodynamic Forces on Airship Hull," NACA Report No. 184, 1924.

[98] Badcock, K. J., Richards, B. E., and Woodgate, M. A., "Elements of Computational Fluid Dynamics on Block Structured Grids using Implicit Solvers," *Progress in Aerospace Sciences*, Vol. 36, No. 5, 2000, pp. 351–392.

[99] Anderson, J. D., *Computational Fluid Dynamics – The basic with applications*, Mechanical Engineering Series, McGraw–Hill International Editions, 1995.

[100] Osher, S. and Chakravarthy, S., "Upwind Schemes and Boundary Conditions with Applications to Euler Equations in General Geometries," *Journal of Computational Physics*, Vol. 50, No. 3, 1983, pp. 447–481.

[101] Van Leer, B., "Towards the Ultimate Conservative Difference Scheme II: Monotonicity and Conservation Combined in a Second Order Scheme," *Journal of Computational Physics*, Vol. 14, No. 4, 1974, pp. 361–374.

[102] Jameson, A., "Time Dependent Calculations Using Multigrid, with Applications to unsteady Flows Past Airfoils and Wings," *AIAA Paper 91–1596*, 1991.

[103] Brandsma, F. J., Kok, J. C., Dol, H. S., and Elsenaar, A., "Leading Edge Vortex Flow Computations and Comparison with DNW–HST Wind Tunnel Data," *Proceeds of the RTO/AVT Symposium on Vortex Flows and High Angle of Attack*, NATO RTO/AVT, 2001.

[104] Rampurawala, A. M. and Badcock, K. J., "Evaluation of a Simplified Grid Treatment for Oscillating Trailing-Edge Control Surfaces," *Journal of Aircraft*, Vol. 44, No. 4, 2007, pp. 1177–1188.

[105] Allan, M. R., Badcock, K. J., and Richards, B. E., "CFD Based Simulation of Longitudinal Flight Mechanics with Control," *43rd AIAA Aerospace Science Meeting and Exhibition*, AIAA–2005–0046, 2005.

[106] Gerhold, T., Galle, M., Friedrich, O., and Evans, J., "Calculation of Complex Three-Dimensional Configurations employing the DLR TAU-Code," AIAA Paper 97-0167, 1997.

[107] Schwamborn, D., Gerhold, T., and Heinrich, R., "The DLR TAU-Code: Recent Applications in Research and Industry," *Proceedings of European Conference on Computational Fluid Dynamics ECCOMAS CFD*, 2006.

[108] Dwight, R., Brezillon, J., and Vollmer, D., "Efficient Algorithms for Solution of the Adjoint Compressible Navier-Stokes Equations with Applications," *Proceedings of the ONERA-DLR Aerospace Symposium (ODAS)*, Toulouse, France, 2006.

[109] Campobasso, M. S., Bonfiglioli, A., and Baba-Ahmadi, M. H., "Development of Efficient and Accurate CFD Technologies for Wind Turbine Unsteady Aerodynamics," *Proceedings of the Conference on Modeling Fluid Flow*, edited by J. Vad, Vol. 2, Department of Fluid Mechanics, Budapest University of Technology and Economics, 2009, pp. 879–886.

[110] Bonfiglioli, A., Campobasso, M. S., and Carpentieri, B., "Parallel Unstructured Three-Dimensional Turbulent Flow Analyses Using Efficiently Preconditioned Newton-Krylov Solver," *19th AIAA Computational Fluid Dynamics Conference*, AIAA Paper 2009-4137, 2009.

[111] Campobasso, M. S., Baba-Ahmadi, M. H., and McLelland, G., "Ad-Hoc Boundary Conditions for CFD Analyses of Turbomachinery Problems With Strong Radial Flow Gradients at Farfield Boundaries," ASME Paper GT2010-22176, 2010, To appear in the ASME Journal of Turbomachinery.

[112] Gottlieb, J. J. and Groth, C. P. T., "Assessment of Riemann Solvers For Unsteady One-dimensional Inviscid Flows of Perfect Gasses," *Journal of Computational Physics*, Vol. 78, No. 2, 1988, pp. 437–458.

[113] Tomaro, R. F., Strang, W. Z., and Sankar, L. N., "An Implicit Algorithm For Solving Time Dependent Flows on Unstructured Grids," AIAA Paper 1997–0333, 1997.

[114] Klein, V., Murphy, P. C., Curry, T. J., and Brandon, J., "Analysis of Wind Tunnel Longitudinal Static and Oscillatory Data of the F-16XL Aircraft," NASA TM–97–206276, December, 1997.

[115] Klein, V. and Noderer, K. D., "Modeling of Aircraft Unsteady Aerodynamic Characteristics. Part 2-Parameters Estimated From Wind Tunnel Data," NASA TM 110161, April, 1995.

[116] Klein, V. and Noderer, K. D., "Modeling of Aircraft Unsteady Aerodynamic Characteristics. Part 1-Postulated Models," NASA TM 109120, May, 1994.

[117] Smith, M. S., "Analysis of Wind Tunnel Oscillatory Data of the X-31A Aircraft," NASA CR 1999–20875, February, 1999.

[118] Morelli, E. A., "High Accuracy Evaluation of the Finite Fourier Transform using Sampled Data," NASA TM 110340, 1997.

[119] Brigham, O. E., *The Fast Fourier Transform*, Prentice-Hall, Englewood Cliffs, N.J., 1974.

[120] Rabiner, L. R., Schafer, R. W., and Rader, C. M., "The Chirp-z Transform Algorithm and Its Application," *The Bell System Technical Journal*, May-June, 1969, pp. 1249–1292.

[121] Junkins, J. L. and Kim, Y., *Introduction to Dynamics and Control of Flexible Structures*, AIAA Education Series, Washington, DC, 1993.

[122] Quarteroni, A., Sacco, R., and Saleri, F., *Numerical Mathematics*, Texts in Applied Mathematics, Springer–Verlag New York, Inc., 2000.

[123] Greenwell, D. J., "Difficulties in the Application of Stability Derivatives to the Maneuvering Aerodynamics of Combat Aircraft," *Proceedings of the 21st Congress of the International Council of the Aeronautical Sciences*, ICAS 1998-3.9.2, 1998.

[124] Orlik-Rückemann, K. J., "Dynamic Stability Testing of Aircraft–Needs versus Capabilities," *Progress in Aerospace Sciences*, Vol. 16, No. 4, 1975, pp. 431–447.

[125] Huang, X. Z., "Wing and Fin Buffet on The Standard Dynamic Model," NATO RTO Report Number, RTO–TR–26, pp. 361–381.

[126] Beyers, M. E., "Subsonic Roll Oscillation Experiments on the Standard Dynamic Model," *AIAA Atmospheric Flight Mechanics Conference*, AIAA–83–2134, 1983.

[127] Jermey, C. and Schiff, L. B., "Wind Tunnel Investigation of the Aerodynamic Characteristics of the Standard Dynamic Model in Coning Motion at Mach 0.6," *12th AIAA Atmospheric Flight Mechanics Conference*, AIAA–85–1828, 1985.

[128] Davari, A. R. and Soltani, M. R., "Effects of Plunging Motion on Unsteady Aerodynamic Behaviour of an Aircraft Model in Compressible Flow," *Iranian Journal of Science and Technology, Transaction B Enginneering*, Vol. 31, No. B1, 2007, pp. 49–63.

[129] Alemdaroglu, N., Iyigun, I., Altun, M., Uysal, H., Quagliotti, F., and Guglieri, G., "Determination of Dynamic Stability Derivatives Using Forced Oscillation Technique," *40th AIAA Aerospace Science Meeting and Exhibition*, AIAA–2002–0528, 2002.

[130] Newsome, R. W., "Euler and Navier-Stokes Solutions for Flow over a Conical Delta Wing," *AIAA journal*, Vol. 24, No. 4, 1986, pp. 552–561.

[131] Da Ronch, A., Vallespin, D., Ghoreyshi, M., and Badcock, K. J., "Evaluation of Dynamic Derivatives Using Computational Fluid Dynamics," *AIAA Journal*, Vol. 40, No. 2, 2012, pp. 470–484, doi: 10.2514/1.J051304.

[132] Ghoreyshi, M., Badcock, K. J., Da Ronch, A., Swift, A., Marques, S., and Ames, N., "Framework for Estabilishing the Limits of Tabular Aerodynamic Models for Flight Dynamics," *AIAA Atmospheric Flight Mechanics Conference*, AIAA–2009–6273, 2009.

[133] Winchenbach, G. L., Uselton, B. L., Hathaway, W. H., and Chelekis, R. M., "Comparison of Free-Flight and Wind Tunnel Data for a Generic Fighter Configuration," *AIAA Paper 82–1365*, 1982.

[134] Kabin, S. V., Kolinko, K. A., Khrabrov, A. N., and Nushtaev, P. D., "Dynamic Test Rig and Test Techniques for the Aircraft Models Unsteady Aerodynamic Characteristics Measurements in High Subsonic and Transonic Wind Tunnels," *18th International Congress on Instrumentation in Aerospace Simulation Facilities*, 1995, pp. 26/1 –26/7.

[135] Murman, S. M., "Reduced-Frequency Approach for Calculating Dynamic Derivatives," *AIAA Journal*, Vol. 45, No. 6, 2007, pp. 1161–1168.

[136] Soltani, M. R. and Rasi Marzabadi, F., "Effect of Reduced Frequency on the Aerodynamic Behavior of an Airfoil Oscillating in a Plunging Motion," *Scientia Iranica, Transaction B: Mechanical Enginneering*, Vol. 16, No. 1, 2009, pp. 40–52.

[137] Mialon, B., Khrabrov, A., Khelil, S. B., Huebner, A., Da Ronch, A., Badcock, K. J., Cavagna, L., Eliasson, L., Zang, M., Ricci, S., Jouhaud, J.-C., Rogé, G., Hitzel, S., and Lahuta, M., "Validation of Numerical Prediction of Dynamic Derivatives: Two Test Cases," *Submitted for publication in Progress in Aerospace Sciences*, Vol. 47, No. 8, 2011, pp. 674–694, doi: 10.1016/j.paerosci.2011.05.002.

[138] Davari, A. R. and Soltani, M. R., "On the Relationship Between Unsteady Forces and Shock Angles on a Pitching Airplane Model," *Scientia Iranica*, Vol. 17, No. 2 B, 2010, pp. 102–107.

[139] McCroskey, W. J., "Unsteady Airfoils," *Annual Review of Fluid Mechanics*, Vol. 14, No. 1, 1982, pp. 285–311.

[140] Huang, X. Z., "Unsteady Behaviour of Leading-Edge Vortex at Static and Dynamic Model Conditions," *Proceedings of the 24th Congress of the International Council of the Aeronautical Sciences*, ICAS 2004-2.9.2, 2004.

[141] Görtz, S. and Rizzi, A., "Computing the High-Alpha Aerodynamics of Delta Wings - Evaluation and Analysis," *AIAA Paper 01–0115*, January 2001.

[142] Smith, M. J. and Huttsell, L. J., "Computational Evaluation of Semispan Straked Delta Wing Flowfields Conducive to LCO," *AIAA Paper 99–1212*, 1999.

[143] Gad-el Hak, M. and Ho, C.-M., "Pitching Delta Wing," *AIAA journal*, Vol. 23, No. 11, 1985, pp. 1660–1665.

[144] Ericsson, L. E. and Beyers, M. E., "Universality of the Moving-Wall Effect," *Journal of Aircraft*, Vol. 37, No. 3, 2000, pp. 508–513.

[145] LeMay, S. P., Batill, S. M., and Nelson, R. C., "Vortex Dynamics on a Pitching Delta Wing," *Journal of Aircraft*, Vol. 27, No. 2, 1990, pp. 131–138.

[146] Brandon, J. M. and Foster, J. V., "Recent Dynamic Measurements and Considerations for Aerodynamic Modeling of Fighter Airplane Configurations," AIAA Paper 98–4447, 1998.

[147] Eliasson, P., Vos, J. B., Da Ronch, A., Zhang, M., and Rizzi, A., "Virtual Aircraft Design of TransCRuiser – Computing Break Points in Pitch Moment Curve," *28th AIAA Applied Aerodynamic Conference*, AIAA–2010–4366, Chicago, IL, 2010.

[148] Khrabrov, A., Kolinko, K., Zhuk, A., and Grishin, I., "Wind Tunnel Test Report," SimSAC Report, Deliverable Number D 6.4–7, March 2010.

[149] Wheeler, A. J. and Ganji, A. R., *Introduction to Engineering Experimenation*, Pearson Education International, Prentice Hall, 2nd ed., 2004.

[150] Da Ronch, A., Ghoreyshi, M., Badcock, K. J., Görtz, S., Widhalm, M., Dwight, R. P., and Campobasso, M. S., "Linear Frequency Domain and Harmonic Balance Predictions of Dynamic Derivatives," *28th AIAA Applied Aerodynamic Conference*, AIAA–2010–4699, Chicago, IL, 2010.

[151] Thompson, J. R., Frink, N. T., and Murphy, P. C., "Guidelines for Computing Longitudinal Dynamic Stability Characteristics of a Subsonic Transport," *28th AIAA Applied Aerodynamic Conference*, AIAA–2010–4819, Chicago, IL, 2010.

[152] Frink, N. T., "Strategy for Dynamic CFD Simulations on SACCON Configuration," *28th AIAA Applied Aerodynamic Conference*, AIAA–2010–4559, Chicago, IL, 2010.

[153] Oppenheim, A. V. and Schafer, R. W., *Discrete-Time Signal Processing*, Prentice-Hall, Englewood Cliffs, N.J., 1989.

[154] Clark, W. S. and Hall, K. C., "A Time-Linearized Navier-Stokes Analysis of Stall Flutter," *Journal of Turbomachinery*, Vol. 122, No. 3, 2000, pp. 467–476, doi: 10.1115/1.1303073.

[155] van der Weide, E., Gopinath, A. K., and Jameson, A., "Turbomachinery Applications with the Time Spectral Method," *35th AIAA Fluid Dynamics Conference and Exhibit*, AIAA Paper 2005–4905, 2005.

[156] Blanc, F., Roux, F. X., and Jouhaud, J. C., "Harmonic-Balance-Based Code-Coupling Algorithm for Aeroelastic Systems Subjected to Forced Excitation," *AIAA Journal*, Vol. 48, No. 11, 2010, pp. 2472–2481, doi: 10.2514/1.45444.

[157] Pechloff, A. and Laschka, B., "Small Disturbance Navier-Stokes Computations for Low-Aspect-Ratio Wing Pitching Oscillations," *Journal of Aircraft*, Vol. 47, No. 3, 2010, pp. 737–753, doi: 10.2514/1.45233.

[158] Dufour, G., Sicot, F., and Puigt, G., "Contrasting the Harmonic Balance and Linearized Methods for Oscillating–Flap Simulations," *AIAA Journal*, Vol. 48, No. 4, April 2010, doi: 10.2514/1.43401.

[159] Maple, R. C., King, P. I., and Oxley, M. E., "Adaptive Harmonic Balance Solutions to Euler's Equation," *AIAA Journal*, Vol. 41, No. 9, 2003, pp. 1705–1714, doi: 10.2514/2.7316.

[160] Maple, R. C., King, P. I., Orkwis, P. D., and Wolff, J. M., "Adaptive Harmonic Balance Method for Nonlinear Time-Periodic Flows," *Journal of Computational Physics*, Vol. 193, No. 2, 2004, pp. 620–641, doi: 10.1016/j.jcp.2003.08.013.

[161] Hall, K. Thomas, J. and Clark, W., "Computation of Unsteady Nonlinear Flows in Cascades Using a Harmonic Balance Technique," *AIAA Journal*, Vol. 40, No. 5, May, 2002, pp. 879–886, doi: 10.2514/2.1754.

[162] Kreiselmaier, E. and Laschka, B., "Small Disturbance Euler Equations: Efficient and Accurate Tool for Unsteady Load Prediction," *Journal of Aircraft*, Vol. 37, No. 5, 2000, pp. 770–778.

[163] Lindquist, D. R. and Giles, M. B., "Validity of Linearized Unsteady Euler Equations with Shock Capturing," *AIAA journal*, Vol. 32, No. 1, 1994, pp. 46–53.

[164] Weishaupl, C. and Laschka, B., "Small Disturbance Euler Simulations for Delta Wing Unsteady Flows due to Harmonic Oscillations," *Journal of Aircraft*, Vol. 41, No. 4, 2004, pp. 782–789.

[165] Pechloff, A. and Laschka, B., "Small Disturbance Navier-Stokes Method: Efficient Tool for Predicting Unsteady Air Loads," *Journal of Aircraft*, Vol. 43, No. 1, 2006, pp. 17–29.

[166] Laschka, B., "Unsteady Flows–Fundamentals and Applications," *Unsteady Aerodynamics–Fundamentals and Applications to Aircraft Dynamics, AGARD 386*, 1985, pp. 1.1–1.21.

[167] Thomas, J. P., Dowell, E. H., Hall, K. C., and Denegri, C. M., "Further Investigation of Modeling Limit Cycle Oscillation Behaviour of the F-16 Fighter Using a Harmonic Balance Approach," *46th AIAA/ASME/ASCE/AHS/ASC Structures, Structural Dynamics and Materials (SDM) Conference*, AIAA Paper 2005–1917, April 2005.

[168] Woodgate, M. and Badcock, K., "Implicit Harmonic Balance Solver for Forced Motion Transonic Flow," *AIAA Journal*, Vol. 47, No. 4, 2008, pp. 893–901.

[169] Campobasso, M. S. and Baba-Ahmadi, M. H., "Analysis of Unsteady Flows Past Horizontal Axis Wind Turbine Airfoils Based on Harmonic Balance Compressible Navier-Stokes Equations with Low-Speed Preconditioning," ASME Paper GT2011–45303, 2011.

[170] Thomas, J. P., Duster, C. H., Dowell, E. H., and Hall, K. C., "Unsteady Flow Computation Using a Harmonic Balance Approach Implemented About the OVERFLOW 2 Flow Solver," *19th AIAA Computational Fluid Dynamics Conference*, AIAA Paper 2009–4270, 2009.

[171] Jackson, A., Campobasso, M. S., and Baba-Ahmadi, M. H., "On the Parallelization of a Harmonic Balance Compressible Navier-Stokes Solver for Wind Turbine Aerodynamics," ASME paper GT2011–45306, 2011.

[172] Widhalm, M., Dwight, R. P., Thormann, R., and Hübner, A. R., "Efficient Computation of Dynamic Stability Data with a Linearized Frequency Domain Solver," *Proceedings of European Conference on Computational Fluid Dynamics ECCOMAS CFD*, 2010.

[173] Landon, R. H., "NACA 0012. Oscillating and Transient Pitching," In Compendium of Unsteady Aerodynamic Measurements, AGARD-R-702, Data Set 3, August 1982.

[174] Green, L. L. and Newman, P. A., "Wall-Interference Assessment and Corrections for Transonic NACA 0012 Airfoil Data from Various Wind Tunnels," NASA Technical Paper 3070, April, 1991.

[175] Batina, J. T., "Unsteady Euler Airfoil Solutions Using Unstructured Dynamic Meshes," *AIAA Journal*, Vol. 28, No. 8, 1990, pp. 1381–1388, DOI: 10.2514/3.25229.

[176] Marques, A. N., Simões, C. F. C., and Azevedo, J. L. F., "Unsteady Aerodynamic Forces for Aeroelastic Analysis of Two-Dimensional Lifting Surfaces," *Journal of the Brazilian Society of Mechanical Sciences and Engineering*, Vol. 28, No. 4, 2006, pp. 474–484, DOI: 10.1590/S1678-58782006000400013.

[177] McMullen, M. S., *The Application of Non-Linear Frequency Domain Methods to the Euler and Navier-Stokes Equations*, Ph.D. thesis, Stanford University, Stanford, CA, USA, March 2003.

[178] Mialon, B., Khelil, S. B., Huebner, A., Jouhaud, J.-C., Roge, G., Hitzel, S., Badcock, K., Eliasson, P., Khrabov, A., and Lahuta, M., "European Benchmark on Numerical Prediction of Stability and Control Derivatives," *AIAA Applied Aerodynamics Conference*, AIAA–2009–4116, 2009.

[179] Mialon, B., Khrabrov, A., Da Ronch, A., Cavagna, L., Zhang, M., and Ricci, S., "Benchmarking the Prediction of Dynamic Derivatives: Wind Tunnel Tests, Validation, Acceleration Methods," *AIAA Guidance, Navigation and Control Conference*, AIAA–2010–8244, Toronto, Ontario, 2010.

[180] Hübner, A. R., Bergmann, A., and Löser, T., "Experimental and Numerical Investigations of Unsteady Force and Pressure Distributions of Moving Transport Aircraft Configurations," *47th AIAA Aerospace Sciences Meeting and Exhibit*, AIAA–2009–0091, 2009.

[181] Ghoreyshi, M., Badcock, K. J., Da Ronch, A., Vallespin, D., and Rizzi, A., "Automated CFD Analysis for the Investigation of Flight Handling Qualities," *Mathematical Modelling of Natural Phenomena*, Vol. 6, No. 3, 2011, pp. 166–188, doi: 10.1051/mmnp/20116307.

[182] Da Ronch, A., McCracken, A., Badcock, K. J., Widhalm, M., and Campobasso, M. S., "Linear Frequency Domain and Harmonic Balance Predictions of Dynamic Derivatives," *Submitted to Journal of Aircraft*, 2011.

[183] Ghoreyshi, M., Vallespin, D., Badcock, K. J., Da Ronch, A., Vos, J., and Hitzel, S., "Flight Manoeuvre Validation of Data Tables Generated Using an Aerodynamic Model Hierarchy," *AIAA Atmospheric Flight Mechanics Conference*, AIAA–2010–8239, Toronto, Ontario, 2010.

[184] Da Ronch, A., Badcock, K. J., Wang, Y., Wynn, A., and Palacios, R., "Nonlinear Model Reduction for Flexible Aircraft Control Design," *Atmospheric Flight Mechanics Conference*, Minneapolis, Minnesota, 2011.

[185] Da Ronch, A., McCracken, A., Badcock, K. J., Ghoreyshi, M., and Cummings, R. M., "Modeling of Unsteady Aerodynamic Loads," *Atmospheric Flight Mechanics Conference*, AIAA–2011–2376, Portland, Oregon, 2011.

[186] Attar, P. J., Dowell, E. H., White, J. R., and Thomas, J. P., "Reduced Order Nonlinear System Identification Methodology," *AIAA Journal*, Vol. 44, No. 8, 2006, pp. 1895–1904.

[187] Rugh, W. J., *Nonlinear System Theory. The Volterra/Wiener Approach*, John Hopkins Univ. Press, Baltimore, MD, 1981.

[188] Silva, W. A., "Application of Nonlinear Systems Theory to Transonic Unsteady Aerodynamics Responses," *Journal of Aircraft*, Vol. 30, No. 5, 1993, pp. 660–668.

[189] Fung, Y. C., *An Introduction to the Theory of Aeroelasticity*, Dover, New York, 1993, pag. 446–447.

[190] Leishman, J., "Indicial Lift Approximations for Two-Dimensional Subsonic Flow as Obtained from Oscillatory Measurements," *Journal of Aircraft*, Vol. 30, No. 3, 1993, pp. 340–351.

[191] Ghoryeshi, M., Jirasek, A., Post, M. L., Cummings, R. M., and Decker, R., "A Computational Investigation into the Use of Response Functions for Aerodynamic Loads Modeling," AIAA Paper 2011–3518, 2011.

[192] Ghoryeshi, M., Jirasek, A., Post, M. L., and Cummings, R. M., "Computational Approximation of Nonlinear Aerodynamics Using and Aerodynamic Model Hierachy," AIAA Paper 2011–3667, 2011.

[193] Rizzi, A., Eliasson, P., McFarlane, C., Goetzendorf-Grabowski, T., and Vos, J., "Virtual–Aircraft Design & Control of TransCruiser – a Canard Configuration," *AIAA Guidance, Navigation and Control Conference*, AIAA–2010–8245, Toronto, Ontario, 2010.

[194] Eliasson, P., "EDGE, a Navier-Stokes Solver for Unstructured Grids," FOI Report, FOI–R–0298–SE, 2005.

[195] Vos, J., Chaput, E., Arlinger, B., Rizzi, A., and Corjon, A., "Recent Advances in Aerodynamics inside the NSMB (Navier-Stokes Multi-Block) Consortium," *36th Aerospace Sciences Meeting and Exhibit*, AIAA–1998–0802.

[196] Bérard, A., Cavagna, L., Da Ronch, A., Riccobene, L., Ricci, S., and Isikveren, A. T., "Development and Validation of a Next-Generation Conceptual Aero-Structural Sizing Suite," *Proceedings of the 26th International Congress of the Aeronautical Sciences*, ICAS 2008–1.6.2, Anchorage, Alaska, USA, 2008.

[197] McFarlane, C., Richardson, T. S., Da Ronch, A., and Badcock, K. J., "Comparison of Conventional and Asymmetric Aircraft Configurations using CEASIOM," *AIAA Guidance, Navigation and Control Conference*, AIAA–2010–8243, Toronto, Ontario, 2010.

[198] Da Ronch, A., Ghoreyshi, M., Vallespin, D., Badcock, K. J., Zhang, M., Oppelstrup, J., and Rizzi, A., "A Framework for Constrained Control Allocation Using CFD-based Tabular Data," *49th AIAA Aerospace Sciences Meeting*, AIAA–2011–925, Orlando, Florida, 2011.

[199] Raveh, D. E., "Maneuver Load Analysis of Overdetermined Trim Systems," *Journal of Aircraft*, Vol. 45, No. 1, 2008, pp. 119–129.

[200] Hübner, A. R., "Final Summary of Wind Tunnel Test (Steady/Unsteady Force and Pressure Measurements of the DLR–F12 Model in the DNW–NWB within the European Research Project SimSAC)," SimSAC–Task 4.1–1, Delivery Number D 4.1–1, 20 April 2008.

[201] Cooper, G. E. and Harper, R. P., "The Use of Pilot Rating in the Evaluation of Aircraft Handling Qualities," NASA TN D–5153, 1969.

[202] Da Ronch, A., McFarlane, C., Beaverstock, C., Oppelstrup, J., Zhang, M., and Rizzi, A., "Benchmarking CEASIOM Software to Predict Flight Control and Flying Qualities of the B–747," *Proceedings of the 27th Congress of the International Council of the Aeronautical Sciences*, ICAS 2010–282, 2010.

[203] Heffley, R. K. and Jewell, N. F., "Aircraft Handling Qualities Data," NASA CR 2144, Dec. 1972.

[204] Rodney, C. H. and Nordwall, D. R., "The Simulation of a Jumbo Jet Transport Aircraft. Volume II. Modelling Data (B747)," The Boeing Company, Wichita Division, 1970.

[205] Winchenbach, G. L., Uselton, R. L., Hathaway, W. H., and Chelekis, R. M., "Free-Flight and Wind-Tunnel Data for a Generic Fighter Configuration," *Journal of Aircraft*, Vol. 21, No. 1, 1984, pp. 5–13.

[206] Nash, S. G. and Sofer, A., *Linear and Nonlinear Programming*, Mechanical Engineering Series, McGraw–Hill International Editions, 1996.

[207] Ross, I., Sekhavat, P., Fleming, A., Gong, Q., and Wei Kang, W., "Pseudospectral Feedback Control: Foundations, Examples and Experimental Results," *AIAA Guidance, Navigation and Control Conference and Exhibit*, AIAA–2006–6354, 2006.

[208] Betts, J. T., "Survey of Numerical Methods for Trajectory Optimization," *Journal of Guidance, Control, and Dynamics*, Vol. 21, No. 2, 1998, pp. 193–207.

[209] Hull, D. G., "Conversion of Optimal Control Problems into Parameter Optimization Problems," *Journal of Guidance, Control, and Dynamics*, Vol. 20, No. 1, 1997, pp. 57–60.

[210] Brinkman, K. and Visser, H. G., "Optimal Turn-Back Manoeuvre after Engine Failure in a Single-Engine Aircraft During Climb-Out," *Proceedings of the Institution of Mechanical Engineers, Part G: Journal of Aerospace Engineering*, Vol. 221, No. 1, 2007, pp. 17–27.

[211] Vallespin, D., Ghoreyshi, M., and Badcock, K. J., "Assessment of the Limits of Tabular Aerodynamic Models for Flight Dynamics Analysis using the SACCON UCAV Configuration," *RAeS Aerodynamic Conference*, 2010.

[212] Lighthill, M. J., "Oscillating Airfoils at High Mach Number," *Journal of the Aeronautical Sciences*, Vol. 20, No. 6, 1953.

[213] Lomax, H., "Indicial Aerodynamics," AGARD Manual of Aeroelasticity, Part II, 1960, Chapter 6.

[214] Raveh, D. E., "Reduced-Order Models for Nonlinear Unsteady Aerodynamics," *AIAA Journal*, Vol. 39, No. 8, 2001, pp. 1417–1429.

[215] Singh, R. and Baeder, J., "Direct Calculation of Three-Dimensional Indicial Lift Response Using Computational Fluid Dynamics," *Journal of Aircraft*, Vol. 34, No. 4, 1997, pp. 465–471.

[216] Jones, R. T., "The Unsteady Lift of a Wing of Finite Aspect Ratio," NACA Report Nr. 681, 1940.

[217] Garrick, I. E., "On Some Reciprocal Relations in the Theory of Non-stationary Flow," NACA Report Nr. 629, 1938.

[218] Jones, W. P., "Aerodynamic Forces on Wings in Non-uniform Motion," Aeronaut. Research Council R. & M., 1945.

[219] Leishman, J. G., "Unsteady Lift of a Flapped Airfoil by Indicial Concepts," *Journal of Aircraft*, Vol. 31, No. 2, 1994, pp. 288–297.

[220] Zaide, A. and Raveh, D., "Numerical Simulation and Reduced-Order Modeling of Airfoil Gust Response," *AIAA Journal*, Vol. 44, No. 8, 2006, pp. 1826–1834, Airfoil gust response;Computational fluid dynamics (CFD);Pitching moment histories;Reduced order modeling;.

[221] Bisplinghoff, R. L., Ashley, H., and Halfman, R. L., *Aeroelasticity*, Dover, New York, 1996, pp. 350–351.

[222] Mazelsky, B. and Drischler, J. A., "Numerical Determination of Indicial Lift and Moment Functions for a Two-Dimensional Sinking and Pitching Airfoil at Mach Numbers 0.5 and 0.6," NACA TN 2793, 1952.

Appendix A

Applications to Flight Dynamics

Six test cases are now presented. Each case study is briefly described and then emphasis is put on table generation and on the application of the aerodynamic database. The details of each study are given in associated references. The point of the discussion here is to illustrate that a variety of applications have been investigated using the framework described in Section 2.3. The first four testcases focus on the prediction of stability and control characteristics, and the last two on some aspects of flight dynamics. Of interest, Appendix A.5 shows that the inclusion of dynamic derivatives may be important in replaying manoeuvres at high angular rates.

A.1 Transonic CRuiser Model

The design of the Transonic CRuiser (TCR) model was made during the SimSAC (Simulating Aircraft Stability and Control Characteristics for Use in Conceptual Design) project [1]. The final configuration includes an all-moving canard for longitudinal control. More details on the model design are given, for example, in [80, 147, 193]. The mission profile is illustrated in Fig. A.1, and shows the requirement for a design cruise speed in the sonic speed range. The specification for a cruise Mach number of 0.97 was set to stress the shortcomings of engineering methods traditionally used in the early design phase. A wind tunnel model was built and wind-tunnel testing for static and dynamic conditions was performed in the wind tunnel facilities at the Central Aerohydrodynamic Institute, TsAGI [148] (Fig. A.2).

Three questions were addressed. First, the availability of wind tunnel measurements made the configuration useful to assess the level and range of validity of several aerodynamic models. Then, the kriging-based framework was tested for the generation of a database of forces and moments calculated from different fidelity models and measured from testing. To evaluate the sensitivity arising from the aerodynamics, the database of numerical data was compared to the database of wind-tunnel data in terms of stability

[1] `http://www.simsacdesign.eu` [retrieved March 19, 2012]

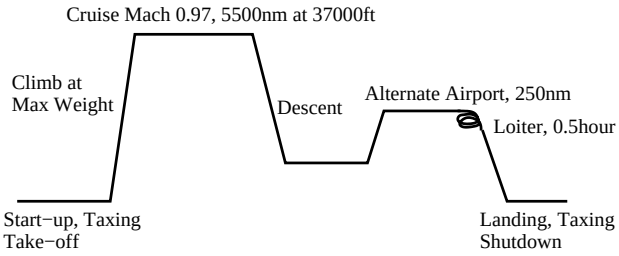

Figure A.1: Mission profile for the TCR configuration

(a) Canard wing on

(b) Canard wing off

Figure A.2: Wind-tunnel testing of the TCR model in TsAGI [148]

and control characteristics at low speed. Finally, the use of CFD to predict the flying characteristics in the transonic speed range was investigated.

Two aerodynamic models were considered. At the low fidelity level, the linear potential method was used to provide computationally cheap estimates of aerodynamic loads. CFD was employed as the high-fidelity option to better represent non-linear compressibility effects and viscous contributions (see Fig. A.3). Three CFD solvers were exercised and compared to experimental data. In addition to RANS simulations, the flow was modeled with the Euler equations in the EDGE [194] and NSMB [195] analyses, while the PMB solver was used for the computation of dynamic stability derivatives from forced motions (see Chap. 3). A grid was generated for each solver. Further details on numerical modelling, static and dynamic cases can be found in [85, 147, 148, 179].

To assess the accuracy of the computations, numerical simulations were compared against wind tunnel measured data. The pitching moment is an interesting figure of merit for stability and control studies, and is shown in Fig. A.4. Low- and high-fidelity aerodynamic models are compared to experimental data. The moment curve exhibits several discontinuity points and a non-linear behaviour, which makes it suitable to show the range of validity of the aerodynamic models. The low-fidelity model predicts

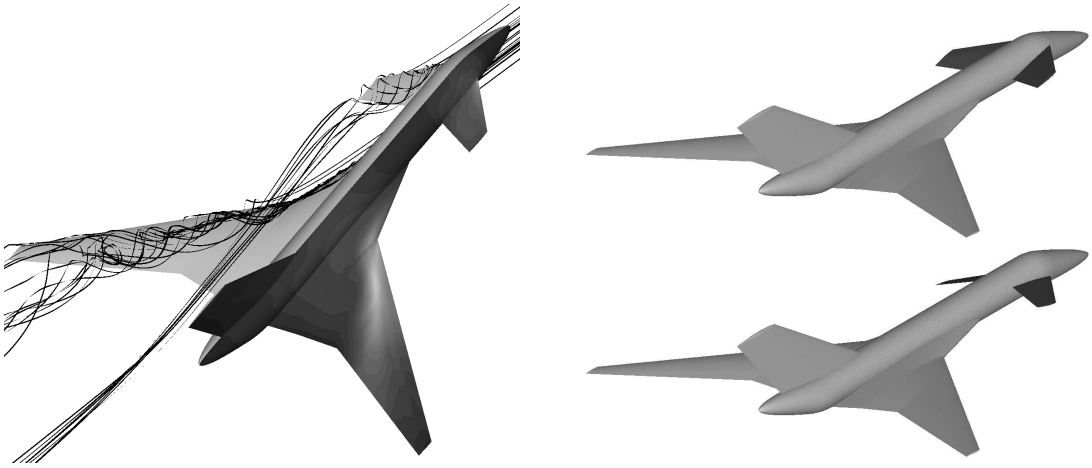

(a) Flowfield visualization (b) Deflected canard wing

Figure A.3: TCR wind tunnel model; in (a), flow development computed using the PMB solver at 18° angle of attack at low speed; in (b), canard deflections of ±10° on a grid for use with the EDGE solver

a linear moment curve with constant negative slope for all angles of attack tested and reasonable estimates are obtained in the range ±5°. A significant improvement in the correlation to experimental data is achieved by the high-fidelity aerodynamic model. Except for a localized deviation at twenty degrees incidence, the CFD results are within a five percent band of the maximum value from the experimental curve up to twenty-five degrees. At higher angles of attack, the CFD solutions are less accurate. More details on flow mechanisms leading to observed non-linearities in the moment curve can be found in [147]. Note that a systematic grid refinement study was not shown in any of the mentioned references.

A factor in using a kriging-based framework is the ability to combine many computationally cheap estimates from the low-fidelity model and few high-quality information from a limited number of expensive high-fidelity simulations. This was key for the generation of aerodynamic data to cover a flight envelope from low speed up to transonic cruise speed. Each aerodynamic model was used in a domain which is the most representative of its validity.

At low speed, a dataset of measured and computed aerodynamic predictions was generated. Each dataset included two sub-tables, that is, a baseline table of static dependencies (α, M, β) and a sub-table for the canard deflection (α, M, δ). The aerodynamic database representative of wind tunnel testing was obtained by compiling in tabular form the measured force and moment coefficients. Static wind tunnel testing was performed at a nominal Mach number of 0.17 for several values of angle of attack. The angle of attack was varied from $-10°$ up to 40°, and the angle of sideslip up to 16°, with a step increment of 2° in both cases. The increments in aerodynamic loads due to canard deflection were measured for deflection angles from $-30°$ up to 10° at

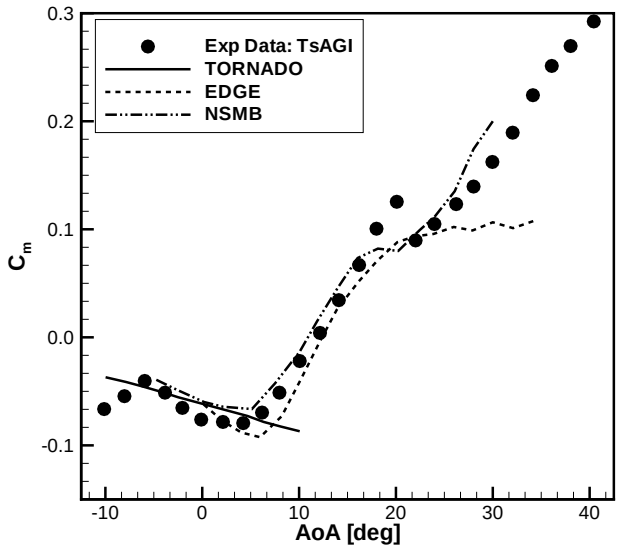

Figure A.4: Pitching moment coefficient at low speed for the TCR model; the reference point is located at the centre of gravity given in Table A.1

increments of 5°. A negative canard deflection indicates trailing-edge down. Kriging interpolation was used to extract the aerodynamic quantities at any combination of flight conditions and canard setting not included in the tabular model.

The database of aerodynamic information from computed results was generated as follows. A low-fidelity representation of the tables was first obtained using the linear potential method. The sampling approach in combination with the RMS criterion filled the baseline table and the sub-table for different canard deflection angles. The flight envelope was limited between $-10°$ and $10°$ for the angle of attack, and from 0.1 up to 0.64 for the Mach number. The low-fidelity database was then incremented by combining it with the high-fidelity aerodynamic results from RANS analyses. The EDGE solver was used in the angle of attack range between $-4°$ and $34°$, and the influence of canard deflection was investigated for a deflection angle of $-5°$ and $-10°$. The NSMB solver provided aerodynamic information for an angle of attack between $-5°$ and $30°$, limiting the sideslip angle up to $5°$. The influence of the canard was computed at $5°$ and $10°$ deflection angles. The PMB solver was considered in the angle of attack range at which measurements were performed, from $-10°$ up to $40°$. A set of static and dynamic stability derivatives was obtained for different reduced frequencies and several angles of attack. Data fusion was used to update the low-fidelity results with these high-fidelity calculations.

In the absence of wind tunnel testing in the transonic speed range, one database of computed aerodynamic loads was generated. Use of CFD was considered the only reasonable option for accurate predictions in this range. All CFD analyses were made

for symmetric flow, a combination of Euler and RANS models was considered and the influence of the Mach number and canard deflection were investigated. Euler analyses were performed using the EDGE solver. The Mach number was set to 0.65, 0.75 and 0.85 and three values of the angle of attack were considered. For all flow combinations, a canard deflection of 5° and 10° was computed. The NSMB solver performed Euler analyses for three values of the angle of attack (−5°, 0° and 5°) and three values of the Mach number (0.60, 0.92 and 0.97). For all combinations of these parameters, the influence of the canard deflection was investigated for angles of −5° and 5°. RANS calculations were made at cruise Mach number and angle of attack of −1°, 0° and 1°. At these flight conditions, aerodynamic increments due to the canard for deflection angles of 5° and 10° were calculated. These CFD runs were used to create the corresponding high-fidelity aerodynamic database at the transonic speed range with kriging interpolation.

The coverage of the angle of attack and Mach number space is illustrated in Fig. A.5 for the low- and high-fidelity aerodynamic models. The shaded area represents many cheap solutions obtained using TORNADO in combination with the sampling approach. The large number of CFD calculations clustering at low speed was motivated by two needs, that is, to benchmark the results obtained using different solvers and to establish the range of their validity. Conditions at which wind tunnel testing was performed are not included as they would cover the CFD data at low speed. The data shown are a fraction of the calculations computed for the complete aerodynamic database. Including the dependencies on the angle of sideslip and deflection of the canard wing, a total of 270 CFD calculations was performed, of which one third were solving the Euler equations.

Flight dynamics studies require information on the mass and inertia properties of the model, which might not be readily available even for flying configurations. Without any other information, the CEASIOM (Computerized Environment for Aircraft Synthesis and Integrated Optimization Methods) software [2] was used to estimate these data [196]. Reference values and predicted mass and inertia information are given in Table A.1. The propulsion system is assumed to provide the necessary thrust during all phases of the flight envelope.

The application of the aerodynamic databases was focused on the prediction of the trim conditions and flight handling qualities. In the subsonic speed range, the databases based on wind tunnel measurements and numerical results were compared in terms of trim conditions. A decrease in trim angle of attack and canard deflection for increasing speed was reported, with a reasonable agreement between tunnel and numerical results. Note that the dynamic pressure was altered to extrapolate the trim conditions for the wind tunnel dataset to higher speeds than the nominal speed at which measurements were performed. At transonic speed and high altitude, the investigations found that a

[2] `http://www.ceasiom.com/` [retrieved March 19, 2012]

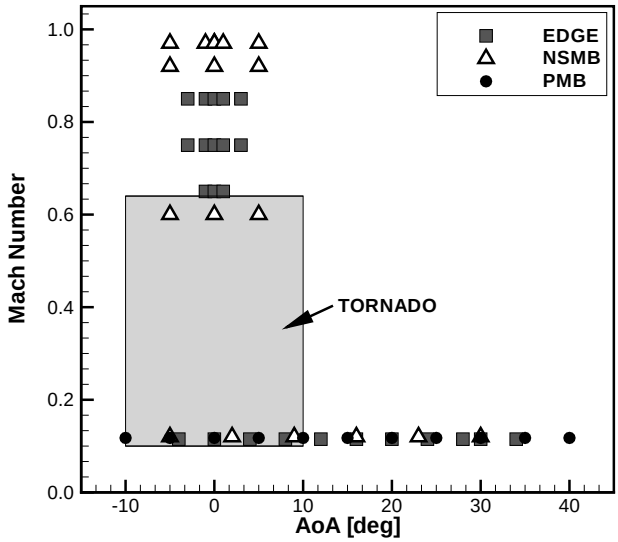

Figure A.5: Distribution of low- and high-fidelity calculations in the two-dimensional parameter space of angle of attack and Mach number; the shaded area illustrates many solutions obtained using the linear potential method, TORNADO; CFD solutions were obtained at an ensemble of isolated points

Parameter	Value
S	$488.96\,m^2$
b	$44.8\,m$
c	$11.772\,m$
d	$63.84\,m$
x_{cg}	$38.33\,m$
z_{cg}	$0.0\,m$
$MTOW$	$208 \times 10^3\,kg$
I_{xx}	$15.17 \times 10^6\,kg{\cdot}\,m^2$
I_{yy}	$17.52 \times 10^6\,kg{\cdot}\,m^2$
I_{zz}	$32.10 \times 10^6\,kg{\cdot}\,m^2$

Table A.1: Reference values and mass and inertia properties of the TCR aircraft model

nearly constant canard deflection was required for trim at all speeds tested except in the vicinity of the speed of sound. The reason for this was related to the formation of shock waves on the main wing aft of the centre of gravity, producing a pitch-down tendency. It is worth mentioning that the trim canard deflection falls outside the range of values at which CFD calculations were computed, and the results presented were possibly extrapolated. Tables should be extended to confirm the results. The assessment of the flight handling qualities indicated poor longitudinal characteristics at low speed, which

were found acceptable in the transonic regime. With the appearance of shock waves, the aerodynamic centre moves away from the centre of gravity. A consideration is for the increasing value of static margin for increasing speed, and illustrates a challenge in designing a transonic airplane.

The point of the discussion of the TCR results was to show what is now possible with the framework described above. Although a large number of CFD calculations at low speed was motivated by the availability of tunnel measurements, different fidelity aerodynamic models were exercised, and predictions combined into one single database. The generation of aerodynamic tables was key to the subsequent investigations into the area of stability and control. It is worth noting that flight dynamics issues such as poor flying qualities at low speed and improved flying qualities across the transonic region were related to what was observed in physics-based simulations.

A.2 Asymmetric Aircraft Model

The purpose of the study detailed in [197] was to investigate whether drag reductions in cruise condition can be achieved for an aircraft by selecting a three-lifting surface asymmetric design. A conventional T-tail design based on the existing Eclipse Aerospace 500 Very Light Jet (EA500), as seen in Fig. A.6(a), was selected as the baseline aircraft, and this was redesigned into a novel asymmetric configuration. Aerodynamic databases were generated for both aircraft based on CFD simulations, and the thrust required to achieve trim in the cruise condition was assessed for each case.

The novel configuration was designed to fullfil the same role as the baseline aircraft, with design decisions made to ensure that any drag reduction was a result of using three-lifting surfaces rather than from relaxing the static margin. The same mass and inertia properties were used for both aircraft to isolate any improvement attributable to the aerodynamics. Look-up tables were generated with the same CFD solver. The asymmetric three-lifting surface aircraft is referred hereafter as the Z-configuration, as opposed to the baseline configuration to indicate the original T-tail design.

The Z-configuration has a split wing, with the starboard semi-wing located low on the fore fuselage, and the port semi-wing located high on the aft fuselage. Both semi-wings have the same area and span but different sweep and dihedral angles. There is no horizontal tail, and the vertical tail is canted to starboard to provide a third lifting surface, with a dihedral angle of 35°. Figure A.7(a) shows an overhead view of the two aircraft configurations. For the Z-configuration, five control surfaces were created. Two ailerons on the outer sections and two elevators on the inner sections of each semi-wing, and a rudder on the canted vertical tail are shown in Fig. A.7(b).

As the interest is around the cruise condition at the higher end of the subsonic speed range, the flow was modeled using the Euler equations. The flow solver used for the aerodynamic predictions was EDGE. The low-fidelity aerodynamic models were not

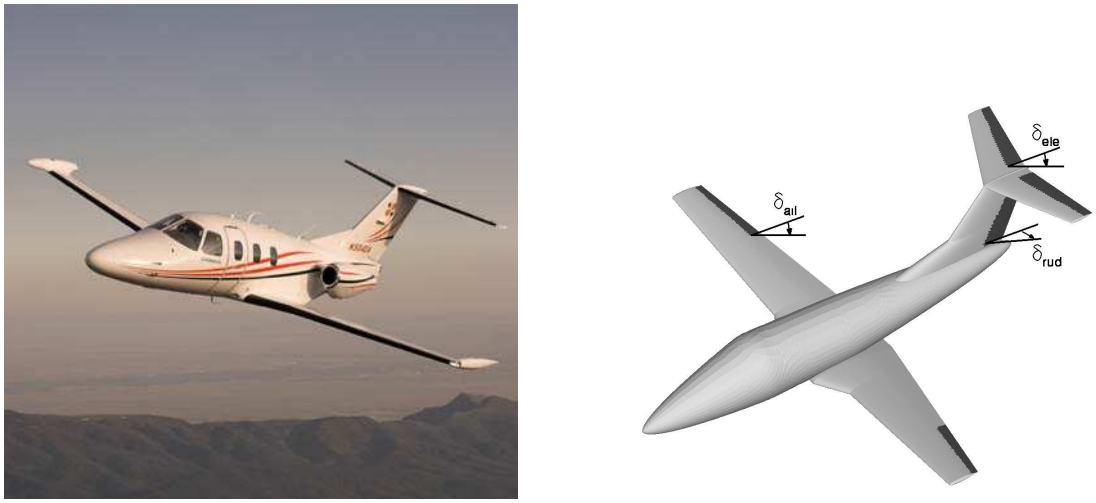

(a) EA500 Very Light Jet (b) Baseline configuration with control surfaces

Figure A.6: Baseline configuration representative of the EA500 Very Light Jet

considered in this case study. A simplified geometry representative of the EA500 was constructed with a best-fit of the overall shape from available three-dimensional views, and is shown in Fig. A.6(b) with positive deflection of control surfaces. Engine nacelles were removed from the model. This was considered a reasonable simplification because the emphasis here is on the comparison between two aircraft configurations using the same aerodynamic model.

An unstructured grid for each configuration was generated. The grid for the baseline configuration was obtained with approximately 130k nodes and 830k edges, whilst the grid for the Z-configuration contains approximately 188k nodes and 1.1 million edges. Grid points were clustered at the leading- and trailing-edges, and a finer spatial resolution was used for the control surfaces. This explains the larger grid size for the Z-configuration with controls extending throughout most of the lifting surfaces. To automate the generation of aerodynamic tables and to work with one single grid for each configuration, the transpiration boundary approach was used to calculate the aerodynamic increments due to control deflection.

A flight envelope around the cruise condition was defined for the generation of the look-up tables. The complete aerodynamic database included the effects of angle of attack, Mach number, sideslip angle and the deflection of control surfaces. The angle of attack varied between $-4°$ and $10°$, the Mach number between 0.20 and 0.65 and the angle of sideslip up to $6°$. The deflection of the ailerons and elevator was limited up to $15°$, while the rudder was deflected up to $20°$. The run matrix included 8 separate values for the angle of attack, 4 for the Mach number and 5 for the sideslip angle. Five values were used for all controls. The aerodynamic dataset for the baseline configuration included a total of 640 flow conditions for different control settings. With the inclusion of more control surfaces, the database of the Z-configuration had a larger number of

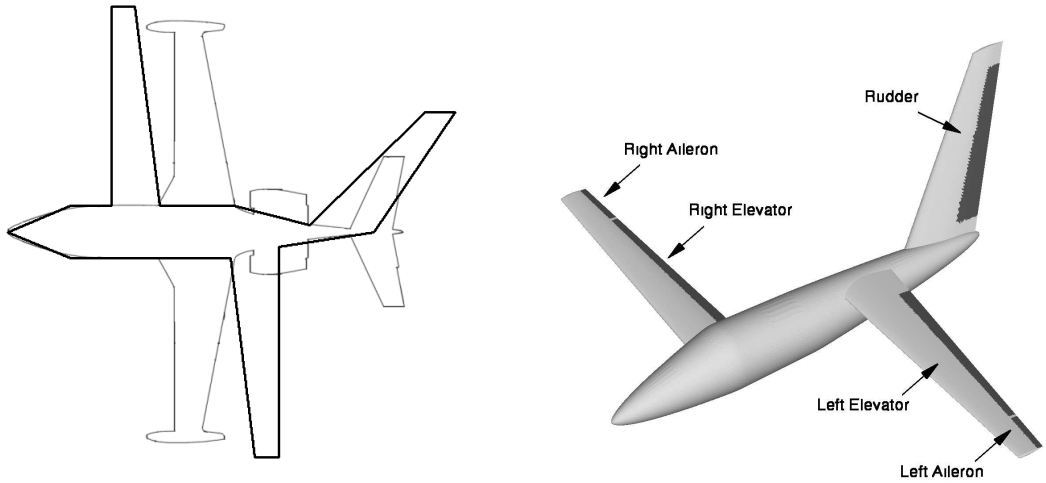

(a) Overlay of original and asymmetric models (b) Z-configuration with control surfaces

Figure A.7: Asymmetric three-lifting surface configuration

table entries. Aerodynamic tables for the baseline configuration were generated using the EDGE solver as the source of the aerodynamic predictions as follows. The sampling approach based on the RMS criterion was used for the generation of the baseline table, and kriging interpolation was then used to interpolate the 45 sample database to the remaining flight conditions. Three sub-tables were then generated to represent the aerodynamic increments due to control deflections. With a general overview of the aerodynamic loads given by the baseline table, sample points were located along the borders of the three-parameter domain to avoid extrapolation. A median location within the parameter space was also chosen. While a few sample points were selected, in the parameter range examined the aerodynamic responses were expected to behave linearly, so that the limited number of calculations was sufficient. Each sub-table was filled out with the co-kriging approach. To verify the quality of the prediction model, additional calculations were performed at a few random untried locations and compared against the predicted value obtained from the tables. In all cases, predicted values from the look-up tables matched well the actual values from simulation. A total of 130 CFD simulations were performed for the baseline configuration to generate all required look-up tables. For the Z-configuration, the baseline table was generated from scratch. Sampling based on the RMS criterion was again used to populate the table. The geometric asymmetry raises the question of how to control the aircraft with the available control surfaces. Five sub-tables were generated using the Euler equations to include the aerodynamic increments arising from the independent deflection of each control surface. Co-kriging was then used to fill out the remaining entries in each sub-table. The same approach as above for selecting sample points was used. About two-hundred calculations were run for the Z-configuration.

The two aircraft configurations were trimmed at cruise for straight and level flight at a Mach number of 0.65 and an altitude of 10000 m. Mass and inertia properties of the EA500 are available, and these were used for both configurations. The mass at cruise condition was set to 2400 kg, and to guarantee the same static margin as that of the baseline configuration, the centre of gravity of the Z-configuration was moved slightly aft. For the baseline configuration, the lift, drag and pitching moment are controlled by adjusting the angle of attack, elevator deflection and thrust. The asymmetry of the Z-configuration results in a coupling of the longitudinal and lateral quantities. Up to eight parameters can be varied to control the six aerodynamic forces and moments acting on the aircraft, and these are the angles of attack and sideslip, the five control surface deflections and the thrust. The system is overdetermined. Trim configurations were analyzed for a sideslip angle set to zero. Several different angles of attack were used in these configurations, with the smallest control surface deflections achieved when the angle of attack was three degrees. This over-determined trim system was solved whilst constraining one independent variable to zero, therefore the proposed solution might be the optimal solution of a subset problem and not a globally optimum solution of the original problem. A more general approach to formulate the problem involves the solution of a control allocation problem. By defining the independent variables as above and restricting their range as problem constraints, an optimal solution is found minimizing an appropriate functional. The objective of the minimization problem is to achieve the trim condition minimizing the trim drag. More details can be found, for instance, in [198, 199].

Comparison of the thrust required for trim demonstrated that the Z-configuration is a less efficient design than the baseline configuration. The increase in drag was related to the use of larger control surface deflections. A key issue of the novel design was identified in a poor control authority in the lateral and directional channels. Because the tail is canted, the rudder has a small effect on the yawing moment, but a large impact on the pitching moment. Deflecting the rudder on the baseline configuration, on the other hand, affects the yawing moment coefficient over ten times more than the pitching moment coefficient.

The results presented show that the CFD-based framework can be used in a routine basis to screen the potential/limitations of novel aircraft configurations. The key issue here is the generality realized in a CFD simulation, and the absence of any restriction, as in the case of traditional engineering methods, when considering new designs.

A.3 DLR-F12 Model

The DLR-F12 model represents a conventional wing-fuselage-tail configuration for a civil passenger transport aircraft designed by the German Aerospace Center (DLR). A wind tunnel model was built and experimental investigations were conducted in the fa-

cilities of the German-Dutch Wind Tunnels (DNW-NWB) during the SimSAC project (Fig. A.8). Further information on static and dynamic investigations can be found, for instance, in [150, 178, 179, 200]. The need to explore the influence of using different fidelity levels in geometry and aerodynamic modelling was assessed in a previous work [181].

Figure A.8: Wind-tunnel testings of the DLR-F12 model in DNW-NWB [200]

Low- and high-fidelity geometric descriptions of the DLR-F12 wind tunnel model were used in combination with several aerodynamic models. The low-fidelity configuration was built to approximate the wind tunnel model using as few as one hundred geometry parameters. With a generic aerofoil section, a simple description of the foremost fuselage section and approximating the wing-fuselage intersection, this geometry is typical of the conceptual design phase. This configuration is referred hereafter as the XML configuration. An unstructured grid was then generated for this geometry for a solution of the Euler equations. The flow solver used was EDGE.

A multi-block structured topology was created around the wind-tunnel model geometry to allow a high-fidelity representation, and the PMB solver was used to solve the Euler and RANS equations. This configuration is referred to as the WT configuration. A comparison of the XML and WT geometries is illustrated in Fig. A.9.

The generation of aerodynamic tables for the low- and high-fidelity aircraft geometries proved useful in highlighting the benefits of sampling and data fusion. Two separate aerodynamic databases for the XML configuration were generated, that is, based on DATCOM and on the EDGE solver using the Euler equations. The tables obtained from EDGE were created from scratch. The baseline table comprised 648 entries. Sampling based on the EIF criterion was used to search for potential non-linear aerodynamic characteristics, and kriging was used to interpolate the 65 CFD solutions to the remaining flight conditions. Sixteen samples were then generated at random flight conditions, and the directly calculated aerodynamic coefficients were compared to those obtained from the baseline table. In all cases and for all coefficients, the RMS error was small indicating that the baseline table reproduced well the aerodynamic

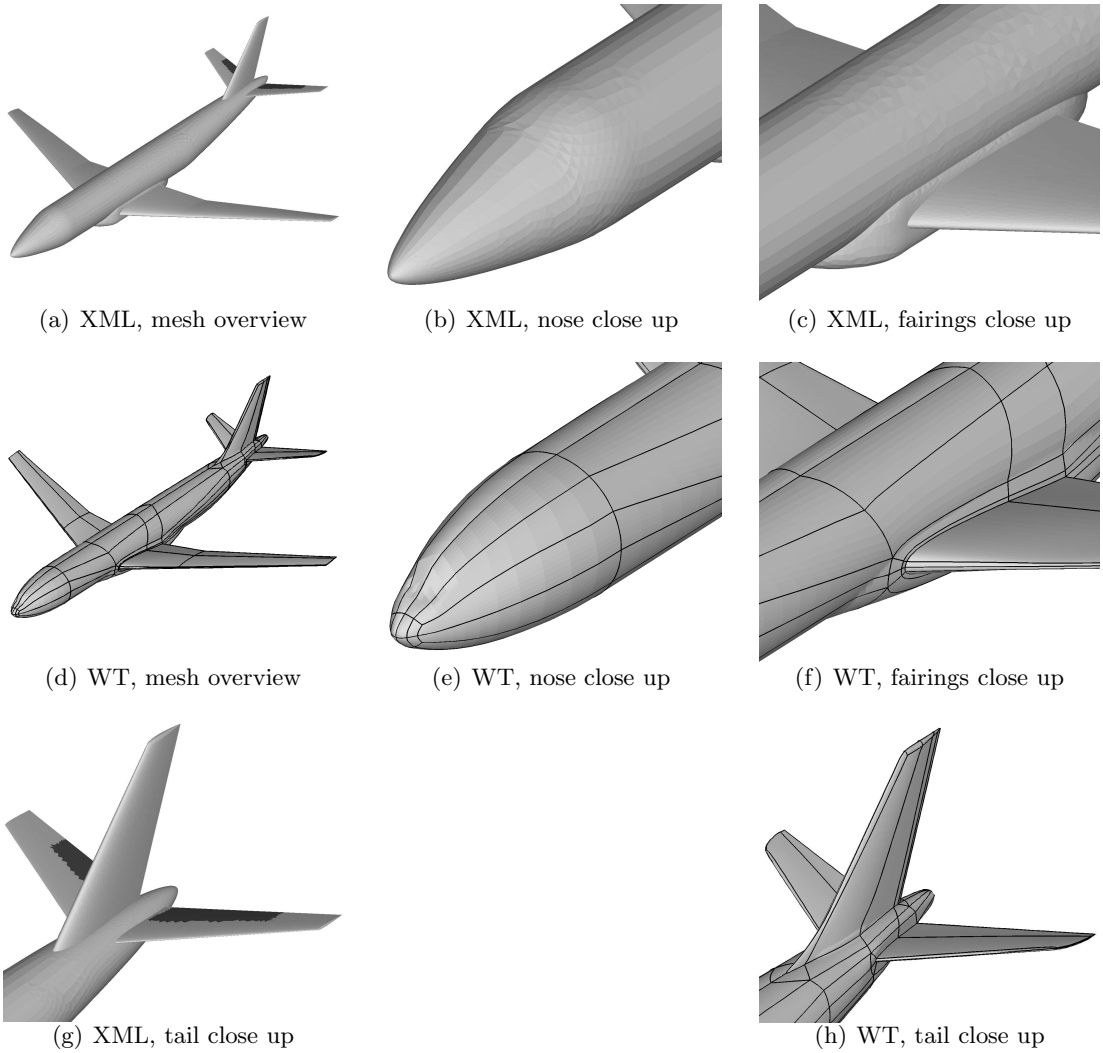

(a) XML, mesh overview (b) XML, nose close up (c) XML, fairings close up

(d) WT, mesh overview (e) WT, nose close up (f) WT, fairings close up

(g) XML, tail close up (h) WT, tail close up

Figure A.9: Different fidelity geometry representations of the DLR-F12 model; XML and WT indicate, respectively, the low- and high-fidelity configurations; the elevator is highlighted in the XML geometry and the WT geometry has been mirrored to facilitate the geometry comparison

characteristics of the underlying XML configuration [181]. The table describing the effect of elevator deflection on aerodynamic loads was then generated. Twelve samples were located along the border of the three-parameter domain and in the non-linear regions observed from the baseline table, such as the combination of high angle of attack and high Mach number. The values at these samples were then used to increment the baseline table using co-kriging. The approach used to calculate the increments due to elevator deflection was based on the transpiration boundary conditions.

Geometry increments from the baseline XML configuration were defined to simulate a design study. Seven parameters were originally investigated, and variations of the wing quarter-chord sweep angle, Λ_w, and wing area, S, are shown in Fig. A.10. The assumption that the flow topology does not change significantly for the incremented geometries is key in this application. For each geometry increment, a baseline table was produced updating the aerodynamic informations from the original XML configuration with additional samples. For each case study, fourteen samples were chosen along the borders of the domain to avoid extrapolation and a few at the higher values of the angle of attack and Mach number. To guarantee that enough information was included in the updated baseline table for the incremented geometries, sixteen additional samples were considered at random locations within the parameter space to check that the tables were adequate. A good accuracy was observed in all cases.

For the WT configuration, a baseline table was constructed based on a few expensive viscous calculations [3]. Twenty samples were chosen in the parameter space, and the PMB solver was used to solve the RANS equations. With the assumption that the WT geometry table is an increment of the XML table, co-kriging was used to update the low-fidelity database and to generate a baseline table for the high-fidelity aerodynamic model. To add the effects of elevator deflection on the baseline WT table, the increments in forces and moments were considered identical to those computed for the XML configuration.

The mass and inertia properties of the DLR-F12 full aircraft model were provided by the DLR. Table A.2 summarizes the reference values, and predicted mass and inertia properties.

The aerodynamic databases for the XML and WT configurations were used to trim the aircraft for a range of flight speeds at an altitude of $6000\,m$. The trim angle of attack, trim elevator deflection and the required thrust are illustrated in Fig. A.11. Results obtained from look-up tables for the two configurations are compared. For the XML configuration, the Euler predictions result in smaller elevator deflection angles than DATCOM, which is explained by the different pitching moment curve slope for the CFD simulations at transonic conditions. The increase in drag force results in an

[3] As an example, while a CFD solution on the XML configuration was obtained in one hour on a single processor, a well converged solution solving the RANS equations on the WT configuration required two hours on thirty-two processors.

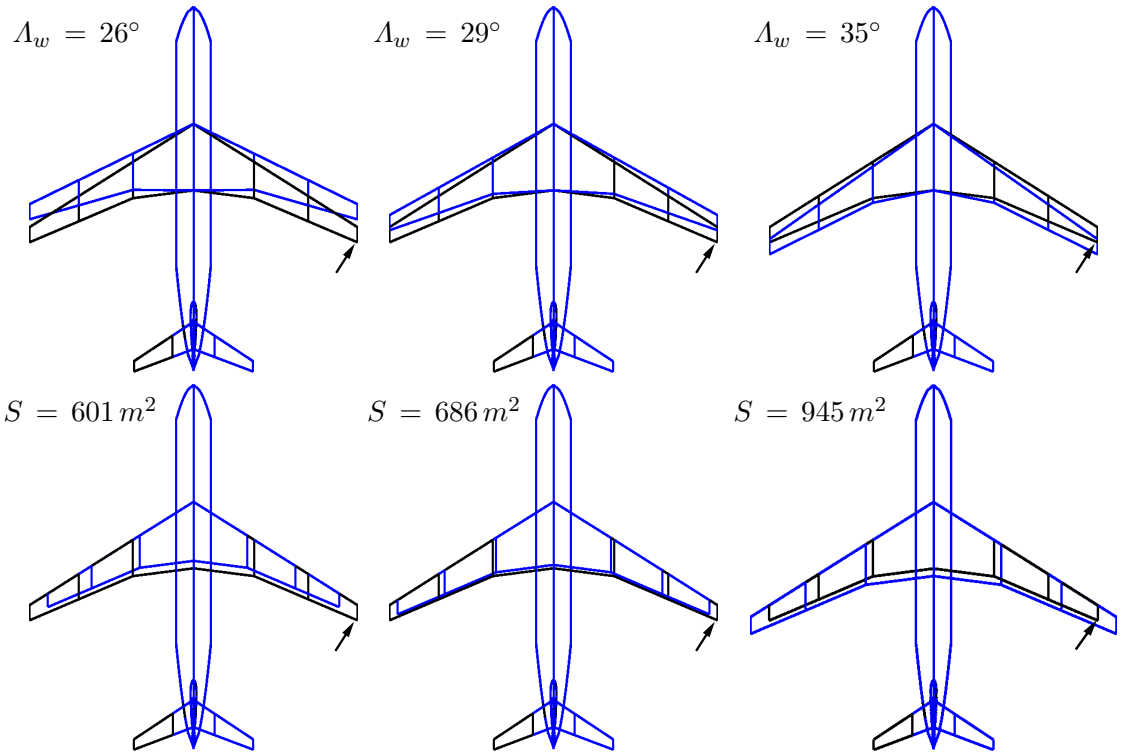

Figure A.10: Geometry increments to simulate a design study, featuring variation of wing quarter-chord sweep angle, Λ_w, and wing area, S; the arrow points at the wing tip trailing-edge of the baseline XML configuration, which represents the original XML design

Parameter	Value
S	$710.62\,m^2$
b	$80.72\,m$
c	$10.105\,m$
x_{cg}	$41.95\,m$
z_{cg}	$-1.21\,m$
$mass$	$115.7 \times 10^3\,kg$
I_{xx}	$11.828 \times 10^3\,kg{\cdot}\,m^2$
I_{yy}	$16.679 \times 10^3\,kg{\cdot}\,m^2$
I_{zz}	$27.163 \times 10^3\,kg{\cdot}\,m^2$

Table A.2: Reference values and mass and inertia properties of the DLR-F12 full aircraft model

increased thrust as the flight speed increases. For the entire speed range, the Euler results for the XML configuration are close and representative of the RANS results for the WT configuration.

Handling qualities were also assessed. Figure A.12 shows the short-period and phugoid characteristics compared to ICAO (International Civil Aviation Organization) opinion-contour graph and using a Cooper-Harper handling qualities rating scale [201].

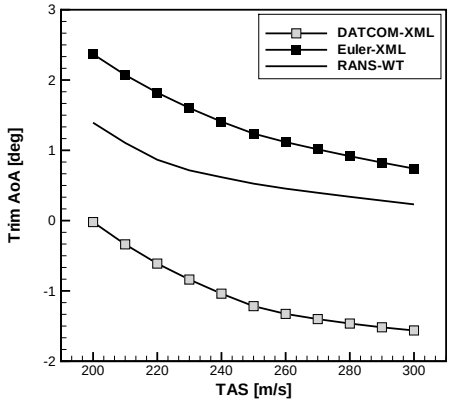

(a) Trim angle of attack

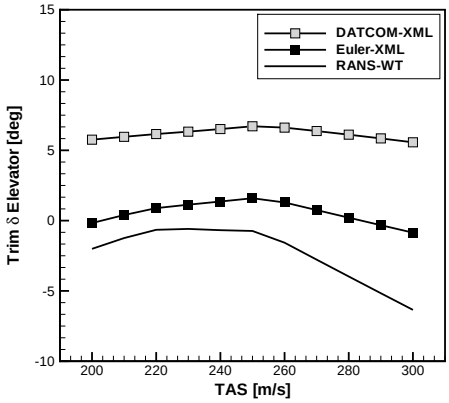

(b) Trim elevator deflection

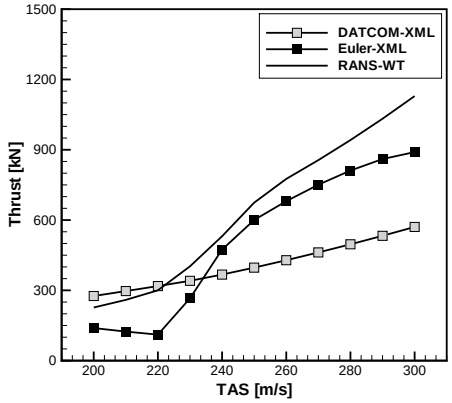

(c) Trim thrust

Figure A.11: Trim conditions for the DLR-F12 full aircraft model at an altitude of 6000 m comparing DATCOM and Euler solutions on the XML configuration and RANS solution on WT configuration

The rating scale establishes a relationship between the stability and control parameters of the airplane and the pilot's opinion of the airplane. The Cooper-Harper handling qualities rating scale goes from 1 to 10 with low numbers corresponding to good flying or handling qualities. The scale is an indication of the difficulty in achieving the desired performance that the pilot expects. Results are based on tables for the XML configuration built using DATCOM and the EDGE solver in Euler mode, and for the WT configuration from the PMB code solving the RANS equations. Two flight speeds, of 200 and $300\,m/s$, are included. For the short-period, DATCOM results are less satisfactory and controllable compared to those found for the Euler option. This is explained considering the very small magnitude of natural frequencies predicted using DATCOM. For the phugoid, a large discrepancy is observed at the higher speed between the Euler-based and DATCOM-based results. This arises from the Euler drag and pitching moment increases at transonic speeds. The Phugoid attributes improve with increasing flight speed for all of the aerodynamic sources, but the DATCOM predicted value is poor. The aircraft natural frequencies are too small when using the DATCOM aerodynamic tables.

The impact of geometry increments on the handling qualities was then investigated. The influence of the wing quarter-chord sweep angle, Λ_w, and wing area, S, on the short-period mode are presented in Fig. A.13. The flight speed is $300\,m/s$ at an altitude of $6000\,m$. While the period, T, depends largely on the pitching moment curve slope, the time to half amplitude, $T_{1/2}$, depends also on the aircraft pitch damping. The predictions include the effect of changes in the moments of inertia and the aircraft mass.

The results suggest that the CFD-based aerodynamic tables provide better understanding of the vehicle handling qualities at transonic conditions, whereas the tables from DATCOM are misleading.

The results presented demonstrate that the CFD-based framework provides a better understanding of the vehicle handling qualities at transonic conditions when compared to results obtained using engineering methods. In addition, the original geometry of the DLR-F12 model was modified to simulate the iterative process of aircraft design. It was shown that a small number of CFD calculations is required to update existing aerodynamic tables, and the impact of some geometric increments on predicted flight handling qualities was assessed.

A.4 Large Transport Civil Aircraft Model

Several aerodynamic models for a large transonic civil aircraft configuration were considered in a previous work [202]. The low-fidelity aerodynamic models were derived from DATCOM and a linear potential solver. For higher fidelity, the flow was mod-

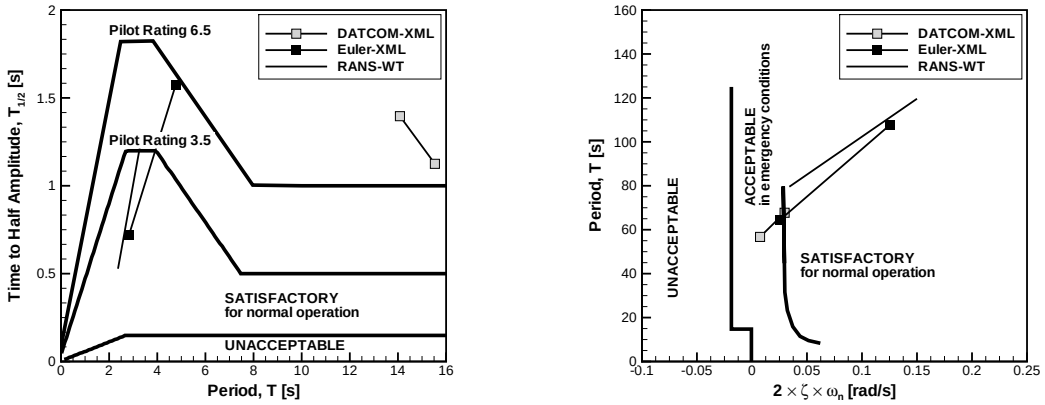

(a) Short-period characteristics

(b) Phugoid characteristics

Figure A.12: Short-period and phugoid characteristics for the DLR-F12 full aircraft model at an altitude of 6000 m compared to ICAO recommendations [201]

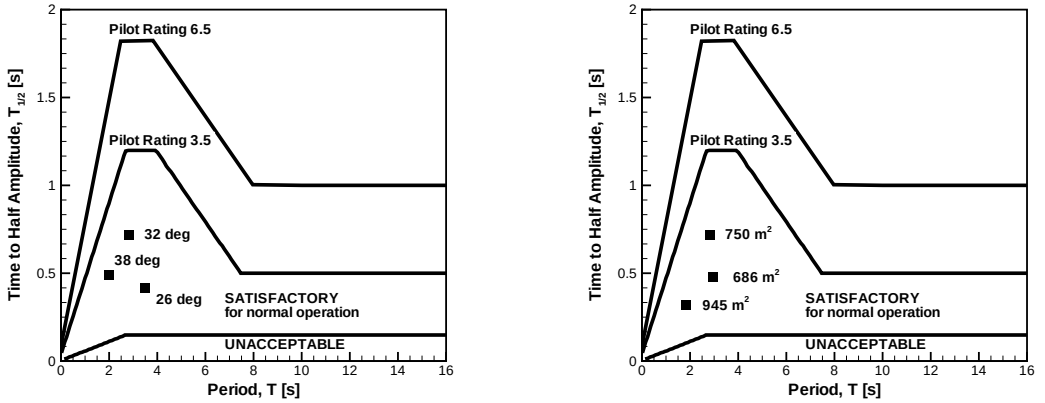

(a) Influence of wing quarter-chord sweep angle

(b) Influence of wing area

Figure A.13: Impact of geometry increments in the short-period characteristics for the DLR-F12 full aircraft model at an altitude of 6000 m

elled using the Euler equations. For shorthand, the configuration is referred to as the B747-like model.

The model geometry was created to best reproduce the layout of the B747 aircraft from available three-dimensional views, as illustrated in Fig. A.14. This simplified geometry, which is well suited in the conceptual design, is built using around one hundred geometric parameters and is shared between all aerodynamic sources. An unstructured grid was generated using the open-source code SUMO [4] for use with the EDGE solver. The grid, suitable to model the flow with the Euler equations, consists of 258 thousand nodes, 1.69 million edges and 1.35 million tetrahedra elements. The surface grid lacks detailed refinement and adopts a simple description for many

[4] `http://larosterna.com/sumo.html` [retrieved March 19, 2012]

components. Control surfaces were sized from the aircraft model. Flaps, inner and outer ailerons on each semi-wing, an all-moving stabilizer, four-segment elevator and two-segment rudder are illustrated in Fig. A.15.

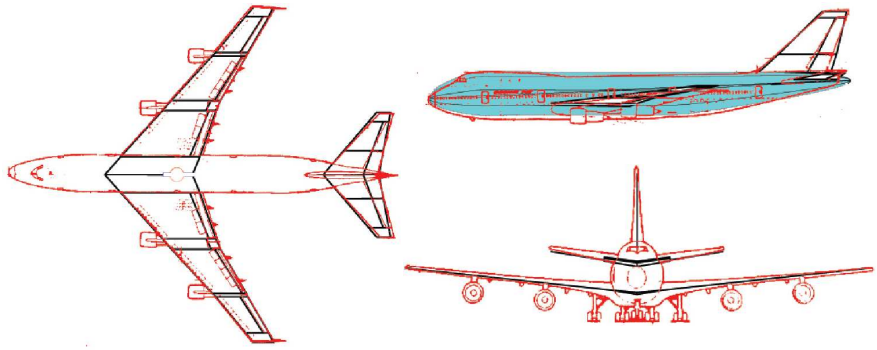

Figure A.14: Overlay of a three-view of a B747 aircraft model and lifting surfaces for low-fidelity aerodynamics

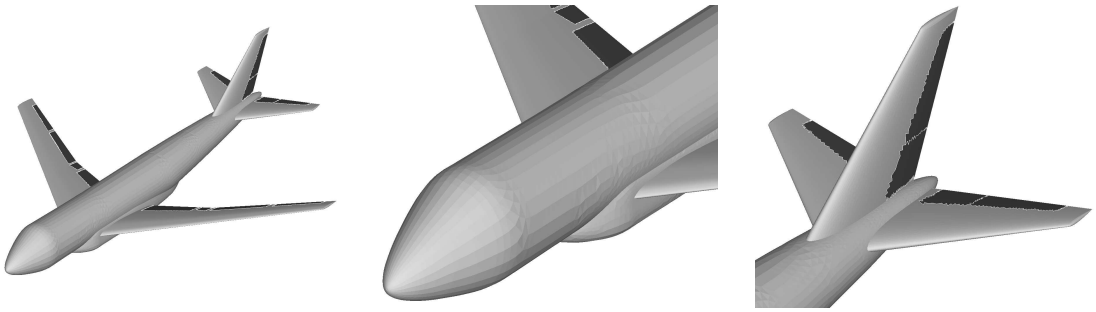

(a) Overview (b) Nose close up (c) Tail close up

Figure A.15: Medium-fidelity surface geometry for the B747-like model with control surfaces

Three aerodynamic databases were created for each aerodynamic model used. To assess accuracy in the results, aerodynamic predictions were compared to experimental data for the B747. Flight handling qualities were also investigated for a transonic cruise condition. The first database to be generated was representative of low-fidelity aerodynamics based on DATCOM estimates. A database was then created using the linear potential method. The corresponding aerodynamic database covered 2160 flight conditions for different control settings. The Mach number varied between 0.1 and 0.9, the angle of attack between $-5°$ and $10°$. The sampling algorithm and the RMS criterion were used to fill out the baseline table. As the dataset was used in a parallel work for a control allocation study [198], control surfaces were independently deflected one at a time. Tables for control surfaces deflection were created using the same sampling approach as for the baseline table.

As most of the benefit in using CFD in Euler mode comes from a better representation of non-linear ompressibility effects, tables representative of this higher-fidelity aerodynamics were generated from scratch for a limited flight envelope around the cruise

speed. In total, the aerodynamic dataset included nearly ten thousand flow conditions. The angle of attack varied between $-5°$ and $10°$, the Mach number between 0.70 and 0.95 and the angle of sideslip up to $6°$. The deflection of the elevator was limited up to $10°$, while the rudder and the ailerons were deflected up to $15°$. The run matrix included 20 separate values for the angle of attack, 10 for the Mach number and 9 for the sideslip angle. For the angular rates and control surface deflections, 15 separate values were selected. The baseline table was created using the sampling methodology in combination with the EIF criterion. The same approach was also used to calculate the increments in aerodynamic loads for the deflection of the two-rudder segments. Due to the aircraft symmetry, only positive deflections were analyzed. Figure A.16 illustrates the variations of aerodynamic coefficients with variations of angle of attack and deflection of the two-rudder segments. As the surfaces shown are for a Mach number of 0.9, they represent a slice through the parameter space $(\alpha, M, \delta_{rud})$. Black cubes indicate actual CFD calculations. In the plots, eight samples were automatically selected at different positions along the borders, mostly at the lower and higher ends of the rudder deflection range. The location and number of samples differ for surfaces at different Mach numbers, and sample points were observed within the surface boundaries for some values of the Mach number. A larger number of sample calculations were placed at the low and high Mach numbers.

Tables for other control surfaces, that is, the all-moving stabilizer, the four-elevator segment and the ailerons, were generated from additional CFD calculations. These sample points were distributed along the border and within the parameter space. One example sample distribution is shown in Fig. A.17 depicting actual CFD calculations and the space spanned by the table for aileron deflections. Co-kriging was then used to update the baseline table for these control deflections. A total of about one hundred CFD calculations was used to fill out the entire aerodynamic database. Transpiration boundary conditions was used throughout this study.

Predictions of aerodynamic loads based on different aerodynamic models were compared to wind tunnel experimental data from [203, 204]. The interest here is on the cruise condition, and more details can be found in [202] for the subsonic speed range.

Fig. A.18 compares aerodynamic coefficients obtained using different fidelity aerodynamic models. For the lift coefficient, the Euler results show the closest correlation to the published data. The actual values and the curve slope compare well to experimental values. DATCOM shows comparable lift curve slope, with the actual values slightly less than experimental data. However, as the Mach number increases, DATCOM results begin to fall away from experimental results. TORNADO results without the compressibility correction remain constant through all Mach numbers, and the offset from experimental data increases because of the more influential effect of compressibility at higher speeds. TORNADO results with the Prandtl-Glauert similarity role overpredict the lift-curve slope, diverging at higher Mach numbers. For the drag

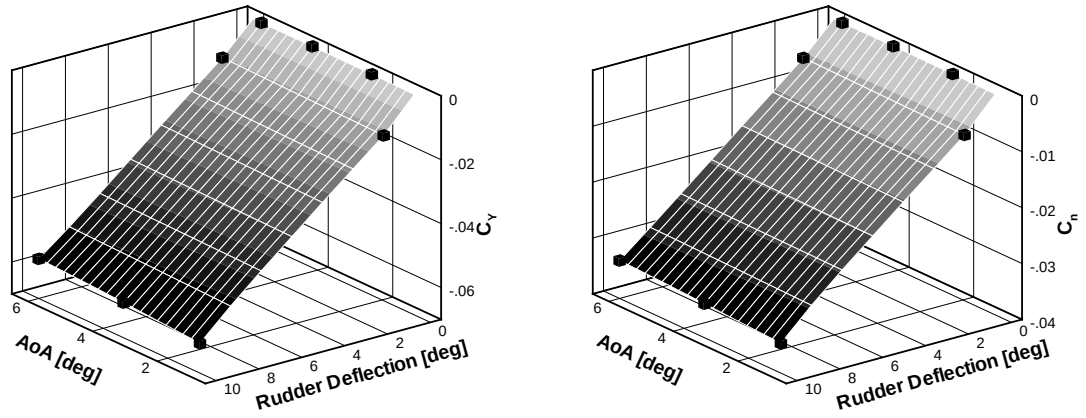

(a) Side force coefficient

(b) Yaw moment coefficient

Figure A.16: Variation of aerodynamic coefficients with angle of attach and rudder deflection at a Mach number of 0.9; the black cubes indicate sample points

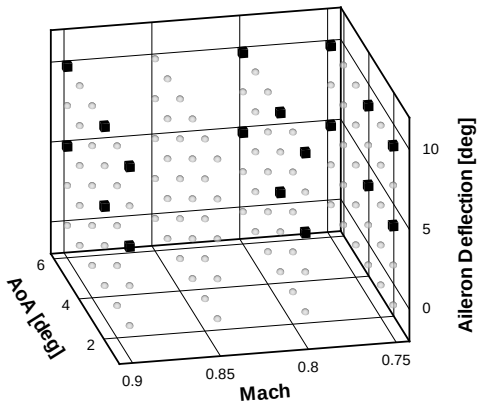

Figure A.17: Illustration of the aerodynamic table for ailerons deflection; black cubes indicate sample points

polar, it is observed that the DATCOM result shows the best correlation with the experimental data. This is not unexpected because DATCOM was developed using conventional configurations and the semi-empirical methods calibrated using, amongst others, data for the B747. The Euler results differ from the viscous experimental data in the absence of any estimate of the drag due to friction. The linear potential results achieve a poor agreement with other data sets. The pitching moment coefficient curve slope is a good indicator of the aircraft static stability. A good correlation of numerical data sets is achieved in terms of stability. However, the numerical values deviate by a constant offset, which suggests discrepancies in the $C_{m\,0}$ value. This is expected because the term is highly dependent on the aerofoil section and fuselage geometry used in the computations. The linear potential results with compressibility correction

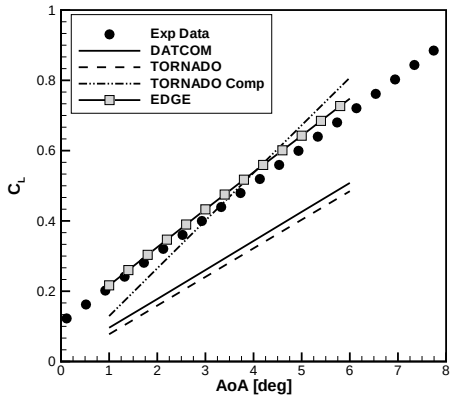

(a) Lift coefficient

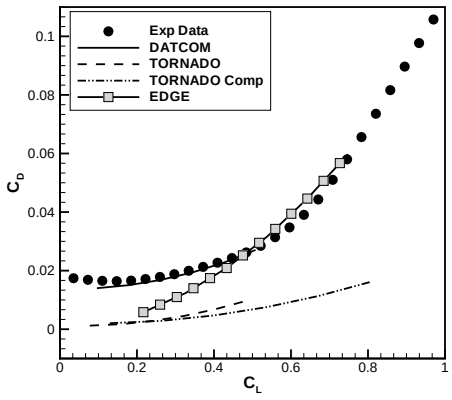

(b) Drag polar

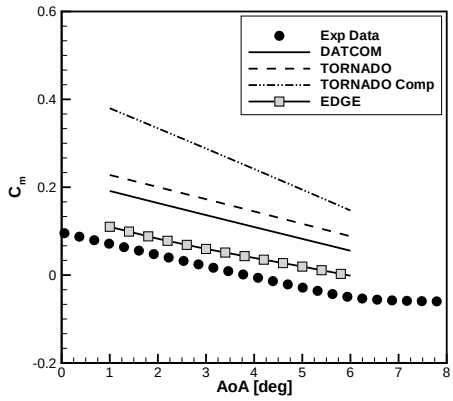

(c) Pitching moment coefficient

Figure A.18: Variable-fidelity aerodynamic predictions compared to experimental data at Mach number of 0.8 for the B747-like model; experimental data are from [204]

overpredicts the curve-slope, amplifying the compressibility effect on the static stability. The Euler results achieve a good comparison with experimental data for the Mach numbers considered. At the higher end of the angle of attack range, the trend line for the experimental data set has non-linear behaviour, possibly caused by interactions of the boundary-layer and shock waves.

For the flight dynamics studies to follow, reference values of the B747-like model are summarized in Table A.3. The mass and inertia properties were estimated, and are given in the same table. The propulsion system was assumed to provide the necessary thrust during all phases of the flight envelope.

Using the available aerodynamic databases, the trim conditions for the B747-like model were computed at cruise altitude of $11000\,m$ for several values of the Mach number. The trim angle of attack and trim elevator deflection are presented in Fig. A.19. The angle of attack required for trim decreases as the Mach number increases, which

Parameter	Value
S	$511.0\,m^2$
b	$59.64\,m$
c	$9.0798\,m$
d	$68.5\,m$
x_{cg}	$29.35\,m$
z_{cg}	$-0.69\,m$
$MTOW$	$367.52 \times 10^3\,kg$
I_{xx}	$32.158 \times 10^6\,kg{\cdot}\,m^2$
I_{yy}	$49.838 \times 10^6\,kg{\cdot}\,m^2$
I_{zz}	$77.613 \times 10^6\,kg{\cdot}\,m^2$

Table A.3: Reference values and mass and inertia properties of the B747-like model

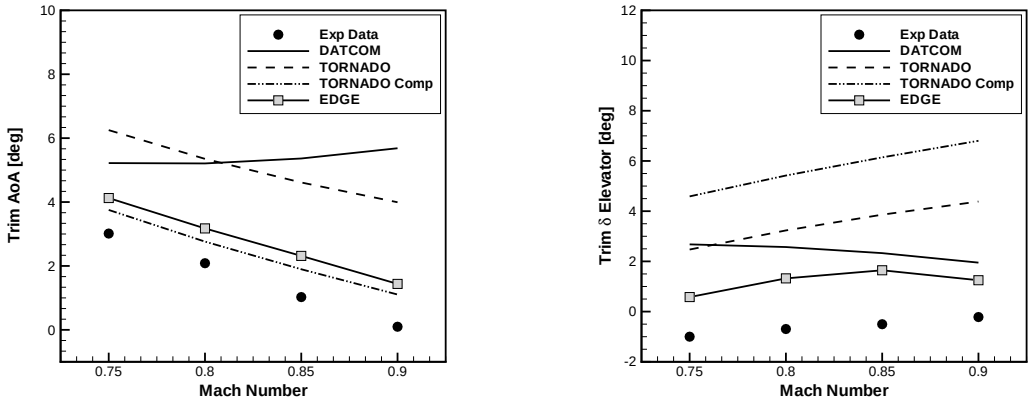

(a) Trim angle of attack

(b) Trim elevator deflection

Figure A.19: Trim conditions at transonic speed range for the B747-like model at an altitude of $11000\,m$ using different fidelity aerodynamic models

is not unexpected due to the corresponding higher dynamic pressure. With significant compressibility effects in the transonic regime, and with shock waves moving downstream on the wings, the aerodynamic centre moves aft and the static margin increases. The required elevator deflection to trim the aircraft also increases. The correlation to experimental data is best for the database of forces and moments generated using the Euler equations. This highlights the shortcomings of engineering methods in the transonic regime, which calls for a higher-fidelity representation of the flow physics as achieved in a CFD simulation. It also indicates that the aerodynamics computed using CFD for the B747-like model is representative of the real aircraft model, and that modelling the flow with the Euler equations on a simplified geometry description can provide the designer with valuable information otherwise not predicted with low-fidelity models.

A.5 Standard Dynamic Model

The framework for generating manoeuvres based on the solution of a time-optimal problem was exercised with the SDM model [23]. More details pertaining the model configuration, block structured grid and numerical simulations were presented in Chapter 3.2.1. To allow manoeuvring the aircraft, control surfaces were added to the computational mesh. Mesh block faces were placed on the control surfaces, and the mesh points on these faces were deflected to define the control surface mode shapes. After the surface grid point deflections are specified, transfinite interpolation is used to distribute these deflections to the volume grid [104]. A view of the surface mesh for the deflected control surfaces is shown in Fig. A.20. An all-moving elevator, ailerons and rudder were used for longitudinal and lateral-directional control.

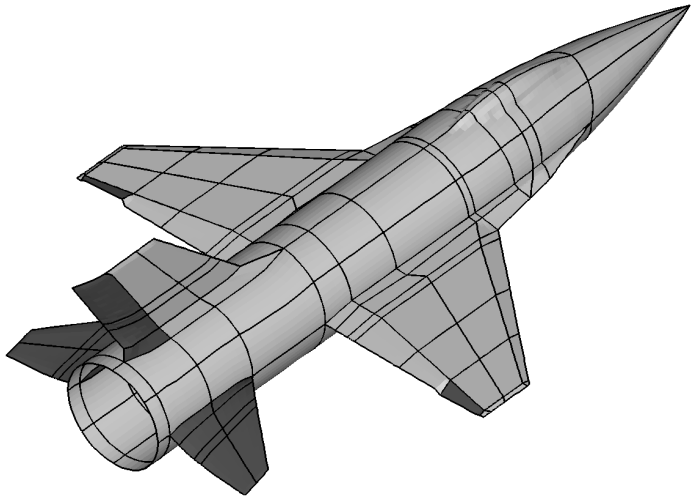

Figure A.20: Deflected control surfaces for the SDM model

Geometry reference values were given in Table 3.1. Mass and inertia properties of the SDM model are available for a free-flight model which represents a 1/72 scale aircraft [205]. These values were scaled-up to match the dimensions of the current computational model. The maximum total thrust force, $T_m = 26.24\,kN$, is assumed to cross the centre of gravity. The direction of the thrust relative to the aircraft is assumed to remain unchanged with altitude and flight speed, and to vary linearly with the engine throttle.

To generate the aerodynamic database of forces and moments, four sub-tables were created, three were for the control surface deflections. The Mach number was varied between 0.1 and 0.4, and all manoeuvres were simulated in the subsonic speed range. The angle of attack was varied between $-14°$ and $28°$, and deflection limit for all controls

Parameter	Value
x_{cg}	$9.91\,m$
$mass$	$9295.44\,kg$
I_{xx}	$12.874 \times 10^3\,kg{\cdot}\,m^2$
I_{yy}	$75.673 \times 10^3\,kg{\cdot}\,m^2$
I_{zz}	$85.552 \times 10^3\,kg{\cdot}\,m^2$

Table A.4: Mass and inertia properties of the SDM model

was set to 20°. Around 6000 table entries were defined. The baseline table consisted of 156 flight conditions, and a brute force approach was considered for varying the Mach number and angle of attack, while keeping the sideslip angle to zero. For the lateral coefficients, a different approach was considered because all the lateral coefficients in the created baseline table were zero. Lateral coefficients obtained using DATCOM were used as low-fidelity data, and then co-kriging with a few Euler results was used to generate the updated baseline table. The dependence of the longitudinal forces and moments on other parameters was assumed to be an increment of the baseline table and the co-kriging data fusion method was used to include these variation in a computationally efficient way. With fifteen additional samples the variation with the elevator, ailerons and rudder was included in the tables. Samples were located at the vertices of the parameter space and at a median value within the domain. The response of the aerodynamic coefficients to variations in angle of attack and elevator deflection at a Mach number of 0.4 is illustrated in Fig. A.21. Considering the non-linear features shown, it can be argued that the number of sample points used was small for an adequate representation of the aerodynamic loads. While static coefficients were adequate to represent aerodynamic loads for slow manoeuvres, the simulation of faster motions included dynamic dependencies. Dynamic derivatives were computed from forced motions, and assumed to be independent of the Mach number and to vary with the angle of attack only. This assumption was demonstrated to be adequate in the speed range below a Mach number of 0.5, as given for example in [85] where dynamic derivatives from low-subsonic to high-transonic regime were compared to experimental results (see also Chapter 3.3.1).

Aerodynamic loads for a set of manoeuvres were predicted using the tabular model of forces and moments, and these were compared to the unsteady CFD solution, which is the reference solution because it is time-accurate. To guarantee a realism in the manoeuvres to be simulated, these were generated solving an optimal control problem. The problem of moving the aircraft from the initial state to the final state is rewritten as a control problem by minimizing a suitable cost function. Constraints are specified for the states, describing the aircraft position and attitude, and for the controls, realizing physical limitations on the use of control effectors. The resulting constrained

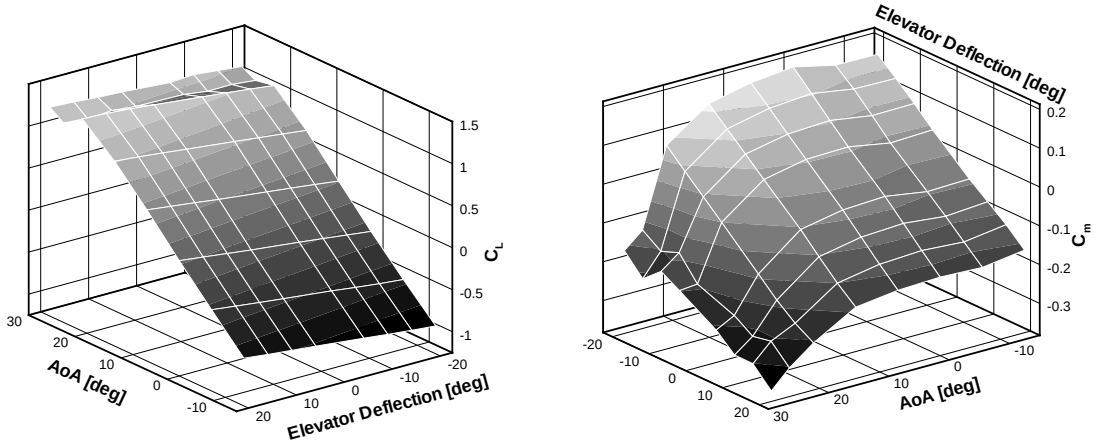

(a) Lift coefficient

(b) Pitching moment coefficient

Figure A.21: Response of aerodynamic coefficients to angle of attach and elevator deflection at a Mach number of 0.4

optimization problem, with the six degrees of freedom equations of motion as a further constraint, can be solved using standard techniques, as in [206]. In the current framework, the DIDO code [5] [207] is used for the solution of the optimal problem, with aerodynamic forces and moments obtained from the look-up tables. Technical details can be found, for instance, in [208–210].

Two sets of manoeuvres were generated using the optimal control problem to demonstrate, first, a good comparison between the tabular model and the CFD solution for slow motions, and, then, to stress the limitations of the tabular model when confronted with flows exhibiting time-history effects. A variety of manoeuvres, two of which are illustrated in Fig. A.22, were simulated at low rate, and the solution of the optimal control problem was found using static tabular data. In all cases presented, the aerodynamic loads from the tabular model compared well with the time-accurate solution. The assumption of quasi-steady aerodynamics describes well the flow around the moving airframe, adapting instantaneously to changes in geometry attitude and without time-history effects influencing its development. The effect of increasing the angular rate for a given manoeuvre was then investigated. The manoeuvre was a pull-up with time-varying angle of attack, and was simulated initially at a pitch rate as low as $2.0°/s$. Whilst for $20.0°/s$ the inclusion of dynamic terms shifted the static prediction to match the time-accurate solution up to high angles of attack, discrepancies were observed at the higher end of the angle of attack range when the pitch rate was increased to $100.0°/s$. Under these circumstances, significant history effects due to vortical interactions are present as illustrated inspecting the vortex surface footprint.

[5] `http://www.elissarglobal.com/` [retrieved March 19, 2012]

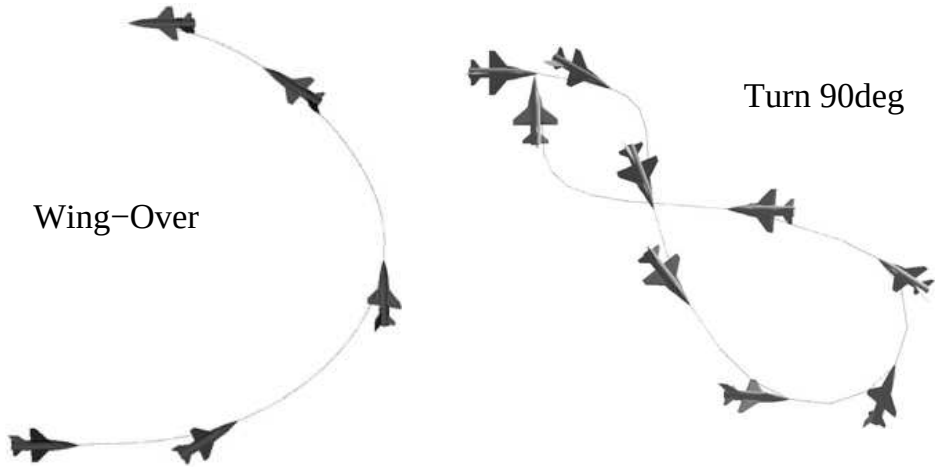

Figure A.22: Wing-over and a 90-degree turn manoeuvres were simulated for the SDM model in [23]

A.6 Ranger 2000 Aircraft

The framework for the replay of manoeuvres was tested for several aerobatic manoeuvres performed with the Ranger 2000 aircraft [183]. The influence of dynamic derivatives, however, was neglected in this study. This aircraft is a mid-wing, tandem seat military training aircraft with a turbofan engine with uninstalled thrust of $14.19\,kN$. A three-view representation of the Ranger 2000 aircraft is shown in Fig. A.23. Reference values, and mass and inertia properties are summarized in Table A.5. Conventional control surfaces are used.

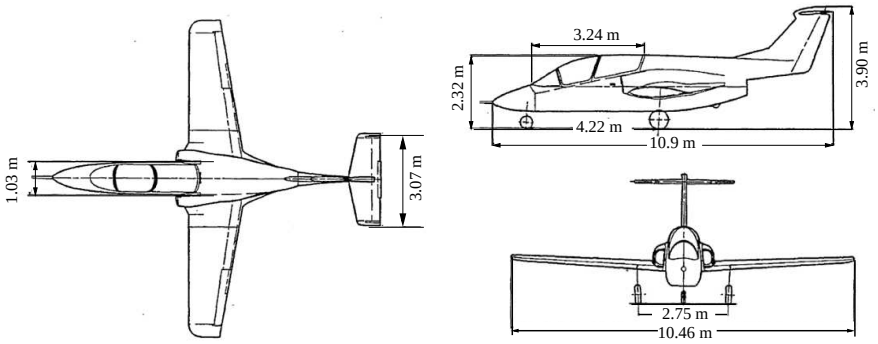

Figure A.23: A three-view of the Ranger 2000 aircraft

A block structured grid for the PMB solver was generated at Liverpool with 14.5 million points for the half-configuration. The flow was modelled using the Euler equations. Control surfaces were included to the grid, and a grid for a full-configuration was used for lateral manoeuvres. Deflected control surfaces are illustrated in Fig. A.24.

The complete aerodynamic database included the effects of angle of attack, Mach number, sideslip angle and the deflection of the three conventional control surfaces. In total, the aerodynamic dataset covered nearly 5900 flow conditions. The angle of attack

Parameter	Value
S	$15.5\,m^2$
b	$10.46\,m$
c	$1.545\,m$
d	$10.39\,m$
$MTOW$	$3765\,kg$
I_{xx}	$9.287 \times 10^3\,kg{\cdot}\,m^2$
I_{yy}	$13.584 \times 10^3\,kg{\cdot}\,m^2$
I_{zz}	$21.237 \times 10^3\,kg{\cdot}\,m^2$

Table A.5: Reference values and mass and inertia properties of the Ranger 2000 aircraft

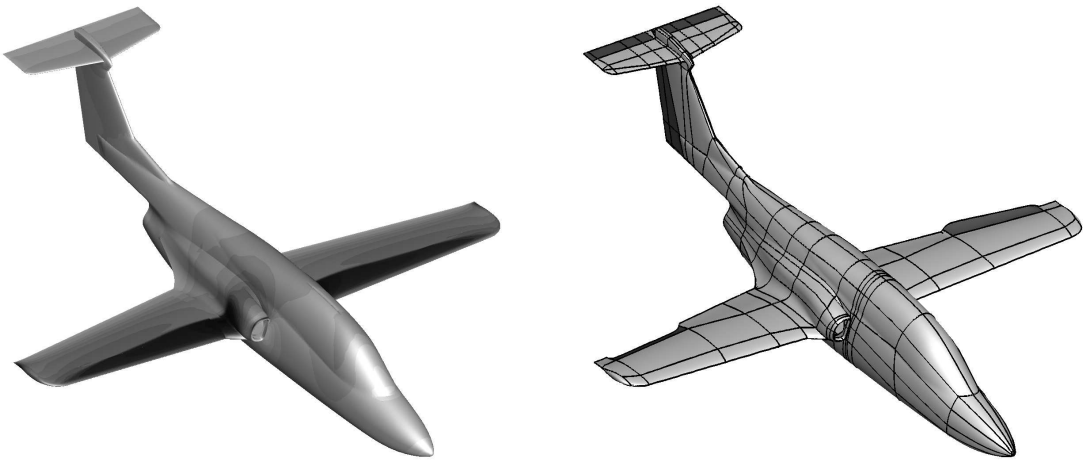

(a) Surface pressure distribution

(b) Deflected control surfaces

Figure A.24: Grid for the Ranger 2000 aircraft; the surface solution is obtained at $\alpha = 6.0°$ and $M = 0.8$

varied between $-10°$ and $12°$, the Mach number between 0.25 and 0.60 and the angle of sideslip up to $20°$. The deflection of the elevator and ailerons was limited between $-25°$ and $15°$, while the rudder was deflected up to $17.5°$. Cases for negative sideslip angles, negative rudder and ailerons deflections were not computed due to geometric symmetry. The run matrix included 23 separate values for the angle of attack, 8 for the Mach number and 9 for the sideslip angle. For the control surfaces, 9 separate values for the elevator and ailerons, and 5 for the rudder were selected.

The baseline table was created from scratch using sampling methodology based on the EIF criterion to efficiently identify non-linearities in the aerodynamic loads. A total of sixty-five CFD calculations was computed for the baseline table and extended to cover the 1656 different combinations of (α, M, β). Figure A.25 illustrates the distribution of sample points obtained with the EIF criterion in the three-parameter space, limited to positive values of the sideslip angle. The figure also shows surface plots of the

aerodynamic coefficients for variations in angle of attack and Mach number. Black cubes indicate CFD calculations at sample points. At low speed, the lift and moment coefficients have a linear behaviour and the drag coefficient behaves as a quadratic function of the angle of attack. As the angle of attack increases at the higher end of the Mach range, the shocks become stronger resulting in a backward shift of the aerodynamic centre.

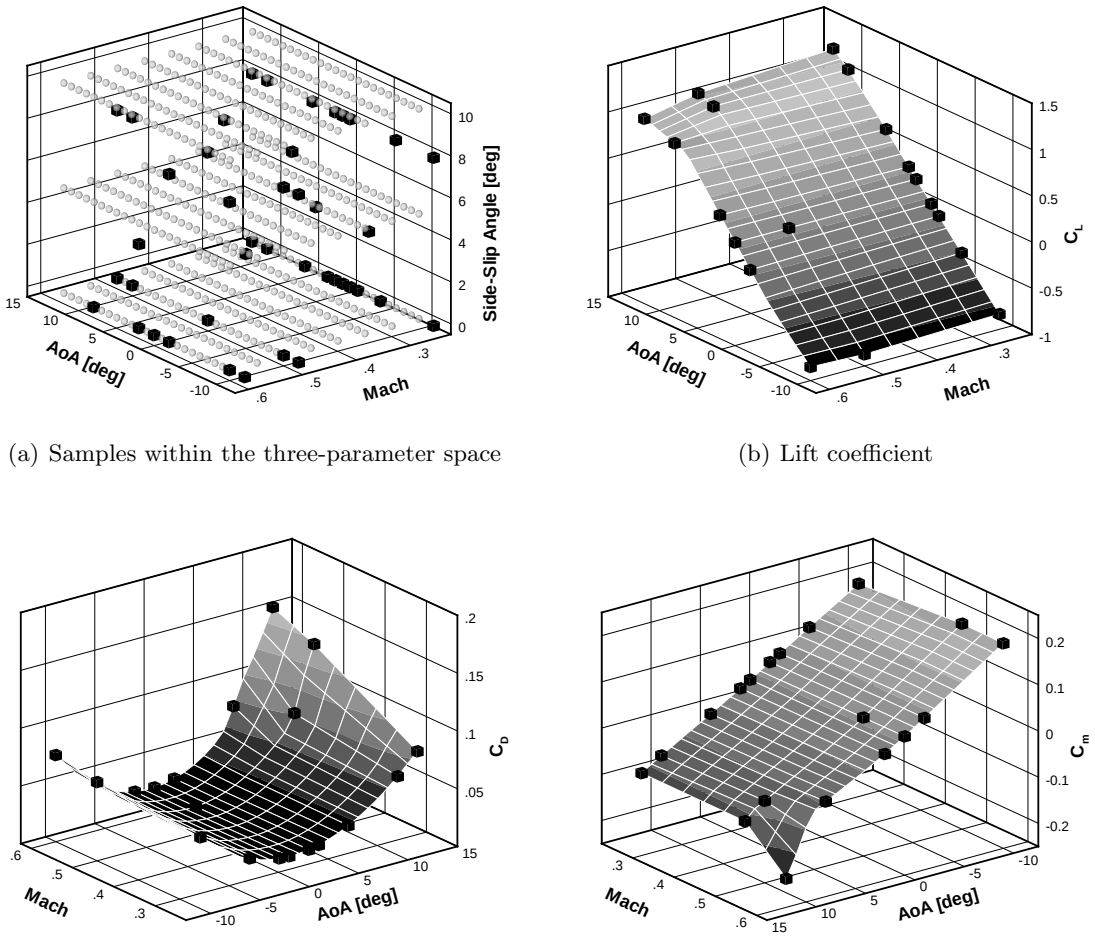

(a) Samples within the three-parameter space

(b) Lift coefficient

(c) Drag coefficient

(d) Pitching moment coefficient

Figure A.25: Response of aerodynamic coefficients to angle of attach and Mach number at zero sideslip angle; the black cubes indicate sample points

To include the aerodynamic increments due to the deflection of control surfaces, three tables were generated for the ailerons, elevator and rudder. CFD calculations were computed at an ensemble of chosen points, and co-kriging was used to update the baseline table with these solutions. Figure A.26 illustrates the position of the chosen sample points in the parameter space for the ailerons, elevator and rudder deflections at a Mach number of 0.25. Black squares indicate actual CFD runs. Calculations at zero deflection angles were made when creating the baseline table. Sample points

were uniformly distributed throughout the parameter space, as seen for the ailerons and for the rudder. A lack of samples at moderate angles of attack is observed for the elevator, and the distribution shown is clearly inadequate to capture any non-linear phenomena associated with the elevator deflection. As the interest in the study was focussed on replaying manoeuvres at subsonic flow, the coverage of the two-dimensional parameter space is poorer at higher Mach numbers. A total of 101 CFD analyses were run to populate an aerodynamic database consisting of nearly 5900 entries. Note that a validation of aerodynamic predictions against wind tunnel data was performed and showed agreement between the two sources in terms of static and control aerodynamic information.

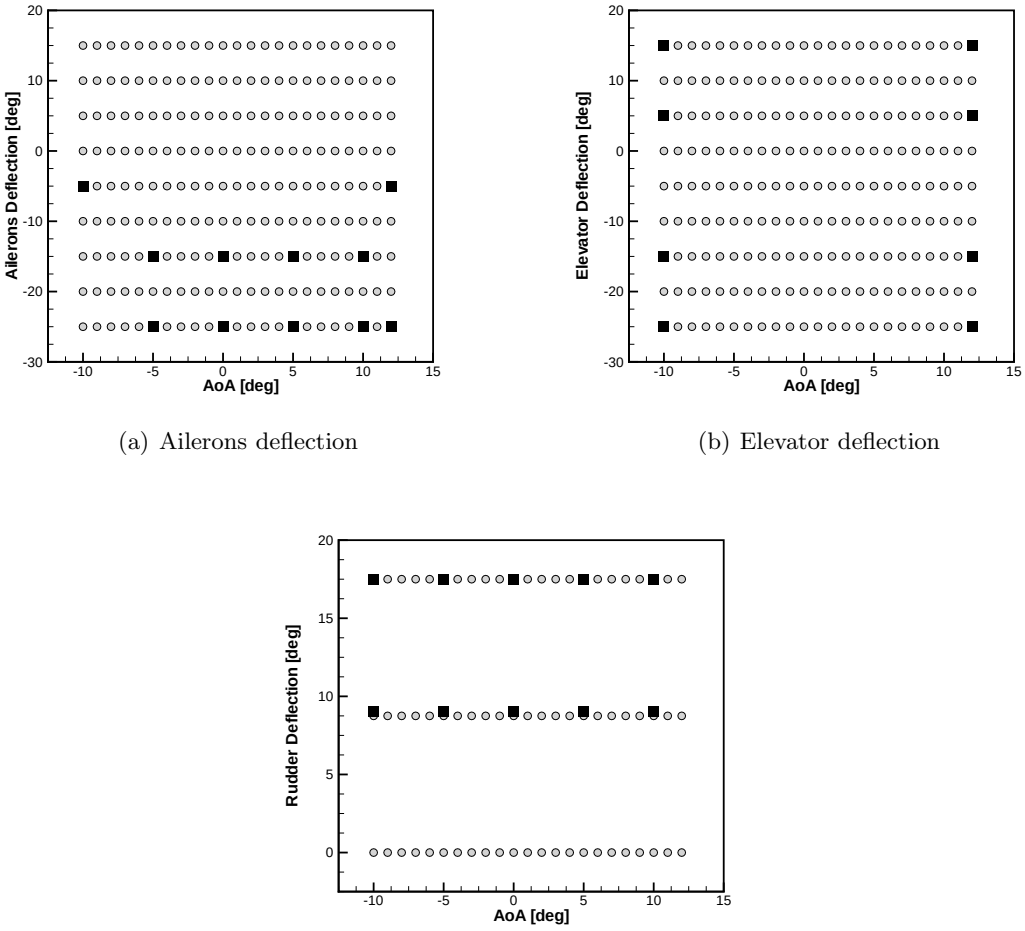

(a) Ailerons deflection

(b) Elevator deflection

(c) Rudder deflection

Figure A.26: Illustration of the aerodynamic tables for deflection of control surfaces at a Mach number of 0.25; black squares indicate sample points

The flight test data consists of all aerodynamic forces and moments with respect to the aircraft states, which include angle of attack, sideslip angle, Mach number, rotational rates, acceleration rates, elevator, rudder, control and the altitude of flight.

Various aerobatic manoeuvres were performed to demonstrate general aircraft handling qualities. These include Barrel Rolls, Clover Leafs, Immelmann Turns, inverted flight, Lazy Eights, Loops, and Split-S. The entry conditions and the time histories for each manoeuvre were provided by EADS military air systems. Figure A.27 illustrates the manoeuvres considered in reference [183].

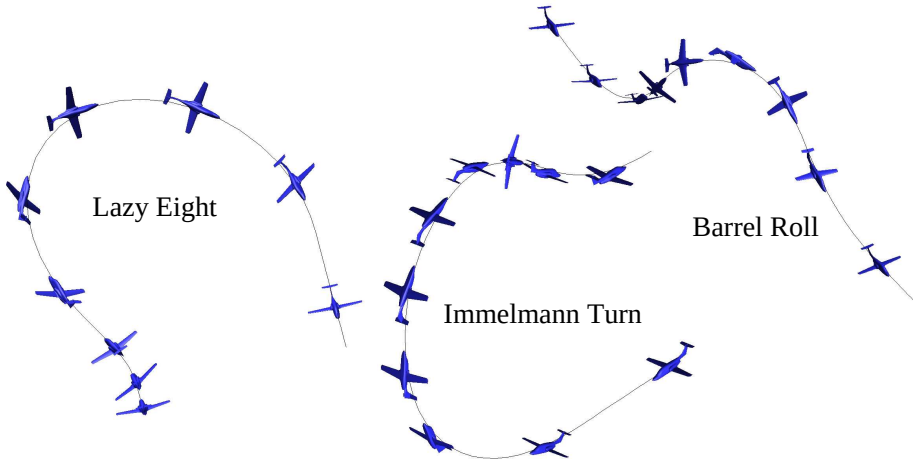

Figure A.27: Simulation of manoeuvres for the Ranger 2000 aircraft compared to flight test data

The time-accurate CFD solution corresponding to the time-optimal manoeuvre was calculated, and compared to the aerodynamic forces extracted from the tabular model. In all cases considered, the solutions from the look-up tables match the time-accurate solutions from the replay. This can be attributed to considering benign flight conditions which do not exhibit significant hysteresis effects, but illustrates the validity of the CFD framework for generating aerodynamic tables and replaying manoeuvres to test the aerodynamic database.

The framework of replaying manoeuvres using CFD was exercised with other configurations, including the Standard Dynamic Model [23] and an unmanned combat air vehicle model [211]. More details on the methodology and testcases can be found in reference [32]. The investigations presented suggest that the tabular model is adequate to represent the aerodynamics of manoeuvring aircraft in benign flow conditions. With topological changes in the flow, the underlying assumptions of linearity and time-invariance are not met, and a loss of accuracy can be experienced. It is worthwhile to investigate the application of alternative mathematical models. In reference [185], several low-order models were compared for ability to predict non-linear unsteady aerodynamic loads for a two-dimensional aerofoil under conditions of shock-induced separation. The model based on aerodynamic derivatives was also included. It was claimed that the training data plays a key role in the development of the model, and dependency upon model parameters was observed. With a lack of robustness, low-order models are

unlikely to replace the current model based on aerodynamic derivatives. The need for improvements opens up large opportunities in this research area.

A.7 Conclusions

Despite possible limitations, this appendix illustrates that CFD can now be used in a reasonably routine fashion for stability and control studies.

Appendix B

Applications of Indicial Aerodynamics

Extensive use of indicial aerodynamic functions in the study of manoeuvring lifting surfaces has been made, see for example Ref. [76]. The indicial aerodynamic response can be thought of as the aerodynamic response, as a function of time, to an instantaneous change in one of the conditions determining the aerodynamic properties of the system in a steady flow. The indicial theory stems from the assumption of linearity. This allows to compute the system response to a simple input function, and any desired output can be calculated from this known response by convolution. When the governing equations are linear, the response $y(t)$ to any forcing function $f(t)$, having a continuous derivative, is obtained by the convolution or Duhamel's integral

$$y(t) = f(0)\,\mathcal{A}(t) + \int_0^t \frac{d\,f(\tau)}{d\tau}\,\mathcal{A}(t-\tau)\,d\tau \tag{B.1}$$

where $\mathcal{A}$ indicates the indicial response to a step change function. The integral can also be written as

$$y(t) = \int_0^t f(\tau)\,\mathcal{H}(t-\tau)\,d\tau \tag{B.2}$$

where $\mathcal{H}$ is the indicial response to a unit-impulse function.

Being a mathematical concept, there are no direct means of measuring the indicial aerodynamic response by experiments. However, attempts were reported to relate experiments for oscillating flows back to the indicial response from the frequency domain [190]. For a compressible flow, there are no exact closed-form analytical solutions for all time. By use of linear piston theory [212], the initial values of the indicial response can be obtained, and the final values are given by a steady-state method. Exact analytical expressions of the indicial response to a step change in angle of attack, a step change in pitch rate and for the penetration into a sharp-edged gust in subsonic

compressible flow were obtained by Lomax [213]. More recently, CFD has been used as the source for the computation of indicial responses, and this is presented next.

Note that the identification of the aerodynamic response to a unit-impulse function has been performed using CFD without great success [214]. This can be attributed to the sensitivity of the response simulated to the time-step size of the unsteady simulation and to the dependence on the amplitude of the applied impulse. It was shown that inaccuracies in the impulse-based response degraded the prediction for any arbitrary input obtained by convolution. Therefore, the approach based on the identification of the unit-impulse response was not pursued in the framework presented.

B.1 Formulation

The first attempts to directly determine the indicial response by CFD were reported in Refs. [34,215]. It was suggested that the numerical simulation of a step change in some motion parameter was likely to present some challenges, as described below. To overcome these issues, previous approaches used an indirect method for the determination of the indicial response [36]. A smoothed function, continuous in time, was preferred to a step change function because the flow is not exposed to any discontinuites. The indicial response of the integrated loads was extracted using the Laplace transform, but in the transformation, insights into the flow development were not attainable.

An alternative is based on the direct determination of the indicial response caused by the step change, but this poses some questions. If the step change is applied as a boundary condition (moving the grid), numerical oscillations may be experienced and non-physical features in the flow observed because of the very large time derivative. A valid consideration is that changes in one parameter may affect another input. Consider, for example, the case of an aerofoil subject to a step change in angle of attack. Because the aerofoil also experiences a very large pitch rate at the initial time, the indicial response computed will be representative of the combined effects of the two parameters. A method was suggested in Refs. [34, 215]. The underlying idea of the field-velocity approach is the equivalence between a moving aerofoil in a stationary flow, and the moving flow over a stationary aerofoil. In this case, the step change in a motion parameter is incorporated into the CFD solver by modification of the grid velocity throughout the flow domain. The grid velocity is the velocity of a grid point during the unsteady motion of the aerofoil. The step change in any input can be thought of as a step change in grid velocity over the entire flow domain. The indicial response to a pitch rate is computed by imposing a grid velocity that varies linearly with the distance from the rotation axis. This avoids the need to move the mesh, and leads to a natural decoupling of the input parameters that influence the aerofoil loading.

The PMB code was enhanced to simulate the time histories of the aerodynamic loads to a step change in any motion parameter and to an arbitrary gust shape. The

two direct methods described above were used to compute the response to a step change in angle of attack. The approach based on grid motion is referred to hereafter as BCA, whereas the field-velocity approach denoted by FVA. The latter was also used for the gust response.

B.2 Validation

Numerical results are compared to exact closed-form expressions obtained for a flat plate [213]. To reduce the effects of thickness, a NACA 0006 aerofoil was used. The computational mesh for the solution of the Euler equations is similar to that described in Chapter 4.3. In all cases, the unsteady simulations used five thousand time steps for a non-dimensional time duration of thirty. Note that calculations were repeated for a smaller time-step, with identical results obtained. It is worth noting that the non-dimensional time used in the analytical formulation below is given by $s = 2\,t\,U_\infty/c$. This is in contrast to the convention commonly adoped in CFD, where the non-dimensional time is defined as $t^* = t\,U_\infty/c$.

Shown in Fig. B.1 is the indicial response of the lift coefficient for a step change in angle of attack, $\Delta\alpha = 4.58°$, for several values of Mach number. For all time, numerical results obtained by grid rotation are virtually identical to results computed using the field velocity approach. The indicial response consists of two distint regions, separated by an intermediate overlapping area. The initial part of the response is representative of the impulsive motion of the body, and of the resulting pressure difference between the upper and lower surfaces where the formation of a compression and expansion wave is observed. The effects of the initial non-circulatory loading are confined within a few chord lengths of the distance traveled. The initial values of the indicial response are given by linear piston theory

$$\frac{C_L\,(0)}{\Delta\alpha} = \frac{4}{M} \tag{B.3}$$

After the decay of initial transients, the response converges asymptotically to the steady-state value correponding to the effective angle of attack caused by the step change. The asymptotic value of the circulatory loading can be obtained by linearized quasi-steady theory

$$\lim_{s\to\infty} \frac{C_L\,(s)}{\Delta\alpha} = \frac{2\,\pi}{\sqrt{1\,-\,M^2}} \tag{B.4}$$

Table B.1 summarizes analytical and numerical results of the asymptotic values of the indical response. Increased differences for the highest Mach number are likely because of non-linear compressibility effects captured by CFD calculations. The Wagner function gives the indicial build-up of the circulatory part of the lift. It accounts for the influence

Mach	Quasi-Steady	CFD
0.3	6.58	6.74
0.5	7.25	7.39
0.8	10.47	12.17

Table B.1: Asymptotic values of the indicial response of lift coefficient for a step change in angle of attack, $C_L(\infty)/\Delta\alpha$

of the shed wake, and is known exactly in terms of Bessel functions. For a practical evaluation of the Duhamel integral, the Wagner function is expressed as an exponential approximation

$$\phi(s) = 1 - \Phi_1 e^{-\varepsilon_1 s} - \Phi_2 e^{-\varepsilon_2 s} \tag{B.5}$$

with the coefficients $\Phi_1 = 0.165$, $\Phi_2 = 0.335$, $\varepsilon_1 = 0.0455$, and $\varepsilon_2 = 0.3$ from R. T. Jones [216]. Several approximations are available in the literature, as given by Garrick [217] and W. P. Jones [218]. Observe that $\phi(0) = 0.5$. No closed-form analytical expressions are available in the intermediate overlapping region. However, the similarity of the results presented in Fig. B.1 with CFD calculations from Ref. [34] is noted.

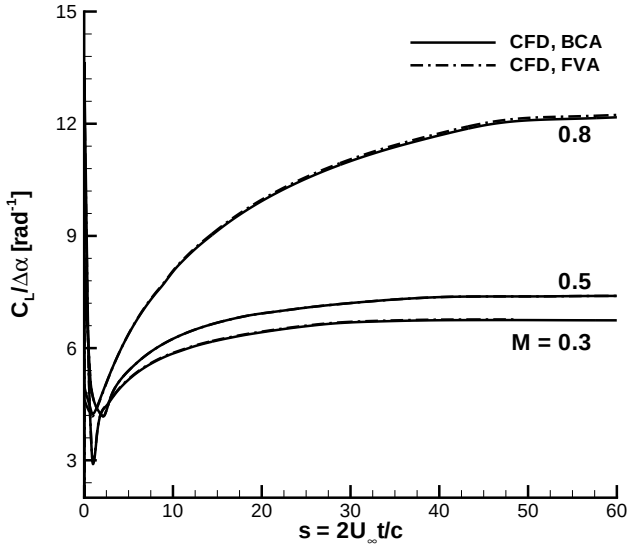

Figure B.1: Indicial response of lift coefficient for a step change in angle of attack ($\Delta\alpha = 4.58°$)

An exact analytical expression was obtained by Lomax [213] for a flat plate in a linearized compressible flow. The expression is valid for small times, less than a chord of

the distance traveled,

$$\frac{C_L(s)}{\Delta\alpha} = \frac{4}{M}\left(1 - \frac{1-M}{2M}\,s\right) \qquad \text{for } 0 \le s \le \frac{2M}{(1+M)} \tag{B.6}$$

Figure B.2 conveys a comparison between the above expression and numerical results. The application of the analytical formulation to the highest Mach number is suspect. A good correlation of numerical data to CFD-based simulations from Ref. [34] is observed.

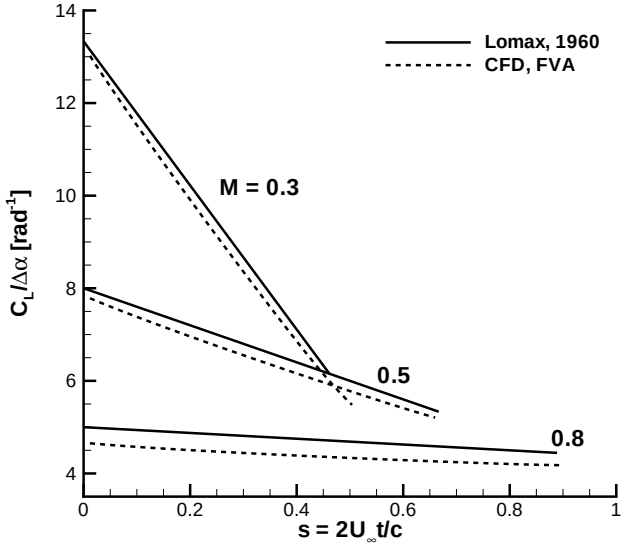

Figure B.2: Indicial response of lift coefficient for a step change in angle of attack for small times ($\Delta\alpha = 4.58°$); reference data are from Lomax [213]

Next, the response to a sharp-edged gust is considered. At the initial time step, the gust front is located at the aerofoil leading-edge. For successive time steps, the gust advances toward the aerofoil and the gust velocity is assigned to all points of the flow domain of coordinate $\bar{x} \le s$, where $\bar{x}$ is the non-dimensional length referred to the aerofoil semichord. A gust velocity of intensity $w_g/U = 0.08$ was selected to induce a net change in angle of attack identical to the previous case. The Küssner function gives the lift build-up for the penetration into a sharp-edged gust. Like the Wagner function, it is known exactly in terms of Bessel functions, but for practical calculations, it is convenient to approximate the Küssner function using an exponential form

$$\psi(s) = 1 - \Psi_1\, e^{-\varepsilon_3 s} - \Psi_2\, e^{-\varepsilon_4 s} \tag{B.7}$$

where the coefficients $\Psi_1 = 0.5792$, $\Psi_2 = 0.4208$, $\varepsilon_3 = 0.1393$, and $\varepsilon_4 = 1.802$ are taken from Ref. [219]. Note that $\Psi(0) = 0$. Figure B.3 shows the lift response for the penetration into a sharp-edged gust. The CFD-based solution was normalized by the

asymptotic value of the lift coefficient, and was obtained at Mach number 0.20. Overall, a good agreement is observed. For increasing Mach number, increasing differences between CFD and the Küssner function are expected due to compressibility effects. Decreasing the Mach number results in the appearance of oscillations of small entity in the numerical solution as the gust travels over the aerofoil surface, as shown in the inset. This phenomenon has been reported in a previous study [220], and attributed to the convergence process as the gust moves between two adjacent grid points. For small

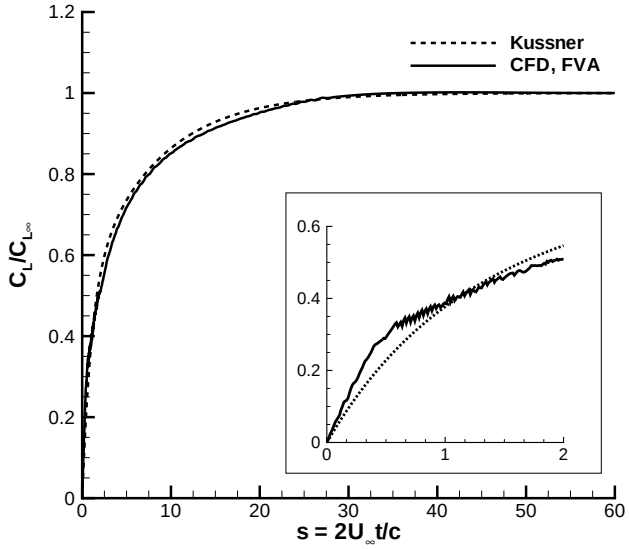

Figure B.3: Indicial response of lift coefficient for a sharp-edged gust at Mach number 0.20 normalized by its asymptotic value ($w_g/U = 0.08$)

times, a closed-form expression was given by Lomax [213] for the penetration into a sharp-edged gust as

$$\frac{C_L(s)}{w_g/U} = \frac{2\,s}{\sqrt{M}} \qquad \text{for } 0 \leq s \leq \frac{2\,M}{1+M} \tag{B.8}$$

Figure B.4 shows the computed and analytical results for small times. At lower Mach numbers, results are virtually identical. At the largest Mach number, differences are attributable to compressibility effects not account for in the analytical formulation.

Results for a sharp-edged gust travelling at constant horizontal speed u_g were also computed. The gust can either advance toward or away from the aerofoil. This is quantified in terms of the advance ratio

$$\lambda = \frac{M}{M + u_g/a} \tag{B.9}$$

where a indicates the speed of sound. For a stationary gust, $\lambda = 1$, and for a step

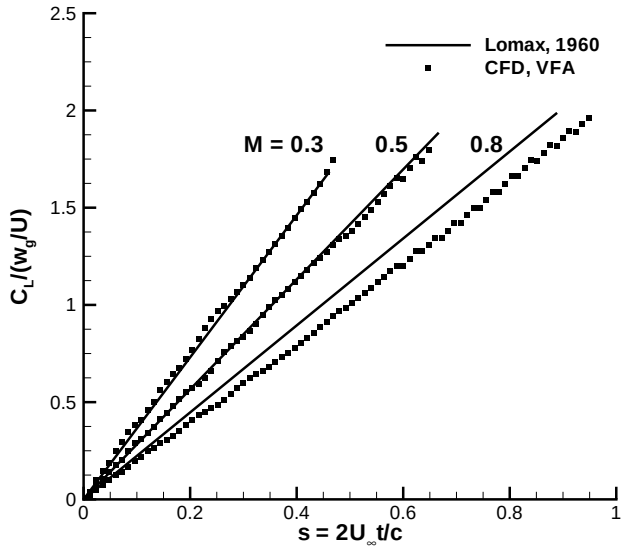

Figure B.4: Indicial response of lift coefficient for a sharp-edged gust for small times ($w_g/U = 0.08$); reference data are from Lomax [213]

change in angle of attack λ approaches zero. Responses of lift coefficient for several values of the advance ratio are shown in Fig. B.5. Results are in agreement with those presented in Ref. [220].

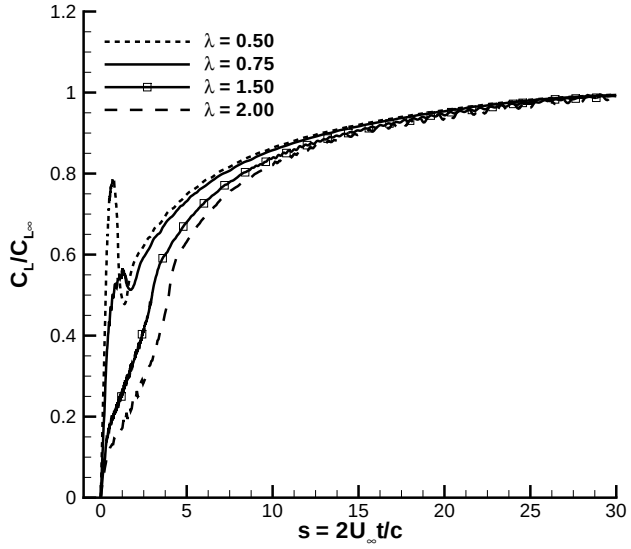

Figure B.5: Indicial response of lift coefficient for a moving sharp-edged gust at Mach number 0.20 normalized by its asymptotic value ($w_g/U = 0.08$); the solution for $\lambda = 1$ is not plotted, see Fig. B.3

B.3 Prediction

With the computation of indicial aerodynamic responses demonstrated above, the prediction of the linear unsteady aerodynamic loads for any arbitrary input time history can be achieved using Eq. (B.1). For the results presented, two deterministic gust models were considered. A sinusoidal gust is expressed as

$$W_g(s) = \frac{w_g}{U} \sin\left(\frac{\pi}{\tau_g} s\right) \tag{B.10}$$

and a one-minus-cosine gust function as

$$W_g(s) = \frac{w_g}{2U} \left(1 - \cos\left(\frac{\pi}{\tau_g} s\right)\right) \tag{B.11}$$

for $0 \leq s \leq 2\tau_g$. The term τ_g indicates the gust gradient. CFD calculations were run using the field velocity approach.

Numerical results are shown in Fig. B.6 for gusts of different wavelengths at two values of Mach number (0.2 and 0.7). The time-accurate CFD simulation is the reference solution for two convolution models. A first convolution model was generated from the CFD-based indicial response to a sharp-edge gust at each Mach number. A second convolution model was constructed based on the Küssner function. The testcase illustrated in Fig. B.6(a) is for a sinusoidal gust of 10 chords at Mach number 0.2. The convolution with the closed-form function is similar in behaviour to CFD results. Differences are representative of those arising in the indicial response between the two models, as seen in Fig. B.1. The CFD-based convolution response is identical to the reference solution. This consolidates the introduced capability of the CFD solver to simulate gust responses and the adequacy of the CFD-based indicial response to serve as a reduced-order model for predicting linear responses to arbitrary gust inputs. The perfect agreement also exemplifies the linearity of the problem. Figure B.6(b) illustrates the results for a one-minus-cosine gust of 25 chords. The similarity of the results computed with the previous testcase is not unexpected because linear aerodynamics is a dominant effect. A more challenging testcase is proposed in Fig. B.6(c) for a Mach number 0.7. For compressible flows, there is an approximate exponential form of the Küssner function, of the form

$$\psi(s) = b_0 + b_1 e^{-\beta_1 s} + b_2 e^{-\beta_2 s} + b_3 e^{-\beta_3 s} \tag{B.12}$$

and this was used in the corresponding convolution model. The coefficients are tabulated in Ref. [221] (taken from Ref. [222]) for several values of Mach number. At Mach number 0.7, $b_0 = 1.400$, $b_1 = -0.563$, $b_2 = -0.645$, $b_3 = -0.192$, $\beta_1 = 0.0542$, $\beta_2 = 0.3125$, and $\beta_3 = 1.474$. The increased gust intensity and the higher Mach num-

ber cause the formation of a shock wave on the upper surface, which moves downstream up to midchord as the aerofoil penetrates into the gust field. Then, the shock moves toward the leading-edge and disappears. The lift coefficient dynamic dependence is not distorted with respect to the subsonic case. The convolution model with the Küssner function in Eq. (B.12) has increasing differences from the CFD solution when the shock is present, $s > 15$. The CFD-based indicial response was computed at Mach number 0.7 for a sharp-edge gust of intensity $w_g/U = 0.035$. There are differences between the CFD-based convolution model and the time-accurate solution, and this suggests that the indicial formulation starts to loose its potential when boring into a small source of non-linearity. In this case, the error in the CFD-based prediction is within 3% of the maximum value of the reference solution.

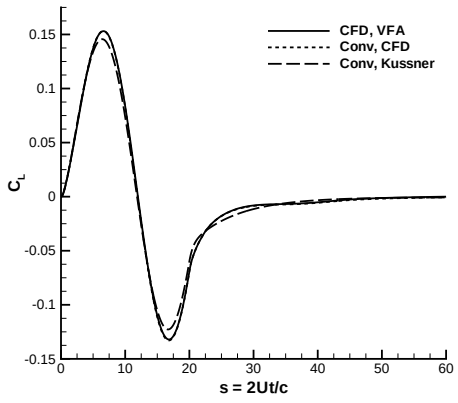

(a) Sinusoidal gust, $M = 0.2$

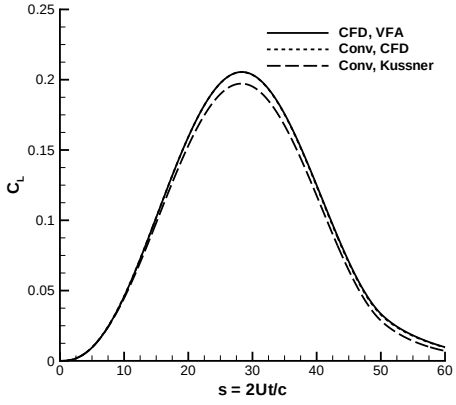

(b) One-minus-cosine gust, $M = 0.2$

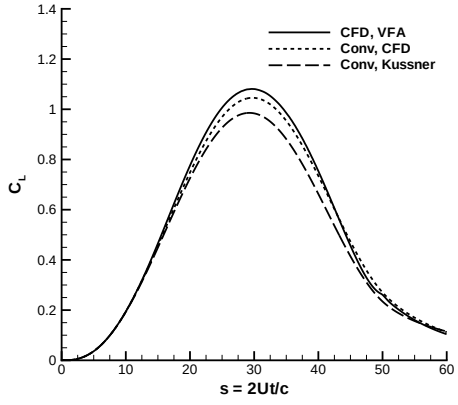

(c) One-minus-cosine gust, $M = 0.7$

Figure B.6: Lift dynamic dependence from unsteady CFD calculations and two convolution models in response to gust of different shapes; in (a), $\tau_g = 10$ and $w_g/U = 0.08$; in (b), $\tau_g = 25$ and $w_g/U = 0.08$; and in (c), $\tau_g = 25$ and $w_g/U = 0.14$

B.4 Conclusions

Based on the results presented, the indicial theory applied to unsteady aerodynamic problems is a simple but powerful predictive tool. The ability to predict the response to an arbitary input comes at the expense of linearity, which is the major limitation of this approach. The inclusion of the field velocity approach into an existing CFD solver is straighforward and well suited to the determination of indicial responses and to the simulation of gust problems. Results presented confirm this. The point to address, however, is that the indicial approach in combination with CFD may be not attractive when extended to non-linear cases. A computational challenge is the calculation of indicial responses at several values of Mach number and angle of attack for a sufficient duration time. This makes the non-linear indicial aerodynamics to loose appeal when CFD is the source of the data. Therefore the extension to a non-linear formulation was not pursued. Finally, note that the concept of field velocity approach is well suited to the determination of quasi-steady dynamic derivatives. By superimposing to the oncoming uniform flow a grid velocity which varies linearly with the distance from the rotation axis, the derivative of the aerodynamic loads with respect to the angular rate, e.g. C_{L_q}, can be predicted from two steady-state runs.

Appendix C

Multi-Linear Interpolation

Consider a regular Cartesian parameter space in d-dimensions, and denote $\mathbf{x} = (x_0, x_1, \ldots, x_{d-1})$ the point at which the evaluation of the function $f : \mathbb{R}^d \to \mathbb{R}$ is desired. The hypercube, which bounds this point, has 2^d points, $\mathbf{z}_i = (z_0, z_1, \ldots, z_{d-1})_i$, at which the values of the function are known. For convenience, map the bounding hypercube to the interval $[0, 1]^d$. The interpolated function, $\tilde{f}$, is obtained from the known values of f at the corners of the hypercube

$$\tilde{f}(\mathbf{x}) \approx \sum_{i=0}^{2^d-1} f(\mathbf{z}_i) \prod_{j=0}^{d-1} \Big(1 - (x_j - z_{ji})\Big) = \sum_{i=0}^{2^d-1} f(\mathbf{z}_i)\, w_i(\mathbf{x}) \tag{C.1}$$

where $f(\mathbf{z}_i)$ are the ordinates to $\tilde{f}(\mathbf{x})$ at 2^d points, and w_i is the basis function associated with the i-th corner point. The term $w_i(\mathbf{x})$ indicates the weight of the i-th corner point in the computation of $\tilde{f}(\mathbf{x})$.

Note that the computation in Eq. C.1 requires 2^d products, each of which is itself the product of d terms involving 2 operations. Hence, it requires $\mathcal{O}\left(2^{d+1}\right)$ operations.